5-3-2024

The Morphology, Spatial Distribution, and Collapse Mechanisms of Volcanoes on Venus

Rebecca Mary Hahn
Washington University in St. Louis

WASHINGTON UNIVERSITY IN ST. LOUIS

Department of Earth, Environmental, and Planetary Sciences

Dissertation Examination Committee:
Paul K. Byrne, Chair
Jeffrey J. Gillis-Davis
Bradley L. Jolliff
Michael J. Krawczynski
Rita Parai

The Morphology, Spatial Distribution, and Collapse Mechanisms of Volcanoes on Venus

by
Rebecca Mary Hahn

A dissertation presented to
Washington University in St. Louis
in partial fulfillment of the
requirements for the degree
of Doctor of Philosophy

May 2024
St. Louis, Missouri

Table of Contents

List of Figures v
List of Tables vii
Acknowledgments viii
Abstract of the Dissertation x
Chapter 1: Introduction 1
References 3
Chapter 2: A Morphological and Spatial Analysis of Volcanoes on Venus 5
Abstract 5
2.1 Introduction 6
2.1.1 Volcanism on Venus 7
2.1.2 Rationale 8
2.2 Methods 9
2.2.1 Mapping 9
2.2.2 Morphological Analysis 11
2.2.3 Spatial Clustering 16
2.2.2 Spatial Statistics 19
2.3 Results 23
2.3.1 Shield Volcano Catalog 23
2.3.2 Volcanic Field Catalog 26
2.3.3 Morphological Analysis 27
2.3.4 Spatial Statistical Analysis 28
2.4 Discussion 34
2.4.1 Morphological 34
2.4.2 Spatial Analysis 40
2.5 Conclusions 53
References 54
Chapter 3: A Global Survey of Gravitationally Deformed Volcanoes on Venus 67
Abstract 67

3.1 Introduction 68
3.1.1 Rationale 69
3.2 Examples of Gravitationally Deformed Volcanoes 69
3.2.1 Landsliding 69
3.2.2 Sector Collapse 71
3.2.3 Spreading 71
3.2.4 Sagging 72
3.3 Methods 74
3.3.1 Structural Mapping 74
3.3.2 Spatial Analysis 77
3.4 Results 78
3.4.1 Deformed Volcano Morphological Analysis 78
3.4.2 Deformed Volcano Spatial Analysis 80
3.5 Comparative Analysis 85
3.5.1 Landsliding Case Studies 86
3.5.2 Sector Collapse Case Study: Vostrukha Mons on Venus and Socompa on Earth 96
3.5.3 Spreading Case Study: Unnamed volcano on Venus and Tharsis Tholus on Mars 99
3.5.4 Sagging Case Study: Tepev Mons on Venus and Ascraeus Mons on Mars 104
3.6 Conclusions 110
References 112
Chapter 4: Kernel Density Analysis for Predicting the Locations of Future Volcano Formation on Venus 126
Abstract 126
4.1 Introduction 127
4.1.1 Study Sites 130
4.2 Methods 137
4.2.1 Kernel Density Estimation 137
4.2.2 Volcano Alignment Analysis 140
4.3 Results 141
4.3.1 Volcano Formation Probability Maps 142
4.3.2 Volcano Alignments 144

4.4 Discussion 148
4.4.1 Regions with Recent Geologic Activity 148
4.4.2 Regions with Volcano Alignments 149
4.4.3 High-volcano-spatial-density-regions 152
4.4.4 Regions Associated with Extensional Structures 154
4.5 Conclusions 156
References 158
Appendix 168
A.1 Datasets used in Chapter 2 168
A 1.1 Brief Description of Datasets used in Chapter 2: 168
A.2 Datasets used in Chapter 3 172
A 2.1 Brief Description of Datasets used in Chapter 3: 172
A.3 Datasets used in Chapter 4 174
A.3.1 Volcano Alignment Analysis Parameters 174

List of Figures

Figure 2.1: Examples of varying-sized edifices on Venus 6
Figure 2.2: Volcano mapping methodology 10
Figure 2.3: Topographic profiles of three large volcanoes 12
Figure 2.4: Schematic profile of a large volcano 14
Figure 2.5: Global map of volcanoes and volcanic fields on Venus 22
Figure 2.6: Volcano size-frequency distributions 24
Figure 2.7: Volcano spatial density estimates 30
Figure 2.8: Global map of volcanic field orientation 32
Figure 2.9: Plots of large volcano morphological properties 35
Figure 2.10: Plots of intermediate-sized volcano morphological properties 37
Figure 2.11: Plots of volcano morphological properties within stereo-derived DEMs 39
Figure 2.12: Global map of crustal thickness on Venus 42
Figure 2.13: Relationships between tectonic structures and volcanic fields 46
Figure 2.14: High-volcano-spatial-density regions compared to other datasets 47
Figure 3.1: Deformed volcano structural sketches 70
Figure 3.2: Global map of deformed volcanoes on Venus 80
Figure 3.3: Deformed volcanoes compared to geophysical datasets for Venus 82
Figure 3.4: Examples of landsliding volcanoes 87
Figure 3.5: Detailed structural map of unnamed Venusian volcano 95
Figure 3.6: Examples of sector collapse volcanoes 96
Figure 3.7: Detailed structural map of Vostrukha Mons, Venus 98
Figure 3.8: Examples of spreading volcanoes 100
Figure 3.9: Examples of sagging volcanoes 105
Figure 4.1: Vent opening probability map of Mount Etna, Italy 128
Figure 4.2: Global map of polygon boundaries for volcano formation probability maps 131
Figure 4.3: Vent opening probability maps for nine topographic rises on Venus 143
Figure 4.4: Vent opening probability maps for nine volcanic fields on Venus 144
Figure 4.5: Polar histograms of intervent alignments at nine topographic rises on Venus 146
Figure 4.6: Polar histograms of intervent alignments at nine volcanic fields on Venus 147

Figure 4.7: Examples of dominant volcano alignments on Venus 150
Figure 4.8: Global map of highest probability regions for new volcano formation on Venus .. 155
Figure 4.9: ESA EnVision ROI's compared to volcano formation probability..... 157

List of Tables

Table 2.1: Total number of features in the global catalog of volcanoes and volcanic fields..... 23
Table 2.2: Morphological properties of volcanoes >5 km in diameter..... 27
Table 2.3: Morphological properties of volcanoes >50 km in diameter within Herrick DEMs... 27
Table 3.1: Morphological structures associated with styles of volcano deformation..... 74
Table 3.2: Summary statistics for deformed volcanoes..... 76
Table 3.3: Comparison of deformed volcanoes with geophysical datasets 78
Table 3.4: Parameters used to calculate sagging parameter for Tepev and Ascraeus Montes ... 108
Table 4.1: Volcano formation probability map properties for topographic rises 132
Table 4.2: Volcano formation probability map properties for volcanic fields 136
Table 4.3: Kernel density optimization algorithm SAMSE properties for topographic rises..... 141
Table 4.4: Kernel density optimization algorithm SAMSE properties for volcanic fields..... 142

Acknowledgments

I would like to acknowledge and thank my research advisor, Paul Byrne, for his guidance, and mentorship over the last five years, and for introducing me to the Magellan datasets during my Master's research and inspiring my love for Venus. I would also like to thank my committee members for their thoughtful comments and feedback on my research over the years, which has helped me refine and improve my analyses and results. I would also like to thank the NASA Planetary Data System for access to their archives, which made my research possible. Lastly, I would like to thank my mom, my dad, my brother, my partner Dan, and my other family members for their unwavering support, and for listening to me ramble on about Venus and volcanoes for the past 6 years.

The mapping phase of this research was supported by a graduate research fellowship from the North Carolina Space Grant Consortium.

Rebecca M. Hahn

Washington University in St. Louis

May 2024

Dedicated to my mom and dad who have helped me move my rock and mineral collection (>100 specimens) on many occasions, and somehow still love and support me.

ABSTRACT OF THE DISSERTATION

The Morphology, Spatial Distribution, and Collapse Mechanisms of Volcanoes on Venus

by

Rebecca Mary Hahn

Doctor of Philosophy in Earth, Environmental, and Planetary Sciences

Washington University in St. Louis, 2024

Professor Paul K. Byrne, Chair

Radar imagery collected by NASA's Magellan spacecraft enabled the recognition and classification of volcanic features and structures across Venus far beyond the scope of earlier missions. These datasets revealed volcanoes that range in size from <5 km to well over 100 km in diameter. Volcanism is clearly a major, widespread process on Venus, and is a principle expression of the planet's secular loss of interior heat. For my doctoral work, I utilized ESRI's ArcMap and ArcGIS Pro to develop a detailed global catalog of volcanoes across Venus to improve our understanding of the morphology, spatial, distribution, and evolution of volcanism on the second planet.

Chapter 2 introduces the creation and implementation of my global catalog of volcanoes and volcanic fields on Venus. This new global dataset includes ~85,000 edifices, ~99% of which are <5 km in diameter and are geographically widespread across the entire planet. With this catalog, I developed an automated approach to delineating volcanic fields—high spatial concentrations of small volcanoes—and also noted a dearth of volcanoes 20–100 km in diameter, which could be related to the eruption rate and/or availability of the underlying magma supply.

Chapter 3 focuses on a unique subset of 162 volcanoes on Venus that appear to have undergone gravitational deformation. These deformed edifices are distributed globally, are situated at a range of elevations, are spatially proximal to a variety of tectonic structures, and are associated with various crustal thickness values, which together suggest that there are numerous drivers of volcano deformation on Venus. Furthermore, I note examples of flank terraces on Tepev Mons, a structural indicator of volcano sagging that has not yet been documented on Venus.

Lastly, Chapter 4 employs kernel density estimation as a tool at nine topographic rises, and nine volcanic fields across Venus to delineate regions where future volcano formation could occur, based on the locations of edifices ≤20 km in diameter from our global catalog developed in Chapter 2. These resulting volcano-formation probability maps reveal that the intensity of volcanism producing volcanoes ≤20 km in diameter in the Beta-Atla-Themis (BAT) region, an area well-known for its enhanced volcanism (Airey et al., 2017), is lower than at topographic rises across the rest of the planet. These maps can also be used to identify specific regions across Venus that future missions such as EnVision and VERITAS can image using their higher-resolution radars and thus search for newly formed volcanoes between the time of those missions and when the Venus surface was originally mapped by Magellan. Based on my analysis, I conclude that these missions should target specific regions of high-volcano-spatial density in and around Atla, Imdr, Themis, and Dione Regiones.

Chapter 1:
Introduction

Global-scale interior processes such as magmatism contribute to a planet's loss of global heat, and are linked to its thermal evolution and geological history (Solomon and Head, 1982; Ivanov and Head, 2013). Volcanism on Venus is ubiquitous, with flows from extrusive volcanism covering ~80% of the surface (Ivanov and Head, 2013), and at least 85,000 volcanic constructs spread across the entire planet (Hahn and Byrne, 2023). In this doctoral work, I utilize my global catalog of volcanoes and volcanic fields on Venus (Hahn and Byrne, 2023) to assess the morphology and spatial distribution of volcanoes and deformed volcanoes across Venus, and to predict the location of future volcanoes at topographic rises across the planet. The goal of the work done for this chapter was to improve our understanding of how and where volcanoes form and deform across Venus, adding to the existing knowledge we have of volcanic behavior on other terrestrial bodies.

In chapter two, I used ESRI ArcMap 10.7.1 and ArcGIS Pro 2.7 software to we develop an extensive dataset of volcanoes on Venus using with the Magellan SAR FMAP (full-resolution radar map) left- and right-look global mosaics (Pettengill, 1991). With this global dataset, I analyzed the geometry of volcanoes >5 km in diameter by calculating their mean basal diameter, area, and aspect ratio, and was able to calculate the height of edifices >50 km in diameter. Furthermore, for a subset of volcanoes >50 km in diameter covered by stereo-derived digital elevation models (DEMs) (Herrick, 2020), I was also able to estimate volcano volume. The spatial distribution of volcanoes and orientation of volcanic fields was assessed through kernel density

analysis (Silverman, 1998) and directional distribution analysis, respectively. The distribution and orientation of volcanoes can provide details on the size and shape of the underlying magma bodies, as well the magma production rate (Connor, 1990). The purpose of this chapter was to place constraints on models of Venus' evolution by analyzing the morphological and spatial patterns of volcanoes identified in my global catalog.

Chapter three is focused on a subset of 162 volcanoes from that global catalog (Hahn & Byrne, 2023) that have undergone gravitational deformation. I classified these deformed edifices into four main categories based on associated deformational structures: landsliding, sector collapse, spreading, and sagging. To better evaluate the mechanisms influencing volcano collapse on Venus, I conducted proximity analysis to identify any nearby tectonic (e.g., rifts) or volcano-tectonic (e.g., coronae) structures that on the basis of superposition relations may have influenced deformed volcano evolution. Furthermore, I compared typical examples of Venusian deformed volcanoes from those four main categories to similarly deformed volcanoes on Earth and Mars to gain insight into collapse mechanisms on Venus. In this part of my doctoral research, I sought to use structural and spatial analysis of deformed volcanoes, along with detailed comparative studies, to quantify the types and possible drivers of volcano gravitational collapse on Venus.

In Chapter four, I employ kernel density analysis (Silverman 1988) as a method for predicting the possible locations of future volcano formation across nine Venusian topographic rises and nine volcanic fields, based on the distribution of past edifices at those sites (Connor & Connor, 2009; Germa et al., 2013). Topographic rises are thought to be situated atop upwelling mantle, and thus represent some of the most promising locations for ongoing or future eruptive activity. After generating volcano-formation probability maps for each rise and field, I augmented my geospatial analysis with geological information related to the locations of recent volcanism

from thermal and radar emissivity studies, edifice alignments, and areas with high spatial densities of volcanoes. Volcano formation probability maps developed in this study can be used to identify regions that are statistically likely to host new edifice formation across Venus and can be verified by future missions such as NASA's VERITAS (Smrekar et al., 2022), and ESA's EnVision (Ghail et al., 2018).

Chapters two (Hahn & Byrne, 2023), and three (Hahn & Byrne, 2024) are both published in the *Journal of Geophysical Research: Planets*. Chapter four will also be submitted to the Journal of Geophysical Research: Planets in spring 2024. I, Rebecca Hahn, conceived and implemented the research presented in this dissertation. For chapters two, three, and four, I was responsible for data compilation and development, data analysis, research, writing the original draft, editing, and figure creation. My co-author and advisor, Paul Byrne, provided guidance, detailed feedback, and edits for all three papers that comprise this dissertation.

References

Airey, M. W., Mather, T. A., Pyle, D. M., & Ghail, R. C. (2017). The distribution of volcanism in the Beta-Atla-Themis region of Venus: Its relationship to rifting and implications for global tectonic regimes. *Journal of Geophysical Research: Planets*, *122*, 1626–164. https://doi.org/10.1002/2016JE005205

Connor, C. B. (1990). Cinder cone clustering in the TransMexican Volcanic belt: Implications for structural and petrologic models. *Journal of Geophysical Research*, **95**(B12), 19395–19405. https://doi.org/10.1029/JB095iB12p19395

Hahn, R. M., & Byrne, P. K. (2023). A morphological and spatial analysis of volcanoes on Venus. *Journal of Geophysical Research: Planets*, **128**(4), e2023JE007753. https://doi.org/10.1029/2023JE007753

Hahn, R. M., & Byrne, P. K. (2024). A global survey of gravitationally deformed volcanoes on Venus. Journal of Geophysical Research: Planets, 129, e2023JE008241. https://doi.org/10.1029/2023JE008241

Herrick, R. R. (2020). Magellan Venus stereo-derived topography Bundle. [Dataset]. Geosciences Node. https://doi.org/10.17189/1519332

Germa, A., Connor, L. J., Cañon-Tapia, E., & Le Corvec, N. (2013). Tectonic and magmatic controls on the location of post-subduction monogenetic volcanoes in Baja California, Mexico, revealed through spatial analysis of eruptive vents. Bulletin of Volcanology, 75, 1-14. https://doi.org/10.1007/s00445-013-0782-6

Ghail, R. C., Hall, D., Mason, P. J., Herrick, R. R., Carter, L. M., & Williams, E. (2018). VenSAR on EnVision: Taking earth observation radar to Venus. International journal of applied earth observation and geoinformation, 64, 365-376. https://doi.org/10.1016/j.jag.2017.02.008

Ivanov, M. A., & Head, J. W. (2013). The history of volcanism on Venus. *Planetary and Space Science*, **84**, 66–92. https://doi.org/10.1016/j.pss.2013.04.018

Pettengill, G. (1991). MGN V RDRS derived mosaic image data record full res V1.0 [Dataset]. NASA Planetary Data System. https://doi.org/10.17189/1522523

Silverman, B. W. (1998). *Density estimation for statistics and data analysis*. Routledge.

Smrekar, S., Hensley, S., Nybakken, R., Wallace, M. S., Perkovic-Martin, D., You, T. H., & Mazarico, E. (2022, March). VERITAS (Venus emissivity, radio science, InSAR, topography, and spectroscopy): a discovery mission. In 2022 IEEE Aerospace Conference (AERO) (pp. 1-20). IEEE. https://doi.org/10.1109/AERO53065.2022.9843269.

Solomon, S. C., & Head, J. W. (1982). Mechanisms for lithospheric heat transport on Venus: Implications for tectonic style and volcanism. *Journal of Geophysical Research: Solid Earth*, *87*(B11), 9236-9246. https://doi.org/10.1029/JB087iB11p09236

Chapter 2:
A Morphological and Spatial Analysis of Volcanoes on Venus

Associated Publication: Hahn, R. M., & Byrne, P. K. (2023). A Morphological and Spatial Analysis of Volcanoes on Venus. *Journal of Geophysical Research: Planets*, 128(4), e2023JE007753. https://doi.org/10.1029/2023JE007753

Abstract

Venus is home to many thousands of volcanic landforms that range in size from much less than 5 km to well over 100 km in diameter. Volcanism is clearly a major, widespread process on Venus, and is a principal expression of the planet's secular loss of interior heat. Without sufficient in situ data to clearly determine its internal structure, we can use the morphological and spatial properties of volcanoes across the planet to help place constraints on our understanding of the volcanic characteristics and history of Venus. With the Magellan synthetic-aperture radar full-resolution radar map left- and right-look global mosaics at 75 m-per-pixel resolution, we developed a global catalog of volcanoes on Venus that contains ~85,000 edifices, ~99% of which are <5 km in diameter. We find that Venus hosts far more volcanoes than previously mapped, and that although they are distributed across virtually the entire planet, size–frequency distribution analysis reveals a relative lack of edifices in the 20–100 km diameter range, which could be related to magma availability and eruption rate. Through spatial density analysis of volcanoes alongside assessments of geophysical data sets and proximal tectonic and volcanic structures, we report on the morphological and spatial patterns of volcanism on Venus to help gain new insights into the planet's geological evolution.

2.1 Introduction

NASA's Magellan spacecraft imaged virtually the entire Venusian surface using synthetic-aperture radar (SAR) as well as nadir-directed altimetry (Airey et al., 2017; G. H. Pettengill et al., 1991; E. Stofan, 2004). The radar image data collected during this mission enabled the recognition and classification of volcanic features and structures across Venus far beyond the scope of earlier missions (e.g., Basilevsky & Head, 1998; Crumpler & Aubele, 2000; Head et al., 1992). The Magellan data revealed a planetary surface covered in volcanic edifices of a range of sizes, as well as a number of volcanic landform types seemingly unique to Venus such as coronae (ring- to oval-shaped features with concentric ridges), arachnoids (concentric features with radial fractures along their periphery), and novae (sets of focused, radial fractures) (Crumpler & Aubele, 2000; Head et

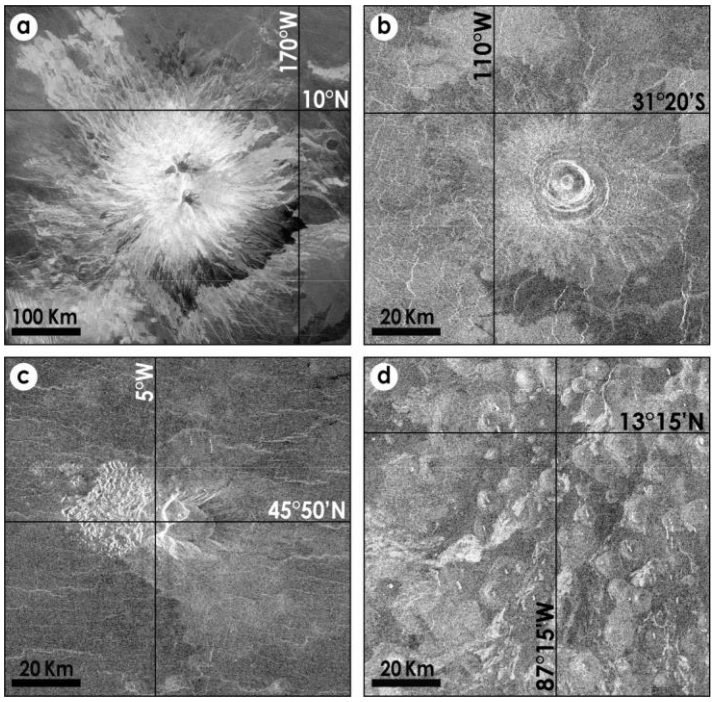

Figure 2.1 Examples of varying-sized edifices on Venus. (**a**) A large edifice (>100 km in diameter), Sapas Mons, which is ~400 km in diameter. (**b**) A so-called intermediate-sized edifice (5–100 km in diameter) that is ~75 km in diameter. (**c**) An example of an intermediate-sized edifices that has undergone some type of gravitational deformation. (**d**) Examples of small edifices (those <5 km in diameter). All images are left-look Magellan radar mosaics shown in an equirectangular projection.

al., 1992; Ivanov & Head, 2013). The radar image data also revealed a surprising dearth of impact craters (Arvidson et al., 1992; Bjonnes et al., 2012; Phillips et al., 1992; Schaber et al., 1992), likely indicating extensive volcanic resurfacing that was either catastrophic, episodic, or steady-state in nature (e.g., Basilevsky & Head, 1998; Bjonnes et al., 2012; Ivanov & Head, 2013, 2015; O'Rourke et al., 2014; Romeo, 2013; Turcotte et al., 1999).

2.1.1 Volcanism on Venus

The surface of Venus host volcanoes that range in size from <5 km in diameter to (in numerous cases) substantially greater than 100 km in diameter. Those edifices classified as "large volcanoes" (i.e., those >100 km in diameter) are generally situated on topographic rises and are surrounded by extensive radial lava flows (Airey et al., 2017; Crumpler & Aubele, 2000; Ivanov & Head, 2013; Mouginis-Mark, 2016; E. Stofan, 2004) **(Figure 2.1a**). Such volcanoes are approximately 2–3 km in height and often display concentric or circular central features (Head et al., 1992; E. R. Stofan, Smrekar, et al., 2001). Edifices we define as "intermediate size" (i.e., 5–100 km in diameter) are smaller in height and typically include symmetrical shields with radial lava flows on the flanks and surrounding plains, as well as flat-topped domes (**Figure 2.1b**) (Crumpler & Aubele, 2000; Head et al., 1992).

Volcanoes we term "small" are those <5 km in diameter; they are abundant across the Venusian plains (Aubele & Slyuta, 1990; Ivanov & Head, 2004) and have been documented as having three broad morphologies: shield-, cone-, and dome-like (Guest et al., 1992; Head et al., 1992) (**Figure 2.1d**). Small shields are typically categorized by visible summit collapse pits and shallow slopes. Conversely, small cones typically lack a central pit and have steeper slopes than shield-like edifices. Lastly, small domes are characterized by their flat-to-slightly-convex tops and steep flanks (Guest et al., 1992).

A widespread phenomenon on the Venusian surface is the volcanic field, also referred to as a "shield field," which is an area with relatively high spatial concentrations of small volcanoes. These volcanoes are topographically low, shield-like to dome-like edifices that are ≤20 km in diameter (Aubele & Slyuta, 1990; Crumpler & Aubele, 2000; Guest et al., 1992; Head et al., 1992; Ivanov & Head, 2013; Thomson & Lang, 2016). Studies of these volcano clusters led to the view that these fields originate from small-scale eruptions via several distinct crustal melt sources (Head et al., 1992; Ivanov & Head, 2004; Thomson & Lang, 2016).

2.1.2 Rationale

The goal of this study is to prepare and analyze a new, global catalog of volcanoes on Venus as a basis for understanding how volcanoes form and develop across the second planet. Among the ways ours expands on previous volcano catalogs (e.g., Crumpler & Aubele, 2000) includes our mapping of features smaller than 20 km in diameter and automating our approach to identifying volcanic fields.

With this new catalog, we seek to address the following broad questions: (a) What is the morphology and distribution of the various sizes of volcanoes on Venus?; (b) How are those volcanoes ≤20 km in diameter grouped into volcanic fields (the size threshold defined by, e.g., Aubele & Slyuta, 1990), and what implications do these groupings have for the underlying source magma bodies?; and (c) Where are volcanoes and volcanic fields located with respect to global geological and geophysical characteristics of Venus? Understanding the morphological and spatial patterns of volcanism on Venus can help us place constraints on models of the planet's geological evolution.

2.2 Methods

2.2.1 Mapping

Some previous studies documented a variety of volcanic structures across Venus (e.g., Aubele, 1996; Aubele et al., 1992; Crumpler & Aubele, 2000; Head et al., 1992), others focused on a specific feature such as coronae (e.g., E. R. Stofan et al., 1992; E. R. Stofan, Smrekar, et al., 2001), and yet others studies proposed global geological interpretations, including units specific to volcanic features such as "shield plains" and "shield clusters" (Ivanov & Head, 2011, 2013). To build upon these earlier works, we used ESRI ArcMap 10.7.1 and ArcGIS Pro 2.7 software to develop a new, global catalog of Venusian volcanic edifices with the Magellan SAR FMAP (full-resolution radar map) left- and right-look global mosaics at 75 m-per-pixel resolution (75 m/px) (G. Pettengill, 1991). We divided the planet into 5° × 5° bins, and thoroughly examined each bin at a view scale of 1:400,000. For the equatorial region between 40°N and 40°S, mapping was completed in an equirectangular projection. To preserve volcano geometry, data sets were projected as north- or south polar stereographic when mapping edifices at latitudes above 40°N and below 40°S, respectively. We recorded the coordinates of 33,359 well-defined volcanic edifices across Venus by mapping features into polygon or point vector shapefiles (e.g., **Figure 2.2**).

We mapped an edifice <5 km in diameter as being "well defined" on the basis of it being a landform that is quasi-circular and approximately conical in plan view, with one side more radar-bright than the opposite side (consistent with being illuminated from a single radar-look direction) (Figure 2); this approach is consistent with how volcanoes were identified in earlier studies (e.g., Head et al., 1992; Ivanov & Head, 2011, 2013; E. Stofan, 2004).

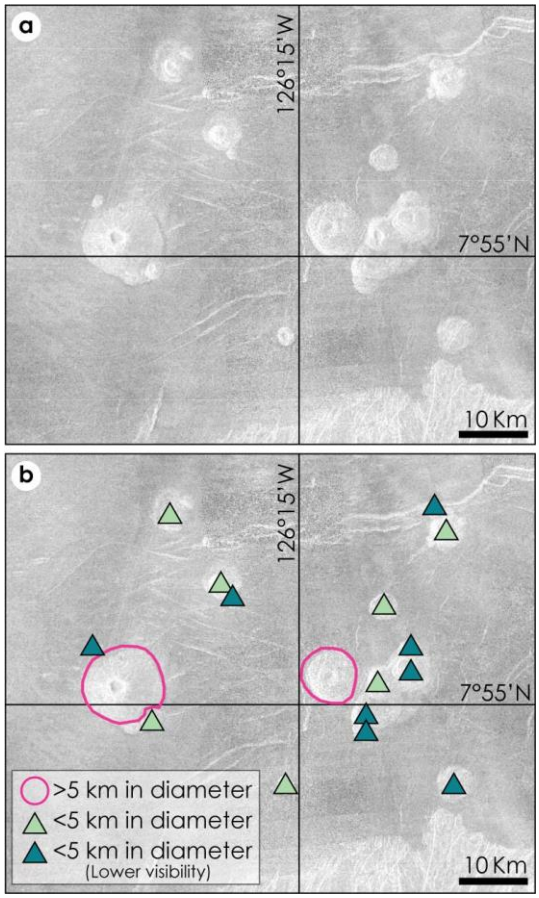

Figure 2.2 The mapping methodology we utilized in developing our global database of volcanoes across Venus. (**a**) Magellan radar image data centered at 126°W, 8°N prior to mapping. (**b**) That same region after features have been mapped. The radar look direction is from the left for each image, which are shown in equirectangular projections.

Prior research used Venera 15 and 16 radar images to identify small volcanoes (defined as 2–20 km in diameter) in the northern 25% of the planet, and found a decrease in the number of edifices <1 km in diameter (Aubele & Slyuta, 1990). This decrease may be a function of the relatively course resolution of the Venera 15 and 16 radar and Magellan SAR data or could represent a lower volcano diameter threshold because of some intrinsic geological processes (Crumpler et al., 1997). To avoid errors associated with delineating the boundaries of these small volcanoes, we define the lower limit of resolution for the identification of the basal outline of volcanoes as 5 km. This threshold is based on the resolution of the Magellan SAR FMAPs, which

were resampled to a nominal 75 m/px resolution from an original resolution of ~120 m/px (Ford et al., 1993). With these FMAP data, a volcano 1 km in diameter is ~7 pixels in diameter—much too low to reliably capture the outline of the edifice. We therefore chose to denote edifices <5 km in diameter only as point features and recorded their latitude and longitude coordinates. Additionally, this lower limit of 5 km in diameter serves as the division between small and intermediate-sized volcanoes within our catalog.

For the purposes of our mapping, well-defined, intermediate-sized volcanoes (5–100 km in diameter) may functionally be larger scale versions of volcanoes <5 km in diameter (Crumpler et al., 1997) and may exhibit radial lava flows around a central vent (e.g., the "anemone-type" of Head et al., 1992). Lastly, well-defined volcanoes >100 km in diameter are those with extensive radial lava flows and/or positive relief. For all edifices ≥5 km in diameter, a polygon outlining the edifice was drawn and the coordinates, area, and perimeter of each polygon recorded.

2.2.2 Morphological Analysis

Morphological analysis of volcanoes relies heavily on the accuracy in delineating the basal outline of each edifice (Grosse et al., 2009, 2012, 2014). During the mapping phase of this analysis (described above in *Section 2.1*), the Magellan SAR FMAPs were used along with topographic profiles obtained from the Magellan altimetry to identify the base of each volcano. We defined the base as that region surrounding locally positive topography that is marked by a concave break in slope (following the approach, e.g., of Favalli et al., 2009; Grosse et al., 2009, 2012, 2014; Kervyn et al., 2007). This break in slope is ideally the contact between the volcano's flank and the surrounding plains (Plescia, 2004). Yet many large volcanoes on Venus are associated with flow materials that extend a considerable distance from their source vents (be they on the flanks or at the summit), and so we typically excluded the full extent of the flow field and instead focused on

the volume of the main edifice (cf. Stofan, Guest, & Copp, 2001). Given the low spatial resolution of the Magellan topography, however, as well as the low slope gradient of edifices on Venus in general (Crumpler et al., 1997), it was not always possible to identify a change in slope that could be taken as the base of a given volcano. Instead, in some cases the basal outline was drawn solely using the FMAP radar imagery as a guide, which leads to an inevitable degree of uncertainty in our final morphometric measurements. This issue was especially common for intermediate-sized volcanoes (i.e., those 5–100 km in diameter) that were ≤20 km in diameter, which in many cases are much too small to be captured by the Magellan altimetry.

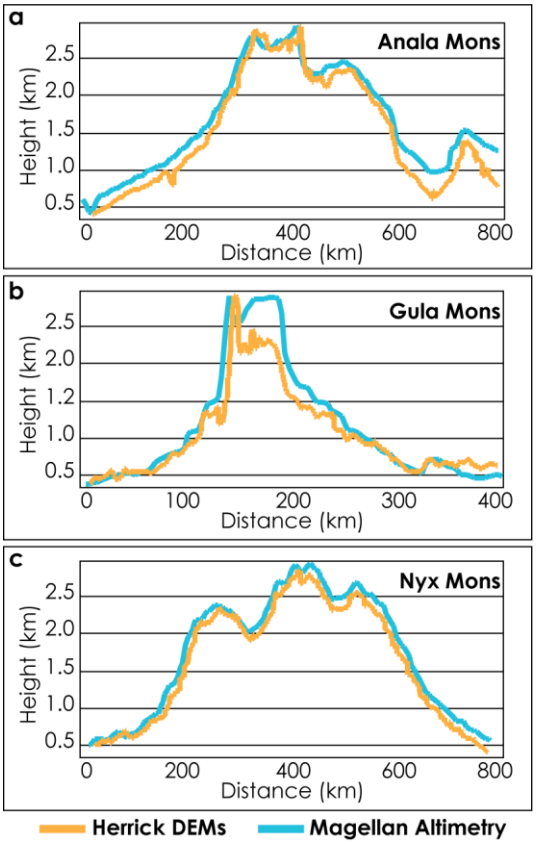

Figure 2.3 E–W topographic profiles of three volcanoes on Venus that fall within both the Herrick (2020) DEMs (orange lines) and the Magellan altimetry (blue lines). The Herrick DEMs can resolve more fine-scale information than the Magellan altimetry. For example, the Herrick DEMs show that Anala Mons (**a**) has a steeper eastern flank than indicated by the Magellan altimetry. Volcano profiles also illustrate that edifices on Venus may have complex summit morphologies.

Morphological properties including area, diameter, and aspect ratio (long axes vs. short axes) were determined for all 847 edifices >5 km in diameter in our catalog. Edifice diameter was calculated by averaging the long and short axes of the base (i.e., the outlines) of each volcano (Favalli et al., 2009). The precision of morphological analyses is also a function of the resolution of the data set. We followed a version of Shannon's sampling theorem (Shannon, 1949), and only considered height measurements for edifices that are at least twice the width of the spatial resolution of the data set (cf. Knicely & Herrick, 2021). For the Magellan altimetry data set, which has a footprint of ~20 × 10 km, we only included volcanoes >50 km in diameter, approximately 2.5 times the width of the spatial resolution (e.g., Knicely & Herrick, 2021). For example, Gula Mons (**Figure 2.3b**) has an elongated summit with a NE-trending rift that is deeper than shown by the Magellan altimetry. Another example is Nyx Mons (**Figure 2.3c**), which contains a central summit bulge and elevated ridges. The vertical exaggeration for profiles (**Figure 2.3a**) and (**Figure 2.3c**) is 200, and for profile (**Figure 2.3b**) is 100.

For the 132 edifices >50 km in diameter that fall within the Magellan global altimetry data set, an approximation of the edifice height was determined with the "Zonal Statistics" tool in ArcGIS Pro. The Magellan global altimetry data were set as the raster layer, and the layer containing the volcano polygons from our global data set was set as the boundary defining the region from which to calculate cell statistics. The resulting data included the minimum (base elevation) and maximum (summit elevation) cell values enclosed by the polygons for each volcano, with which we could then determine an approximation of maximum height for all edifices >50 km in diameter within our global catalog. Our height values here are derived from a horizontal reference plane representing the lowest elevation of each volcano, following established practice (Grosse & Kervyn, 2018; Grosse et al., 2012, 2014) and are therefore height estimate maxima.

For a subset of volcanoes >50 km in diameter, more precise morphological measurements were made with stereo-derived digital elevation models (DEMs), which cover ~20% of Venus (Herrick, 2020). These stereo-derived DEMs have a footprint of ~1–2 km and a vertical error of 50–100 m, allowing for the examination of smaller volcanoes that are typically inaccessible with the Magellan altimetry (e.g., Gleason et al., 2010; Herrick et al., 2012; Knicely & Herrick, 2021), as well as more detailed analysis of larger volcanoes (e.g., McGovern et al., 2014) (**Figure 2.3**). With the improved vertical precision and accuracy of the Herrick (2020) DEMs (hereafter referred to as "stereo-derived DEMs"), we acquired volume and height measurements for 21 volcanoes >50 km in diameter that fall within that newer data set. Based on previous volumetric analysis methods, we employed the direct-integration approach for calculating volcano volume.

Direct-Integration Method for Volume Estimation:

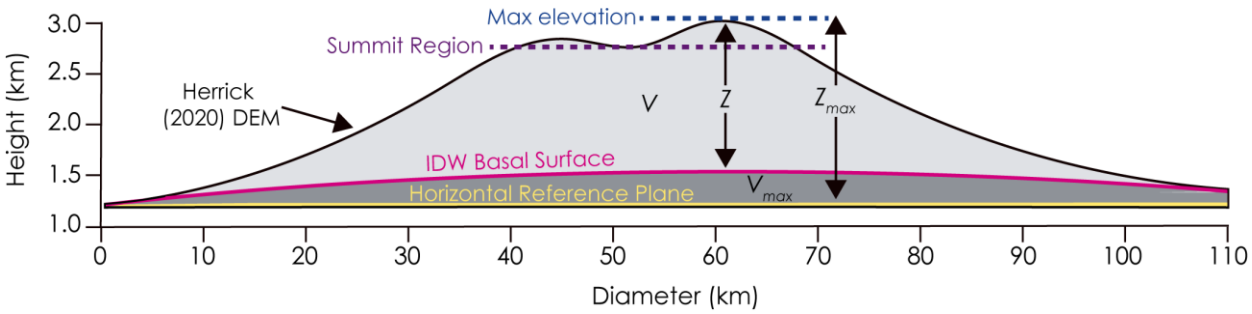

Figure 2.4 A schematic profile of a shield volcano on Venus showing the volcano volume (*V*) and height (*Z*) derived from the IDW (inverse distance weighting)-derived basal surface (pink line), as well as the maximum height (Z_{max}) and volume (V_{max}) derived from the horizontal reference plane (yellow line) corresponding to the lowest elevation around the base of each volcano. Figure adapted from Grosse et al. (2012) and Grosse and Kervyn (2018).

We used a direct-integration approach to determine the volume (*V*) of each volcano by integrating the sum of the difference between the stereo-derived DEMs and a basal surface raster (Grosse & Kervyn, 2018; Grosse et al., 2009, 2012, 2014; Ricci et al., 2015). Essentially, for each cell, the square of the cell size (0.6 km × 0.6 km for the stereo-derived DEMs) was multiplied by

the edifice height (i.e., the difference between the stereo-derived DEM edifice height values and the basal surface raster).

Basal surface rasters have been generated using a variety of different methods including fitting a polynomial surface through the outline of the volcano (Grosse et al., 2009) and generating a triangular irregular network (TIN) with the basal outline (Favalli et al., 2009; Grosse et al., 2012). Here, we generated the basal surface raster using inverse distance weighting (IDW) interpolation (e.g., Grosse & Kervyn, 2018; Grosse et al., 2014) in the ArcGIS Pro environment. IDW generates cell values using a linearly weighted combination of a set of sample points (Watson & Philip, 1985), which we created by extracting stereo-derived DEM elevation values in one-km intervals around the digitized outline of each volcano. The stereo-derived DEMs were then clipped to the extent of the digitized outlines for each volcano. In ArcGIS Pro, we subtracted the clipped DEMs from the IDW basal surface rasters with the "Raster Calculator" function to create DEMs that represent the actual height (Z) in each cell. These resulting height DEMs were then multiplied by the square of the cell size of the stereo-derived DEMs to calculate the volume of each individual cell the volcano occupies, and then these individual cell volumes were summed to determine the total volume (V) of each volcano.

In addition to using an IDW-generated basal surface, we calculated maxima for volcano height (Z_{max}) and volume (V_{max}) from a horizontal reference plane containing the lowest-elevation value around the base of each edifice (**Figure 2.4**). The actual height and volume of these volcanoes are likely somewhere in between the Z and Z_{max} and V and V_{max} values, respectively (Grosse et al., 2014). Although the direct-integration method can provide approximate height and volume estimates, it does not take into account effects arising from volcano sagging (e.g., as has taken place at Mars' Elysium Mons: Byrne et al., 2009, 2013), irregular terrain (e.g., scoria cones

on the flanks of Mt. Etna: Favalli et al., 2009), or overlapping edifices (e.g., in the Michoacán–Guanajuato volcanic field, Mexico: Favalli & Fornaciai, 2017) (Grosse et al., 2012, 2014).

Uncertainties in our height calculation were estimated by multiplying the height of each edifice by the average vertical error of the stereo-derived DEMs, that is, 75 m. Volume uncertainty was estimated by finding the volume error associated with each cell and propagating that error across the entire edifice (cf. Ricci et al., 2015). Cell volume error was found by multiplying the square of the cell size of the stereo-derived DEMs by the vertical error (0.62×0.075 km = 0.027 km^3). The cell volume error (2.7×10^{-2} km^3) was then multiplied by the raster containing the height of the edifice to yield the total volume error associated with the edifice.

2.2.3 Spatial Clustering

The Venera 15 and 16 radar data, as well as Magellan SAR data, revealed quasi-equidimensional clusters of shield volcanoes approximately ≤20 km in diameter scattered across the Venusian surface. The diameter threshold is somewhat arbitrary and is based on observations made by Aubele and Slyuta (1990), who used the Verena 15 and 16 radar imagery to map edifices ≤20 km in diameter and found a notable decrease in the number of edifices >20 km in diameter. These volcanic fields, often referred to as "shield fields" by Venus researchers, typically contain ~100 volcanoes and range in spatial density from four to 10 edifices per 1,000 km^2 (Aubele & Slyuta, 1990; Crumpler & Aubele, 2000; Ivanov & Head, 2004; Kreslavsky & Head, 1999). Fields of volcanoes are not unique to Venus and in fact have been extensively documented on Earth (Le Corvec et al., 2013; Tadini et al., 2014), on Mars (Bleacher et al., 2009; Greeley et al., 2006; Richardson et al., 2013), and on the Moon (Spudis, 2015). Examples of volcanic fields on Earth include the Abu monogenetic volcano group in Japan (Kiyosugi et al., 2010), the Camargo volcanic field in Mexico (Aranda-Gómez et al., 2010), the Snake River Plain in Idaho, USA

(Morgan & McIntosh, 2005), as well as the expansive seamount population on Earth's seafloor (Aubele & Slyuta, 1990; Crumpler & Aubele, 2000; Guest et al., 1992). On Earth, a volcanic field is described as a group of small, monogenetic, and dominantly basaltic volcanoes (Cañon-Tapia, 2016). These fields may contain tens to hundreds of small edifices (each with a volume less than 1 km^3) and have been identified in subduction zones, rift systems, hot spots, and intraplate settings (Connor & Conway, 2000).

Previous work on Venusian volcanic fields focused on providing descriptive characteristics for fields (Aubele & Slyuta, 1990; Aubele et al., 1992; Crumpler et al., 1997; Guest et al., 1992; Head et al., 1992) as well as stratigraphic relationships relative to mapped units (Addington, 2001; Aubele, 1995, 1996; Guest & Stofan, 1999; Ivanov & Head, 2004). Here, we have developed an automated approach to grouping volcanoes ≤20 km in diameter from our global catalog of volcanoes into volcanic fields to better assess the size, shape, and distribution of such volcano clusters across Venus.

In total, our catalog contains 84,811 volcanoes ≤20 km in diameter—84,172 < 5 km in diameter, and an additional 639 volcanoes 5–20 km in diameter. For volcanoes 5–20 km in diameter in our catalog, which are classified as intermediate-sized volcanoes and have a digitized polygon delineating their outline, the coordinates of the outlining polygon's centroid were used to define the latitude and longitude points for each edifice.

Density-based clustering algorithms have been widely used by the planetary community to examine craters on the Moon (Robbins et al., 2014), Mars (Laura et al., 2017) and in the Pluto–Charon system (Robbins et al., 2017). DBSCAN, or "density-based spatial clustering of applications with noise," is an algorithm that identifies arbitrarily shaped clusters and noise (outliers) within a data set (Ester et al., 1996) and requires a user-defined search distance to

perform cluster analysis. Recently, a more data-driven approach called HDBSCAN has been developed, which builds on the DBSCAN algorithm by converting it into a hierarchical (hence the "H") clustering algorithm and removes the need for a user-defined search distance (Campello et al., 2013, 2015; McInnes et al., 2017). Previous workers visually identified fields of small volcanoes using Magellan FBIDR (full-resolution basic image data record) and C1-MIDR (for "compressed, once-mosaicked image data records") (Crumpler & Aubele, 2000) or large-format Magellan FMAP prints and digital tiles (Addington, 2001). In this study, we utilized the freely available "hdbscan" Python package (McInnes et al., 2017) to identify clusters of shield volcanoes as an automated approach to mapping volcanic fields.

The HDBSCAN algorithm requires as inputs the latitude and longitude of each volcano and a minimum number of neighbors ("minpts"). For the minpts parameter, that is, the minimum number of volcanoes required to form a volcanic field, we used a value of 25 on the basis of earlier studies (e.g., Addington, 2001; Crumpler & Aubele, 2000). The Magellan volcanic and magmatic feature catalog developed by Crumpler and Aubele (2000) includes the latitude, longitude, approximate diameter, and description of 646 volcanic fields or shield fields. Although the total number of volcanoes within each volcanic field was not documented in that study, the descriptions therein did include a semiquantitative description of the field (e.g., "high-number density" or "low-number density"). We randomly selected 10 volcanic fields that were described as "low-number density" and counted the number of volcanoes within each field, finding that on average they contained 40 edifices. We also examined the descriptions of the 179 volcanic fields from seven quadrangles documented by Addington (2001) and established that the smallest volcanic field documented in that study contains seven volcanoes. For our analysis, we averaged the smallest volcanic fields documented in each study (40 from Crumpler and Aubele, 2000 and seven from

Addington, 2001) to arrive at a representative number of 25 volcanoes per volcanic field. With this minpts parameter, our analysis using the HDBSCAN algorithm results in a total of 566 volcanic fields on Venus.

2.2.2 Spatial Statistics

The distribution and orientation of volcanoes may provide insight into the size and shape of the underlying magma sources, the mechanisms of magma production, and the states of stress in the crust (e.g., Cañon-Tapia & Mendoza-Borunda, 2014; Connor, 1990; Kear, 1964; Le Corvec et al., 2013; Nakamura, 1977). One method for analyzing the distribution of edifices on a global level is by employing kernel density functions. Kernel density functions are nonparametric density estimation tools (Silverman, 1998) that have been widely used by the planetary community to examine crater spatial density (e.g., Kinczyk et al., 2020; Robbins et al., 2018; Wang et al., 2015), as well as volcano spatial density on Mars (e.g., Connor et al., 2018; Richardson, 2016), and Venus (e.g., Cañon-Tapia & Mendoza-Borunda, 2014). Additionally, the kernel density function can be used to characterize past patterns of volcanism and infer the possible geological origins for these patterns (Germa et al., 2013).

The kernel density function consists of two parts: the probability density function (PDF) and the bandwidth or smoothing parameter (Cañon-Tapia & Mendoza-Borunda, 2014). The PDF spreads probability away from the event (i.e., the volcano) based on the bandwidth, and the shape of the kernel density function (Kiyosugi et al., 2010). The bandwidth value greatly impacts the smoothness of the resulting density plot. A small bandwidth value, or smoothing parameter, will concentrate the probability close to the locations of the mapped volcanoes, whereas a larger value will distribute the probability more widely. For this analysis, we employed two optimized bandwidth algorithms: the “sum of the asymptotic mean square error” (SAMSE) algorithm (Duong

& Hazelton, 2003) and the "smoothed cross validation" (SCV) (Hall et al., 1992) algorithm. Optimized bandwidth algorithms mitigate the subjectivity of the user having to arbitrarily select a bandwidth value, and instead provide an unbiased estimate of bandwidth elements based on distances between neighboring events (again, in this case, volcanoes). Additionally, the SAMSE and SCV algorithms produce an elliptical kernel (described by the matrix parameter H) instead of the more common circular kernel (e.g., Cañón-Tapia, 2013; Weller et al., 2006). Elliptical kernels are more sensitive to tectonic/structural controls on volcano distribution and alignment (Connor et al., 2018; Kiyosugi et al., 2010). Here, we employed a two-dimensional, direction-varying elliptical kernel bandwidth to calculate the spatial variation in density, $\hat{\lambda}(s)$, which is given (Wand & Jones, 1993, 1994) by:

$$\hat{\lambda}(s) = \frac{1}{2\pi\sqrt{|H|}} \sum_{i=1}^{N} exp\left[-\frac{1}{2} b^T b\right]$$

where,

$$b = H^{-\frac{1}{2}} d.$$

The elliptical kernel bandwidth, described here by the matrix parameter, H, is a 2 × 2 element matrix, $|H|$ is the determinant of H, and $H^{-\frac{1}{2}}$ is the inverse of the square root of H. The total number of edifices is given by N. The variable d is a 1 × 2 distance matrix (i.e., the x and y distance from a point s to an event), b is the cross product of d and $H^{-\frac{1}{2}}$, and b^T is the transform of b. Therefore, the spatial intensity at a given point is calculated by applying the Gaussian kernel function using the distance to each volcano, smoothing the intensity as specified by the bandwidth (in this case, the SAMSE- and SCV-derived bandwidth values), and then summing each volcano's

contribution to the intensity estimation (Germa et al., 2013). The resulting maps of volcano spatial density reveal areas with both higher and lower concentrations of volcanoes. Regions with higher concentrations of volcanoes (high-volcano-spatial-density regions) can then be extracted for further analysis (see *section 2.4.2*). Both the SAMSE and SCV algorithms are available for free in the *R* statistical software library as part of the '*ks*' package (Duong et al., 2007).

Several sources of uncertainty exist in spatial density estimates. These uncertainties can stem from parameters such as the bandwidth estimate and the volcano locations (Connor and Connor, 2009; Connor et al., 2018). Here, we sought to minimize uncertainty arising from bandwidth selection by employing two different bandwidth optimization algorithms that use a data-driven approach to identifying the ideal bandwidth value. The relatively low resolution of the Magellan SAR data has led to a degree of uncertainty in mapping smaller edifices (i.e., those <5 km in diameter), and in delineating the basal outline of volcanoes ≤20 km in diameter (see *section 2.1*). Volcanoes documented within our catalog were checked by multiple researchers in an attempt to reduce errors and subjectivity in identification.

Other methods of spatial analysis such as vent-alignment analysis (Wadge and Cross, 1988; Connor, 1990; Bleacher et al., 2009; Richardson et al., 2021) and directional-distribution analysis (e.g., Bishop, 2007; Haag et al., 2019) have been applied in the search for preferred orientations of clusters of shield volcanoes on Earth (Cebria et al., 2011; Roberts et al., 2011) and on other planets (Richardson et al., 2013; Thomson and Lang, 2016). In this study, we utilized the "Directional Distribution (Standard Deviational Ellipse)" tool in ArcGIS Pro 2.7 to identify the orientation of the volcanoes within each volcanic field. This tool works by calculating the standard distance between a set of points (i.e., each volcano within the field) in both the *x* and *y* directions. The resulting measurements are the axes of an ellipse that encompasses the distribution of features

of interest, and reveals the overall orientation of (in this case) the volcanoes in a given volcanic field. The orientation of the resulting ellipse and the degree of eccentricity were both analyzed for all 566 volcanic fields.

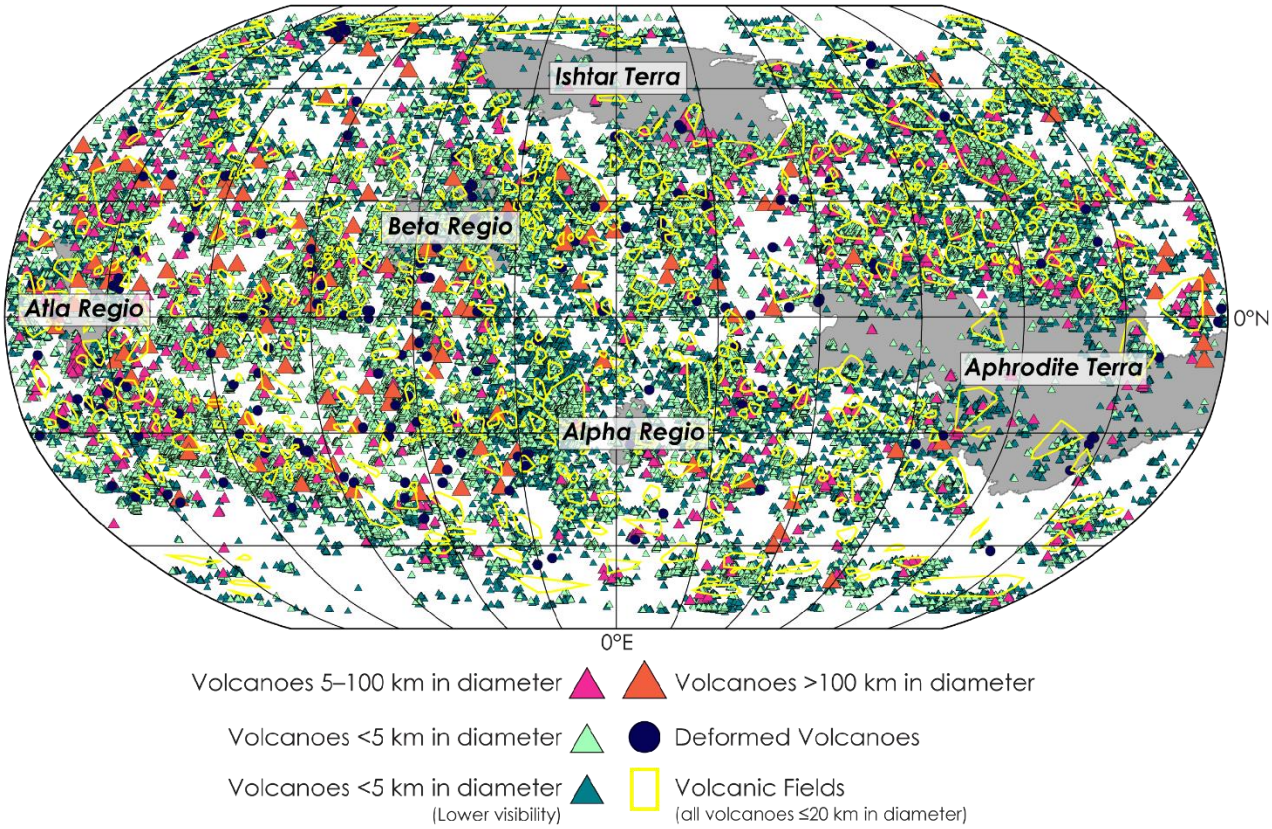

Figure 2.5 Our completed global survey of volcanic edifices and volcanic fields on Venus. This survey includes 32,512 volcanic edifices <5 km in diameter (aqua triangles), 51,660 edifices <5 km in diameter for which only geographic coordinates were recorded because of locally poor radar image quality (teal triangles), 729 edifices 5–100 km in diameter (pink triangles), 118 edifices >100 km in diameter (orange triangles), and 182 edifices (of all diameters) that show evidence for gravitational deformation (purple circles). Additionally, we include 566 volcanic fields containing high spatial concentrations of edifices <20 km in diameter (yellow outlines). The outlines of major Venusian physiographic features are shown in grey for geographic context. The map is in Robinson projection, centered at 0°E.

2.3 Results

2.3.1 Shield Volcano Catalog

Table 2.1
Total Number of Features in the Global Catalog of Volcanoes and Volcanic Fields

Category	Count	Appendix A.1
Volcanoes <5 km in diameter	32,512	01_small_lessthan5km.shp/ 01_small_lessthan5km.csv
Volcanoes <5 km in diameter (low visibility)	51,660	02_small_lessthan5km_lowres.shp/ 02_small_lessthan5km_lowres.csv
Volcanoes 5–100 km in dimeter	729	03_intermediate_5to100km.shp/ 03_intermediate_5to100km.csv/ 04_intermediate_greaterthan50km.shp/ 04_intermediate_greaterthan50km.csv/ 06_greaterthan50km_Herrick.shp/ 06_greaterthan50km_Herrick.shp
Volcanoes >100 km in diameter	118	05_large_greaterthan100km.shp/ 05_large_greaterthan100km.csv/ 06_greaterthan50km_Herrick.shp/ 06_greaterthan50km_Herrick.shp
Deformed Volcanoes	182	07_deformed.shp 07_deformed.csv
Volcanic Fields	566	08_volcanic_fields.shp/ 08_volcanic_fields.csv

Our global catalog comprises 32,512 well-defined volcanic edifices <5 km in diameter, 729 edifices that are 5–100 km in diameter, 118 edifices >100 km in diameter, and 182 edifices (of all diameters) that show evidence for gravitational deformation, for example, flank collapse, scalloped margins, sagging, and spreading (**Figure 2.1c**) (Hahn & Byrne, 2020) (**Table 2.1**). Volcanoes are often gravitationally unstable landforms, and frequently undergo gravity-driven deformation that can alter the shape of the edifice. Further analysis of these and comparisons to those on Earth may aid in characterizing volcano growth and subsequent collapse on Venus.

We also included an additional 51,660 edifices <5 km in diameter that we considered “low visibility,” as these landforms were more difficult to robustly identify (e.g., they have poorly

resolved summit craters or bases) because of variable quality of the SAR data and difficulties in parsing variations in radar backscatter as discrete volcanoes (**Table 2.1**). These edifices differ from the "well-defined volcanic edifices" in that they lack either a defined smooth circular base or a radar-bright central pit with available Magellan data. In total, then, our global catalog includes

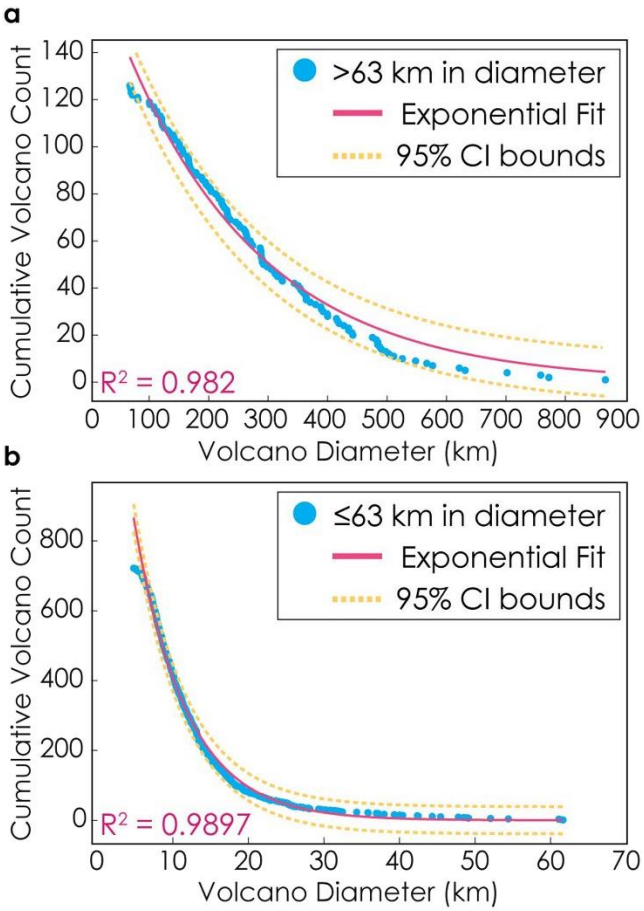

Figure 2.6 Venus volcano cumulative size–frequency distributions for volcanoes >5 km in diameter. Mixture-model analysis identified two subpopulations of volcano diameters that both follow and exponential distribution: (**a**) volcanoes >63 km in diameter and (**b**) volcanoes ≤63 km in diameter. Individual volcano diameters are shown as blue circles, lines of best fit are shown in pink with associated R^2 values, and 95% confidence interval bounds are shown as dashed yellow lines.

~85,000 total edifices, almost 50 times more than any previous catalog (Crumpler and Aubele, 2000) **(Figure 2.5)**. Although our catalog certainly does not document *every* edifice on Venus, we have mapped smaller edifices (<5 km in diameter) on a larger scale than any previous workers, allowing for the most detailed analysis yet of the most common volcanic feature on the surface of

Venus. The goal of this catalog is to provide a dataset that can be used to better understand how discrete volcanic activity is manifest across the surface of Venus.

Previous authors found that both exponential and power-law distributions offer acceptable fits for volcano diameter–frequency distributions on Venus (Aubele and Slyuta, 1990; Guest et al., 1992; Romeo and Turcotte, 2009). Based on the distribution of volcano diameter values for all edifices >5 km in diameter (of which 85% are ≤50 km in diameter), and the poor fit of a single power law or exponential distribution to our dataset, we opted to employ a statistical approach termed "mixture modeling" to establish if there are multiple, discrete populations of volcanoes (as defined by diameters) within our dataset.

Mixture modeling is a flexible modeling approach that treats data as coming from several classes, components, or clusters (Everitt and Hand, 1981; McLachlan and Basford, 1988; Titterington et al., 1990; Wallace and Dowe, 2000). This approach is useful for identifying differences in datasets that cannot be accurately described by a single distribution (Peel and McLachlan, 2000). For this analysis, we employed the MATLAB package 'SNOB' (Edwards and Dowe, 1998; Wallace, 1998, 2005; Wallace and Dowe, 2000; Schmidt and Makalic, 2012). SNOB is a MATLAB implementation of finite-mixture models that uses a minimum-message-length criterion to estimate the structure of the mixture model and outputs the number of components, the relative amount of each component, and the distribution parameters for each component (Wallace and Dowe, 2000). Mean diameter (km) values of volcanoes >5 km in diameter (n = 847) were the input dataset, and both exponential and power law distributions were tested. The SNOB analysis that best fit the dataset resulted in two distinct exponential distributions within our data, defined by a break in diameter at 63 km. The first distribution contains 126 volcanoes that are >63 km in

diameter (**Figure 2.6a**), and the second contains 721 volcanoes that are ≤63 km in diameter (**Figure 2.6b**).

2.3.2 Volcanic Field Catalog

Our global catalog of volcanic fields includes 566 fields (**Figure 2.5**). Of the 84,811 shield volcanoes ≤20 km in diameter (84,172 edifices <5 km in diameter and an additional 639 edifices 5–20 km in diameter), the HDBSCAN algorithm identified 55,132 shields that were part of a "cluster" or volcanic field, and the remaining 29,679 shields were classified as "noise" or outliers that did not belong to a volcanic field based on our *minpts* input criterion. The average number of volcanoes per field is 97, with a median value of 65, a maximum value of 807, and a minimum value of 25 (because of the *minpts* value of 25). The average volcanic field diameter, calculated by averaging each field's long- and short-axes lengths, is 360 km, with the smallest and largest fields measuring 83 km and 2,032 km in diameter, respectively. The median diameter is 298 km, with 83% of volcanic fields ≤500 km in diameter.

To assess the accuracy of the automated delineation of volcanic fields by the HDBSCAN algorithm, we compared the locations of our volcanic fields with those documented in the Magellan volcanic and magmatic feature catalog of Crumpler and Aubele (2000). Of the 643 volcanic fields (referred to as "shield fields" in their study) those authors identified, 432 (67%) coincide with one of our 566 volcanic fields and an additional 35 (5%) volcanic fields are within 20 km of one of our fields. The remaining fields noted by Crumpler and Aubele (2000) that do not overlap with one of our volcanic fields can be accounted for because those in our database are a priori required to contain at least 25 volcanoes (per the *minpts* value in HDBSCAN algorithm), and not every field documented by Crumpler and Aubele (2000) contains at least 25 volcanoes.

2.3.3 Morphological Analysis

Table 2.2
Average Measurements of Morphological Properties for All Volcanoes >5 km in Diameter

Edifice Diameter (km)	Count	Aspect Ratio[a]	Diameter (km)	Area (km²)	Height (km)[b]
5–100	729	0.90	14 ± 9.5	225 ± 484	0.36[c] ± 0.41
>100	118	0.88	300 ± 158	101,000 ± 111,000	2.05[d] ± 1.08

[a]Aspect ratios were calculated using volcano basal width versus basal length.
[b]Height calculations were acquired with Magellan altimetry.
[c]For volcanoes 5–100 in diameter, height estimates were found only for those volcanoes >50 km in diameter, given Magellan altimetry resolution constraints.
[d]Height excludes one volcano that was not covered by Magellan altimetry.

Table 2.3
Average Measurements of Morphological Properties for Volcanoes >50 km in Diameter Within the Herrick. (2020) Stereo-Derived DEMs

Edifice Diameter (km)	Count	Aspect Ratio[a]	Diameter (km)	Area (km²)	Height (km)[b]	Max Height (km)[c]	Volume (km³)[d]	Max Volume (km³)[d]
50–100	2	0.88	71.5 ± 8.2	4,000 ± 900	0.58 ± 0.04	0.76 ± 0.06	417.2 ± 31.3	1317.3 ± 99
>100	19	0.88	368 ± 178	105,000 ± 118,000	2.07 ± 0.16	2.8 ± 0.21	59,000 ± 4,400	163,000 ± 12,200

[a]Aspect ratios were calculated using volcano basal width versus basal length.
[b]Height calculations were acquired using the Herrick (2020) stereo-derived DEMs and IDW basal surface interpolation.
[c]Max height calculations were acquired with the Herrick (2020) stereo-derived DEMs and by finding the lowest elevation value around the base of each edifice.
[d]Volume calculations were acquired with the Herrick (2020) DEMs and the Direct Integration approach; volume calculations are based off the IDW-generated basal surface, and maximum volume calculations used a horizontal reference plane equal to the lowest basal elevation around the edifice (see *Section 2.2.2*).

Average values for volcano morphological properties including area, diameter, and aspect ratio were determined for all 847 edifices >5 km in diameter in our catalog. The minimum and maximum basal axes values were also used to derive the aspect ratio of each edifice. Approximate measures of height were also found for all volcanoes >50 km in diameter (**Table 2.2**) that are covered by the Magellan altimetry. In **Table 2.2**, diameter, area, and height are given plus or minus one standard deviation. Additionally, maximum and mean volume and height approximations were determined for 21 volcanoes >50 km in diameter that are covered by the stereo-derived DEMs (**Table 2.3**). For **Table 2.3**, diameter and area are given plus or minus one standard deviation, and height and volume are given plus or minus DEM uncertainty values (see *section 2.2.1* for our approach for estimating volume uncertainties).

2.3.4 Spatial Statistical Analysis

Kernel density analysis was conducted in the *R* environment with functions from the '*ks*' package (Duong et al., 2007). The latitude and longitude of the centroid of each volcano in our global catalog were used as the input points. The dataset was divided into two groups, volcanoes >63 km in diameter (n = 126) and volcanoes ≤63 km in diameter (n = 84,893) based on the results from the mixture model analysis (see *section 3.1*). Here, we include the 84,172 volcanoes <5 km in diameter from our global catalog in addition to the 721 volcanoes 5–63 km in diameter that were identified by the mixture model. Kernel density analysis using both SAMSE and SCV algorithms were performed for each of the two size groups, resulting in four volcano spatial density maps (**Figure 2.7**). Note that, of the 182 deformed volcanoes within our catalog, we omitted 160 from this analysis. Many deformed volcanoes have deformational structures such as landslides or debris aprons that extend beyond the boundary of the edifice. These edifices were excluded because their

diameter technically includes these runout structures, which so alter the size–frequency distribution of the dataset and the subsequent mixture model.

For the 126 edifices >63 km in diameter, the SAMSE and SCV bandwidth selector algorithms each yield a 2 × 2 element matrix:

$$SAMSE\ \sqrt{H} = \begin{bmatrix} 32.68 & -1.33 \\ -1.33 & 12.20 \end{bmatrix}$$

and

$$SCV\ \sqrt{H} = \begin{bmatrix} 36.43 & -1.98 \\ -1.98 & 15.00 \end{bmatrix}.$$

For the 84,893 edifices ≤63 km in diameter, the SAMSE and SCV bandwidth selector algorithms yield:

$$SAMSE\ \sqrt{H} = \begin{bmatrix} 5.13 & 0.04 \\ 0.04 & 2.06 \end{bmatrix}$$

and

$$SCV\ \sqrt{H} = \begin{bmatrix} 4.89 & 0.12 \\ 0.12 & 2.20 \end{bmatrix}.$$

The lower-right and upper-left diagonal elements in each matrix represent the smoothing (in km) in the N–S and E–W directions, respectively, with the positive off-diagonal elements representing the clockwise rotation of the kernel, and negative elements representing the counter-clockwise rotation (Connor and Connor, 2009). For edifices >63 km in diameter, both the SAMSE and SCV algorithms resulted in an elongated ellipse that trends to the N–NW (negative off-diagonal elements). The size and shape of the kernels for both algorithms are similar, with a smoothing distance of 24–30 km (12–15 × 2) in the N–S direction and 66–74 km (33–37 × 2) in the E–W direction.

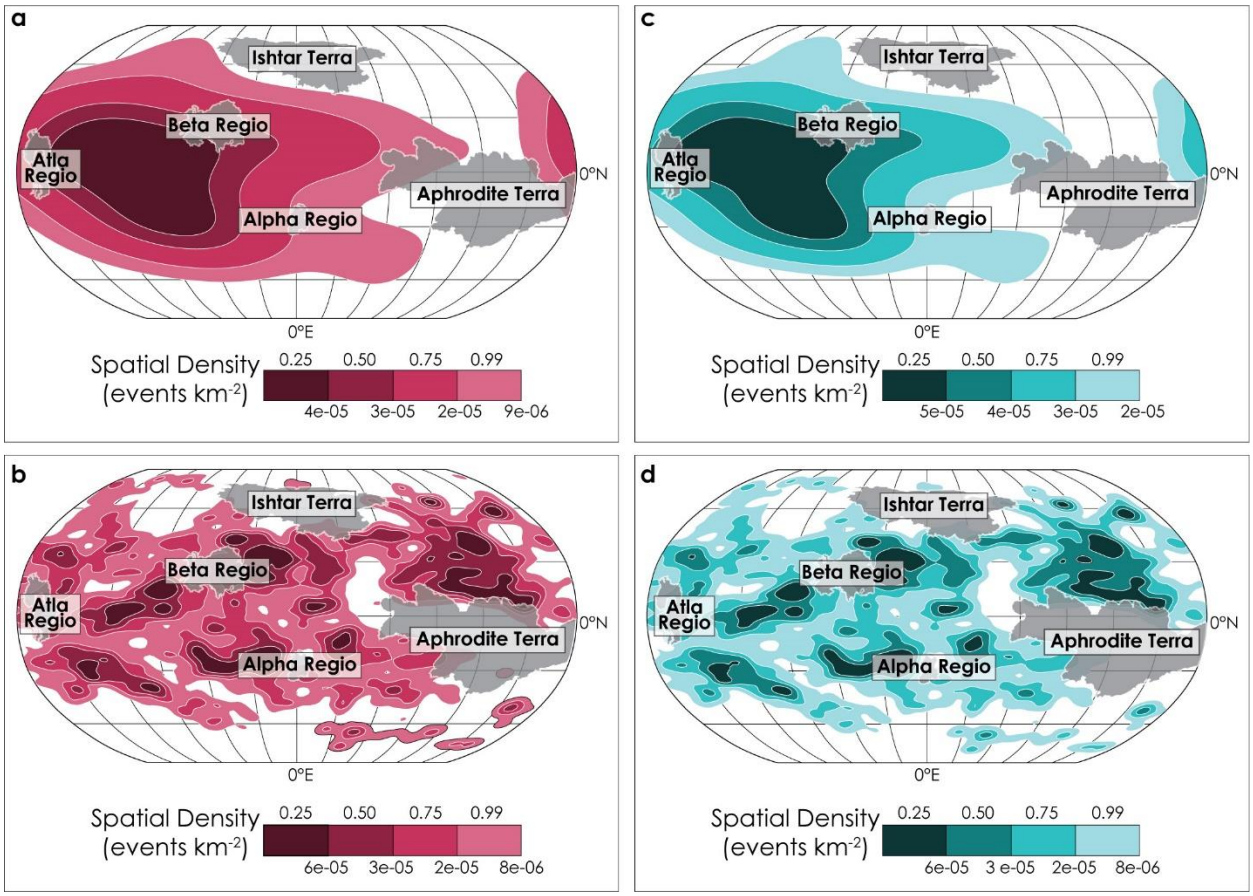

Figure 2.7 Spatial density estimates for (**a**, **c**) volcanoes >63 km and (**b**, **d**) volcanoes ≤63 km in diameter (**b** & **d**) utilizing the SCV (pink) and SAMSE (blue) bandwidth optimization algorithms. Contours are shown at 25th, 50th, 75th, and 99th percentiles. The outlines of major Venusian physiographic features are shown in grey for geographic context. All maps are in Robinson projection, centered at 0°E.

Spatial density estimates for both algorithms show a high spatial concentration of volcanoes >63 km in diameter within the Beta–Atla–Themis (BAT) region, an approximately triangular area bounding three large rift zones connecting the Beta, Atla, and Themis regiones (e.g., Crumpler et al., 1997; Airey et al., 2017). The highest and lowest volcano spatial density regions are shown in the darkest pink and darkest blue and lightest pink and lightest blue regions, respectively in **Figures 2.7a** and **2.7c**. Contours shown in **Figure 2.7** correspond to the probability of future volcanoes forming in each quartile. For example, on map **2.7a,** locations with the 3.3e-05 contour (i.e., the 50th quartile) will have spatial density >3.3 × 10^{-5} km^{-2}; given a volcanic event,

there is a 50% chance it will occur in this quartile. The high-volcano-spatial-density zone, or the 25th percentile contour, for the SCV and SAMSE maps (**Figure 2.7a** and **2.7c**) overlap substantially, with both regions spanning over 11,000 km and centered at around 5°N, 100°W. The main difference between the two algorithms is that the SCV tends to encompass slightly broader regions for each percentile contour than the SAMSE algorithm, a difference most evident in the 99th-percentile contour—where the SCV contour extends past the SAMSE 99th percentile contour by as much as 3,000 km in some places.

Similarly, the kernel density maps produced by each algorithm for volcanoes ≤63 km in diameter are nearly identical. Both the SCV (**Figure 2.7b**) and SAMSE (**Figure 2.7d**) algorithms returned an elliptical kernel that is very slightly oriented N–NE, and that has a smoothing distance of ~10 km in the E–W direction and ~4 km in the N–S direction. High-volcano-spatial-density regions (e.g., the darkest pink region in **Figure 2.7b** and darkest blue region in **2.7d**) are concentrated broadly in the equatorial regions, with few volcanoes extending toward the north pole. High-volcano-spatial density regions in the western hemisphere are again within the BAT region, and are commonly bound by, or overlap with, rift zones, coronae, and large (>100 km in diameter) volcanoes. The high-volcano-spatial density regions in the eastern hemisphere are also proximal to, and overlap with, major volcanotectonic landforms, although there are fewer instances of such features in this hemisphere. Once again, although these two algorithms produce very similar kernel density maps, there are some differences between the two: in several places, the SCV method tends to cluster the data more (e.g., the 25th percentile contour centered at 26.1°S, 128.7°W than the SAMSE algorithm, which produces a smoother map with slightly less clustering. Differences in the orientations and sizes of the kernel bandwidths for volcanoes >63 km in

diameter and volcanoes ≤63 km in diameter may indicate differences in the tectonic controls on magma ascent and/or source melt production (Cappello et al., 2012; Richardson et al., 2013).

Directional Distribution Analysis:

Analysis of the Directional Distribution elliptical polygon outputs reveals that there is no global preferred orientation of volcanic fields. Nonetheless, we found that 42% of these fields are oriented E–W, with only 13% aligned N–S. The percentage of fields angled to the NW–SE is 24% and the remaining 21% of fields are aligned and NE–SW **(Figure 2.8**).

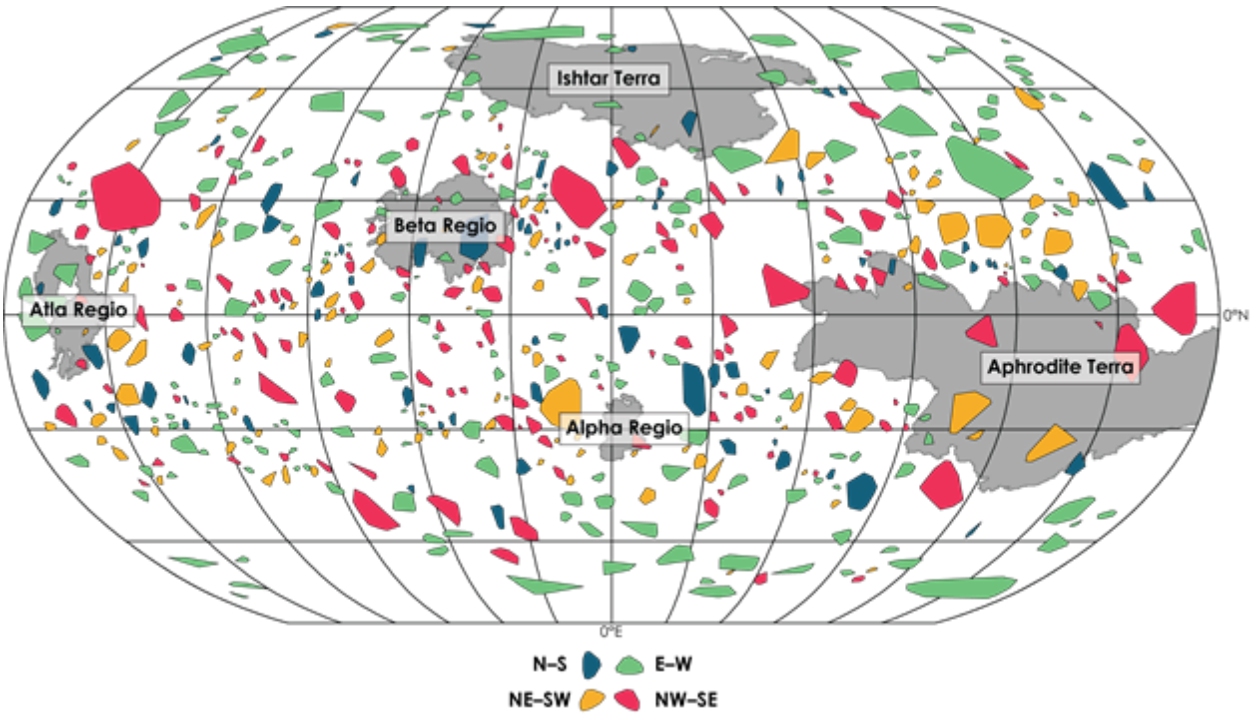

Figure 2.8 Our global database of volcanic fields (*n* = 566), colored to correspond to the orientation of the volcanoes within each volcanic field based on the results from the Directional Distribution analysis. The outlines of major Venusian physiographic features are shown in grey for geographic context. The map is in Robinson projection, centered at 0°E.

That there is no single dominant orientation of volcanic fields suggests that individual field orientation is largely controlled by tectonic stresses that are local, rather than stresses acting on a global or regional scale. To test this hypothesis, we appraised each volcanic field individually and documented any proximal landforms that are resolvably tectonic (e.g., rift zones, grove belts,

tesserae) or volcanic (e.g., shield plains, volcanic plains, coronae) in nature, and then compared the orientations of these components relative to the major axis of the ellipse bounding each volcanic field. We also noted any nearby craters that could have plausibly influenced the evolution of the volcanic field.

Of the 566 such fields, the boundaries of 86% (n = 489) encompass some type of tectonic structure. Of those 489 fields, we find that 26% of fields are exclusively associated with shortening structures, 35% with extensional tectonics, and 39% linked to both types of structure. Of the volcanic fields that have long axes parallel to adjacent tectonic structures, 38% are associated with shortening structures, 26% are associated with extensional structures, 20% are linked to both, and 16% do not contain a tectonic component that is aligned parallel to the long axis of the volcanic field. Those volcanic fields with long axes perpendicular to proximal tectonic landforms are associated with shortening, extensional, or both types of structure 41%, 29%, or 17% of the time, respectively; in 13% of instances, the volcanic field does not contain any tectonic component aligned perpendicular to the long axis of the volcanic field. Analysis of the orientation of the tectonic component indicates that extensional and shortening tectonic structures are almost equally likely to be oriented perpendicular or parallel to the long axis of a given volcanic field.

Overall, we found that "groove belts"—the term used in the Venus literature for localized, narrow extensional systems—are heavily associated with the map unit labeled "shield plains" (shortened to "psh") by Ivanov and Head (2011) in their global map: 60% of the volcanic fields contain groove belts and, of those fields, virtually all (~98%) also host shield plains. The shield plains unit was described by Ivanov and Head (2011) as having abundant, small, shield-like volcanic landforms. These edifices and the surrounding plains are morphologically smooth, and the unit is generally only mildly deformed by tectonic structures (Ivanov and Head, 2011).

We also find that 14% of volcanic fields are not associated with any tectonic components. Unsurprisingly, many of the volcanic fields within our catalog are collocated with instances of the shield plains units. Volcanic fields with no tectonic structures within their boundaries are typically dominated by the shield plains unit, which may have obscured previously visible tectonic structures; alternatively, there may simply have been no tectonic structures in that region in the first place when the cluster of volcanoes constituting the volcanic field were formed.

2.4 Discussion

2.4.1 Morphological

Volcanoes >100 km in Diameter:

We examined 118 volcanoes >100 km in diameter from our global catalog (see Appendix A.1). Predictably, we find a strong positive correlation between volcano diameter and area (**Figure 2.9a**), with four of the largest diameter volcanoes falling off the trend line by having slightly larger areas than is proportional for the population as a whole. These four large volcanoes are associated with Beta, Laufey, and Bell regiones, which are interpreted to be volcanic rises (Brian et al., 2004) that are the surface manifestations of mantle upwellings (Stofan et al., 1995). The large surface areas of these four volcanoes could be a reflection of the size and shape of that upwelling. We also note a weak positive correlation between volcano area and height (**Figure 2.9b**). These findings indicate that large volcanoes on Venus follow approximately linear growth patterns, with mean basal diameter increasing with height, and that these volcanoes also have a wider distribution in range of heights than is the case for edifices 5–100 km in diameter. We find no meaningful correlation between volcano diameter and aspect ratio (**Figure 2.9c**). This last finding is as expected, since large volcanoes on Venus have a wide range of morphologies and may not always

have a circular base (such as, for instance, volcanoes situated on a rift zone, which may be elongated along the axis of the rift trend: Crumpler et al., 1997).

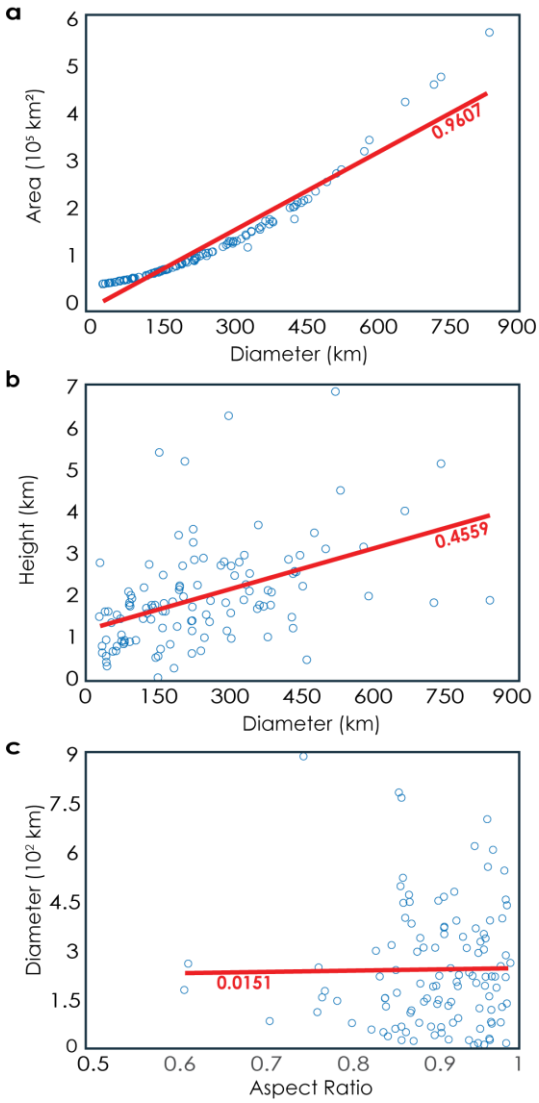

Figure 2.9 Plots detailing morphological properties for all volcanoes >100 km in diameter. There is (**a**) a strong positive relationship between volcano planform area and diameter, but (**b**) a weak positive relationship between volcano diameter and height. (**c**) There is no correlation between aspect ratio and diameter. Best-fit lines for plots (**a**)–(**c**) are shown in red with coefficient of determination (R^2) also shown in red below the line.

Volcanoes 5–100 km in Diameter:

A total of 729 volcanoes 5–100 km in diameter are documented in our catalog (see Appendix A.1). The average diameter of these edifices is 14 km, of which 88% are <20 km in diameter; there is thus a relative lack of edifices in the 20–100 km diameter range on Venus. The Crumpler and Aubele (2000) volcano catalog shows a similar lack of edifices in the 30–100 km in diameter range, with 70% of "intermediate size" edifices measuring <30 km in diameter. Together, these findings suggest that volcano formation mechanisms on Venus preferentially form smaller (<20–30 km in diameter) or larger (>100 km in diameter) edifices. This relative lack of volcanoes in the 20–100 km range may be related to the availability and/eruption rate of the underlying magma source(s) that are more suited to building either a single large edifice or many small edifices.

For edifices 5–100 km in diameter, we find a strong positive correlation between volcano area and diameter (**Figure 2.10a**), with the exception of about 10 edifices with large diameters and areas that diverge above the trend line. Based on the shape of the intermediate volcano diameter–area distribution, we were also able to fit an exponential distribution to these data. Doing so resulted in a lower R^2 value than the corresponding value for the polynomial distribution (shown in **Figure 2.10a**), but this fit was able to account for volcanoes with very large areas and diameters.

For volcanoes 50–100 km in diameter (n = 14) (see Appendix A.1), there appears to be no meaningful correlation between volcano area and height (**Figure 2.10b**). This result is likely due in part to the low spatial resolution of the Magellan topographic data, which do not allow for reliable height value measurements.

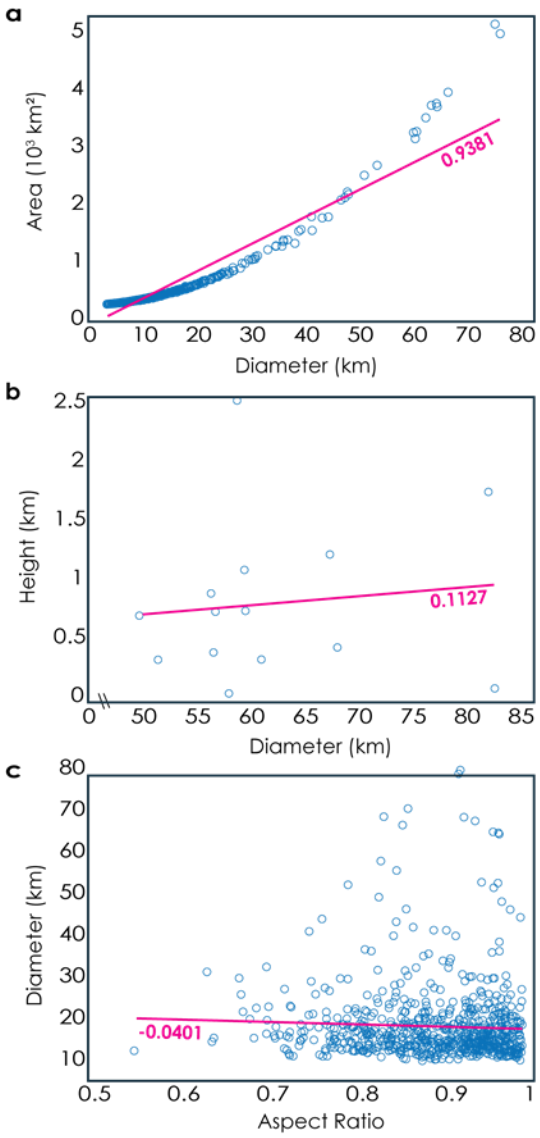

Figure 2.10 Plots detailing morphological properties for all volcanoes 5–100 km in diameter. Height measurements were only calculated for volcanoes >50 km in diameter because of limitations of Magellan altimetry. We note (**a**) a strong positive relationship between volcano planform area and diameter and (**b**) a weak positive correlation between volcano diameter and height. (**c**) Over 50% of volcanoes in this size range have aspect ratios greater than 0.9. Best-fit lines for plots (a)–(c) are shown in pink, with R^2 values also shown in pink below the lines.

Lastly, we find that volcanoes 5–100 km in diameter have aspect ratios ranging from 0.5 to 1.0, with 52% greater than 0.9 (**Figure 2.10c**). Edifices with aspect ratios below 0.6 are all <20 km in diameter, suggesting that there may be some diameter threshold needed to form a relatively

circular volcano base. Alternatively, smaller volcanoes are more likely to reflect the irregular geometry of their driving magmatic plumbing system than larger edifices.

Edifices >50 km in Diameter Within Stereo DEMs:

For edifices >50 km in diameter covered by the stereo-derived DEMs, we employed the Direct Integration method to calculate volcano volume (see *section 2.4*) (see Appendix A.1). Volume estimates generated using this approach rely heavily on the selection of the basal reference plane. Here, we used IDW interpolation to derive the basal reference plane for subsequent height and volume calculations. We also employed a horizontal reference plane equal to the lowest elevation around the base of each edifice to calculate height and volume maxima values. We determined the total volume of 19 large edifices (>100 km in diameter) with coverage in the stereo-derived DEMs to be ~1.1 x 10^6 km^3, which, when extrapolated to the entire population of large volcanoes on Venus, is ~5.5 x 10^6 km^3. This aggregate value is smaller than previously estimated values calculated under the assumption that all volcanoes on Venus are conical in shape (e.g., Ivanov and Head. 2013). Yet large edifices on Venus have diverse morphologies that range from a relatively simple symmetrical outline with flows emanating from a summit region (e.g., Tuulikki Mons) to volcanoes that have features such as summit calderas, radial rifts, and fractures (e.g., Gula and Sapas Montes) (Head et al., 1992b; Crumpler et al., 1997) (**Figure 2.3**). Our volcano volume estimate is likely more accurate than those derived by equating a volcano to a simple cone due to improved volumetric analysis using

the Direct Integration method and given the higher topographic resolution of the stereo-derived DEMs over Magellan altimeter data. Total volumes of large volcanoes on Venus, and the timing of volcano formation, can be used to estimate the magmatic flux at large volcanic centers (McGovern and Solomon, 1997). Subsequently, previous estimates of magma flux integrated over

all volcanoes on Venus may be overestimated, even with the far greater of much smaller volcanoes in this catalog than reported before, which has implications for calculations of resurfacing rates and the interpretation of Venus' volcanic character and geological evolution.

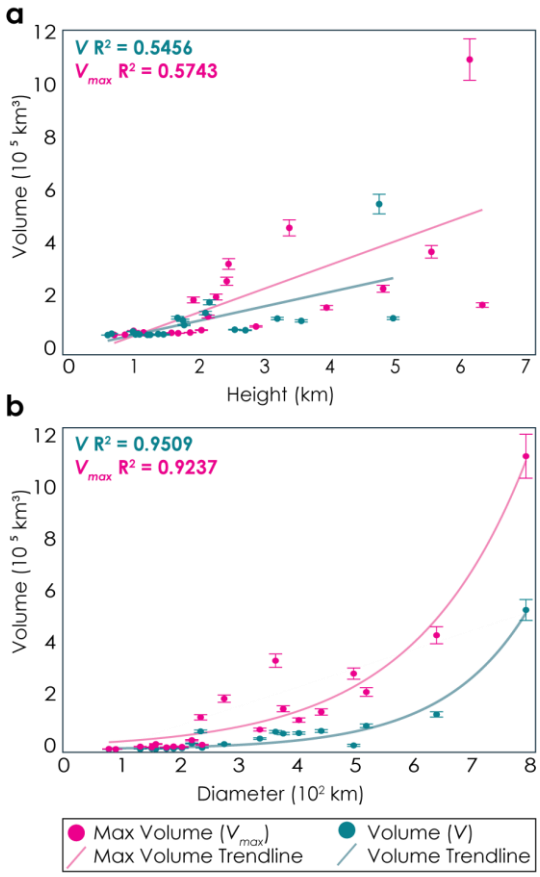

Figure 2.11 Plots showing morphological properties for volcanoes >50 km in diameter that fall within the boundaries of the stereo-derived DEMs. (**a**) Volcano volume and height are roughly correlated, but two volcanoes that skew the distribution. (**b**) Volcano volume and diameter are positively correlated. Volume uncertainty bars are shown for both volume calculations in both plots. R^2 values for volcano volume (V) and max volcano volume (V_{max}) are shown in the upper left of each plot.

The volume of volcanoes >50 km within the stereo DEMs generally increases with height (**Figure 2.11a**), with the exception of one volcano, Tepev Mons, which stands ~5 km high but is only ~220 km in diameter and ~64,000 km^3 in volume. Most large volcanoes (>100 km in diameter) on Venus are ~ 2–3 km tall (Head et al., 1992; Crumpler et al., 1997), with our calculations yielding an average summit elevation of ~2.1 km within the region covered by the

stereo-derived DEMs. Unsurprisingly, we note that volcano volume and diameter are highly correlated and are best fit by an exponential distribution (**Figure 2.11b**). This finding indicates that, of the largest volcanoes on Venus, many are closer to the lower bound of 100 km in diameter. For example, within the stereo-derived DEM coverage, we note 17 volcanoes 100–500 km in diameter but only two exceeding 500 km in diameter. Generally, uncertainty in estimates of volcano volume based on the methods we use here increases with volcano diameter and height due to an increase in the total number of pixels occupied by the edifice. The lack of an obvious, positive correlation between volcano diameter and height could be the result of a relatively small population of volcanoes >50 km in diameter within the stereo-derived DEMs (n = 21).

2.4.2 Spatial Analysis

Large Volcanoes:

Large volcanoes (>100 km in diameter) (see Appendix A.1) are primarily located in the equatorial regions and have an average basal elevation of 1.67 km (relative to the mean planetary radius value of 6,051 km); there are virtually no large volcanoes at the south pole and few near the north pole. We find that 42% (n = 49) of the large volcanoes in our catalog are within the BAT region. Previous workers also noted the relative abundance of large volcanoes in this region, which is not surprising given the prevailing view of major and recent volcanism here, thought to be driven by mantle upwelling on the basis of observations of the topographic highs, large gravity anomalies, and large geoid-to-topography ratios in this region (Stofan et al., 1995; Smrekar et al., 1997; Stofan and Smrekar, 2005; Yang et al., 2016). The BAT region is also dominated by rift zones and extensional structures (Head et al., 1992; Ivanov and Head, 2015; Airey et al., 2017). We note that of the large volcanoes in the BAT region, 84% (n = 41) are within 500 km of a rift zone and, of those, 61% (n = 27) are situated on or directly *within* a rift zone—suggesting that the magma

erupted from these volcanoes is at least in part originally from deep-source mantle upwellings (e.g., Senske et al., 1992).

Numerous models have been developed to quantitatively estimate the global crustal thickness on Venus with topography and gravity data collected by the Magellan mission (e.g., Anderson and Smrekar., 2006; James et al., 2013; Jiménez-Díaz et al., 2015; Yang et al., 2016). The global crustal thickness model developed by James et al. (2013) established the mean crustal thickness on Venus to be ~15 km. With this model, we found the average crustal thickness associated with large volcanoes in the BAT region to range 11.0–24.1 km, with an average thickness of 16.5 km. These values are slightly greater than the corresponding values for large volcanoes outside of the BAT region, which range from 11.0–21.1 km, with an average thickness of 15.9 km. We utilized a non-parametric two-sample Kolmogorov–Smirnov (KS) test to evaluate the difference between the cumulative distribution functions (CDFs) of the distributions of average crustal thickness values for large volcanoes within and outside of the BAT region. The test rejected the null hypothesis that the average crustal thickness values for large volcanoes within and outside of the BAT region are from the same continuous distribution at the 0.05% significance level. This finding supports the interpretation that there is a statistically significant difference in crustal thickness associated with large volcanoes within and outside of the BAT region.

If so, then relatively higher crustal thickness values for volcanoes within the BAT region may be because many volcanoes in this region are associated with volcanic rises, themselves characterized by relatively high crustal thickness values (James et al., 2013; Jimenez-Diaz et al., 2015) (**Figure 2.12**). An analysis of large volcano diameter versus crustal thickness within the

BAT region reveals a weak positive correlation, whereas no meaningful correlation is found for large volcanoes outside that region.

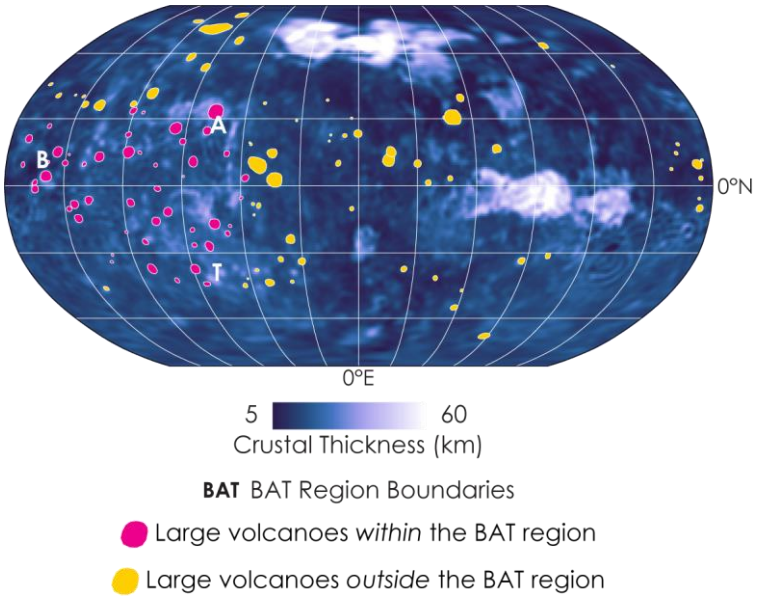

Figure 2.12 A map of global crustal thickness values on Venus (James et al., 2013). The Beta, Atla, and Themis (BAT) regiones are denoted by the letters B, A, and T, starting from the left and moving clockwise. Large volcanoes (>100 km in diameter) from our global catalog that fall within the BAT region are shown in pink; those large volcanoes outside of the BAT region are in yellow. The map is in Robinson projection centered at 0°E.

On Mars, the Tharsis Montes and nearby Olympus Mons are associated with the greatest crustal thickness values found anywhere on that planet (Solomon and Head, 1982; Zuber et al., 2000; Neumann et al., 2004; Andrews-Hanna et al., 2008). The three Tharsis Montes volcanoes span in diameter from 300 to 400 km; Olympus Mons, situated at the northwestern margin of the Tharsis Rise, is ~550 km diameter across (Plescia, 2004). On Venus, high crustal thickness values are associated with volcanic rises that range from ~200 to as much as 900 km in diameter—indicating that volcanoes on Venus can be situated over crust that is as thick as that under volcanoes two or more times greater in diameter on Mars. Venusian volcanoes are also much shorter than Martian volcanoes, presumably in part due to the lower gravity on Mars, but perhaps also because of differences in lithospheric thickness (McGovern et al., 2013) and/or magma

reservoir vertical migration. Vertical migration of neutral buoyancy zones (NBZs) on Venus may be inhibited, causing magma reservoirs to remain in the crust longer, which in turn results in more vertical than horizontal extrusion and shorter volcanoes than on Mars or Earth (Head and Wilson 1986; 1992). Gravity signatures of volcanic rises on Venus indicate deep levels of isostatic compensation, consistent with hotspots that are underlain by mantle upwellings (Grimm and Philips 1992; Stofan et al., 1995; Anderson and Smrekar, 2006).

Intermediate-Size Volcanoes:

Intermediate-size volcanoes (i.e., those 5–100 km in diameter) (see Appendix A.1) are slightly more spatially concentrated in the eastern than the western hemisphere of Venus, with most occurring at relatively low latitudes. Again, we note a higher spatial concentration of volcanoes within the BAT region than elsewhere on Venus, hosting ~57% of intermediate-size volcanoes. We note that intermediate-size edifices surround but typically do not overlap tesserae terrain or rift zones. As a whole, intermediate-sized edifices are much less abundant below the mean planetary radius (6,051 km) and have an average basal elevation of 743 m, in line with observations by previous authors (e.g., Head et al., 1992).

Deformed Volcanoes:

Volcanoes identified as having undergone gravitational deformation (see Appendix A.1) are typically of the intermediate size (5–100 km in diameter), with collapse features (e.g., scarps on the volcano summit and proximal debris avalanches with hummocky terrain: Bulmer et al., 1996; Lopez, 2011) noticeably absent from volcanoes >100 km in diameter (McGovern and Solomon, 1997; Lopez, 2011). We do note, however, that some volcanoes >100 km in diameter on Venus do exhibit evidence of sagging (Byrne et al., 2013), such as Tepev Mons. We find that deformed edifices are geographically widespread, although as for the largest category of

volcanoes, relatively few occur at the NW or SW polar regions and are more are situated within the BAT region than not. Few deformed edifices are located in the lowlands, with but a handful (n = 10) occurring near Guinevere Planitia.

Many deformed edifices are associated with coronae: 38% (n = 70) occur within 200 km of, and and additional 17% (n = 31) overlap, such landforms. Coronae are widely accepted to have formed via mantle upwellings at the base of the lithosphere, causing an initial upwelling and subsequent flattening and gravitational relaxation and resulting in the characteristic annular structure (Pronin and Stofan. 1990; Stofan and Head, 1990; Stofan et al., 1992; Gülcher et al., 2020). This spatial association with deformed edifices may point to some genetic link between coronae formation and the evolution and gravity-driven failure of the flanks of intermediate-sized volcanoes.

Small Volcanoes:

Overall, our results indicate the Venus hosts far more volcanoes <5 km (see Appendix A.1) in diameter than previously recognized. We note a distinct decrease in the spatial density of edifices <5 km in diameter in the lowlands at high southern latitudes, particularly in the southwestern quadrant near Nsomeka and Nuptadi planitiae. Most edifices <5 km in diameter are situated in topographically low-lying regions with an average basal elevation of 625 m (relative to the mean planetary radius value of 6,051 km) and are associated with an average crustal thickness of 13.9 km (James et al., 2013).

Volcanic Fields:

Spatial analysis of the crustal thickness values for our database of volcanic fields (see Appendix A.1) reveals a strong negative correlation, with volcanic fields typically located in areas of relatively thinner crust. The average crustal thickness across the footprint of a volcanic field is

~14.3 km, 0.7 km below the average crustal thickness for Venus (James et al., 2013). Volcanic fields are thought to form from distinct, small-scale eruptions fed from shallow magma reservoirs (Ernst and Desnoyers, 2004; Ivanov and Head, 2004). Terran analogs to Venusian volcanic fields include the expansive seamount populations on the seafloors of Earth (Aubele and Slyuta, 1990; Guest et al., 1992; Crumpler and Aubele, 2000), some of which are associated with thinner oceanic crust (e.g., mid-ocean ridge seamounts) (Wessel, 2007) This tectonic setting differs from other terrestrial shield fields on Earth that are situated over thicker continental crust (e.g., Auckland Volcanic Field, NZ (Lindsay et al., 2011)) and may indicate that volcanic field formation on Venus is similar to that on Earth's seafloor at divergent plate boundaries. If formational processes are indeed similar, then it is unsurprising that volcanic fields on Venus are located over regions of relatively thinner crust as they may mark regions of the lithosphere that has been locally thinned (Ernst and Desnoyers, 2004).

Directional Distribution Interpretation:

Unsurprisingly, there is no dominant global orientation of volcanic fields across Venus. However, we find that within latitude intervals of 30°, volcanic fields are most commonly oriented E–W (53%) and least commonly aligned N–S (14%). The eccentricity of the directional distribution ellipse lessens slightly closer to the poles. Those fields that are elongated (or at least not equant) could reflect the effects of resurfacing and embayment by surrounding plains. Ivanov and Head (2011) described the regional plains unit (shortened to "rp") as plains of volcanic materials. This unit is present within 84% of the volcanic fields in our catalog, so embayment is likely a common occurrence and may play an important role in shaping the outlines of volcanic

fields. We also note that the mean eccentricity of the entire population of volcanic fields is 0.75, with those fields containing the regional plains unit virtually the same with an eccentricity of 0.76.

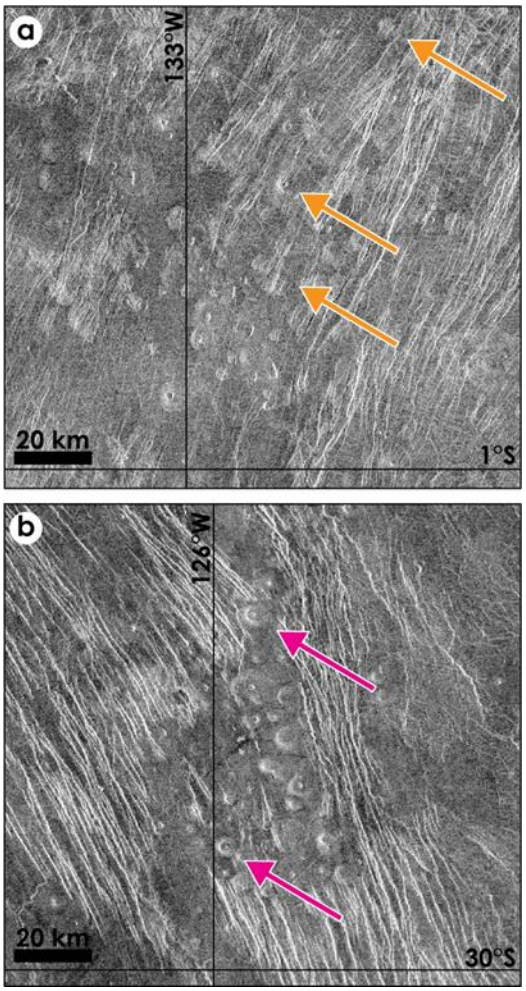

Figure 2.13 Example relationships between tectonic structures and volcanoes within volcanic fields. (**a**) Volcanic field formation was likely not influenced by tectonic structures if the volcanoes within the field are stratigraphically older and show evidence of tectonic structures superposing volcanoes (orange arrows). (**b**) In contrast, volcanic fields with volcanoes that postdate and appear on top of or on the margins of tectonic structures (pink arrows) may have been influenced by those pre-existing tectonic structures. These examples only show portions of volcanic fields. The radar look direction is from the left for each image, and each is shown in an equirectangular projection with (**a**) centered at 0.59°S, 132.85°W and (**b**) centered at 29.66°S, 125.92°W.

Further examination of the dominant tectonic structures at each of the 566 volcanic fields in our catalog reveals that, in some cases, structures postdate volcanoes within the volcanic field and thus likely had no influence on the orientations of the groupings of edifices therein (**Figure**

2.13a), whereas in other cases tectonic structures may have influenced the overall orientation of the clustered volcanoes within the volcanic field (**Figure 2.13b**). Although this analysis revealed no meaningful patterns on a global scale, the orientation of the volcanoes within each volcanic field may provide insight into the geometry of the locally dominant magma plumbing system during the time of eruption. Indeed, further, detailed mapping of the orientation of volcanoes within volcanic fields that both pre- and postdate tectonic structures may give useful insight into the dominant stress fields at varying times, spatial scales, and locations in Venus' history.

Kernel Density Interpretation: Volcanoes >63 km in Diameter:

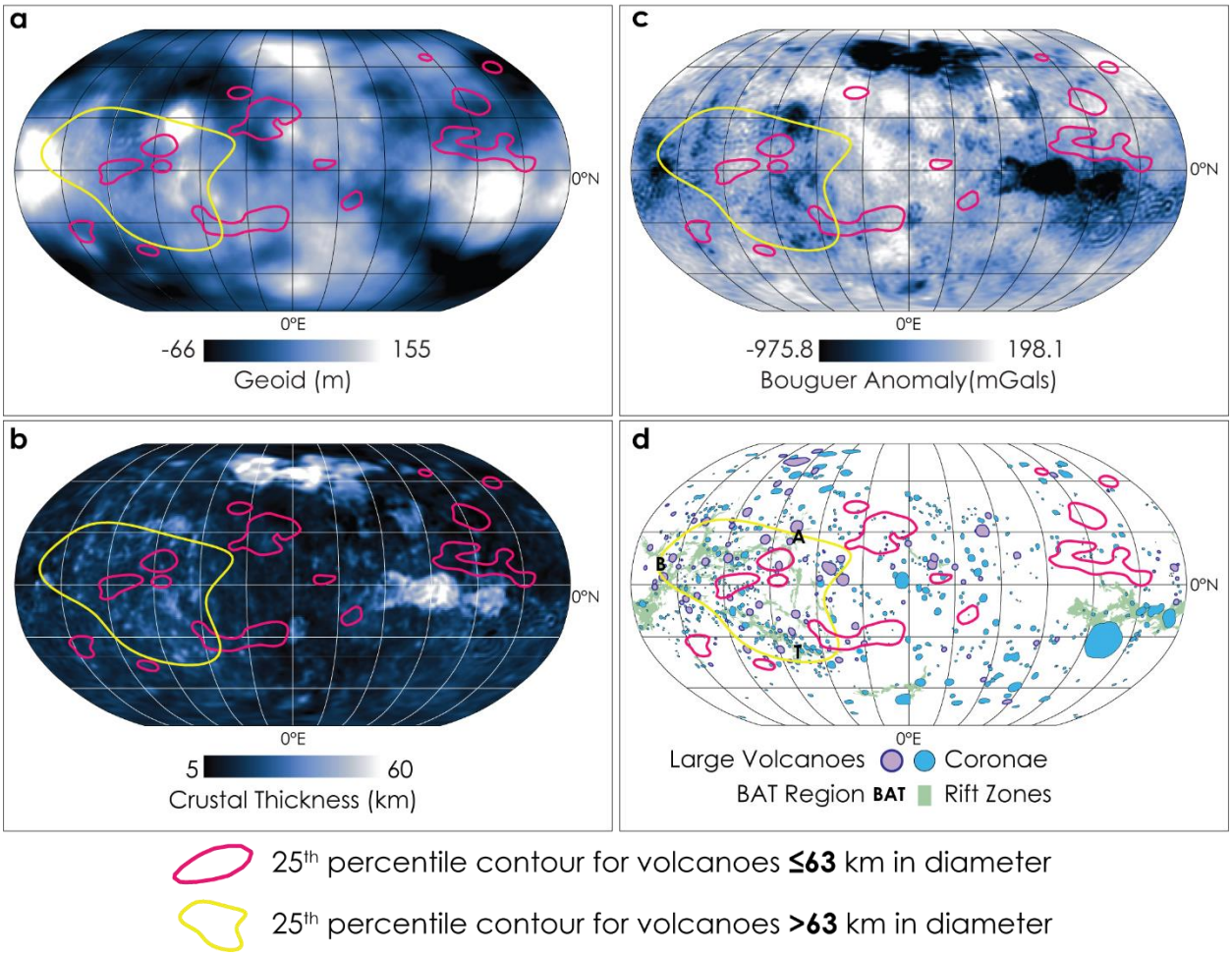

Figure 2.14 SAMSE algorithm-generated 25th-percentile regions for volcanoes ≤63 km in diameter (pink outlines) and SAMSE algorithm-generated 25th-percentile regions for volcanoes >63 km in diameter (yellow outline) superimposed over (**a**) the Venusian geoid (Sjogren, 1997), (**b**) the Bouguer gravity anomaly (Sjogren, 1997), and (**c**) global crustal thickness (James et al.,

2013). (**d**) These clusters are shown in relation to large volcanoes from our global catalog (purple circles with dark blue outlines), as well as rift zones (pale green) and coronae (light blue circle) from the global geologic map of Venus of Ivanov and Head (2011). The Beta, Atla, and Themis (BAT) regiones are denoted by the letters B, A, and T, starting from the left and moving clockwise. All maps are shown in Robinson projection centered at 0°E.

Both the SAMSE and SCV algorithms produce similar spatial density estimates for volcanoes >63 km in diameter. Here, we extract the boundary of the SAMSE high-volcano-spatial-density region, or the 25th percentile contour (yellow outline in **Figure 2.14**), for further analysis. This contour represents the area where the spatial density of volcanoes >63 km in diameter is greatest at > 4.5×10^{-5} per 100 km^2 (**Figure 2.7c**). We note that this region nearly perfectly aligns with the boundaries of the BAT region, where numerous volcanic rises are interpreted to form via deep mantle upwellings (Stofan et al., 1995; Smrekar et al., 1997; Stofan and Smreakar, 2005; Anderson and Smrekar, 2006). To further explore the geology and geophysics associated with the high-volcano-spatial-density region, we compared the area with Magellan-derived geoid (**Figure 2.14a**) and Bouguer gravity anomaly maps (Sjogren, 1997) (**Figure 2.14b**), a crustal thickness map itself based on Magellan gravity measurements (James et al., 2013) (**Figure 2.14c**), and map vector datasets outlining rift zones, coronae (Ivanov and Head, 2013), and large (>100 km in diameter) volcanoes (**Figure 2.14d**). Here, we assumed that gravity datasets either reflect recent volcanism in the BAT region based on VIRTIS (Visual and Infrared Thermal Imaging Spectrometer) on the European Space Agency's Venus Express spacecraft) emissivity data (e.g., Smrekar et al., 2010; Shalygin et al., 2015; Stofan et al., 2016), or that the long-wavelength gravity signatures on Venus are stable over long periods of time (e.g., Benešová and Čížková, 2012).

A comparison of the boundaries of this high-volcano-spatial-density region with Magellan-derived Bouguer anomaly maps developed by Sjogren (1997) shows that the average Bouguer anomaly associated with this region is around –200 mGals (**Figure 2.14b**). Bouguer gravity

anomalies are those that remain when the gravitational signature of topography is removed and, as such, reveal spatial variations in subsurface density (Stofan et al., 2016). A high negative Bouguer anomaly within this region could be associated with the presence of a low-density material at depth such as a mantle upwelling (Stofan et al., 2016).

Magellan geoid anomaly data (Sjogren, 1997) show positive values in this region of 57 m; the crustal thickness here is ~16.3 km (James et al., 2013) (**Figure 2.14a**). On Earth, large positive geoid anomalies are associated with hotspots and subduction zones (Crough and Jurdy, 1980; Richards and Hager; 1988) and, on Venus, large positive geoid anomalies are associated with large volcanic shields (Bindschadler et al., 1992). Additionally, we note an abundance of rift zones and triple junctions in this region, which are also commonly linked to the presence of a mantle upwelling at depth (Ernst and Desnoyers, 2004) (**Figure 2.14d**). Large volcanoes within this high-volcano-spatial-density region are thus perhaps fed from shallow magma reservoirs that originate from deep-seated mantle melt sources. Although we note that this 25th percentile region for large volcanoes is within the BAT regions, there are large volcanoes outside of this region. Edifices outside of the BAT region may be the products of thermally relaxed, older upwellings (Ernst and Desnoyers, 2004), or may simply be the result of shallow melt source capable of producing locally large quantities of magma (Stofan et al., 1992).

Kernel Density Interpretation: Volcanoes ≤63 km in Diameter:

Again, the SAMSE and SCV algorithms produced nearly identical spatial density maps for volcanoes ≤63 km in diameter, and here we extract the ~14 high-volcano-spatial-density regions generated by the SAMSE algorithm for further discussion. The high-volcano-spatial-density regions (25th percentile contour) for volcanoes ≤63 km are widespread both within and beyond the BAT region, and range in diameter from ~1,000 km to 6,000 km. The Bouguer gravity anomaly

(Sjogren, 1997) associated with these high-volcano-spatial-density-regions is approximately –62 mGals, much smaller than the value associated with the high-volcano spatial-density-region for volcanoes >63 km in diameter. This small negative Bouguer anomaly value still corresponds to a subsurface negative density anomaly (Stofan et al., 2016), which suggests that there is some degree of lateral density variations within the lithosphere beneath these smaller volcanoes (**Figure 2.14b**). Particularly, we note that the high-volcano-spatial-density regions for edifices ≤63 km in diameter within the BAT region have a larger negative anomaly (~–101 m Gals) than those outside the BAT (~–18 mGals), which, again, is likely related to the numerous mantle upwellings proposed in the BAT region (Stofan et al., 1995; Smrekar et al., 1997; Stofan and Smreakar, 2005; Anderson and Smrekar, 2006). Similarly, the geoid anomaly (Sjogren, 1997) is slightly higher within the BAT region at ~39 m (**Figure 2.14a**) and the average crustal thickness (James et al., 2013) is 14.8 km (**Figure 2.14c**). Outside the BAT region, the geoid is ~21 m, and the crust is slightly thinner averaging 13.3 km. A higher geoid anomaly and thicker crust within the BAT region is also likely linked to the volcanic rises within the region.

On Earth, the formation of small volcano clusters instead of a single, large, polygenetic volcano is thought to be heavily dependent on rates of magma emplacement (Connor et al., 1992; Crumpler et al., 1994). Large volcanoes suggest the presence of a shallow magma reservoir, with a moderate rate of emplacement that is, for example, approximately equivalent to the rate of intrusion and eruption at the Hawaiian hotspot averaged over the past 70 Myr (Shaw, 1985; Crumpler et al., 1997). Rates below this value can result fields of small volcanoes (e.g., the Springerville volcanic field: Connor et al., 1992; Crumpler at al., 1994). Volcanic conduits might not be readily preserved if the magma supply rate is too low, such that small magma batches could ascend through varying paths to the surface to create numerous smaller volcanoes, instead of

ascending through a single path repeatedly and producing a larger volcano (Fedotov, 1981). Of the ~14 high-volcano-spatial-density regions, half encompass or are within 50 km of at least one large volcano (>100 km in diameter) from our global catalog, with small shields manifesting near the summits and along the flanks, similar to shield volcanoes on Earth such as Mauna Kea and Mount Etna.

Similarly, ~80% (11/14) of the high-volcano-spatial-density regions contain at least one corona, with some regions encompassing as many as 17 (**Figure 2.14d**). Coronae are typically associated with volcanism, and the proximity of high volcano spatial concentrations to coronae and large volcanoes suggests that the coronae and large volcanoes had access to a localized, shallow magma reservoir (Head, et al., 2015), and that these spatial clusters may have formed as a result of a waning magma supply to the larger edifices/coronae present in the area that led to the formation of smaller volcanoes surrounding a larger edifice (Crumpler et al., 1997).

A similar process of a declining magma supply and limited main-flank development has resulted in distributed volcanism and parasitic cones on Hawaiian shield volcanoes (Bleacher and Greely, 2008), and is attributed to the formation of volcanic fields surrounding large volcanoes such as Pavonis Mons on Mars (Hughes et al., 2005). Alternatively, clusters of small edifices may form from a unique source that is unrelated to the proximal large volcano. In contrast to Hughes et al. (2005), Bleacher et al. (2009) proposed that Martian volcanic fields south of Pavonis Mons formed independently from processes related to the construction of Pavonis' main flanks. The fields appears to be spatially linked to buried, Noachian-aged tectonic structures and could have formed from the ascent of independent shallow magma chambers (Bleacher et al., 2009). The genetic relationship between large volcanoes (>100 km in diameter) and clusters of small volcanoes on Venus is difficult to distinguish, but structural mapping with the Magellan SAR data

within the high-volcano-spatial-density regions for volcanoes ≤63 km in diameter, together with vent alignment analysis, could reveal links or patterns between small volcanoes and tectonic structures.

Additionally, data derived from future planned missions could provide further insight into this relationship. For example, the Venus Subsurface Radar Sounder (SRS) onboard ESA's EnVision spacecraft will be used to search for stratigraphic relations between different geological units to allow for the identification of buried structures and strata (Bruzzone et al., 2020) that could be directly linked to the manifestation of volcanoes on the surface. Similarly, the Venus Emissivity Mapper (VEM) onboard NASA's Venus Emissivity, Radio science, InSAR, Topography, and Spectroscopy (VERITAS) spacecraft will provide low-resolution but spatially extensive information on the composition of surface materials (Smrekar et al., 2022), which could offer with a general idea of surface composition associated with large volcanoes and volcanic fields.

As on Venus, volcanic fields on Mars are not always spatially proximal to larger edifices, such as for the case of volcanic fields located in the Tempe–Mareotis and Syria Planum regions (Richardson et al., 2021). On Venus, high-volcano-spatial-density clusters that are not physically close to either large volcanoes (those >100 km in dimeter) or coronae could simply be the products of comparatively low magma supply rates. Small edifices (those <5 km in diameter, which represent ~99% of the volcanoes in our catalog) likely formed from a relatively low but steady supply of magma from a melt anomaly for a brief period of geological time, magma that probably did not reside in a shallow reservoir for extended periods (Crumpler et al., 1997; Ivanov & Head, 2004). Alternatively, since ~80% (11/14) of the high-volcano-spatial-density clusters contain a rift zone or ridge belt, small volcanoes in these regions could be the products of dike emplacement associated with the local extensional stresses. Again, detailed structural mapping and vent

alignment analysis would be required to accurately assess any causal relations between edifices within these high-volcano-spatial-density regions with surrounding tectonic structures.

The 14 regions of high-volcano-spatial-density for edifices ≤63 km in dimeter reflect the localized differences in magma supply and ascent in each area. Some such clusters of volcanoes are likely linked to mantle upwellings, whereas others could be the surface manifestation of a waning melt anomaly. The assessment of spatial and temporal relations between features such as large volcanoes, coronae, and rift zones, in conjunction with geophysical datasets, could shed light on possible interpretations of the spatial density maps (**Figure 2.7**). Our use of our catalog here is to draw regional- and global-scale findings and inferences, rather than to account for the details of particular volcanoes or groupings of edifices, which offer fruitful avenues for future study.

2.5 Conclusions

Venus hosts a range of volcanic landforms that offer insight into how Earth-sized rocky bodies evolve and lose heat without Earth-like plate tectonics. Here, we present the most comprehensive global dataset of volcanoes and volcanic fields on Venus yet compiled, which can be used to evaluate the morphology and spatial relationships of volcanoes and other volcanic (e.g., corona) or tectonic (e.g., rift zones) structures on the second planet. Stereo-derived DEMs (Herrick 2020) provide improved topographic resolution over Magellan altimetry and facilitate the calculation of more accurate height and volume measurements for more volcanoes on Venus than were previously possible. Volcanoes covered by the stereo-derived DEMs generally have relatively low relief, with intermediate-sized edifices (5–100 km in diameter) and large edifices (>100 km in diameter) being ~0.23 km and~2.4 km tall, respectively.

Size–frequency distributions of edifices >5 km in diameter reveal that there are two distinct exponential size–frequency distributions of volcanoes on Venus: those greater than, and those less than, 63 km in diameter. Size–frequency distributions also indicate a relative lack of edifices in the 20–100 km diameter range. These finding suggest that there is some control on magma availability, production rate, and/or emplacement that makes it less likely that volcanoes 20–100 km in diameter form on Venus. We employed kernel density analysis to better establish the spatial distribution of volcanoes on Venus. We find that high-volcano-spatial-density regions for volcanoes >63 km mainly correspond to the BAT region and are likely surface expressions of mantle upwellings. Kernel density map results for volcanoes ≤63 km in diameter are more varied, as smaller volcanoes manifest nearly globally on Venus. We find it likely that high-volcano-spatial-density regions for volcanoes ≤63 km in diameter may both be genetically tied to proximal large volcanoes (>100 km in diameter) or coronae or have formed independently via magma emplacement from buried tectonic structures or dike emplacement.

References

Addington, E. A. (2001). A stratigraphic study of small volcano clusters on Venus. *Icarus*, 149, 16–36. https://doi.org/10.1006/icar.2000.6529

Airey, M. W., Mather, T. A., Pyle, D. M., & Ghail, R. C. (2017). The distribution of volcanism in the Beta-Atla-Themis region of Venus: Its relationship to rifting and implications for global tectonic regimes. *Journal of Geophysical Research: Planets*, *122*, 1626–164. https://doi.org/10.1002/2016JE005205

Anderson, F. S., & Smrekar, S. E. (2006). Global mapping of crustal and lithospheric thickness on Venus. *Journal of Geophysical Research: Planets*, *111*, E08006. https://doi.org/10.1029/2004JE002395

Andrews-Hanna, J. C., Zuber, M. T., & Banerdt, W. B. (2008). The Borealis basin and the origin of the martian crustal dichotomy. *Nature*, *453*, 1212–1215. https://doi.org/10.1038/nature07011

Aranda-Gómez, J. J., Housh, T. B., Luhr, J. F., Noyola-Medrano, C., & Rojas-Beltrán, M. A. (2010). Origin and formation of neck in a basin landform: Examples from the Camargo

volcanic field, Chihuahua (México). *Journal of Volcanology and Geothermal Research, 197*, 123–132. https://doi.org/10.1016/j.jvolgeores.2009.08.004

Aubele, J. C., & Slyuta, E. N. (1990). Small domes on Venus: Characteristics and origin. *Earth, Moon, and Planets, 50*, 493–532. https://doi.org/10.1007/BF00142404

Aubele, J. C., Head, J. W., Crumpler, L. S., Guest, J. E., & Saunders, R. S. (1992). Fields of small volcanoes on Venus (shield fields): Characteristics and implications. In *LPSC 23rd*. Lunar and Planetary Institute.

Aubele, J. C. (1995). Stratigraphy of small volcanoes and plains terrain in Vellamo Planitia-Shimti tessera region, Venus. In *LPSC 26th*. Lunar and Planetary Institute.

Aubele, J. C. (1996). Akkruva small shield plains: Definition of a significant regional plains unit on Venus. In *LPSC 27th*. Lunar and Planetary Institute.

Arvidson, R. E., Greeley, R., Malin, M. C., Saunders, R. S., Izenberg, N., Plaut, J. J., & Shepard, M. K. (1992). Surface modification of Venus as inferred from Magellan observations of plains. *Journal of Geophysical Research: Planets*, *97*,13303–13317. https://doi.org/10.1029/92JE01384

Basilevsky, A. T., & Head III, J. W. (1998). The geologic history of Venus: A stratigraphic view. *Journal of Geophysical Research: Planets, 103*, 8531–8544. https://doi.org/10.1029/98JE00487

Benešová, N., & Čížková, H. (2012). Geoid and topography of Venus in various thermal convection models. *Studia Geophysica et Geodaetica, 56*, 621–639. https://doi.org/10.1007/s11200-011-0251-7

Bindschadler, D. L., Schubert, G., & Kaula, W. M. (1992). Coldspots and hotspots: Global tectonics and mantle dynamics of Venus. *Journal of Geophysical Research: Planets, 97*, 13495–13532. https://doi.org/10.1029/92JE01165

Bishop, M. A. (2007). Point pattern analysis of eruption points for the Mount Gambier volcanic sub-province: a quantitative geographical approach to the understanding of volcano distribution. *Area*, *39*, 230–241. https://doi.org/10.1111/j.1475-4762.2007.00729.x

Bjonnes, E. E., Hansen, V. L., James, B., & Swenson, J. B. (2012). Equilibrium resurfacing of Venus: Results from new Monte Carlo modeling and implications for Venus surface histories. *Icarus, 217*, 451–461. https://doi.org/10.1016/j.icarus.2011.03.033

Bleacher, J. E., Glaze, L. S., Greeley, R., Hauber, E., Baloga, S. M., Sakimoto, S. E., & Glotch, T. D. (2009). Spatial and alignment analyses for a field of small volcanic vents south of Pavonis Mons and implications for the Tharsis province, Mars. *Journal of Volcanology and Geothermal Research*, *185*, 96–102. https://doi.org/10.1016/j.jvolgeores.2009.04.008

Bleacher, J. E., & Greeley, R. (2008). Relating volcano morphometry to the developmental progression of Hawaiian shield volcanoes through slope and hypsometric analyses of SRTM data. *Journal of Geophysical Research: Solid Earth*, *113*. https://doi.org/10.1029/2006JB004661

Brian, A. W., Stofan, E. R., Guest, J. E., & Smrekar, S. E. (2004). Laufey Regio: A newly discovered topographic rise on Venus. *Journal of Geophysical Research: Planets*, *109*. https://doi.org/10.1029/2002JE002010

Bruzzone, L., Bovolo, F., Thakur, S., Carrer, L., Donini, E., Gerekos, C., Paterna, S., Santoni, M. & Sbalchiero, E. (2020). Envision mission to venus: Subsurface radar sounding. In *IGARSS 2020-2020 IEEE International Geoscience and Remote Sensing Symposium*.

Bulmer, M. H., & Guest, J. E. (1996). Modified volcanic domes and associated debris aprons on Venus. *Geological Society, London, Special Publications*, *110*, 349–371. https://doi.org/10.1144/GSL.SP.1996.110.01.25

Byrne, P. K., de Vries, B. V. W., Murray, J. B., & Troll, V. R. (2009). The geometry of volcano flank terraces on Mars. *Earth and Planetary Science Letters*, *281*, 1–13. https://doi.org/10.1016/j.epsl.2009.01.043

Byrne, P. K., Holohan, E. P., Kervyn, M., de Vries, B. V. W., Troll, V. R., & Murray, J. B. (2013). A sagging-spreading continuum of large volcano structure. *Geology*, *41*, 339–342. https://doi.org/10.1130/G33990.1

Campello, R.J.G.B., Moulavi, D., Sander, J. (2013). Density-Based Clustering Based on Hierarchical Density Estimates. In: Pei, J., Tseng, V.S., Cao, L., Motoda, H., Xu, G. (Eds) Advances in Knowledge Discovery and Data Mining. PAKDD 2013. Lecture Notes in Computer Science (Vol. 7819). Springer, Berlin, Heidelberg. https://doi.org/10.1007/978-3-642-37456-2_14

Campello, R. J., Moulavi, D., Zimek, A., & Sander, J. (2015). Hierarchical density estimates for data clustering, visualization, and outlier detection. *ACM Transactions on Knowledge Discovery from Data (TKDD)*, *10*, 1–51. https://doi.org/10.1145/2733381

Cappello, A., Neri, M., Acocella, V., Gallo, G., Vicari, A., & Del Negro, C. (2012). Spatial vent opening probability map of Etna volcano (Sicily, Italy). *Bulletin of Volcanology*, *74*, 2083–2094. https://doi.org/10.1007/s00445-012-0647-4

Cañon-Tapia, E., & Mendoza-Borunda, R. (2014). Insights into the dynamics of planetary interiors obtained through the study of global distribution of volcanoes I: Empirical calibration on Earth. *Journal of Volcanology and Geothermal Research*, *281*, 53–69. https://doi.org/10.1016/j.jvolgeores.2014.05.013

Cañón-Tapia, E. (2013). Volcano clustering determination: Bivariate Gauss vs. Fisher kernels. *Journal of Volcanology and Geothermal Research*, *258*, 203–214. https://doi.org/10.1016/j.jvolgeores.2013.04.015

Cañon-Tapia, E. (2016). Reappraisal of the significance of volcanic fields. *Journal of volcanology and Geothermal Research*, *310*, 26–38. https://doi.org/10.1016/j.jvolgeores.2015.11.010

Cebriá, J. M., Martín-Escorza, C., López-Ruiz, J., Morán-Zenteno, D. J., & Martiny, B. M. (2011). Numerical recognition of alignments in monogenetic volcanic areas: Examples from the Michoacán-Guanajuato Volcanic Field in Mexico and Calatrava in

Spain. *Journal of Volcanology and Geothermal Research*, *201*, 73–82. https://doi.org/10.1016/j.jvolgeores.2010.07.016

Connor, C. B. (1990). Cinder cone clustering in the TransMexican Volcanic Belt: implications for structural and petrologic models. *Journal of Geophysical Research: Solid Earth*, *95*, 19395–19405. https://doi.org/10.1029/JB095iB12p19395

Connor, C. B., Condit, C. D., Crumpler, L. S., & Aubele, J. C. (1992). Evidence of regional structural controls on vent distribution: Springerville Volcanic Field, Arizona. *Journal of Geophysical Research: Solid Earth*, *97*, 12349–12359. https://doi.org/10.1029/92JB00929

Connor, C. B., & Connor, L. J. (2009). Estimating spatial density with kernel methods. In C.B. Connor, N.A. Chapman, and L.J. Connor (Eds), *Volcanic and tectonic hazard assessment for nuclear facilities*, (pp. 346–368). Cambridge University Press.

Connor, C. B., Connor, L. J., Germa, A., Richardson, J. A., Bebbington, M. S., Gallant, E., & Saballos, A. (2018). How to use kernel density estimation as a diagnostic and forecasting tool for distributed volcanic vents. *Statistics in Volcanology*, *4*, 3. https://doi.org/10.5038/2163-338X.4.3

Connor, C. B. & Conway, F. M. (2000). Basaltic volcanic fields. In H. Sigurdsson, B. Houghton, S.R. McNutt, H. Rymer, & J. Stix (Eds,), *Encyclopedia of Volcanoes* (Vol. 1, pp. 331–343). Cambridge, MA: Academic Press.

Crough, S. T., & Jurdy, D. M. (1980). Subducted lithosphere, hotspots, and the geoid. *Earth and Planetary Science Letters*, *48*, 15–22. https://doi.org/10.1016/0012-821X(80)90165-X

Crumpler, L. S., Aubele, J. C., & Condit, C. D. (1994). Volcanoes and neotectonic characteristics of the Springerville volcanic field, Arizona. *New Mexico Geological Society Guidebook*, 147–164. https://doi.org/10.56577/FFC-45.147

Crumpler, L. S., Aubele, J. C., Senske, D. A., Keddie, S. T., Magee, K. P., & Head, J. W. (1997). Volcanoes and centers of volcanism on Venus. In S.W. Bougher, D.M. Hunten & R.J. Philips (Eds.) *Venus II: Geology, Geophysics, Atmosphere, and Solar Wind Environment*, (pp. 697–756). Tucson, AZ: The University of Arizona Press. https://doi.org/10.2307/j.ctv27tct5m.26

Crumpler, L.S., Aubele, J., (2000). Volcanismon Venus. In: Sigurdson, H., Houghton, B., Rymer, H., Stix, J., McNutt, S. (Eds.), Encyclopedia of Volcanoes. (pp. 727–770). Academic Press: San Diego, San Francisco, New York, Boston, London, Sydney, Toronto.

Duong, T. (2007). ks: Kernel density estimation and kernel discriminant analysis for multivariate data in R. *Journal of Statistical Software*, *21*, 1–16. https://doi.org/10.18637/jss.v021.i07

Duong, T., & Hazelton, M. (2003). Plug-in bandwidth matrices for bivariate kernel density estimation. *Journal of Nonparametric Statistics*, *15*, 17–30. https://doi.org/10.1080/10485250306039

Edwards, R. T., & Dowe, D. L. (1998). Single factor analysis in MML mixture modelling. In *Pacific-Asia Conference on Knowledge Discovery and Data Mining* (pp. 96-109). Springer, Berlin, Heidelberg.

Ernst, R. E., & Desnoyers, D. W. (2004). Lessons from Venus for understanding mantle plumes on Earth. *Physics of the Earth and Planetary Interiors*, *146*, 195–229. https://doi.org/10.1016/j.pepi.2003.10.012

Everitt, B. S., & Hand, D. J. (1981). Mixtures of discrete distributions. In *Finite Mixture Distributions* (pp. 89–105). Springer, Dordrecht.

Ester, M., Kriegel, H. P., Sander, J., & Xu, X. (1996). A density-based algorithm for discovering clusters in large spatial databases with noise. *Knowledge Discovery and Data Mining Proceedings*, *96*, 226–231.

Favalli, M., & Fornaciai, A. (2017). Visualization and comparison of DEM-derived parameters. Application to volcanic areas. *Geomorphology*, *290*, 69–84. https://doi.org/10.1016/j.geomorph.2017.02.029

Favalli, M., Karátson, D., Mazzarini, F., Pareschi, M. T., & Boschi, E. (2009). Morphometry of scoria cones located on a volcano flank: a case study from Mt. Etna (Italy), based on high
resolution LiDAR data. *Journal of Volcanology and Geothermal Research*, *186*, 320–330. https://doi.org/10.1016/j.jvolgeores.2009.07.011

Fedotov, S. A. (1981). Magma rates in feeding conduits of different volcanic centres. *Journal of Volcanology and Geothermal Research*, *9*, 379–394. https://doi.org/10.1016/0377-0273(81)90045-7

Ford, P. G. (1992). MGN V RDRS 5 GLOBAL DATA RECORD TOPOGRAPHIC V1.0 [Data set]. NASA Planetary Data System. https://doi.org/10.17189/1522522

Ford, J. P., Plaut, J. J., Weitz, C. M., Farr, T. G., Senske, D. A., Stofan, E. R., Michaels, G., & Parker, T. J. (1993). Guide to Magellan Image Interpretation. *JPL Publication*, *93-24*, 1–18.

Germa, A., Connor, L. J., Cañon-Tapia, E., & Le Corvec, N. (2013). Tectonic and magmatic controls on the location of post-subduction monogenetic volcanoes in Baja California, Mexico, revealed through spatial analysis of eruptive vents. *Bulletin of Volcanology*, *75*, 1-–4. https://doi.org/10.1007/s00445-013-0782-6

Gleason, A. L., Herrick, R. R., & Byrnes, J. M. (2010). Analysis of Venusian steep-sided domes utilizing stereo-derived topography. *Journal of Geophysical Research: Planets*, *115*, E06004. https://doi.org/10.1029/2009JE003431

Greeley, R., Bleacher, J. E., Cave, S. R., Williams, D. A., Werner, S. C., & Neukum, G. (2006). Fields of small shield volcanoes in the Tharsis region: Mars Express HRSC results. In *European Planetary Science Congress*, Berlin, Germany.

Grimm, R. E., & Phillips, R. J. (1992). Anatomy of a Venusian hot spot: Geology, gravity, and mantle dynamics of Eistla Regio. *Journal of Geophysical Research: Planets*, *97*, 16035–16054. https://doi.org/10.1029/92JE01500

Grosse, P., & Kervyn, M. (2018). Morphometry of terrestrial shield volcanoes. *Geomorphology*, *304*, 1–14. https://doi.org/10.1016/j.geomorph.2017.12.017

Grosse, P., Euillades, P. A., Euillades, L. D., & Van Wyk de Vries, B. (2014). A global database of composite volcano morphometry. *Bulletin of Volcanology*, *76*, 1–16. https://doi.org/10.1007/s00445-013-0784-4

Grosse, P., de Vries, B. V. W., Euillades, P. A., Kervyn, M., & Petrinovic, I. A. (2012). Systematic morphometric characterization of volcanic edifices using digital elevation models. *Geomorphology*, *136*, 114–131. https://doi.org/10.1016/j.geomorph.2011.06.001

Grosse, P., de Vries, B.V.W. , Petrinovic, I. A., Euillades, P. A., & Alvarado, G. E. (2009). Morphometry and evolution of arc volcanoes. *Geology*, *37*, 651–654. https://doi.org/10.1130/G25734A.1

Guest, J. E., Beratan, K., Head, J. W., Bulmer, M. H., Weitz, C., Greeley, R., et al. (1992). Small volcanic edifices and volcanism in the plains of Venus. *Journal of Geophysical Research*, 97, 15949. https://doi.org/10.1029/92JE01438

Guest, J. E., & Stofan, E. R. (1999). A new view of the stratigraphic history of Venus. *Icarus*, *139*, 55–66. https://doi.org/10.1006/icar.1999.6091

Gülcher, A. J., Gerya, T. V., Montési, L. G., & Munch, J. (2020). Corona structures driven by plume–lithosphere interactions and evidence for ongoing plume activity on Venus. *Nature Geoscience*, *13*, 547–554. https://doi.org/10.1038/s41561-020-0606-1

Haag, M. B., Baez, W. A., Sommer, C. A., Arnosio, J. M., & Filipovich, R. E. (2019). Geomorphology and spatial distribution of monogenetic volcanoes in the southern Puna Plateau (NW Argentina). *Geomorphology*, *342*, 196–209. https://doi.org/10.1016/j.geomorph.2019.06.008

Hahn, R.M., and Byrne, P.K., (2020). Mapping a Volcanic World: A New Understanding of Shield Volcano Morphology and Spatial Relationships on Venus. Geological Society of America, *Abstracts with Programs.* Vol 52, No. 6. https://doi.org/10.1130/abs/2020AM-355002

Hahn, R., & Byrne, P. K. (2022). A Global Catalog of Volcanoes and Volcanic Fields on Venus [V2] (Version 2) [Data set]. Washington University in St. Louis. https://doi.org/10.7936/8XY0-X885

Hall, P., Marron, J. S., & Park, B. U. (1992). Smoothed cross-validation. *Probability Theory and Related Fields*, *92*, 1–20. https://doi.org/10.1007/BF01205233

Head, J. W., Crumpler, L. S., Aubele, J. C., Guest, J. E., & Saunders, R. S. (1992). Venus volcanism: Classification of volcanic features and structures, associations, and global distribution from Magellan data. *Journal of Geophysical Research: Planets*, 97, 13153–13197. https://doi.org/10.1029/92JE01273

Head, J. W., Crumpler, L. S., & Aubele, J. C. (1992b). Large shield volcanoes on Venus: distribution and classification. In *LPSC 23rd*. Lunar and Planetary Institute.

Head, J. W., & Wilson, L. (1986). Volcanic processes and landforms on Venus: Theory, predictions, and observations. *Journal of Geophysical Research: Solid Earth*, *91*, 9407–9446. https://doi.org/10.1029/JB091iB09p09407

Head, J. W., & Wilson, L. (1992). Magma reservoirs and neutral buoyancy zones on Venus: Implications for the formation and evolution of volcanic landforms. *Journal of Geophysical Research: Planets*, *97*, 3877–3903. https://doi.org/10.1029/92JE00053

Herrick, R. R. (2020). Magellan Venus Stereo-Derived Topography Bundle [Data set]. Geosciences Node. https://doi.org/10.17189/1519332

Herrick, R. R., Stahlke, D. L., & Sharpton, V. L. (2012). Fine-scale Venusian topography from Magellan stereo data. Eos, *Transactions American Geophysical Union*, *93*, 125–126. https://doi.org/10.1029/2012EO120002

Hughes, S. S., Sakimoto, S. E. H., Gregg, T. K. P., & Brady, S. M. (2005, March). Petrologic Evidence for Multiple, Chemically Evolved Magma Batches and Implications for Plains Volcanism on Earth and Mars. *In LPSC 36th*. Lunar and Planetary Institute.

Ivanov, M. A., & Head, J. W. (2004a). Stratigraphy of small shield volcanoes on Venus: Criteria for determining stratigraphic relationships and assessment of relative are and temporal abundance. *Journal of Geophysical Research: Planets*, *109*, E10001. https://doi.org/10.1029/2004JE002252

Ivanov, M. A., & Head, J. W. (2011). Global geological map of Venus. *Planetary and Space Science*, *59*, 1559–1600. https://doi.org/10.1016/j.pss.2011.07.008

Ivanov, M. A., & Head, J. W. (2013). The history of volcanism on Venus. *Planetary and Space Science*, *84*, 66–92. https://doi.org/10.1016/j.pss.2013.04.018

Ivanov, M. A., & Head, J. W. (2015). The history of tectonism on Venus: A stratigraphic analysis. *Planetary and Space Science*, *113*, 10–32. https://doi.org/10.1016/j.pss.2015.03.016

James, P. B., Zuber, M. T., & Phillips, R. J. (2013). Crustal thickness and support of topography on Venus. *Journal of Geophysical Research: Planets*, *118*, 859–875. https://doi.org/10.1029/2012JE004237

Jiménez-Díaz, A., Ruiz, J., Kirby, J. F., Romeo, I., Tejero, R., & Capote, R. (2015). Lithospheric structure of Venus from gravity and topography. *Icarus*, *260*, 215–231. https://doi.org/10.1016/j.icarus.2015.07.020

Kear, D. (1964). Volcanic alignments north and west of New Zealand's central volcanic region. *New Zealand Journal of Geology and Geophysics*, *7*, 24–44. https://doi.org/10.1080/00288306.1964.10420155

Kervyn, M., et al. (2007). Mapping volcanic terrain using high-resolution and 3D satellite remote sensing. *Geological Society, London, Special Publications*, *283*, 5–30. https://doi.org/10.1144/SP283.2

Kinczyk, M. J., Prockter, L. M., Byrne, P. K., Susorney, H. C., & Chapman, C. R. (2020). A morphological evaluation of crater degradation on Mercury: Revisiting crater classification with MESSENGER data. *Icarus*, *341*, 113637. https://doi.org/10.1016/j.icarus.2020.113637

Kiyosugi, K., Connor, C. B., Zhao, D., Connor, L. J., & Tanaka, K. (2010). Relationships between volcano distribution, crustal structure, and P-wave tomography: an example from the Abu Monogenetic Volcano Group, SW Japan. *Bulletin of volcanology*, *72*, 331–340. https://doi.org/10.1007/s00445-009-0316-4

Knicely, J. J. C., & Herrick, R. R. (2021). Survey of mid-sized Venusian volcanoes using stereo-derived topography. *Icarus*, *368*, 114577. https://doi.org/10.1016/j.icarus.2021.114577

Kreslavsky, M. A., & Head III, J. W. (1999). Morphometry of small shield volcanoes on Venus: Implications for the thickness of regional plains. *Journal of Geophysical Research: Planets*, *104*, 18925–18932. https://doi.org/10.1029/1999JE001042

Laura, J. R., Hare, T. M., Gaddis, L. R., Fergason, R. L., Skinner, J. A., Hagerty, J. J., & Archinal, B. A. (2017). Towards a planetary spatial data infrastructure. *ISPRS International Journal of Geo-Information*, *6*, 181. https://doi.org/10.3390/ijgi6060181

Le Corvec, N., Spörli, K. B., Rowland, J., & Lindsay, J. (2013). Spatial distribution and alignments of volcanic centers: clues to the formation of monogenetic volcanic Fields. *Earth-Science Reviews*, *124*, 96–114. https://doi.org/10.1016/j.earscirev.2013.05.005

Lindsay, J. M., Leonard, G. S., Smid, E. R., & Hayward, B. W. (2011). Age of the Auckland Volcanic Field: a review of existing data. *New Zealand Journal of Geology and Geophysics*, *54*, 379–401. https://doi.org/10.1080/00288306.2011.595805

López, I. (2011). Embayed intermediate volcanoes on Venus: Implications for the evolution of the volcanic plains. *Icarus*, *213*, 73–85. https://doi.org/10.1016/j.icarus.2011.02.022

McGovern, P. J., Galgana, G. A., Verner, K. R., & Herrick, R. R. (2014). New constraints on volcano-tectonic evolution of large volcanic edifices on Venus from stereo topography–derived strain estimates. *Geology*, *42*, 59–62. https://doi.org/10.1130/G34919.1

McGovern, P. J., & Solomon, S. C. (1997). Filling of flexural moats around large volcanoes on Venus: Implications for volcano structure and global magmatic flux. *Journal of Geophysical Research: Planets*, *102*, 16303–16318. https://doi.org/10.1029/97JE01318

McGovern, P. J., Rumpf, M. E., & Zimbelman, J. R. (2013). The influence of lithospheric flexure on magma ascent at large volcanoes on Venus. *Journal of Geophysical Research: Planets*, *118*, 2423–2437. https://doi.org/10.1002/2013JE004455

McInnes, L., Healy, J., & Astels, S. (2017). hdbscan: Hierarchical density based clustering. *Journal of Open Source Software*, *2*, 205. https://doi.org/10.21105/joss.00205

McLachlan, G. J., & Basford, K. E. (1988). Mixture models: Inference and applications to clustering (Vol. 38). New York: M. Dekker.

Morgan, L. A., & McIntosh, W. C. (2005). Timing and development of the Heise volcanic field, Snake River Plain, Idaho, western USA. *Geological Society of America Bulletin*, *117*, 288–306. https://doi.org/10.1130/B25519.1

Mouginis-Mark, P. J. (2016). Geomorphology and volcanology of Maat Mons, Venus, *Icarus*, *277*, 433–441. https://doi.org/10.1016/j.icarus.2016.05.022

Nakamura, K. (1977). Volcanoes as possible indicators of tectonic stress orientation—principle and proposal. *Journal of Volcanology and Geothermal Research*, *2*, 1–16. https://doi.org/10.1016/0377-0273(77)90012-9

Neumann, G. A., Zuber, M. T., Wieczorek, M. A., McGovern, P. J., Lemoine, F. G., & Smith, D. E. (2004). Crustal structure of Mars from gravity and topography. *Journal of Geophysical Research: Planets*, *109*, E08002. https://doi.org/10.1029/2004JE002262

O'Rourke, J. G., Wolf, A. S., & Ehlmann, B. L. (2014). Venus: Interpreting the spatial distribution of volcanically modified craters. *Geophysical Research Letters*, *41*, 8252–8260. https://doi.org/10.1002/2014GL062121

Peel, D., & McLachlan, G. J. (2000). Robust mixture modelling using the t distribution. *Statistics and Computing*, *10*, 339–348. https://doi.org/10.1023/A:1008981510081

Pettengill, G. (1991). MGN V RDRS DERIVED MOSAIC IMAGE DATA RECORD FULL RES V1.0 [Data set]. NASA Planetary Data System. https://doi.org/10.17189/1522523

Pettengill, G. H., Ford, P. G., Johnson, W. T., Raney, R. K., & Soderblom, L. A. (1991). Magellan: Radar performance and data products. *Science*, *252*, 260–265. https://doi.org/10.1126/science.252.5003.260

Phillips, R. J., Raubertas, R. F., Arvidson, R. E., Sarkar, I. C., Herrick, R. R., Izenberg, N., & Grimm, R. E. (1992). Impact craters and Venus resurfacing history. *Journal of Geophysical Research: Planets*, *97*, 15923–15948. https://doi.org/10.1029/92JE01696

Plescia, J. B. (2004). Morphometric properties of Martian volcanoes. *Journal of Geophysical Research: Planets*, *109*, E03003. https://doi.org/10.1029/2002JE002031

Pronin, A. A., & Stofan, E. R. (1990). Coronae on Venus: Morphology, classification, and distribution. *Icarus*, *87*, 452–474. https://doi.org/10.1016/0019-1035(90)90148-3

Ricci, J., Lahitte, P., & Quidelleur, X. (2015). Construction and destruction rates of volcanoes within tropical environment: Examples from the Basse-Terre Island (Guadeloupe, Lesser Antilles). *Geomorphology*, *228*, 597–607. https://doi.org/10.1016/j.geomorph.2014.10.002

Richards, M. A., Hager, B. H., & Sleep, N. H. (1988). Dynamically supported geoid highs over hotspots: Observation and theory. *Journal of Geophysical Research: Solid Earth*, *93*, 7690–7708. https://doi.org/10.1029/JB093iB07p07690

Richardson, J. A. (2016). *Modeling the construction and evolution of distributed volcanic fields on Earth and Mars (*Doctoral dissertation*)*. Retrieved from ProQuest (10076376). Tampa, FL: University of South Florida.

Richardson, J. A., Bleacher, J. E., Connor, C. B., & Glaze, L. S. (2021). Small Volcanic Vents of the Tharsis Volcanic Province, Mars. *Journal of Geophysical Research: Planets*, *126*, e2020JE006620. https://doi.org/10.1029/2020JE006620

Richardson, J. A., Bleacher, J. E., & Glaze, L. S. (2013). The volcanic history of Syria Planum, Mars. *Journal of volcanology and geothermal research*, *252*, 1–13. https://doi.org/10.1016/j.jvolgeores.2012.11.007

Robbins, S. J., Antonenko, I., Kirchoff, M. R., Chapman, C. R., Fassett, C. I., Herrick, R. R., ... & Gay, P. L. (2014). The variability of crater identification among expert and community crater analysts. *Icarus*, *234*, 109–131. https://doi.org/10.1016/j.icarus.2014.02.022

Robbins, S. J., Singer, K. N., Bray, V. J., Schenk, P., Lauer, T. R., Weaver, H. A. & Stern, S. A. (2017). Craters of the Pluto-Charon system. *Icarus*, *287*, 187–206. https://doi.org/10.1016/j.icarus.2016.09.027

Robbins, S. J., Riggs, J. D., Weaver, B. P., Bierhaus, E. B., Chapman, C. R., Kirchoff, M. R., & Gaddis, L. R. (2018). Revised recommended methods for analyzing crater size-frequency distributions. *Meteoritics & Planetary Science*, *53*, 891–931. https://doi.org/10.1111/maps.12990

Roberts, K. S., Stewart, S. A., Davies, R. J., & Evans, R. J. (2011). Sector collapse of mud volcanoes, Azerbaijan. *Journal of the Geological Society*, *168*, 49–60. https://doi.org/10.1144/0016-76492010-115

Romeo, I. (2013). Monte Carlo models of the interaction between impact cratering and volcanic resurfacing on Venus: The effect of the Beta-Atla-Themis anomaly. *Planetary and Space Science*, *87*, 157–172. https://doi.org/10.1016/j.pss.2013.07.010

Romeo, I., & Turcotte, D. L. (2009). The frequency-area distribution of volcanic units on Venus: Implications for planetary resurfacing. *Icarus*, *203*, 13–19. https://doi.org/10.1016/j.icarus.2009.03.036

Schaber, G. G., Strom, R. G., Moore, H. J., Soderblom, L. A., Kirk, R. L., Chadwick, D. J., ... & Russell, J. (1992). Geology and distribution of impact craters on Venus: What are they telling us? *Journal of Geophysical Research: Planets*, *97*, 13257–13301. https://doi.org/10.1029/92JE01246

Schmidt, D. F., & Makalic, E. (2012). Minimum message length inference and mixture modelling of inverse Gaussian distributions. In Australasian Joint Conference on Artificial Intelligence (pp. 672-682). Springer, Berlin, Heidelberg. https://doi.org/10.1007/978-3-642-35101-3_57

Senske, D. A., Schaber, G. G., & Stofan, E. R. (1992). Regional topographic rises on Venus: Geology of western Eistla Regio and comparison to Beta Regio and Atla Regio. *Journal of Geophysical Research: Planets*, *97*, 13395–13420. https://doi.org/10.1029/92JE01167

Shalygin, E. V., Markiewicz, W. J., Basilevsky, A. T., Titov, D. V., Ignatiev, N. I., & Head, J. W. (2015). Active volcanism on Venus in the Ganiki Chasma rift zone. *Geophysical Research Letters*, *42*, 4762–4769. https://doi.org/10.1002/2015GL064088

Shannon, C. E. (1949). Communication in the presence of noise. *Proceedings of the Institute of Electrical and Electronics Engineers*, *37*, 10–21. https://doi.org/10.1109/JRPROC.1949.232969

Shaw, H. R. (1985). Links between magma-tectonic rate balances, plutonism, and volcanism. *Journal of Geophysical Research: Solid Earth*, *90*, 11275–11288. https://doi.org/10.1029/JB090iB13p11275

Silverman, B.W. (1998). *Density Estimation for Statistics and Data Analysis*. New York: Routledge.

Sjogren. W.L. (1997). MGN V RSS SPHERICAL HARMONIC AND GRAVITY MAP DATA V1.0 [Data set]. NASA Planetary Data System. https://doi.org/10.17189/1522521

Smrekar, S., Hensley, S., Nybakken, R., Wallace, M. S., Perkovic-Martin, D., You, T. H. & Mazarico, E. (2022). VERITAS (Venus emissivity, radio science, InSAR, topography, and spectroscopy): a discovery mission. In *2022 IEEE Aerospace Conference*.

Smrekar, S. E., & Stofan, E. R. (1997). Corona formation and heat loss on Venus by coupled upwelling and delamination. *Science*, *277*, 1289–1294. https://doi.org/10.1126/science.277.5330.1289

Smrekar, S. E., Stofan, E. R., Mueller, N., Treiman, A., Elkins-Tanton, L., Helbert, J., ... & Drossart, P. (2010). Recent hotspot volcanism on Venus from VIRTIS emissivity data. *Science*, *328*, 605–608. https://doi.org/10.1126/science.1186785

Solomon, S. C., & Head, J. W. (1982). Evolution of the Tharsis province of Mars: The importance of heterogeneous lithospheric thickness and volcanic construction. *Journal of Geophysical Research: Solid Earth*, *87*, 9755–9774. https://doi.org/10.1029/JB087iB12p09755

Spudis, P. D. (2015). Volcanism on the Moon. In H. Sigurdsson, B. Houghton, S.R. McNutt, H. Rymer, & J. Stix (Eds,), *The Encyclopedia of Volcanoes* (Vol. 2, pp. 689–700). Cambridge, MA: Academic Press. https://doi.org/10.1016/c2015-0-00175-7

Stofan, E. R., & Head, J. W. (1990). Coronae of Mnemosyne Regio: morphology and origin. *Icarus*, *83*, 216–243. https://doi.org/10.1016/0019-1035(90)90016-3

Stofan, E. R., Sharpton, V. L., Schubert, G., Baer, G., Bindschadler, D. L., Janes, D. M., & Squyres, S. W. (1992). Global distribution and characteristics of coronae and related features on Venus: Implications for origin and relation to mantle processes. *Journal of Geophysical Research: Planets*, *97*, 13347–13378. https://doi.org/10.1029/92JE01314

Stofan, E. R., Smrekar, S. E., Bindschadler, D. L., & Senske, D. A. (1995). Large topographic rises on Venus: Implications for mantle upwelling. *Journal of Geophysical Research: Planets*, *100*, 23317–23327. https://doi.org/10.1029/95JE01834

Stofan, E. R., Smrekar, S. E., Tapper, S. W., Guest, J. E., & Grindrod, P. M. (2001a). Preliminary analysis of an expanded corona database for Venus. *Geophysical Research Letters*, *28*, 4267–4270. https://doi.org/10.1029/2001GL013307

Stofan, E. R., Guest, J. E., & Copp, D. L. (2001b). Development of large volcanoes on Venus: constraints from Sif, Gula, and Kunapipi Montes. *Icarus*, *152*, 75–95. https://doi.org/10.1006/icar.2001.6633

Stofan, E. (2004). Earth's Evil Twin: The volcanic world of Venus. In E. Stofan (Ed.), *Volcanic Worlds* (pp. 61–79). Heidelberg NY: Springer-Praxis.

Stofan, E. R., & Smrekar, S. E. (2005). Large topographic rises, coronae, large flow fields, and large volcanoes on Venus: Evidence for mantle plumes?. In G.R. Foulger, J.H. Natland, D.C. Presnall, D.L. Anderson (Eds), *Plates, Plumes and Paradigms* (Vol. 338, pp. 861). Boulder, CO: Geological Society of America. https://doi.org/10.1130/0-8137-2388-4.841

Stofan, E. R., Smrekar, S. E., Mueller, N., & Helbert, J. (2016). Themis Regio, Venus: Evidence for recent (?) volcanism from VIRTIS data. *Icarus*, *271*, 375–386. https://doi.org/10.1016/j.icarus.2016.01.034

Tadini, A., Bonali, F. L., Corazzato, C., Cortes, J. A., Tibaldi, A., & Valentine, G. A. (2014). Spatial distribution and structural analysis of vents in the Lunar Crater Volcanic Field (Nevada, USA). *Bulletin of Volcanology*, *76*, 1–15. https://doi.org/10.1007/s00445-014-0877-8

Thomson, B. J., & Lang, N. P. (2016). Volcanic edifice alignment detection software in MATLAB: Test data and preliminary results for shield fields on Venus. *Computers & Geosciences*, *93*, 1–11. https://doi.org/10.1016/j.cageo.2016.04.012

Titterington, D. M. (1990). Some recent research in the analysis of mixture distributions. *Statistics*, *21*, 619–641. https://doi.org/10.1080/02331889008802274

Turcotte, D. L., Morein, G., Roberts, D., & Malamud, B. D. (1999). Catastrophic resurfacing and episodic subduction on Venus. *Icarus*, *139*, 49–54. https://doi.org/10.1006/icar.1999.6084

Wadge, G., & Cross, A. (1988). Quantitative methods for detecting aligned points: an application to the volcanic vents of the Michoacan-Guanajuato volcanic field, Mexico. *Geology*, *16*, 815–818. https://doi.org/10.1130/0091-7613(1988)016<0815:QMFDAP>2.3.CO;2

Wallace, C. S. (1998). Intrinsic Classification of Spatially Correlated Data. *The Computer Journal*, *41*, 602–611. https://doi.org/10.1093/comjnl/41.8.602

Wallace, C. S. (2005). Statistical and Inductive Inference by Minimum Message Length. New York, New York: Springer. https://doi.org/10.1007/0-387-27656-4

Wallace, C. S., & Dowe, D. L. (2000). MML clustering of multi-state, Poisson, von Mises circular and Gaussian distributions. *Statistics and Computing*, *10*, 73–83. https://doi.org/10.1023/A:1008992619036

Wand, M. P., & Jones, M. C. (1993). Comparison of smoothing parameterizations in bivariate kernel density estimation. *Journal of the American Statistical Association*, *88*, 520–528. https://doi.org/10.1080/01621459.1993.10476303

Wand, M. P., & Jones, M. C. (1994). Multivariate plug-in bandwidth selection. *Computational Statistics*, *9*, 97–116.

Wang, Y., Yang, G., & Guo, L. (2015). A novel sparse boosting method for crater detection in the high resolution planetary image. *Advances in Space Research*, *56*, 982–991. https://doi.org/10.1016/j.asr.2015.05.014

Watson, D. F., and G. M. Philip. (1985). A Refinement of Inverse Distance Weighted Interpolation. *Geoprocessing 2*, 315–327. https://doi.org/10.1016/S0735-1097(97)00186-1

Weller, J. N., Martin, A. J., Connor, C. B., Connor, L. J. & Karakhanian, A. (2006) Modelling the spatial distribution of volcanoes: An example from Armenia. In H.M. Mader, S.G. Coles, C.B. Connor & L.J. Connor (Eds.) *Statistics in Volcanology*, (pp. 77–88). Geological Society of London. https:/doi.org/10.1144/IAVCEI001.7. 17

Wessel, P. (2007). Seamount Characteristics. In Pitcher, T.J., Morato, T., Hart, P.J.B., Clark, M.R., Haggan, N., Santos, R.S. (Eds), *Seamounts: Ecology, Fisheries, and Conservation*. Blackwell Publishing Ltd. https://doi.org/10.1002/9780470691953.ch1

Yang, A., Huang, J., & Wei, D. (2016). Separation of dynamic and isostatic components of the Venusian gravity and topography and determination of the crustal thickness of Venus. *Planetary and Space Science*, *129*, 24–31. https://doi.org/10.1016/j.pss.2016.06.001

Zuber, M. T., Solomon, S. C., Phillips, R. J., Smith, D. E., Tyler, G. L., Aharonson, O., & Zhong, S. (2000). Internal structure and early thermal evolution of Mars from Mars Global Surveyor topography and gravity. *Science*, *287*, 1788–1793. https://doi.org/10.1126/science.287.5459.1788

Chapter 3:
A Global Survey of Gravitationally Deformed Volcanoes on Venus

Associated Publication: Hahn, R. M., & Byrne, P. K. (2024). A global survey of gravitationally deformed volcanoes on Venus. Journal of Geophysical Research: Planets, 129, e2023JE008241. https://doi.org/10.1029/2023JE008241

Abstract

Gravitational instabilities can develop at volcanoes of any size and in any geological setting, and can lead to various types of volcano deformation, ranging from small-scale landslides on the flanks of the edifice to large, deep-seated sector collapses. As volcanoes grow, they impose an increasing load on the underlying basement, which can result in styles of gravitational deformation wherein the edifice sags or spreads outward under its own weight. In this study, we utilize our previously developed global catalog of volcanoes on Venus to analyze a subset of edifices that appears to have undergone gravitational deformation. We identify 162 volcanoes that display morphological evidence for gravitational deformation, and classify them into four main categories based on associated deformational structures: landsliding, sector collapse, spreading, and sagging. Volcanoes that have undergone landsliding on their flanks or a sector collapse are the most common and geographically widespread deformational styles on Venus, and account for ~64% of our dataset. Edifices exhibiting structures linked to volcano spreading and sagging are relatively rare; nonetheless, we note for the first time on Venus the presence of flank terraces on a shield volcano, structures linked to sagging. We find that deformed volcanoes are distributed globally, are found at a range of elevations, are spatially proximal to a variety of tectonic structures,

and are associated with various crustal thickness values, which together suggest that there are numerous drivers of volcano deformation on Venus.

3.1 Introduction

Volcanoes are generally unstable landforms, and frequently undergo gravity-driven deformation that can alter their shape. This phenomenon is common for both subaerial (e.g., Mount St. Helen, USA and Stromboli, Italy) and submarine (e.g., Monowai, NZ and Kick 'em Jenny, Grenada) volcanoes on Earth, as well as on Mars (e.g., Tharsis Tholus and Olympus Mons). Gravitationally deformed volcanoes have further been identified on Venus, with numerous edifices exhibiting evidence for landsliding on their flanks and large-scale debris aprons (Guest et al., 1992; Bulmer and Wilson, 1999; Ivanov and Head, 1999), and some volcanoes even exhibit structures linked to lithospheric flexure (Smrekar, 1994; Rogers and Zuber, 1998; McGovern and Solomon, 1998), similar to their counterparts on Earth (e.g., Hawaii and Mount Etna), and Mars (e.g., Olympus Mons).

Many factors contribute to the instability of a volcano, and some edifices are more prone to collapse than others depending on the individual volcano structure and environment (McGuire, 2003). Processes related to magmatic activity (e.g., Mount St. Helen) such as dike emplacement (Delaney et al., 1999; Tibaldi, 2001), volcanic activity (Capra et al., 2002), and viscous magma intrusion (Richards and Villeneuve, 2001) can mechanically or thermally weaken and deform rocks, resulting in a destabilization of faults within the edifice (Voight and Elsworth, 1997). The stability of an edifice can also be directly linked to basement fault movement, with flank destabilization controlled by the geometries and kinematics of basement faults (Francis and Self 1987; Carracedo 1994; Tibaldi 1995). Volcanoes built upon weak basements or layers (e.g., clays)

are also more susceptible to gravitational collapse, because those weak basal materials enable the outward spread of the edifice particularly if they serve to decouple the edifice from its underlying basement (Borgia et al., 2000; Acocella and Neri, 2009; Byrne et al., 2009; Holohan et al., 2023).

3.1.1 Rationale

In compiling a new global catalog of shield volcanoes containing ~85,000 edifices across Venus (Hahn and Byrne, 2023a), we noted several dozen volcanoes that appear on the basis of their morphology to have undergone gravitational deformation. Structural and spatial analysis of these volcanoes, along with detailed comparative studies, can help quantify the types and possible drivers of volcano gravitational collapse on Venus.

3.2 Examples of Gravitationally Deformed Volcanoes

In this study, we examine in detail four main types of gravity-driven volcano deformation: landsliding, sector collapse, spreading, and sagging. Although these categories do not encompass every known style of volcano deformation, they include a sufficiently diverse set of deformation morphologies for useful comparison with gravitationally deformed volcanoes on Earth and Mars.

3.2.1 Landsliding

Small-scale landslides (up to a few hundred cubic kilometers in volume) are a common occurrence on the flanks of both subaerial (Chigira 2002; Madonia et al., 2019) and submarine volcanoes (Quartau et al., 2010; Casalbore et al., 2015, 2020) on Earth. For example, very small-scale (<1 km^3) landslides occurred on the flanks of Casita Volcano in Nicaragua in 1988 as a result of instabilities from heavy rainfall (Cecchi et al, 2005). Similar landsliding events have been identified on Monowai, a submarine volcano in the Kermadec Arc in the southwest Pacific Ocean,

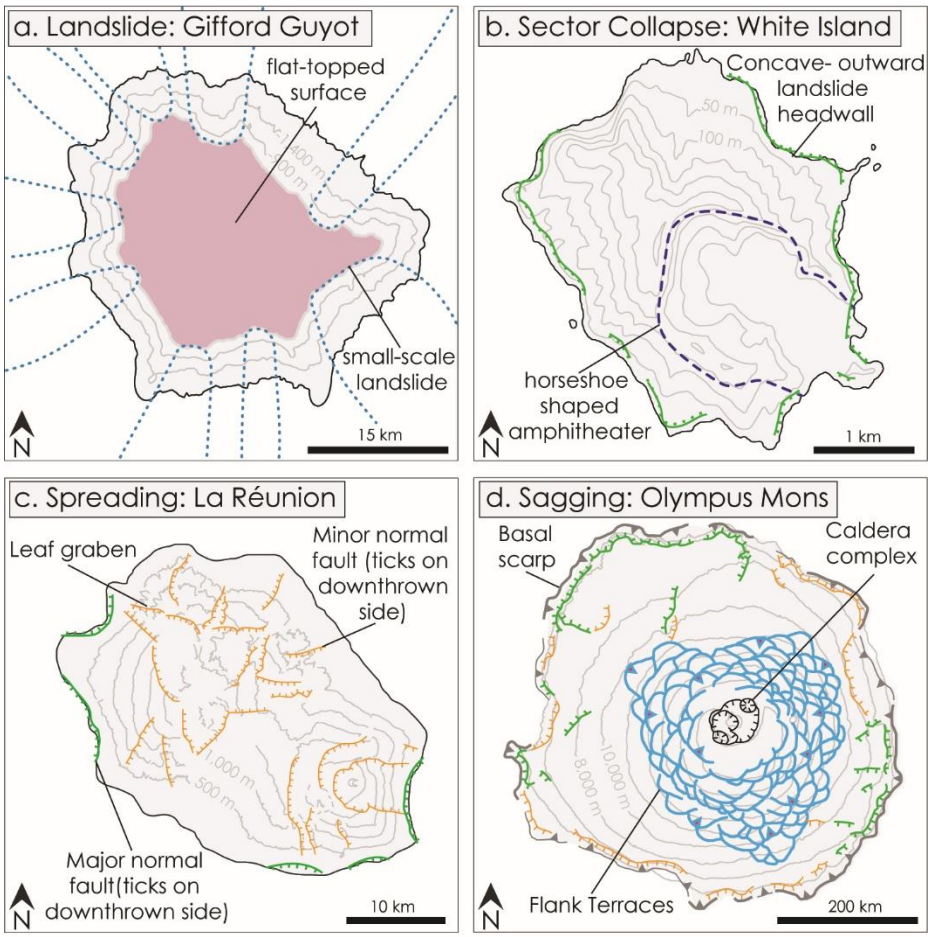

Figure 3.1 Example structural sketches showing morphological structures associated with four major types of gravity-driven volcano deformation: (a) landsliding (Gifford Guyot, Earth); sector collapse (White Island, Earth); spreading (La Réunion, Earth); and (d) sagging (Olympus Mons, Mars). The sketches in panels (c) and (d) are from Byrne et al. (2013); panel (d) is modified from Byrne et al. (2009) and McGovern and Morgan (2009).

with bathymetric datasets over consecutive years (Wright et al., 2008). Notably, the morphology of submarine volcanoes, or seamounts, ranges from a conical shape with a distinct peak, to multiple irregular branches that resemble a star shape, to guyots or flat-topped seamounts (Schmidt and Schmincke, 2002) (**Figure 3.1a**). Seamounts with irregular morphologies are thought to form from progressive, small-scale slope failures (Chaytor et al., 2007), or from the formation of flank rift zones that alter seamount shape from small and circular to large and stellate (Fiske and Jackson, 1972; Bulmer and Wilson, 1999; Mitchell, 2001). Similarly, small-scale landslides on the flanks of intermediate-sized (5–100 km in diameter) volcanoes are widespread on Venus. These

volcanoes were referred to as “scalloped margin domes” or “stellate domes” in previous studies (Guest et al., 1992; Bulmer and Guest, 1996; Bulmer and Wilson, 1999; Ivanov and Head, 1999), to describe their overall shape.

3.2.2 Sector Collapse

A large-scale (up to thousands of km^3), gravity-driven, deep-seated, lateral collapse of a volcano is referred to as a sector collapse (Acocella and Tibaldi, 2005; Casalbore et al., 2020; Romero et al., 2021). The destabilizing mechanism behind a sector collapse can be magmatic or tectonic, such as dike emplacement (Delaney et al., 1999), volcanic activity (Capra et al., 2002), basal failure (Acocella and Tibaldi, 2005), or earthquakes (Acocella and Neri, 2009). Sector collapses are common on Earth (e.g., Mount Saint Helen, USA; Bezymianny, Russia; Mount Unzen, Japan), and evidence for this type of gravitational deformation has also been reported for Venus (Bulmer and Guest, 1996; Bulmer and Wilson, 1999). Structures associated with sector collapses on Earth include a characteristic horseshoe-shaped collapse scar, or amphitheater (Francis and Self, 1987; Coombs et al., 2007; Romero et al., 2021), steep-sided scarps (Coombs et al., 2007; Martinez-Moreno et al., 2018), and debris avalanches (Capra et al., 2002; Bernard et al., 2008) (**Figure 3.1b**). Similar morphological structures have been documented on Venus, with several earlier studies identifying deformed volcanoes with debris aprons (Guest et al., 1992; Bulmer and Wilson, 1999; Lopez, 2011) and/or large arcuate backscarps (Bulmer and Guest, 1996).

3.2.3 Spreading

As volcanoes grow and become larger, they exert an increasing load onto their substrata. If the substrata contains low-strength materials (e.g., clays, evaporates), the volcano may slowly

spread outward along a basal detachment or décollement (Borgia et al., 2000; Marquez et al., 2008; Byrne et al., 2013). Through analogue modeling experiments, Byrne et al. (2013) found that end-member spreading occurs when a decoupled volcano collapses outward across a rigid (e.g., thick) basement. On Earth for example, volcanoes such as Concepción and Maderas in Nicaragua are built upon weak Quaternary clay-rich sediments from Lake Nicaragua, effectively decoupling them mechanically from their underlying basements and facilitating their outward spread. Both volcanoes exhibit structures associated with spreading (Van Wyk de Vries and Borgia, 1996; Borgia, 2000) such as volcano-concentric folds and thrusts near the base of the edifice and radial normal faults or "leaf graben" on the edifice flanks (Borgia 2000; Byrne et al., 2013; Van Wyk de Vries and Davies, 2015) (**Figure 3.1c**). Evidence of volcano spreading has also been documented on Tharsis Tholus, a volcano in the eastern Tharsis region of Mars that has normal faults cross-cutting the entire edifice (Borgia 2000; Platz et al., 2011). Structures associated with spreading have not been widely recognized on Venus, possibly because of the low resolution of Magellan synthetic-aperture radar (SAR) data, with only a handful of volcanoes boasting normal faults that cross their flanks.

3.2.4 Sagging

Volcano spreading results in the outward displacement of the edifice, whereas volcano sagging leads to inward displacement. That is, sagging occurs when a volcano's weight down-flexes the underlying lithosphere, leading to horizontal constriction of the central edifice and extension of the lower flanks and base (Byrne et al., 2013, Van Wyk de Vries and Davies, 2015). Unlike the decoupled edifice and rigid basement associated with volcano spreading, Byrne et al. (2013) found that end-member sagging architecture occurs when a volcano and its less rigid (e.g., thin) basement are coupled and deform as a single mechanical unit. Volcano sagging and spreading

are two end-members of a continuum of volcano gravitational deformation that is dependent on the extent to which an edifice is mechanically coupled or decoupled to/from its basement, as well as the flexural properties (effectively the rigidity) of that underlying basement (Byrne et al., 2013; Holohan et al., 2023).

Morphological structures associated with volcano sagging include an edifice-encircling flexural trough and bulge, with graben focused along the flexural bulge, and imbricate flank terraces on the edifice itself (Byrne et al., 2009, 2012, 2013; Kervyn et al., 2010) (**Figure 3.1d**). Flank terraces have been documented on Martian volcanoes (Carr et al., 1977; Morris 1982; Thomas et al., 1990; Byrne et al., 2009, 2012), and are topographically subtle structures with a convex cross-sectional profile and a map pattern that resembles fish scales (Byrne et al., 2009). Evidence for volcano sagging has been documented on Earth at Hawaii, with terracing present on the NW flanks and a flexural bulge and trough surrounding the island (Byrne et al., 2013; Holohan et al., 2023). Likewise, structures associated with volcano sagging occur on Martian volcanoes, with flank terraces present on almost a dozen volcanoes, including Elysium and Olympus Montes (Byrne et al., 2013). Indications of volcano sagging on Venus are rare, but not entirely absent. Flexural bulges and troughs are seemingly uncommon, with only a few large (>100 km in diameter) edifices exhibiting evidence of volcanic flows ponding in moats, and circumferential graben attributed to basement downflexing (McGovern and Solomon, 1997; Rogers and Zuber, 1998).

Table 3.1.
Morphological Structures Associated with Different Types of Gravitational Deformation

Deformation type	Landsliding[a–f]	Sector collapse[c–k]	Spreading[m–p]	Sagging[n,o,q–t]
Associated structures	• Stellate/star-shaped planforms • Steep backscarps • Debris aprons	• Horseshoe-shaped collapse scars • Steep backscarps • Debris avalanches	• Folds and thrusts at or beyond edifice base • Normal faults and leaf graben cross-cutting flanks	• Flexural troughs and bulges • Peripheral graben on flexural bulge • Flank terraces

[a]Schmidt and Schmincke (2002). [b]Fiske and Jackson (1972). [c]Bulmer and Wilson (1999). [d]Guest et al. (1992). [e]Bulmer and Guest (1996). [f]Ivanov and Head (1999). [g]Coombs et al. (2007). [h]Romero et al. (2021) [i]Martinez-Moreno et al. (2018). [j]Capra et al. (2002). [k]Bernard et al. (2008). [l]Lopez (2011). [m]Borgia (2000). [n]Byrne et al. (2013). [o]Van Wyk de Vries and Davies, (2015). [p]Van Wyk de Vries and Borgia, (1996). [q]Byrne et al. (2009). [r]Holohan et al. (2023). [s]Kervyn et al. (2010). [t]Byrne et al. (2012).

3.3 Methods

3.3.1 Structural Mapping

We carried out geospatial analysis and structural mapping of deformed volcanoes with the Magellan SAR FMAP (full-resolution radar map) left- and right-look global mosaics, which have a nominal 75 meters-per-pixel (75 m/px) resolution (Ford et al., 1993), in the ESRI ArcGIS Pro 2.7 environment. We employed our recently published global catalog of volcanoes on Venus (Hahn and Byrne, 2023a), which we developed using ArcMap 10.7.1, and ArcGIS Pro 2.7 by dividing the planet into 5° × 5° bins, and thoroughly examining each bin at a view scale of 1:400,000. The resulting database contains shapefiles denoting the point locations of 83,977 volcanoes <5 km in diameter, and polygons outlining 847 volcanoes ≥5 km in diameter. Furthermore, during the development of our global catalog, we also noted 182 volcanoes ≥5 km

in diameter that appear to have undergone gravitational deformation based on the presence of the morphological features described in *section 3.2*.

To build upon this dataset, and to ensure consistency with earlier such works, we also consulted existing databases that note deformed volcanoes on Venus. These datasets include the Magellan Volcano Catalog (Crumpler and Aubele, 2000) and a catalog published by Bulmer (1994); both databases describe instances of "modified domes" on Venus. We also analyzed edifices from the Magellan Volcano Catalog (Crumpler and Aubele, 2000) that were described by Lopez (2011) as having steep scarps and evidence of flank failure, but that do not have an obvious, associated debris apron. The deformed or modified edifices described in these earlier studies are of intermediate size—that is, none is larger than 100 km in diameter.

In this study, we expand our analysis to large volcanoes (>100 km in diameter) by analyzing the dataset of large volcanoes on Venus we previously compiled (Hahn and Byrne, 2023a) and identifying morphological indicators of deformation (**Table 3.1**). For the equatorial region between 40°N and 40°S, mapping was completed in an equirectangular projection. To preserve volcano geometry, datasets were projected as north- or south polar stereographic when mapping deformed volcanoes at latitudes above 40°N and below 40°S, respectively.

After consulting existing deformed volcano datasets (e.g., Bulmer, 1994; Crumpler and Aubele, 2000), analyzing volcanoes >100 km in diameter from our global catalog (Hahn & Byrne 2023a), and double-checking the original 182 deformed volcanoes identified in our global catalog, we refined our dataset down to 162 deformed volcanoes >5 km in diameter. A polygon shapefile outlining the full extent of the volcano and associated deformational structures (debris aprons, faults, etc.) was drawn for each deformed edifice. These volcanoes were then visually examined at a view scale that ranged from 1:2,000,000 for edifices >100 km in diameter, down to 1:300,000

for edifices 5–100 km in diameter, and classified as having undergone a landslide, sector collapse, sagging or spreading, based on the associated deformational structures listed in **Table 3.1**. We compiled a fifth subset of edifices that are deformed in multiple styles or are otherwise difficult to classify with available data, and so were listed as "indeterminate". Lastly, we termed edifices that have undergone numerous sector collapses or landsliding events such that approximately less than half of their original shape remains as "remnant" volcanoes.

Table 3.2
Summary Statistics for Deformed Volcano Morphology

Deformation type	Count (n = 162)	Percent of total (%)	Mean diameter (km)[d]	Mean area (km^2)[d]
Landsliding	51	31.5	32 ± 13	1,055 ± 954
Sector Collapse	37	23	25 ± 13	672 ± 660
Landsliding/Sector Collapse[a]	16	10	36 ± 20	1,448 ± 1,742
Spreading	4	2.5	122 ± 211[e]	40,932 ± 81,416
Sagging	4	2.5	325 ± 309[e]	157,465 ± 245,800
Remnant[b]	17	10.5	24 ± 11	556 ± 562
Indeterminate[c]	33	20	33 ± 32	1,781 ± 4,492

[a]We typically classify edifices that have structures associated with more than one deformation as "indeterminate", but here we report specific instances where deformed edifices have structures we attribute to both landsliding and sector collapse.
[b]We classify "remnant" volcanoes as those that have undergone multiple landsliding or sector collapse events and, as such, less than 50% of the original edifice remains.
[c]Indeterminate volcanoes are deformed in multiple styles or are otherwise difficult to classify with available Magellan SAR data.
[d]Mean area and diameter are given together with one standard deviation.
[e]The standard deviation associated with the mean diameter for sagging and spreading volcanoes is large, and is likely not statistically significant as the population size for each dataset is only four volcanoes.

Mean deformed volcano diameter was calculated by averaging the long and short axes of each edifice, excluding any collapse related structures such as a debris apron (which would not have constituted part of the original edifice). Deformed volcano mean diameter and area are reported with one standard deviation in **Table 3.2**.

3.3.2 Spatial Analysis

The spatial distribution of volcanoes can offer valuable insight into the geometry of underlying magma bodies, stress orientations within the crust, and magma generation mechanisms (e.g., Cañon-Tapia & Mendoza-Borunda, 2014; Connor, 1990; Kear, 1964; Le Corvec et al., 2013; Nakamura, 1977). In this study, we used the distribution of deformed volcanoes on Venus to better understand possible collapse mechanisms, and to gain insight into why particular volcanoes might deform.

Motion on nearby tectonic structures (or even impact events) could plausibly generate sufficient seismic energy to trigger a volcano deformation event. To assess this possibility, we noted the spatial relationship between each of the deformed volcanoes in our catalog and any proximal tectonic (e.g., rifts and ridge belts) and volcano-tectonic (e.g., coronae) structures. This analysis was completed within ArcGIS Pro 3.0 by creating three circular buffers of gradually increasing diameter (50, 100, and 200 km) around each deformed edifice. The goal in selecting these distances was to ensure the identification of structures in direct proximity to the deformed edifices, yet also taking into account regional structures that may play a role in volcano collapse. The buffered regions around each deformed volcano were then thoroughly examined and the presence of any tectonic structures, impact craters, or other deformed volcanoes were documented in the attribute table (see Appendix A.2 for more details on the deformed volcano datasets). To aid in the identification of rifts and ridge belts, we utilized the shape files denoting the boundaries of these features developed by Ivanov and Head (2011) as part of their global geological map of Venus. Furthermore, we used the coronae shapefiles also included in the Ivanov and Head (2011) geological map. The geodesic distance in kilometers between each deformed volcano in our dataset and the nearest coronae was calculated and added to the attribute table for those edifices.

Table 3.3
Comparison of Deformed Volcanoes with Geophysical Datasets

Deformation type	Number of volcanoes	Mean crustal thickness (km)[a]	Mean elevation (km)[b]
Landsliding	51	16 ± 1	1.0 ± 0.3
Sector collapse	37	15 ± 2	1.3 ± 0.3
Landsliding/sector collapse	16	16 ± 1	0.8 ± 0.4
Spreading	4	22 ± 1	1.7 ± 0.2
Sagging	4	16 ± 2	1.9 ± 0.4
Remnant	17	14 ± 2	0.7 ± 0.2
Indeterminate	33	14 ± 1	0.8 ± 0.2

[a]Crustal thickness values are extracted from a map produced by James et al., (2013) with ± one standard deviation.
[b]Mean elevation based on Magellan altimetry data. All values are km above the mean Venus planetary radius (6,051 km) plus the average altimetry error (Ford, 1992).

In addition to analyzing the relationship between deformed volcanoes and possibly relevant structures locally, we also assessed deformed volcanoes in terms of the associated geophysical properties of the underlying lithosphere in an effort to characterize gravitational deformation at a global scale. This component of our analysis was completed in ArcGIS Pro 3.0 by extracting each deformed volcano polygon boundary from both the Magellan altimetry map (Ford, 1992) and a crustal thickness map based on Magellan gravity measurements (James et al., 2013). The resulting values were then averaged for each style of deformation, and are given in **Table 3.3**. The James et al. (2013) crustal thickness map is derived using gravity data compiled from the Magellan and Pioneer Venus missions (Konopliv et al., 1999), and has a nominal global resolution of ~270 km.

3.4 Results

3.4.1 Deformed Volcano Morphological Analysis

We report summary statistics of deformed volcano morphology on Venus in **Table 3.2**. Our total number of deformed volcanoes of all styles is 162. Of those, 96 (59.3%) are classified

into one of our four deformation styles described in detail in *section 3.2*. A further 16 (9.9%) show features of both landsliding and sector collapse. Edifices we determined to be "remnant" constructions total 17 (10.5% of the total set), and 33 (20.4%) were indeterminate (i.e., showed insufficiently preserved morphologies to be readily classified into one or more deformation styles).

Within our dataset, we note 51 volcanoes that have undergone one or more landsliding events, and 37 that exhibit signs of a sector collapse. Less material is excavated from an edifice when it undergoes a landslide versus a sector collapse (Chigira 2002; Madonia et al., 2019; Casalbore et al., 2020; Romero et al., 2021), and this difference in material loss is reflected by the average diameter of landsliding and sector-collapse volcanoes in our dataset. Volcanoes that have undergone landsliding events have a larger diameter (32 km) than those that had a sector collapse (25 km), presumably because more material was removed from the edifice during the deep-seated collapse of an entire flank (**Table 3.2**). Furthermore, the 17 volcanoes classified as "remnant" have an average diameter of ~24 km, which suggests that these edifices have experienced numerous collapse events that have left only a small portion of the original edifice intact.

We also analyzed a subset of deformed volcanoes that have structures associated with both landsliding and sector collapses (**Table 3.2**). Interestingly, these volcanoes have an average diameter of ~36 km, which is greater than the mean diameters for volcanoes that are classified solely as showing evidence for a landslide or sector collapse. An increase in volcano diameter following numerous collapse events could indicate that these edifices were volcanically active and continued to grow after at least one instance of collapse. Alternatively, these volcanoes may have initially been larger than volcanoes exclusively exhibiting a flank landslide or sector collapse, and remained larger even after multiple collapse events.

Volcanoes that have experienced spreading or sagging are rare on Venus, with only four volcanoes identified in each category. We note that, at ~325 km, sagging volcanoes have the greatest mean diameter of all deformed edifices, which is three to ten times greater than the mean diameter of deformed volcanoes in any other category (**Table 3.2**). This finding suggests that only the very largest Venusian volcanoes are sufficiently massive to downflex the underlying lithosphere.

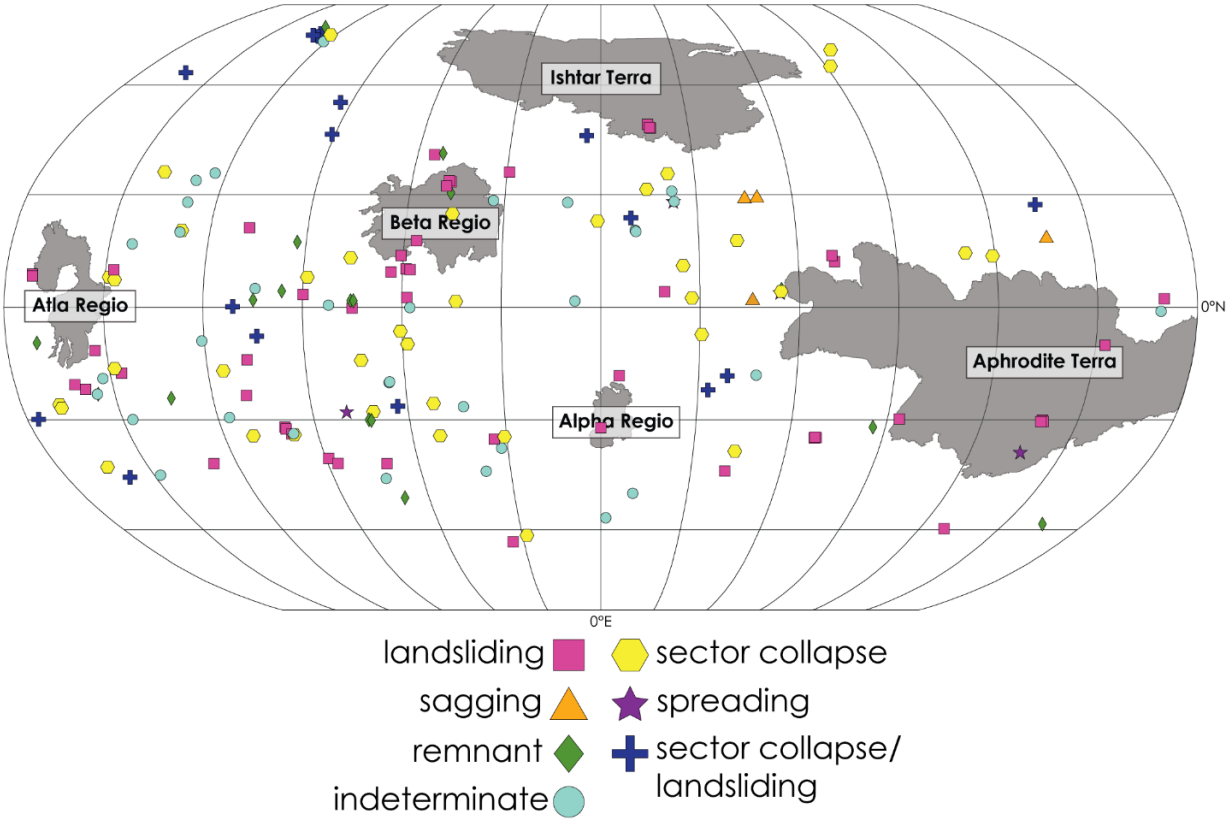

Figure 3.2 Global survey of deformed volcanoes on Venus grouped by deformation type. The outlines of major Venusian physiographic features are shown in grey for geographic context and are labeled. The map is in Robinson projection, centered at 0°E.

3.4.2 Deformed Volcano Spatial Analysis

We find that deformed volcanoes are nearly geographically widespread across Venus, with very few extending into the south pole, and almost none surrounding Ishtar Terra in the north polar region (**Figure 3.2**). Deformed volcanoes are also more spatially concentrated within the Beta–

Atla–Themis (BAT) region, an approximately triangular area bounding three large rift zones connecting the Beta, Atla, and Themis regiones (Airey et al., 2017; Crumpler et al., 1997). The BAT region is characterized by enhanced volcanism and is dominated by rift zones, coronae, and extensional structures (Airey et al., 2017; Head et al., 1992; Ivanov & Head, 2015), and volcanoes of all diameters are present in this region (Hahn & Byrne, 2023a)—so it is unsurprising that there should also be an increased number of deformed volcano in this area. In fact, we find that of the 847 volcanoes ≥5 km from our global catalog (excluding deformed volcanoes) (Hahn and Byrne 2023a), 254 (~30%) are concentrated within the BAT region, and of the 162 deformed volcanoes described here, we note that 65 (~40%) are also concentrated in the BAT region. This finding suggests that volcanoes within the BAT region are more likely to undergo some style of gravitational collapse, perhaps due to the increased volcanism and tectonics within the region.

Volcanoes that appear to have flanks marked by landslides are typically found within the mid-latitudes, are situated on crust with an average thickness of 16 km, and a mean elevation (relative to the planetary mean) of 1 km (**Table 3.3 & Figure 3.3**). We find that 33% (17/51) of landsliding volcanoes are clustered (within 50 km) with other landsliding volcanoes in groups of two to three. This finding suggests that volcanoes within each of these clusters could have some common control (e.g., composition or response to local tectonics) that results in slope instabilities and landsliding. For example, on Earth, numerous serpentinite seamounts on the Mariana forearc exhibit basal thrust faults linked to volcano spreading (Oakley et al., 2007). In that case, the similar

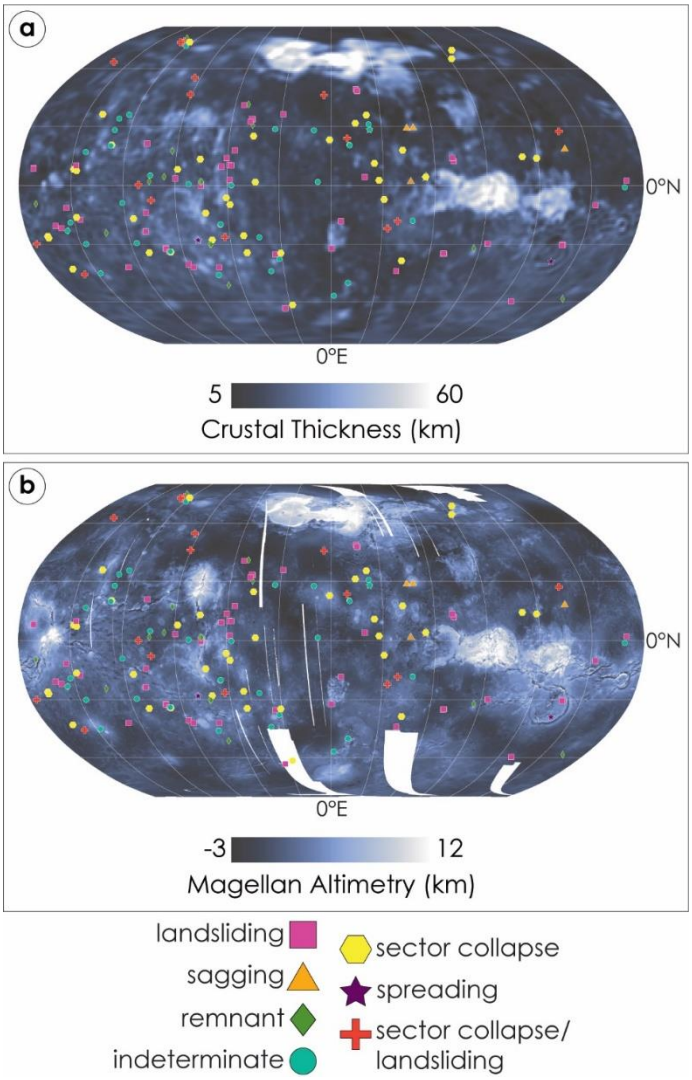

Figure 3.3 Maps of deformed volcanoes classified by deformation type superimposed over (a) a map of global crustal thickness (James et al., 2013), and (b) a map of Magellan altimetry (Ford, 1992). Both maps are in Robinson projection, centered at 0°E.

compositions and emplacement conditions of volcanoes resulted in the same deformational style, which suggests that an analogous process could apply to Venus facilitated by some low-strength layer, e.g., ash deposits. Furthermore, we find that, of these landsliding volcano clusters on Venus, three are situated within a corona and one cluster is just outside of another corona, suggesting that processes linked to corona evolution might also play a role in driving landsliding on the flanks of intermediate-sized volcanoes (of diameter 32 ± 13 km: see **Table 3.2**).

Volcanoes that have experienced a sector collapse are also commonly found in the mid-latitudes, with several extending into the north polar regions. Sector-collapse volcanoes are associated with slightly lower crustal thickness values (~15 km) and generally have slightly higher elevations (1.3 km) than volcanoes with flank landslides (**Table 3.3** & **Figure 3.3**). The similarities in elevation and crustal thickness between these two styles of gravitational deformation indicates that there may be common controls that result in landslides and sector collapses on volcanoes on Venus. Additionally, we note 16 edifices that show structures associated with both types of deformation that have similar diameters (**Table 3.2**), associated crustal thicknesses, and elevation (**Table 3.3**) as those classified as landsliding or sector-collapse volcanoes. It may be, then, that there is a continuum of increasing deformation that initiates with landsliding on the flanks of a given volcano, which then may promote the development of larger-scale sector collapses, such that a range of morphologies between both main deformation styles results. A similar phenomenon was described at Casita volcano in Nicaragua, where numerous small-scale landslides preceded a larger sector collapse (van Wyk de Vries et al., 2000).

Unlike landsliding volcanoes that are occasionally found in clusters, we find no instances of two or more sector collapse volcanoes within 50 km of one another. However, we note three occurrences where sector collapse volcanoes are spatially proximal (within 50 km) to an indeterminate or remnant edifice. Around 35% (13/37) of sector collapse volcanoes overlap with or are on the border of an extensive rift system, suggesting that some of these deep-seated failures could be linked to seismicity along large, rift-associated normal faults; indeed, several collapsed edifices have debris aprons that superpose fractures, consistent with their having collapsed after motion on the rift faults. Another possibility is that magmatic activity, facilitated by the favorable stress states in these extensional systems (Cas and Wright, 1987; Watanabe et al., 1999), resulted

in structural failure of the edifice. Intrusions of new magma via in dyke emplacement can fill any open conduits within a volcano, changing the pore pressure in the edifice and leading to sector collapse (Elsworth and Voight; 1996).

Edifices exhibiting signs of sagging and spreading are the least common styles of deformation on Venus. All four sagging volcanoes are located in the mid-latitudes in the eastern hemisphere, and do not appear to be associated with the BAT region. The four spreading volcanoes are also mostly found in the eastern hemisphere, with one extending into the western hemisphere. We note that spreading volcanoes are associated with the highest crustal thickness values and both sagging and spreading volcanoes are situated at higher elevations compared to all other deformational categories (**Table 3.3**). Further, volcanoes we classify as sagging are, on average, 200 km larger in diameter than spreading volcanoes (**Table 3.2**), but are situated on crust that is ~6 km thinner than that associated with volcanoes that have spread.

Proximity with Tectonic Structures:

We find that deformed volcanoes are frequently associated with extensional structures, with 78% of deformed edifices within 50 km of rifts, fractures, linaments, or graben. Specifically, we note that 92% (47/51) of landsliding volcanoes, 65% (24/37) of sector collapse volcanoes, 75% (3/4) of spreading volcanoes, and half (2/4) of sagging volcanos are within a 50-km radius of an extensional structure. This finding is unsurprising, as on Earth volcano instability is commonly linked to regional tectonics, and particularly extensional systems (e.g., Ollagüe Volcano in Chile/Bolivia, Kilauea in the Hawaiian Islands, and Mount Etna in Italy) (Tibaldi et al., 2006; McGuire, 2003).

In contrast, we find that deformed volcanoes are less frequently associated with shortening structures, with only 55% of deformed volcanoes within 50 km of landforms such as wrinkle ridges

or ridge belts, both of which are generally regarded as surface manifestations of crustal shortening (Solomon et al., 1992; Guest and Stofan 1998). Overall, we note that 41% (21/51) of landsliding volcanoes, 62% (23/37) of sector collapse volcanoes, and half (2/4) of both sagging and spreading volcanoes are within 50 km of a shortening structure.

Of the 51 volcanoes with landslides on their flanks, 22% (11/51) are situated within a corona, and a further 12% (6/51) are within a 50 km radius of a corona. Similarly, 24% (9/37) of sector collapse volcanoes, and half (2/4) of spreading volcanoes are also encompassed by or are within a 50 km radius of a corona—again, on the basis of spatial proximity, suggestive of a possible causal link between volcano deformation and coronae on Venus. Coronae are associated with voluminous magmatism, and are generally accepted to have formed from mantle upwellings at the base of the lithosphere, resulting in an initial upwelling, followed by flattening and gravitational relaxation (Gülcher et al., 2020; Stofan and Head, 1990; Stofan et al., 1992). Processes related to coronae gravitational relaxation or collapse due to magma withdrawal could lead to instabilities associated with volcanoes located within the coronae itself and explain the numerous instances of deformed volcanoes associated with coronae. For a detailed description of deformed volcano proximity to nearby tectonic structures, see Appendix A.2.

3.5 Comparative Analysis

To better assess the mechanisms responsible for gravitational deformation on Venus, we conducted a comparative analysis of typical examples of deformed volcanoes from each of our four main categories for Venus (landsliding, sector collapse, spreading, and sagging) with volcanoes on Earth or Mars that appear to have undergone a similar deformational process.

3.5.1 Landsliding Case Studies

Of the 51 volcanoes across Venus that show landslides on their flanks, all are either flat-topped or dome-shaped, with a stellate or star-shaped planform. Numerous studies have identified steep-sided, flat-topped domes—landforms we regard as and so refer to as volcanoes—across Venus (e.g., Pavri et al., 1992; Bulmer and Wilson, 1999; Ivanov and Head, 1999; Stofan et al., 2000). Moreover, many researchers have noted that Terran seamounts may represent useful analog for these volcanoes (e.g., Head and Wilson, 1986; Aubele and Slyuta, 1990; Guest et al., 1992; Smith 1996; Bridges, 1995; 1997a). Eruptive conditions on Earth's seafloor and on Venus (at least the lowlands) are both defined by high surface pressures and rapid cooling of lavas (Aubele and Slyuta, 1990; Grosfils, 2000), which together contribute to volcano shape (Smith, 1996). Here, we compare and contrast the morphology and landslide structures associated with a cluster of edifices on both Venus and the seafloor, and also compare a single edifice on Venus and the seafloor. Specifically, we compare a group of steep-sided, flat-topped volcanoes on Venus, with the Taney seamount chain (a group of seamounts off the coast of San Francisco, CA), and separately, compare an unnamed, flat-topped volcano on Venus with a seamount in the Hawaiian seamount chain.

We downloaded digital elevation models (DEMs) of submarine volcanoes with the Global Multi-Resolution Topography (GMRT) v4.1.1 synthesis tool (Ryan et al., 2009). The GMRT consists of a compilation of multibeam sonar data collected by institutions across the world and is continuously updated. DEMs of the Taney seamount chain, and the seamount in the Hawaiian seamount chain, are derived from ship-based, multibeam swath bathymetry data with a nominal resolution of 100 m/px, which is comparable to the Magellan FMAP SAR data resolution of 75 m/px.

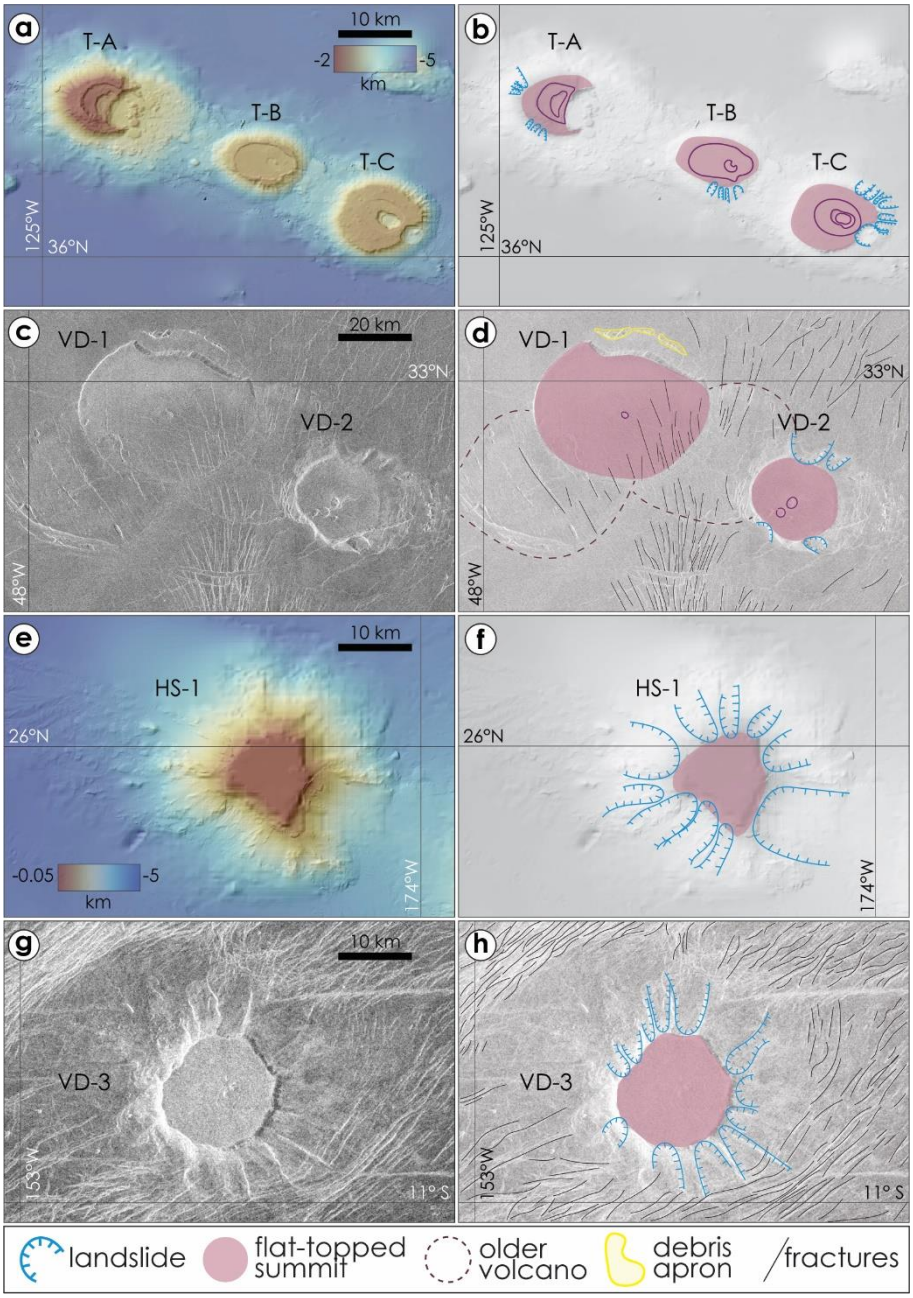

Figure 3.4 Comparative structural analysis between Taney seamount chain (a & b) and Venusian steep-sided, flat-topped volcanoes (c & d), and between a seamount in the Hawaiian–Emperor seamount chain (e & f) and a flat-topped volcano on Venus (g & h). Magellan SAR data are shown in an equirectangular projection, and radar illumination is from the left (c & g). Seamounts are shown as hillshade maps generated from bathymetric DEMs with elevation-colored DEMs draped on top. DEMs show depth below sea level, with warm colors indicating shallow depths and cool colors indicating greater depths (a & e). Panels (b), (d), (f), and (h) show deformational structures associated with volcano landsliding and are slightly transparent, grey-scaled versions of panels (a), (c), (e), and (g), respectively.

Morphological Descriptions of Flank Landslide Case Study 1: Taney Seamount Chain:

Situated on the Pacific plate, the Taney seamount chain comprises five northwest-to-southeast trending, near-ridge submarine volcanoes off the coast of California situated at depths of 2.5–3.5 km (Clague et al., 2000a; Coumans et al., 2015). These seamounts, designated T-A to T-E (after Clague et al., 2000a) **(Figure 3.4a**) from northeast to southeast, formed adjacent to the subducted Farallon plate (Coumans et al., 2015). For this study, we examined in detail the morphology of seamounts T-A, T-B, and T-C, which all exhibit structures linked to landsliding on their flanks (see **Table 3.1** for more details). Seamount T-A has an estimated volume of 187 km^3, a height of 2 km, and a diameter of ~15 km at its base (Clague et al., 2000a). Three successive caldera collapses have severely modified the southeast flank of T-A such that the majority of the summit platform is gone (Clague et al., 2000a; McClain and Lundsten 2014; Coumans et al., 2015) (**Figure 3.4b**). The flat-topped, 1.2 km tall, T-B seamount is located ~9 km to the southeast of T-A. Seamount T-B has a basal diameter of ~11 km, and a summit diameter of ~5.5 km, with several nested summit calderas (Clague et al., 2000a), and multiple small-scale landslides on the southern flank of the edifice. Lastly, T-C seamount is located ~25 km to the southeast of T-A, and has a height of ~1.3 km. The T-C seamount has an estimated volume of 116 km^3, a basal diameter of 12 km, and a summit platform diameter of 5.5 km (Clague et al., 2000a). Two nested calderas are centered in the summit platform of T-C, and a third is situated on the southeast summit rim (Clague et al., 2000a) (**Figure 3.4b**).

On Venus, just north of Zemire Corona and centered at 33.6°N, 48.2°W, sits a cluster of four steep-sided, flat-topped, coalesced volcanoes. This cluster consists of two older volcanoes, each ~45 km in diameter, superposed by two edifices that have clearly undergone gravitational collapse. Here, we focus on the two younger volcanoes, which we term VD-1 and VD-2,

respectively (**Figure 3.4c**). The larger of the two edifices, VD-1, has a mean diameter of 51 km with a ~2 km-diameter summit pit, and an estimated height of 0.9 km. The north margin of the edifice has collapsed, resulting in a ~35 km-long scarp with hummocky debris remnants ~7 km north of the edifice. VD-1 has a relatively smooth upper surface (Stofan et al., 2000) with several fractures oriented north to south and pit craters on the south portion of the edifice (**Figure 3.4d**). Approximately 20 km to the southeast of VD-1 is VD-2, the smaller of the two edifices we focus on here. This volcano is ~1.1 km in height, has a mean basal diameter of ~38 km, and a ~25 km-diameter flat-topped surface. VD-2 has partially collapsed margins, and the southeast edge is crossed by a pit crater chain (**Figure 3.4d**).

Morphological Description of Landsliding Case Study 2: Hawaiian Seamount:

The Hawaiian–Emperor island/seamount chain is a prime example of intraplate seamounts that form from local melt anomalies or "hotspots" (Buchs et al., 2015). Along the northwest portion of the Hawaiian ridge, just northwest of Neva Shoal, is an unnamed seamount ~45 km in diameter at its base, and with a height of ~5 km. This unnamed seamount, hereafter referred to as HS-1 (**Figure 3.4e**), has a flat-topped summit region that measures ~16 km in diameter that is ~46 m below sea level, and has a stellate planform from numerous landslides along its flanks (**Figure 3.4f**).

On Venus, an unnamed, flat-topped volcano is located within the BAT region, centered at 11.4°S, 153.3°W. This edifice, hereafter referred to as VD-3 (**Figure 3.4g**), has a basal diameter of ~36.5 km, a flat-topped summit diameter of ~16 km, and an estimated height of ~2 km. VD-3 has a stellate planform as a result of numerous landslides along its summit margins (**Figure 3.4h**). Extensional structures aligned northeast to southwest are arranged around VD-3, but do not appear to crosscut the edifice. Another younger set of extensional structures aligned east to west appears

to cut through portions of VD-3's stellate margins, but not through the summit of the edifice itself (**Figure 3.5**).

Comparison Between Flat-Topped Venusian Volcanoes and Seamounts:

The majority of seamounts in Earth's oceans are volcanic in origin and composed of basalt, with slight differences in the chemical and isotopic composition depending on the geological setting and magma source (e.g., Wessell, 2007). The composition of Venusian steep-sided, flat-topped volcanoes remains unknown, although one view holds that the edifices are made up of evolved lavas with a high viscosity, resulting in the flat-topped morphology similar to rhyolitic and dacitic domes on Earth (Guest et al., 1992; Pavri et al., 1992; Head et al., 1992). Another possibility is that the volcanoes are basaltic in composition and their flat-topped morphology is a result of an extrusion of a high-viscosity basaltic foam (Head et al., 1992; Pavri et al., 1992). Through thermal modeling, Stofan et al. (2000) found that, under Venusian ambient temperatures, a rhyolitic lava would quickly form a thick crust and break into large bocks, and thus flat-topped, steep-sided volcanoes on Venus are more consistent with a basaltic composition. More recently, Quick et al. (2016) used both a constant-volume and a time-variable model to investigate steep-sided, flat-topped volcano emplacement on Venus and found that, in both models, viscosities imply that compositions are most consistent with basaltic andesites on Earth. Here, based on those previous studies, we assume that Venusian, steep-sided, flat-topped volcanoes and seamounts on Earth are essentially basaltic (i.e., relatively low in silica) in nature.

Seamounts and steep-sided, flat-topped volcanoes on Venus share numerous morphological similarities. Both are generally round in shape, are flat-topped, and have flanks with average slopes of ~20° to 30° (Bulmer and Wilson, 1999; Smith, 1998; Bridges, 1996). On Earth, seamounts with a flat-topped morphology have been identified around the Hawaiian Islands

(Bridges, 1997b; Bulmer and Wilson, 1999), in the Gulf of Alaska (Chaytor et al., 2007), and along southern (Scheirer et al., 1996) and northern (Scheirer and Macdonald, 1995) portions of the East Pacific Rise. Numerous processes have been proposed to explain the presence of flat summit plateaus on submarine volcanoes. Wave-base truncation and subsidence are likely responsible for many flat-topped seamounts (Staudigel and Kopers, 2015), particularly those at depths <200 m (e.g., HS-1) (Casalbore, 2018).

Yet some seamounts never reach sea level and would not be influenced by wave motion (Simkin, 1973; Wessel, 2007), and are therefore relevant to volcanoes on Venus. Instead, the flat-topped morphology of such deeper volcanoes could be a result of eruptions along circular ring faults (Simkin, 1973; Fornari et al., 1988; Batiza, 1989) or from cone sheets (Mitchell, 2001). Researchers studying flat-topped seamounts in the Taney seamount chain (e.g., T-A and T-C) (Clague et al., 2000a) found that the flat-topped plateaus are likely generated by the continuous eruption of and lava ponding within large, early-stage calderas (**Figure 3.4b**). Evidence for this hypothesis is provided by seamount T-B (**Figure 3.4a & 3.4b**), which features a summit caldera that is almost entirely filled with erupted lavas. Clague et al. (2000) suggested that only a few more cubic kilometers of lava would have completely erased any evidence of the existence of a summit caldera, leading to a smooth, flat-topped morphology.

Similarly, Stofan et al. (2000) pointed to the fracture patterns and pits on the surface of many steep-sided, flat-topped Venusian volcanoes as evidence for endogenous growth, where the crust continuously annealed as the edifice grew by inflation. Pits on the surface of Venusian volcanoes, such as on VD-1 and VD-2, suggest the presence of a fluid interior or lava lake beneath a rapidly cooling carapace (Stofan et al, 2000). Furthermore, VD-1 and VD-2 superpose two other edifices (**Figure 3.4d**), indicative of subsequent eruptive events. The flat-topped volcano VD-3

may have also formed via continuous lava emplacement, but there are no pits or fractures visible on its surface in the Magellan SAR data.

Localized landslides are well documented for seamounts on Earth and steep-sided, flat-topped volcanoes on Venus (e.g., Bulmer and Wilson, 1999). These shallow, small-scale landslides produce a stellate planform, steep backscarps, and, in some cases, debris aprons (e.g., **Table 3.1**). Internal slope failure on Venus is most commonly attributed to oversteepening of flanks during edifice growth (Guest, et al., 1992; Bulmer and Guest, 1996; Crumpler et al., 1997; Bulmer, 2012), where intrusion and/or extrusion of magma can cause overloading at the surface of the volcano and result in failure (McGuire, 1996). The high ambient temperature on Venus (~464 °C) could lead to the development of weakly solidified carapaces on the fronts of lava flows. Subsequent oversteepening of these weak carapaces during dome growth, or from tectonic or other seismic activity, could result in slope failure (Guest et al., 1992; Bulmer, 2012). Furthermore, the flat tops of many of these volcanoes have angular fracture patterns, perhaps due to episodic growth (Stofan et al., 2000)—and those fractures would have been predisposed to failure along joints and other discontinuities (Bulmer, 2012).

As we note above, conditions on Earth's seafloor are characterized by high pressure and rapid cooling of lavas (Smith, 1996). The transition from a circular to a stellate seamount is thought to be controlled by the formation of flank rift zones. These rift zones are elongated protuberances that extend out from the center of volcanic edifices and are interpreted to form via an injection from a shallow reservoir after magma rises into the central conduit (Fiske and Jackson, 1972; Vogt and Smoot 1984; Barone and Ryan 1988). As the seamount grows in height, it is more susceptible to lateral collapse along the boundaries of these rift zones (Mitchell, 2001). Mitchell (2001) estimated that the transition to a stellate seamount form is gradual and occurs when volcanoes

reach ~3 km in height, which approximately corresponds to the height at which the magma chamber buoyantly migrates from the basement into the edifice itself (Walker, 1989). Once a chamber is established in the edifice proper, magma can more efficiently move into lateral rift zones rather than erupting out of the central vent (Vogt and Smoot, 1984; Mitchell, 2001).

The Taney seamounts T-A–C are all ≤2 km in height, suggesting that the scalloped margins observed on T-B and T-C are not from failure along flank rift zones but are instead because of flank oversteepening, possibly linked to the lava ponding and continuous eruptions that give the seamounts their flat-topped morphology. In contrast, the Hawaiian seamount HS-1 is entirely surrounded by scalloped margins (**Figure 3.4f**) and is nearly 5 km in height, and so could plausibly have undergone failure along its internal rift zones, as many of the seamounts within the Hawaiian seamount chain have, such as Kilauea (Ryan et al., 1981). Vogt and Smoot (1984) proposed that a seamount is initially round and becomes ever more stellate with increasing volume until the flank rifts extend up to 100 km (e.g., Hawaii). The longest flank rift associated with HS-1 is ~10 km in length; under this scenario, HS-1 is still in a transitional stage of growth, and could eventually develop longer and more pronounced flank rifts as the edifice grows in volume.

Based on our observations, Venusian volcanoes VD-1–3 could have formed flat-topped surfaces from episodic magma emplacement, in a manner similar to Taney seamounts T-A–C, whereas the flat-topped summit at HS-1 is likely because of wave erosion given its proximity to the sea surface. The high mean atmospheric pressure (~92 bars) at the surface of Venus reduces volatile exsolution and inhibits the formation of neutral buoyancy zones and shallow magma reservoirs, particularly in the lowlands where the atmospheric pressure is the highest (Head and Wilson, 1992). Venusian domes VD-1 and VD-2 are located at relative elevations of –500 m and –400 m, respectively. Based on models presented by Head and Wilson (1992) the low elevations

of these edifices suggest that neutral buoyancy zones did not form within the actual volcanoes, and so magma ascended without pausing at a shallow level. Without a shallow magma reservoir, the formation of flank rift zones was likely inhibited. We therefore interpret the shallow landslides on the flanks of VD-1 and VD-2 as being the result of oversteepening during episodic growth, similar to the Taney seamounts.

Venusian volcano VD-3 is situated at an elevation (+1.3 km relative to Venus "sea level"), where models developed by Head and Wilson (1992) suggest that the decrease in atmospheric pressure allows for volatile exsolution and the formation of lower-density vesicular rock at the surface. As this low-density material accumulates, buoyantly rising magma will begin to stall and a shallow magma reservoir could form. For a magma of a given volatile content, the depth to the neutral buoyancy zone increases with elevation, and failure of the reservoir as a result of overpressurization will gradually favor lateral dike injection over surface eruption with increasing neutral buoyancy depth (Parfitt et al., 1993; Grosfils and Head 1995). The reduced pressure conditions at VD-3 could have led to the development of a shallow magma reservoir, which in turn might have resulted in the formation of lateral dikes—in a manner not unlike the formation of flank rift zones on seamounts on Earth. However, other volcanic constructs on Venus interpreted to form from dike emplacement such as novae, which are landforms with radially fractured centers that form a starburst pattern (Head et al., 1992; Krassilnikov and Head, 2003), do not resemble VD-3. Novae have mean diameters of ~325 km (Galgana et al., 2013), which is an order of magnitude greater than VD-3 and are not associated with a flat-topped morphology. Given the dissimilarities in size and morphology between VD-3 and novae, we posit that the landslides on the flanks of VD-3 are likely not linked to dike emplacement, but possibly a response to tectonics.

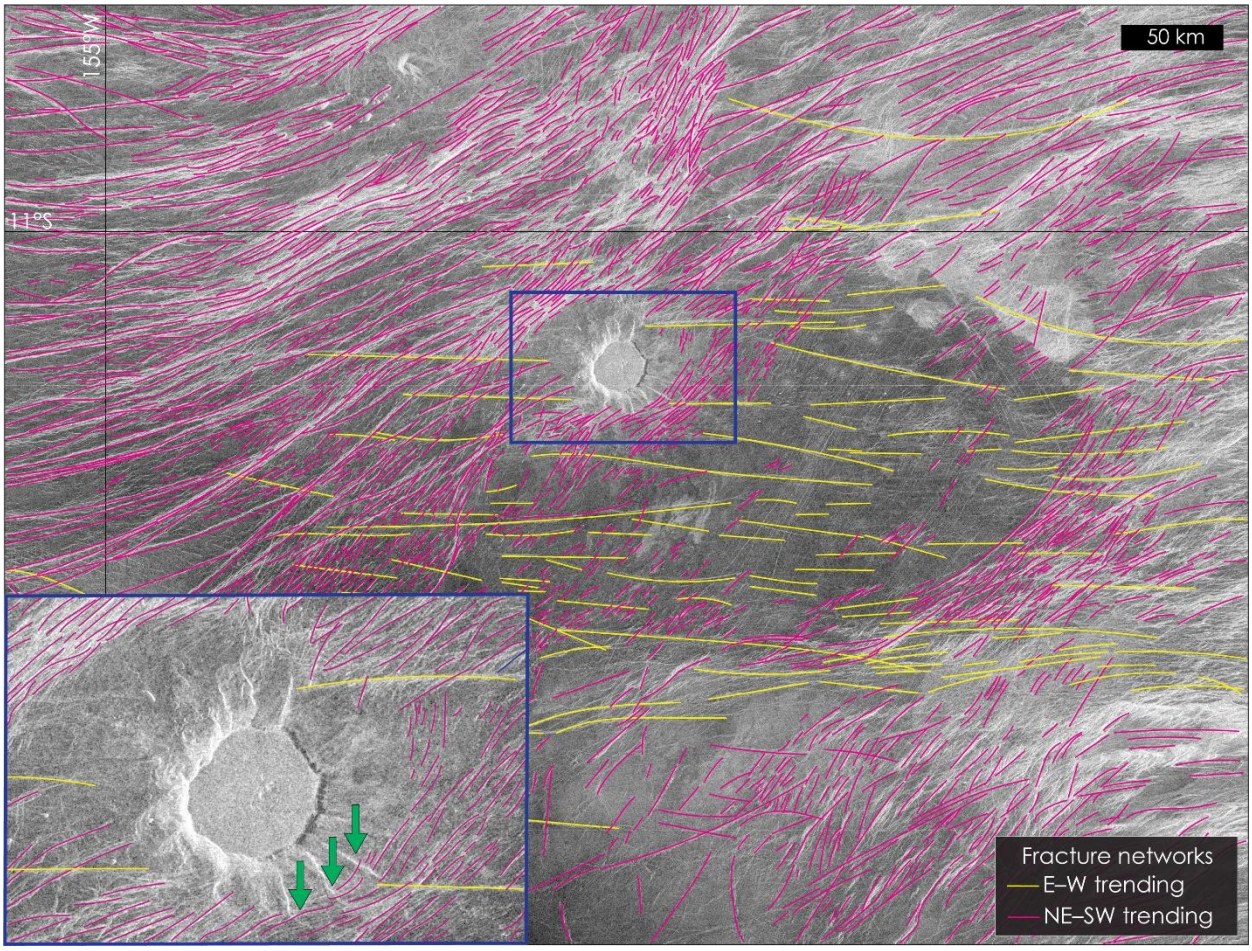

Figure 3.5 Detailed structural mapping of the region surrounding the unnamed Venusian volcano VD-3. Yellow and pink lines show fracture networks oriented approximately E–W and NE–SW, respectively. The blue box corresponds to the zoomed-in region shown in the bottom-left corner of the figure. Green arrows in the inset box point to instances where the fractures superpose the landslide scarps. Magellan SAR data, shown in an equirectangular projection and with radar illumination from the left.

Indeed, landslides on the edifices we consider in this study could form in response to local tectonic activity. For example, there is a large extensional system that extends ~125 km south of VD-1 and VD-2. These extensional structures are oriented north–northwest and could have triggered the collapsed margins located along the north–northeast edges of both VD-1 and VD-2. Similarly, VD-3 is located on the south edge of an extensional system ~600 km in length and ~200 km across that strikes northeast to southwest (**Figure 3.5**). The flat-topped summit of VD-3 is not crosscut by any faults, but some of the landform's landslide scarps *are* crossed by these faults—

indicating that the extensional system predates VD-3 but that portions of the flanks collapsed during or after fault slip (e.g., green arrows in **Figure 3.5**). We therefore posit that landslides on the flanks VD-3 could be directly driven by movement along these adjacent tectonic structures.

3.5.2 Sector Collapse Case Study: Vostrukha Mons on Venus and Socompa on Earth

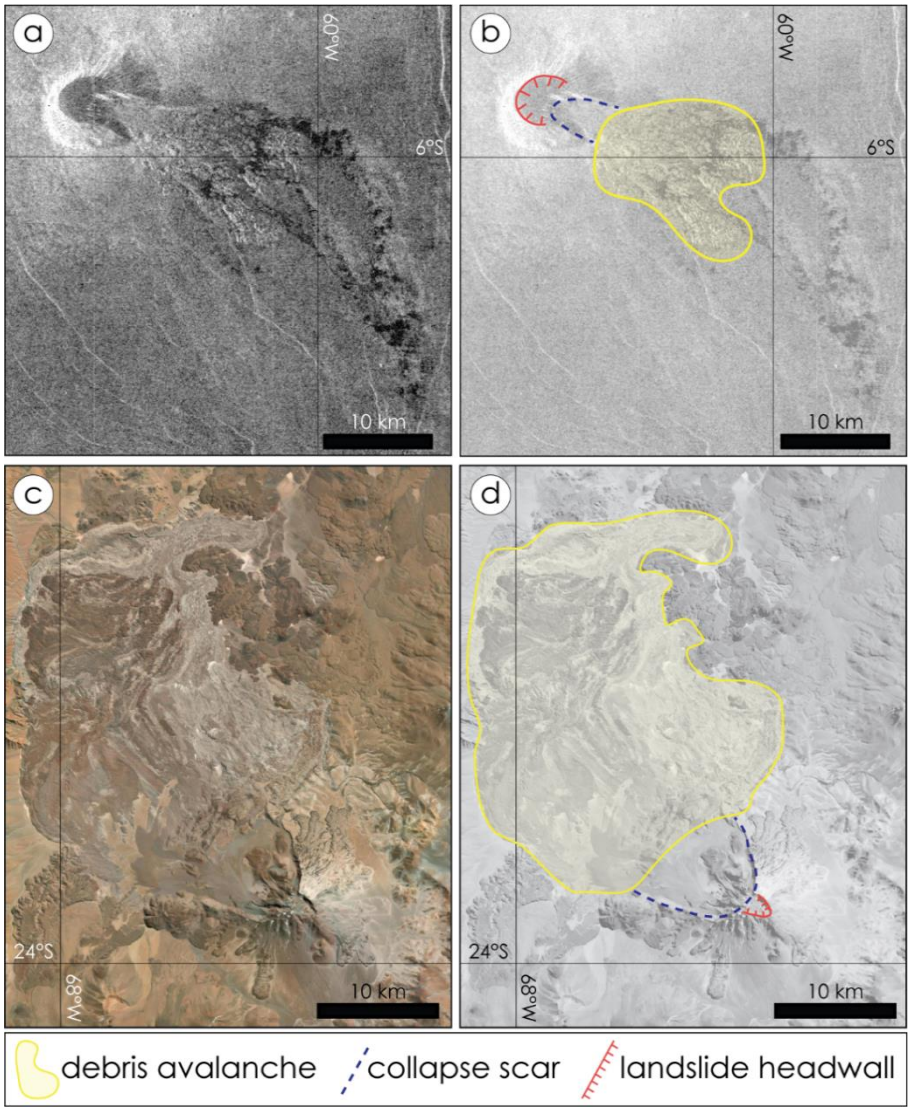

Figure 3.6 Comparative morphological analysis between Vostrukha Mons on Venus (a & b) and Socompa Volcano in Argentina/Chile (c & d). Socompa imagery is from Google Earth (c & d). Panels (b) and (d) show deformation structures associated with sector collapse and are transparent, grey-scaled versions of panels (a) and (c), respectively. Magellan SAR data, shown in an equirectangular projection and with radar illumination from the left; the Google Earth imagery is in WGS84 geographic projection.

We document a total of 37 Venus volcanoes that show evidence for having undergone a sector collapse. Included in this subset is Vostrukha Mons, a ~180 km-diameter volcano situated to the northeast of Phoebe Regio, and centered at 6.2°S, 60.6°W. Here, we focus on a ~15 km-diameter edifice positioned at the summit of Vostrukha Mons that has had a sector collapse (**Figure 3.6a**). The southeast flank of the volcano has fallen apart leaving a ~four km-wide, horseshoe-shaped collapse scar and a hummocky debris apron that extends up to 19 km away from the edifice (**Figure 3.6b**).

Our Terran analogue to the collapsed volcano on Vostrukha Mons is Socompa, a 6 km-tall composite Andean volcano that lies on the southwest margin of the Atacama basin, within the borders of Argentina and Chile (Wadge et al., 1993; van Wyk de Vries et al., 2001) (**Figure 3.6c**). Socompa hosts one of Earth's largest sector collapses and is extremely well preserved, due to the arid climate of the Atacama Desert (Wadge et al., 1993; van Wyk de Vries et al., 2001; Camiz et al., 2013). Approximately 7.5 ka the northwest flank of Socompa collapsed, leaving a 12 km-wide amphitheater and an associated debris avalanche that flowed a maximum distance of 40 km across a flat plain to the northwest of the edifice (Francis et al., 1985; Wadge et al., 1993, van Wyk de Vries et al., 2001) (**Figure 3.6d**).

Comparison Between Vostrukha Mons on Venus and Socompa on Earth:

Both Vostrukha Mons and Socompa exhibit morphological structures indicative of sector collapse, including a horseshoe-shaped collapse scar and an associated debris avalanche (**Figure 3.6b** & **3.6d**). The collapse mechanism at Socompa was initially attributed to magmatic activity resulting in a Mount St. Helens-style lateral blast (Ramirez, 1988). More recently, the sector collapse has been attributed to gravitational spreading over a failing substrate comprising gravels, conglomerates, and ignimbrites (Wadge et al., 1993; van Wyk de Vries et al., 2001; Wooler et al.,

2004). A similar style of precursory slow spreading that may eventually trigger a flank collapse was also identified at Mombacho volcano in Nicaragua (van Wyk de Vries and Francis, 1997).

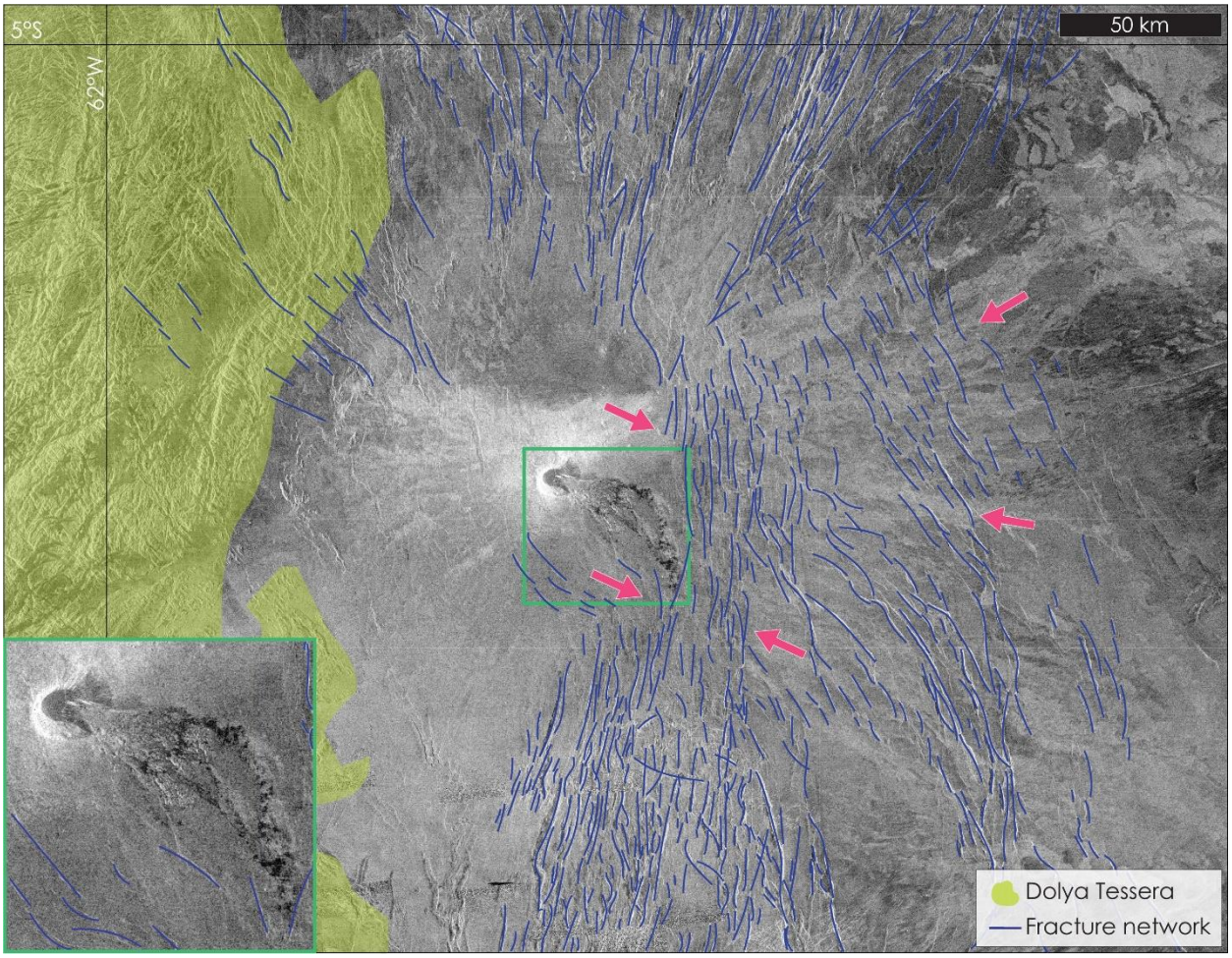

Figure 3.7 Detailed structural mapping of the region surrounding Vostrukha Mons, Venus. The yellow shaded region shows the extent of Dolya Tessera, and blue lines indicate a network of normal faults oriented approximately NE–SW, respectively. The green box corresponds to the zoomed-in region shown in the bottom-left corner of the main figure. Pink arrows point to general area where the fractures appear to bend around the deformed edifice. Magellan SAR data, shown in an equirectangular projection, and with radar illumination from the left.

On Venus, Vostrukha Mons is bounded to the west by Dolya Tessera, an ~ 1,100 km region characterized by tesserae terrain which is comprised of numerous sets of intersecting tectonic features (Bindschadler and Head, 1991; Ghent and Hansen, 1999). A mostly linear network of normal faults surrounds Vostrukha Mons to the east, north, and south, and has an overall northeast-to-southwest orientation (**Figure 3.7**). These faults extend several hundred kilometers beyond the

edifice and appear to be deflected around the base of the edifice (pink arrows in **Figure 3.7**). A similar "wristwatch-like" pattern was identified by Lopez et al. (2008) at a volcano from the Magellan Volcano Catalog (Crumpler and Aubele 2000), centered at 21.6°N, 40.2°W, on Earth at Mount Fantale in Ethiopia (van Wyk de Vries and Matela, 1998), and on Mars at Alba Patera (McGovern et al., 2001). In extensional systems, these fracture patterns emerge as a result of combined volcanic loading and lithospheric flexure (McGovern et al., 2001; Lopez et al., 2008), suggesting that the weight of Vostrukha Mons may have downflexed the lithosphere in a manner similar to volcano sagging (*see section 3.5.4*).

The sector collapse on the edifice atop Vostrukha Mons could be directly linked to these regional scale rift zones, as rift zones can not only influence the lateral collapse direction, but can also trigger edifice failure in the first place (Tibaldi et al., 2008). Field studies and modeling of deformed volcanoes on Earth (e.g., Stromboli, Italy and Ollagüe, Bolivia/Chile) show that lateral collapse typically develops at an angle perpendicular to regional structures such as rift zones (Siebert, 1984; Francis and Wells, 1988; Tibaldi, 1995; Tibaldi et al., 2008). Indeed, the lateral collapse on the dome atop Vostrukha Mons is oriented northwest to southeast, making it perpendicular to the regional rift zones that are aligned northeast to southwest (**Figure 3.7**). Gravitational collapse could have been enabled by the volcanic substrates (e.g., volcanic plains materials, ash deposits) dipping towards the rift, as is the case for the Stromboli and Ollagüe volcanoes (Tibaldi et al., 2008, 2009).

3.5.3 Spreading Case Study: Unnamed volcano on Venus and Tharsis Tholus on Mars

Volcano spreading occurs as a volcano grows; that growth exerts an increasing load on the substrata and, if that supporting basement is sufficiently rigid, results in the outward spread of the edifice, typically along a weaker substrate (Borgia et al., 2000; Marquez et al., 2008). We note

only four examples of volcano spreading on Venus and, of those examples, three are volcanoes <20 km in diameter. Here, we compare a small, unnamed volcano on Venus that exhibits structures related to spreading with the Martian volcano Tharsis Tholus, situated within the Tharsis Rise.

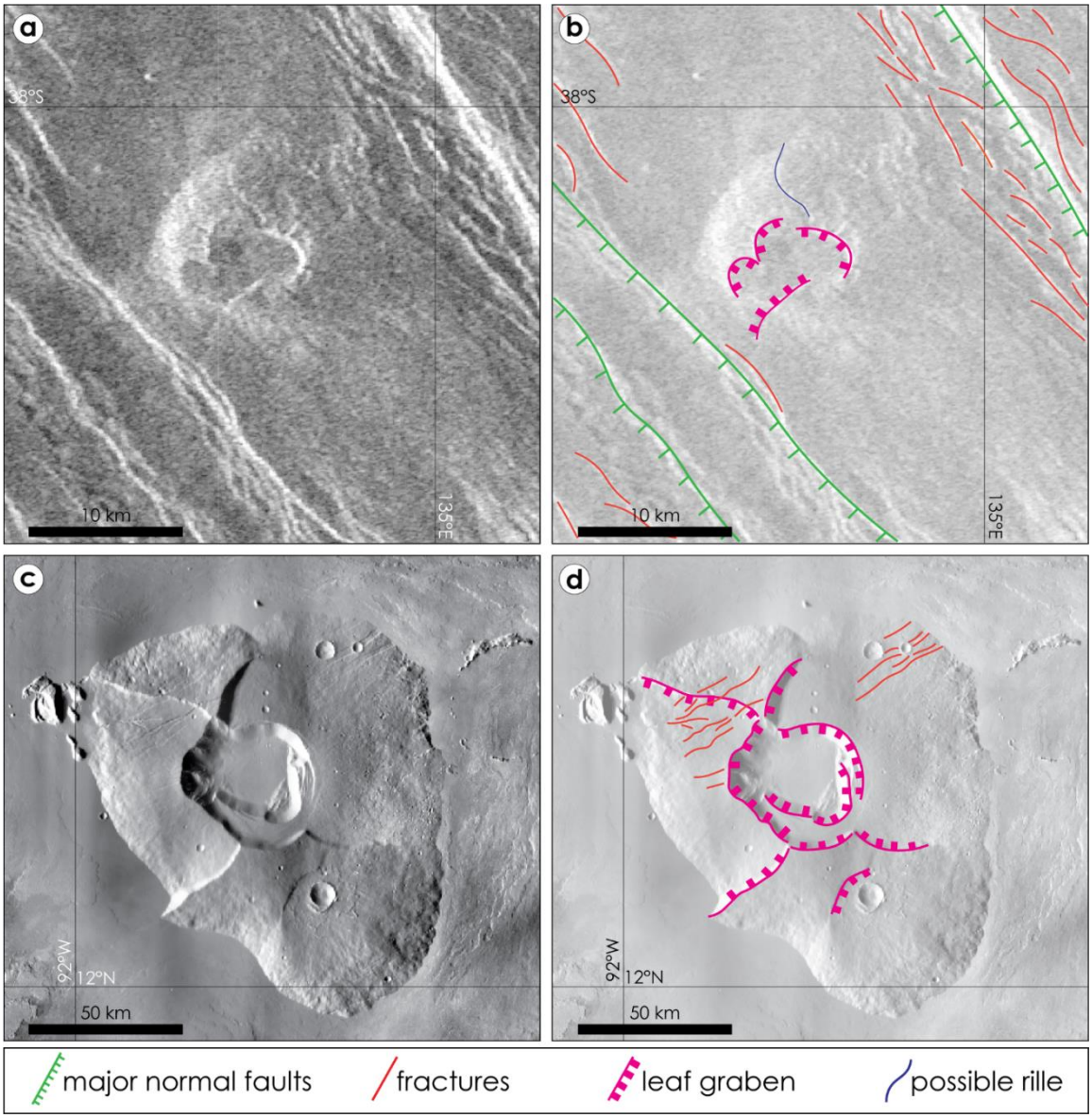

Figure 3.8 Comparative structural analysis between an unnamed volcano on Venus (a & b) and Tharsis Tholus on Mars (c & d). The unnamed Venusian edifice is shown with Magellan SAR data in an equirectangular projection and with radar illumination from the left (a); Tharsis Tholus is shown with THEMIS Day-Infrared imagery (c). Panels (b) and (d) show deformation structures associated with volcano spreading and are transparent, grey-scaled versions of panels (a) and (c), respectively.

On Venus, within the southeast quadrant of Artemis Corona and approximately centered at 38.4°S, 135.7°E, is an unnamed volcano that has a basal diameter of ~12 km (**Figure 3.8a**). The summit and portions of the SW flank appear to be dissected by normal faults and "leaf gaben," structures attributed to volcano spreading (Byrne et al., 2013, Borgia et al., 2000; van Wyk de Vries and Borgia, 1996). Additionally, this volcano is bounded to the northeast and southwest by an extensive network of normal faults that are oriented north to northwest (**Figure 3.8b**).

Our counterpart to the unnamed spreading volcano on Venus is Tharsis Tholus, located in the east Tharsis region of Mars (**Figure 3.8c**). The volcano stands ~8 km tall, and has a basal diameter of ~158 × 131 km, with a summit caldera complex about 48 km in diameter (Plescia, 2004; Platz et al., 2011). The flanks of Tharsis Tholus are broken into blocks by normal faults (Crumpler et al., 1996), and have subsequently been embayed by lava flows (Plescia, 2003) (**Figure 3.8d**).

Comparison of a Spreading Unnamed Volcano on Venus and Tharsis Tholus on Mars:

The flanks of both Tharsis Tholus on Mars and this unnamed Venusian edifice are cross-cut by normal faults and "leaf graben" that indicate the flanks of both volcanoes have been extended (**Figure 3.8b** & **3.8d**). A spreading volcano exhibits extensional structures on its flanks, such as edifice-radial normal faults and leaf graben, as well as shortening structures around its base such as edifice-concentric folds and thrust faults (Holohan et al., 2023). Although both edifices show evidence of extension on their flanks, neither obviously has shortening structures around their bases. In the case of Tharsis Tholus, this apparent dearth of a basal thrust system could be explained by the embayment of younger lava flows that cover the volcano's lower slopes and thus conceal a flexural rise, trough, or any attendant extensional structures surrounding the edifice

(Borgia et al., 2000). However, the unnamed edifice on Venus is completely bound by rifts, with no evidence of any shortening structures, concentric to the volcano or otherwise.

Volcano spreading is the result of gravity acting on an edifice decoupled from a rigid basement, with movement enabled by a low-strength layer beneath the edifice (van Wyk de Vries and Matela, 1998). For example, Mars' Tharsis Tholus is hypothesized to be underlain by a low-strength layer consisting of ice- or water-rich material (Plescia 2003), evaporates (Andrews-Hanna, 2009), or phyllosilicates (McGovern et al., 2015); that such materials might be present beneath Tharsis Tholus is evidenced by geological observations (Borgia et al., 2000; Plescia, 2003; Holohan et al., 2023) and supported by analogue modeling (Platz et al., 2011). On Earth, Nicaraguan volcanoes like Concepción and Maderas are underlain by weak, clay-rich sediments that help enable horizontal spreading (Borgia et al., 2000). On Venus, there is little indication of sedimentation given the lack of an eroding agent (e.g., water) and the seemingly limited aeolian redistribution of impact generated dust (Arvidson et al., 1992). Thus, it may be that volcanoes on Venus are mechanically attached, and therefore coupled, to their underlying basement. Such a welded basal boundary condition is further evidenced by the absence of flank failures and Hawaiian-style rift zones on large volcanoes (> 100 km in diameter) across Venus (McGovern and Solomon 1998).

However, the unnamed volcano in our study, which is only ~12 km in diameter (compared to the ~158 × 131 km diameter Tharsis Tholus), may appear to be basally welded but could be detatched from the lithosphere, and underlain by a low-strength layer (e.g., ash deposits, layered volcanic materials) that is acting as a slip surface and allowing for the outward spread of the edifice. Researchers analyzing the morphology of volcanic flow features, as well as radar-bright deposits across the surface of Venus, have identified numerous areas (e.g., Eistla and Dione

Regiones) where pyroclastic materials are associated with volcanoes, coronae, or rift zones (Keddie and Head, 1995; Ghail and Wilson, 2015; Campbell et al., 2017). Based on radar properties, these pyroclastic materials could comprise coarse debris (e.g., small rock fragments) and/or ash deposits, which would have created a thin veneer over the existing features at a depth of tens of centimeters up to a few meters (Campbell et al., 2017). This lower-strength pyroclastic layer might act as a basal detachment surface for volcanoes built on top to spread outward. Such a scenario is similar to the spreading process that occurred at Mombacho volcano in Nicaragua, which is built upon ignimbrites and marine flysch (Borgia et al., 2000). Although there is no evidence of pyroclastic flows linked to the unnamed volcano analyzed in this study, it is possible that the edifice could be built atop pyroclastic deposits that were buried by subsequent lava flows, particularly since this volcano is located within Artemis Corona, which is associated with considerable extrusive volcanism (Bannister and Hansen, 2010).

Alternatively, this unnamed volcano may actually be basally welded to the crust but underlain by a less competent material (e.g., ash deposits or other layered volcanic materials) that caused the edifice to spread outward, much like the process of "substratum spreading" described by van Wyk de Vries and Matela (1998). Substratum spreading occurs when a basal, ductile layer is coupled with the edifice and that ductile material is capable of dragging the volcano outward because viscous forces in the layer exceed the failure strength of the overlying edifice (van Wyk de Vries and Matela 1998; Lopez et al., 2008; McGovern et al., 2015). Here, ductile refers to nonrecoverable strain accommodated by microfracturing; this deformation takes place at far too low a temperature to permit crystal plastic processes.

On Venus, substratum spreading could plausibly occur if an edifice were basally welded to a, say, volcanic plains material that is more competent than one of the numerous volcanic layers

underneath (e.g., as a function of differing proportions of ashfall or variations in composition) (Treiman, 2007). For the unnamed volcano in this study, it appears to be situated directly atop volcanic flows that may be underlain by various deposits from the nearby Ceres, Bona, and Miralaidji coronae, as well as numerous layers of volcanic plains materials (Bannister and Hansen, 2010). Should those now-buried layers be mechanically weaker than the overlying lava flows because of composition, cohesion, or even from chemical weathering when the unit was exposed to the atmosphere (Gilmore et al., 2023), it is possible that the edifice underwent some degree of substratum spreading resulting in the formation of structures characteristic of volcano spreading, such as edifice radial normal faults and leaf graben.

3.5.4 Sagging Case Study: Tepev Mons on Venus and Ascraeus Mons on Mars

Unlike numerous examples on Mars and Earth, very few volcanoes on Venus seem to exhibit structures associated with volcano sagging. Nyx and Tepev Montes are two large Venusian edifices located in the southwestern region of Bell Regio and centered at ~ 30°N, 46°E. Nyx Mons is ~800 km in diameter and 5 km in height, and Tepev Mons is smaller at ~300 km in diameter, but standing 6 km tall with two large calderas at the summit region (**Figure 3.9a**). Both volcanoes exhibit peripheral circumferential graben (Rogers and Zuber, 1998; McGovern and Solomon, 1998) and pit crater chains (Campbell and Rogers, 1994; Rogers and Zuber, 1998). Tepev Mons also displays flank terraces on the slopes of the eastern caldera, an observation to our knowledge not reported before, as well as a circumferential, flexural moat along the northwest and northeast quadrant of the edifice (Solomon and Head, 1990; McGovern and Solomon, 1992; Campbell and Rogers, 1994). Here, we specifically focus on the morphology of Tepev Mons (**Figure 3.9b**) and its similarities with the Martian volcano Ascraeus Mons.

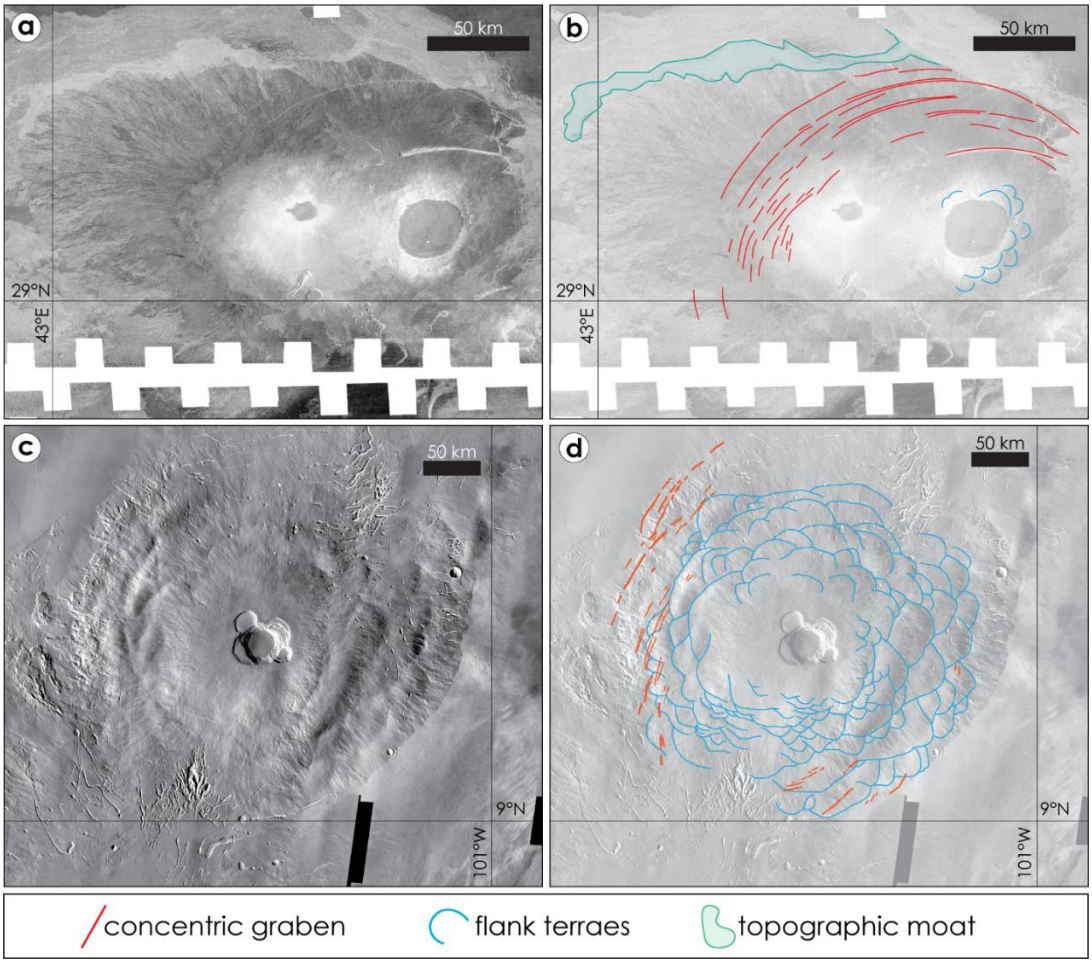

Figure 3.9 Comparative structural analysis between Tepev Mons on Venus (a & b) and Ascraeus Mons on Mars (c & d). Tepev Mons is again shown with Magellan SAR data in an equirectangular projection and with radar illumination from the left (a), and Ascraeus Mons is shown with THEMIS Day-Infrared imagery (c). Panels (b) and (d) show deformation structures associated with volcano sagging and are transparent, grey-scaled versions of panels (a) and (c), respectively. Structures associated with Ascraeus Mons are from those mapped by Byrne et al. (2012).

The Tharsis rise is home to several giant Martian volcanoes including the tallest, Ascraeus Mons, which has a summit 18.2 km above the surrounding plains. Ascraeus has a basal diameter of ~ 375 km by 870 km, and has a volume of 1.1×10^6 km^3 (Plescia, 2004) (**Figure 3.9c**). The Ascraeus summit hosts a prominent caldera complex (Zimbleman and Edgett, 1992). These calderas are generally steep-sided, overlapping structures that have terraced walls and flat floors (Crumpler et al., 1996). The flanks of Ascraeus Mons host pit crater chains oriented concentric to the summit (Wyrick et al., 2004), and flank terraces on the mid flanks at all azimuths (Byrne et al.,

2012). On the edge of the west and northwest flanks of Ascraeus Mons and into the northwest plains are arcuate grabens oriented concentric to the volcano (Byrne et al., 2012) (**Figure 3.9d**).

Comparison of Tepev Mons on Venus and Ascraeus Mons on Mars:

Both Tepev and Ascraeus Montes exhibit several morphological structures characteristic of volcano sagging, including flank terraces and concentric graben surrounding the edifice (**Figure 3.9b** & **3.9d**). Flank terraces are well-documented as a structural indicator of volcano sagging (McGovern and Solomon, 1993; Byrne et al., 2009; Byrne et al., 2012; Holohan et al., 2023) and have been recognized on Earth (e.g., Galapagos and Hawaii) and on Mars (e.g., Elysium, Olympus, and Ascraeus Montes), but have not yet been described on Venus. In our structural analysis of Tepev Mons, we note these subtle fish scale like structures on the north, east, and south flanks of the larger eastern caldera (**Figure 3.9b**). These structures, although fewer in number (n =12) (possibly due to the low resolution of the Magellan SAR data), are comparable in planform shape and location on the upper portion of the edifice to flank terraces documented on Ascraeus.

Both volcanoes also show evidence of extension surrounding their bases. A set of narrow graben is situated 50–100 km north from the center of Tepev Mons, and additional, edifice-concentric graben may be obscured by radar-bright lobate materials originating from Otafuku Tholi situated to the southeast of Tepev Mons (Campbell and Campbell, 2002) (**Figure 3.9a**). These deformational structures have been used to infer the thickness of the lithosphere at the time of edifice formation. McGovern and Solomon (1993) used a flexural model and the position and extent of the flexural moat to the north of Tepev Mons to calculate an elastic thickness of 10–20 km. This estimate is comparable to values derived by Anderson and Smrekar (2006) for all of Bell Regio (the broader location of Tepev Mons), which ranges from 10 to 40 km.

Like Tepev Mons, Ascraeus Mons also exhibits circumferential graben attributed to lithospheric flexure (Comer et al., 1985) (**Figure 3.9b** & **3.9d)**. On the basis of their size and distribution, Comer et al. (1985) used the graben to calculate an elastic lithosphere of thickness ~22 km beneath Ascraeus. With gravity–topography admittance spectra from the Mars Global Surveyor spacecraft, McGovern et al. (2004) estimated the best-fit elastic thickness values at Ascraeus Mons to range from 32 to 46 km. Likewise, analysis of a combination of gravity and topography data from the Mars Express Orbiter and Mars Reconnaissance Orbiter missions returned estimates of the elastic thickness at Ascraeus Mons of ~20–60 km, with best fits of <40 km (Beuthe et al., 2012).

Although specific deformational structures (e.g., flank terraces, edifice-concentric graben) can indicate volcano sagging, we validated this interpretation by use of a dimensionless, semi-quantitative parameter, Π_{Sag}, which was proposed by Byrne et al. (2013) to provide an estimate for whether a volcano's basement would conceptually flex in response to the volcanic load. The Π_{Sag} parameter relates the geometry and gravitational load of the edifice (modeled as a cone) to the effective flexural rigidity of the basement (Byrne et al., 2013), and is defined as

$$\Pi_{Sag} = \frac{(4.11 \times \rho \times g \times R^2 \times H^2)(1 - v^2)}{(E \times B^3)}.$$

The equation considers volcano height (H), volcano radius (R), the thickness of the brittle lithosphere (B), the density of that lithosphere (ρ), surface gravitational acceleration (g), and Young's Modulus (E) and Poisson's ratio (v) values appropriate to the likely composition of the upper lithosphere (Byrne et al., 2013). Resulting Π_{Sag} values for Tepev and Ascraeus Montes are given in **Table 3.4**.

Analogue models developed by Byrne et al., (2013) revealed two sagging architectures, an end-member sagging regime and a hybrid sagging-spreading regime. Here, we focus on the end-

member sagging regime, which occurs when the cone and its basement are coupled and deform together as one unit. In this model, when $2.4 > \Pi_{Sag} > 0.017$, the cone subsided within a trough surrounded by a bulge, normal faults and fissures formed around the periphery of the cone, and horizontal constriction of the cone resulted in flank terraces along the mid-to lower flanks (Byrne et al., 2013).

Table 3.4
Parameters used to calculate Π_{Sag} for Tepev and Ascraeus Montes

Parameter	Symbol	Unit	Tepev Mons (Venus)	Ascraeus Mons (Mars)
Cone height[d,e]	H	m	5×10^3	14.9×10^3
Cone radius[d,e]	R	m	1.1×10^5	3×10^5
Brittle lithosphere thickness[a–c,e,f]	B	m	min: 1.0×10^4	min: 2.0×10^4
			max: 4.0×10^4	max: 10.5×10^4
Density[a,e,f]	ρ	$kg.m^{-3}$	3.0×10^3	2.6×10^3
Gravitational acceleration	g	$m.s^{-2}$	8.87	3.71
Young's Modulus[b,e]	E	Pa	1×10^{11}	1×10^{11}
Poisson's ratio[b,e]	v	-	3.3×10^{-1}	2.5×10^{-1}
Sagging parameter[g]	Π_{Sag}	-	min: 0.005	min: 0.006
			max: 0.295	max: 0.928

[a]Beuthe et al. (2012). [b]Belleguic et al. (2005). [c]McGovern and Solomon (1993). [d]Plescia (2004). [e]Rogers and Zuber (1998). [f]Solomon and Head (1990). [g]The sagging parameter relates the geometry and gravitational load of the edifice (modeled as a cone) to the effective flexural rigidity of the basement (Byrne et al., 2013).

The modeled end-member sagging architecture closely aligns with deformational structures on Tepev and Ascraeus Montes, consistent with the interpretation that both edifices lack an effective basal decoupling (Byrne et al., 2013). On Venus, this lack of decoupling may be attributed to the basal welded boundary conditions at many volcanoes (McGovern and Solomon, 1998), allowing the edifice and basement to deform as one mechanical unit. For Tepev Mons, $\Pi_{Sag} \approx 0.005–0.295$ (**Table 3.4**), with Π_{Sag} increasing as brittle lithospheric thickness (B) decreases. If we assume B values ranging from 10 km to 26 km (c.f., McGovern and Solomon, 1993), Π_{Sag}

values fall exactly within the modeled range for end-member sagging ($2.4 > \Pi_{Sag} > 0.017$), and this process could account for the edifice-concentric graben and flank terraces associated with Tepev Mons (Byrne et al., 2013). Volcano sagging at Ascraeus Mons has been well studied through detailed structural mapping and analogue modeling (e.g., Byrne et al., 2009; 2012; 2013). We calculate $\Pi_{Sag} \approx 0.006–0.928$ at Ascraeus Mons, which also agrees with expected sagging if we assume a *B* value of 20–75 km.

Estimates for the thickness of the brittle lithosphere beneath Ascraeus Mons are generally greater than for Tepev Mons (**Table 3.4**), and Ascraeus has a volume of 1.1×10^6 km^3 (Plescia, 2004), two orders of magnitude larger than the volume of Tepev, 6.4×10^4 km^3 (Hahn and Byrne, 2023a). If Tepev Mons has indeed downflexed its basement, then it appears that comparatively small volcanoes on Venus are capable of downflexing their supporting basement. This finding is likely linked to the relatively thin upper brittle lithosphere on Venus (Ghail 2015; James et al., 2013), which is probably capable of downflexing more readily than the thick brittle lithosphere on Mars (Belleguic et al., 2005)—allowing comparatively smaller-sized volcanoes on Venus to sag despite the higher surface gravity on Venus (8.9 m/s^2) compared to Mars (3.8 m/s^2).

The formation of the large volcanoes and extensive igneous activity in the Tharsis region is commonly linked to mantle plumes (Carr, 1974; Kiefer and Hager, 1989; Mège and Masson, 1996; McKenzie et al., 2002; Roberts and Zhong, 2004, 2006; Belleguic et al., 2005; Plesa et al., 2018). Whether the plume is currently active (Plesa et al., 2018) or not (Roberts and Zhong 2004, 2006), at some point the weight of Ascraeus Mons exceeded the yield strength of the supporting basement, which began to bend. Similar to the proposed lithospheric flexure hypothesis for Tepev and Nyx Montes (Smrekar, 1994), the Tharsis region (and thus Ascraeus Mons) may no longer be dynamically supported by a plume at depth (Spohn et al., 2001). Alternatively, Ascraeus Mons

may have simply begun sagging as a viscoelastic response to the increasing size of the edifice (Byrne et al., 2012), perhaps coupled with an ice-saturated and thus weakened Martian crust, with some bending resulting from pressure- and thermal melting (Murray et al., 2010).

3.6 Conclusions

With Magellan SAR imagery, we have identified 162 volcanoes that have undergone gravitational deformation and classified them into four main categories: landsliding, sector collapse, spreading, and sagging. Volcanoes exhibiting signs of landslides or sector collapse are most common across Venus, comprising cumulatively 54.5% of our dataset, whereas volcanoes showing evidence for spreading or sagging comprise only ~5% of our dataset. The remaining volcanoes in our dataset (40.5%) are classified as indeterminate, which includes remnant edifices, volcanoes that exhibit structures associated with more than one main deformational category, or deformed volcanoes that are too difficult to unequivocally classify with Magellan SAR data. Deformed volcanoes are distributed globally, are found spatially proximal to a variety of tectonic structures, and are associated with various crustal thicknesses and at a range of elevations, suggesting that there are numerous drivers of deformation on Venus. Through comparative analysis of deformed volcanoes on Earth and Mars, we can gain further insight into the mechanisms of volcano gravitational deformation on Venus.

Through detailed analysis of several seamounts on Earth and steep-sided, flat-topped volcanoes on Venus (which we here term VD-1–3), we propose that volcanoes on Venus could deform in a manner similar to the Taney Seamounts (T-A–C) on Earth. The low heights and relative elevations of the Venusian volcanoes suggests that flank rift zones were unable to form. Instead, we contend that VD-1–3 probably deformed in response to over steepening during episodic growth or as a result of activity associated with nearby extensional structures.

Analysis of Vostrukha Mons on Venus and Socompa volcano on Earth reveals similar structures associated with sector collapse. Although deformational structures are morphologically comparable at each edifice, the collapse mechanisms are probably different: volcano spreading likely triggered the collapse at Socompa, whereas tectonic stresses external to the volcano drove the collapse at Vostrukha Mons. We hypothesize that a regional-scale rift zone located adjacent to Vostrukha Mons triggered the flank collapse via fault slip and dike emplacement, possibly augmented by the effect of dipping substrata associated with the rift zone itself.

Although spreading volcanoes are common on Earth and have even been documented on Mars, this type of deformation is relatively rare on Venus—but not entirely absent. Volcanoes on Venus have been hypothesized to be basally welded to their underlying basement (McGovern and Solomon, 1998; McGovern et al., 2015), yet they could be welded to a thin but mechanically strong layer that itself is underpinned by a less competent material, a combination that results in a sort of "substratum spreading" (van Wyk de Vries and Matela, 1998; Lopez et al., 2008; McGovern et al., 2015) that leads to the outward spread of the edifice. Alternatively, some volcanoes on Venus may not be directly coupled to their basement but could be built atop weaker pyroclastic and/or ash deposits that act as a slip surface that enables spreading. It is further possible that both scenarios apply to volcanoes on Venus.

We note only four instances of volcanoes sagging on Venus. It is conceivable that there are additional volcanoes that exhibit sagging structures, but the relatively low resolution and poor signal-to-noise ratio of the Magellan SAR data prevents the identification of these structures, which are most easily identified with high-resolution topographic data (Byrne et al., 2009). In any case, despite substantial differences in their sizes, Tepev Mons on Venus, and Ascraeus Mons on

Mars share similar morphological structures associated with volcano sagging, and are likely both downflexing their underlying lithosphere.

Higher-resolution radar imagery and topographic data from future missions, such as NASA's VERITAS mission (Smrekar et al., 2022) and ESA's EnVision mission (Ghail et al., 2018), will improve our ability to identify structures associated with volcano deformation across Venus, particularly subtle features such as flank terraces. Furthermore, we note many similarities in the morphology of different styles of volcano deformation at volcanoes on Venus compared with volcanoes and seamounts on Earth and edifices on Mars. Such higher-resolution data of deformed volcanoes on Venus will help us better understand the mechanisms contributing to different styles of deformation on the planet, and how they resemble or differ from styles of volcano deformation on Earth and Mars.

References

Acocella, V., & Neri, M. (2009). Dike propagation in volcanic edifices: Overview and possible developments. Tectonophysics, 471(1–2), 67–77.https://doi.org/10.1016/j.tecto.2008.10.002

Acocella, V., & Tibaldi, A. (2005). Dike propagation driven by volcano collapse: A general model tested at Stromboli, Italy. Geophysical Research Letters, 32(8), L08308. https://doi.org/10.1029/2004GL022248

Airey, M. W., Mather, T. A., Pyle, D. M., & Ghail, R. C. (2017). The distribution of volcanism in the Beta-Atla-Themis region of Venus: Its relationship to rifting and implications for global tectonic regimes. Journal of Geophysical Research: Planets, 122(8), 1626–1649. https://doi.org/10.1002/2016JE005205

Anderson, F. S., & Smrekar, S. E. (2006). Global mapping of crustal and lithospheric thickness on Venus. Journal of Geophysical Research, 111(E8), E08006. https://doi.org/10.1029/2004JE002395

Andrews-Hanna, J. C. (2009). A mega-landslide on Mars. Nature Geoscience, 2(4), 248–249. https://doi.org/10.1038/ngeo483

Arvidson, R. E., Greeley, R., Malin, M. C., Saunders, R. S., Izenberg, N., Plaut, J. J., & Shepard, M. K. (1992). Surface modification of Venus as inferred from Magellan observations of plains. Journal of Geophysical Research, 97(E8), 13303–13317. https://doi.org/10.1029/92JE01384

Aubele, J. C., & Slyuta, E. N. (1990). Small domes on Venus: Characteristics and origin. Earth, Moon, and Planets, 50(1), 493–532. https://doi.org/10.1007/BF00142404

Bannister, R. A., & Hansen, V. L. (2010). Geologic map of the Artemis Chasma quadrangle (V-48). U.S. Geological Survey Scientific Investigations Map 3099.

Barone, A. M., & Ryan, W. B. (1988). Along-axis variations within the plate boundary zone of the southern segment of the Endeavour Ridge. Journal of Geophysical Research, 93(B7), 7856–7868. https://doi.org/10.1029/JB093iB07p07856

Batiza, R. (1989). Seamounts and seamount chains of the eastern Pacific. In E. L. Winterer, D. M. Hussong, & R. W. Decker (Eds.), The eastern Pacific Ocean and Hawaii (pp. 289–306). The Geological Society of America.

Belleguic, V., Lognonné, P., & Wieczorek, M. (2005). Constraints on the Martian lithosphere from gravity and topography data. Journal of Geophysical Research, 110(E11), E11005. https://doi.org/10.1029/2005JE002437

Bernard, B., de Vries, B. V. W., Barba, D., Leyrit, H., Robin, C., Alcaraz, S., & Samaniego, P. (2008). The Chimborazo sector collapse and debris avalanche: Deposit characteristics as evidence of emplacement mechanisms. Journal of Volcanology and Geothermal Research, 176(1), 36–43. https://doi.org/10.1016/j.jvolgeores.2008.03.012

Beuthe, M., Le Maistre, S., Rosenblatt, P., Pätzold, M., & Dehant, V. (2012). Density and lithospheric thickness of the Tharsis Province from MEX MaRS and MRO gravity data. Journal of Geophysical Research, 117(E4), E04002. https://doi.org/10.1029/2011JE003976

Bindschadler, D. L., & Head, J. W. (1991). Tessera terrain, Venus: Characterization and models for origin and evolution. Journal of Geophysical Research, 96(B4), 5889–5907. https://doi.org/10.1029/90JB02742

Borgia, A., Delaney, P. T., & Denlinger, R. P. (2000). Spreading volcanoes. Annual Review of Earth and Planetary Sciences, 28(1), 539–570. https://doi.org/10.1146/annurev.earth.28.1.539

Bridges, N. T. (1995). Submarine analogs to Venusian pancake domes. Geophysical Research Letters, 22(20), 2781–2784. https://doi.org/10. 1029/95GL02662

Bridges, N. T. (1997a). Ambient effects on basalt and rhyolite lavas under Venusian, subaerial, and subaqueous conditions. Journal of Geophysical Research, 102(E4), 9243–9255. https://doi.org/10.1029/97JE00390

Bridges, N. T. (1997b). Characteristics of seamounts near Hawaii as viewed by GLORIA. Marine Geology, 138(3–4), 273–301. https://doi.org/10.1016/S0025-3227(96)00114-4

Buchs, D. M., Hoernle, K., & Grevemeyer, I. (2015). Seamounts. In J. Harff, M. Meschede, S. Petersen, & J. Thiede (Eds.), Encyclopedia of marine geosciences. Springer. https://doi.org/10.1007/978-94-007-6644-0_34-1

Bulmer, M. H. (1994). Small volcanic edifices in the plains of Venus: With particular reference to the evolution of scalloped margin domes. University of London, University.

Bulmer, M. H. (2012). 32 Landslides on other planets. In J. J. Clague & D. Stead (Eds.), Landslides: Types, mechanisms and modeling (pp. 393–420). Cambridge University Press.

Bulmer, M. H., & Guest, J. E. (1996). Modified volcanic domes and associated debris aprons on Venus. Geological Society, London, Special Publications, 110(1), 349–371. https://doi.org/10.1144/GSL.SP.1996.110.01.25

Bulmer, M. H., & Wilson, J. B. (1999). Comparison of flat-topped stellate seamounts on Earth's seafloor with stellate domes on Venus using side-scan sonar and Magellan synthetic aperture radar. Earth and Planetary Science Letters, 17(2), 277–287. https://doi.org/10.1016/S0012-821X(99)00154-5

Byrne, P. K., de Vries, B. V. W., Murray, J. B., & Troll, V. R. (2009). The geometry of volcano flank terraces on Mars. Earth and Planetary Science Letters, 281(1–2), 1–13. https://doi.org/10.1016/j.epsl.2009.01.043

Byrne, P. K., Holohan, E. P., Kervyn, M., de Vries, B. V. W., Troll, V. R., & Murray, J. B. (2013). A sagging-spreading continuum of large volcano structure. Geology, 41(3), 339–342. https://doi.org/10.1130/G33990.1

Byrne, P. K., van Wyk de Vries, B., Murray, J. B., & Troll, V. R. (2012). A volcanotectonic survey of Ascraeus Mons, Mars. Journal of Geophysical Research, 117(E1). https://doi.org/10.1029/2011JE003825

Camiz, S., Poscolieri, M., & Roverato, M. (2013). Comparison of three Andean volcanic complexes through multidimensional analyses of geomorphometric data. In EICES (pp. 52–74).

Campbell, B. A., & Campbell, P. G. (2002). Geologic map of the Bell Regio quadrangle (V-9).

Campbell, B. A., Morgan, G. A., Whitten, J. L., Carter, L. M., Glaze, L. S., & Campbell, D. B. (2017). Pyroclastic flow deposits on Venus as indicators of renewed magmatic activity. Journal of Geophysical Research: Planets, 122(7), 1580–1596. https://doi.org/10.1002/2017JE005299

Campbell, B. A., & Rogers, P. G. (1994). Bell Regio, Venus: Integration of remote sensing data and terrestrial analogs for geologic analysis. Journal of Geophysical Research, 99(E10), 21153–21171. https://doi.org/10.1029/94JE01862

Cañon-Tapia, E., & Mendoza-Borunda, R. (2014). Insights into the dynamics of planetary interiors obtained through the study of global distribution of volcanoes I: Empirical calibration on Earth. Journal of Volcanology and Geothermal Research, 281, 53–69. https://doi.org/10.1016/j.jvolgeores.2014.05.013

Capra, L., Macıas, J. L., Scott, K. M., Abrams, M., & Garduño-Monroy, V. H. (2002). Debris avalanches and debris flows transformed from collapses in the Trans-Mexican Volcanic Belt, Mexico–behavior, and implications for hazard assessment. Journal of Volcanology and Geothermal Research, 113(1–2), 81–110. https://doi.org/10.1016/S0377-0273(01)00252-9

Carr, M. H. (1974). Tectonism and volcanism of the Tharsis region of Mars. Journal of Geophysical Research, 79(26), 3943–3949. https://doi.org/10.1029/JB079i026p03943

Carr, M. H., Greeley, R., Blasius, K. R., Guest, J. E., & Murray, J. B. (1977). Some Martian volcanic features as viewed from the Viking orbiters. Journal of Geophysical Research, 82(28), 3985–4015. https://doi.org/10.1029/JS082i028p03985

Carracedo, J. C. (1994). The canary islands: An example of structural control on the growth of large oceanic-island volcanoes. Journal of Volcanology and Geothermal Research, 60(3–4), 225–241. https://doi.org/10.1016/0377-0273(94)90053-1

Cas, R. A. F., & Wright, J. V. (1987). Volcanic successions (p. 528). Allen and Unwin, St. Leonards, N. S. W., Australia.

Casalbore, D. (2018). Volcanic islands and seamounts. Submarine geomorphology, 333–347. https://doi.org/10.1007/978-3-319-57852-1_17

Casalbore, D., Passeri, F., Tommasi, P., Verrucci, L., Bosman, A., Romagnoli, C., & Chiocci, F. L. (2020). Small-scale slope instability on the submarine flanks of insular volcanoes: The case-study of the Sciara del Fuoco slope (Stromboli). International Journal of Earth Sciences,109(8), 2643–2658. https://doi.org/10.1007/s00531-020-01853-5

Casalbore, D., Romagnoli, C., Pimentel, A., Quartau, R., Casas, D., Ercilla, G., et al. (2015). Volcanic, tectonic and mass-wasting processes off shore Terceira island (Azores) revealed by high-resolution seafloor mapping. Bulletin of Volcanology, 77(3), 24. https://doi.org/10.1007/s00445-015-0905-3

Cecchi, E., van Wyk de Vries, B., & Lavest, J. M. (2004). Flank spreading and collapse of weak-cored volcanoes. Bulletin of Volcanology, 67(1), 72–91. https://doi.org/10.1007/s00445-004-0369-3

Chaytor, J. D., Keller, R. A., Duncan, R. A., & Dziak, R. P. (2007). Seamount morphology in the Bowie and Cobb hot spot trails, Gulf of Alaska. Geochemistry, Geophysics, Geosystems, 8(9), 37. https://doi.org/10.1029/2007GC001712

Chigira, M. (2002). Geologic factors contributing to landslide generation in a pyroclastic area: August 1998 Nishigo Village, Japan. Geomorphology, 46(1–2), 117–128. https://doi.org/10.1016/S0169-555X(02)00058-2

Clague, D. A., Reynolds, J. R., & Davis, A. S. (2000). Near-ridge seamount chains in the northeastern Pacific Ocean. Journal of Geophysical Research, 105(B7), 16541–16561. https://doi.org/10.1029/2000JB900082

Comer, R. P., Solomon, S. C., & Head, J. W. (1985). Mars: Thickness of the lithosphere from the tectonic response to volcanic loads. Reviews of Geophysics, 23(1), 61–92. https://doi.org/10.1029/RG023i001p00061

Connor, C. B. (1990). Cinder cone clustering in the TransMexican volcanic belt: Implications for structural and petrologic models. Journal of Geophysical Research, 95(B12), 19395–19405. https://doi.org/10.1029/JB095iB12p19395

Coombs, M. L., White, S. M., & Scholl, D. W. (2007). Massive edifice failure at Aleutian arc volcanoes. Earth and Planetary Science Letters, 256(3–4), 403–418. https://doi.org/10.1016/j.epsl.2007.01.030

Coumans, J. P., Stix, J., Clague, D. A., & Minarik, W. G. (2015). The magmatic architecture of Taney seamount-A, NE Pacific Ocean. Journal of Petrology, 56(6), 1037–1067. https://doi.org/10.1093/petrology/egv027

Crumpler, L. S., & Aubele, J. C. (2000). Volcanism on Venus. In H. Sigurdsson, B. Houghton, H. Rymer, J. Stix, & S. McNutt (Eds.), Encyclopedia of volcanoes (pp. 727–770). Academic Press.

Crumpler, L. S., Aubele, J. C., Senske, D. A., Keddie, S. T., Magee, K. P., & Head, J. W. (1997). Volcanoes and centers of volcanism on Venus. In S. W. Bougher, D. M. Hunten, & R. J. Philips (Eds.), Venus II: Geology, geophysics, atmosphere, and solar wind environment (pp. 697–756).The University of Arizona Press. https://doi.org/10.2307/j.ctv27tct5m.26

Crumpler, L. S., Head, J. W., & Aubele, J. C. (1996). Calderas on Mars: Characteristics, structure, and associated flank deformation. Geological Society, London, Special Publications, 110(1), 307–348. https://doi.org/10.1144/GSL.SP.1996.110.01.24

Delaney, P. T., & Denlinger, R. P. (1999). Stabilization of volcanic flanks by dike intrusion: An example from Kilauea. Bulletin of Volcanology, 61(6), 356–362. https://doi.org/10.1007/s004450050278

Edwards, C. S., Nowicki, K. J., Christensen, P. R., Hill, J., Gorelick, N., & Murray, K. (2011). Mosaicking of global planetary image datasets: 1. Techniques and data processing for thermal emission imaging system (THEMIS) multi-spectral data. Journal of Geophysical Research,116(E10), E10008. https://doi.org/10.1029/2010JE003755

Elsworth, D., & Voight, B. (1996). Evaluation of volcano flank instability triggered by dyke intrusion. Geological Society, London, Special Publications, 110(1), 45–53. https://doi.org/10.1144/GSL.SP.1996.110.01.03

Fiske, R. S., & Jackson, E. D. (1972). Orientation and growth of Hawaiian volcanic rifts: The effect of regionalstructure and gravitational stresses. Proceedings of the Royal Society of London. A. Mathematical and Physical Sciences, 329, 299–326. https://doi.org/10.1098/rspa.1972.0115

Ford, J. P. (1993). Guide to Magellan image interpretation. National Aeronautics and Space Administration, Jet Propulsion Laboratory.

Ford, P. G. (1992). MGN V RDRS 5 global data record topographic V1.0 [Dataset]. NASA Planetary Data System. https://doi.org/10.17189/1522522

Fornari, D. J., Garcia, M. O., Tyce, R. C., & Gallo, D. G. (1988). Morphology and structure of Loihi seamount based on seabeam sonar mapping. Journal of Geophysical Research, 93(B12), 15227–15238. https://doi.org/10.1029/JB093iB12p15227

Francis, P. W., Gardeweg, M., Ramirez, C. F., & Rothery, D. A. (1985). Catastrophic debris avalanche deposit of Socompa volcano, northern Chile. Geology, 13(9), 600–603. https://doi.org/10.1130/0091-7613(1985)13<600:CDADOS>2.0.CO;2

Francis, P. W., & Self, S. (1987). Collapsing volcanoes. Scientific American, 256(6), 90–99. https://doi.org/10.1038/scientificamerican0687-90

Francis, P. W., & Wells, G. L. (1988). Landsat thematic mapper observations of debris avalanche deposits in the central Andes. Bulletin of Volcanology, 50(4), 258–278. https://doi.org/10.1007/BF01047488

Galgana, G. A., Grosfils, E. B., & McGovern, P. J. (2013). Radial dike formation on Venus: Insights from models of uplift, flexure and magmatism. Icarus, 225(1), 538–547. https://doi.org/10.1016/j.icarus.2013.04.020

Ghail, R. C. (2015). Rheological and petrological implications for a stagnant lid regime on Venus. Planetary and Space Science, 113, 2–9. https:// doi.org/10.1016/j.pss.2015.02.005

Ghail, R. C., Hall, D., Mason, P. J., Herrick, R. R., Carter, L. M., & Williams, E. (2018). VenSAR on EnVision: Taking earth observation radar to Venus. International Journal of Applied Earth Observation and Geoinformation, 64, 365–376. https://doi.org/10.1016/j.jag.2017.02.008

Ghail, R. C., & Wilson, L. (2015). A pyroclastic flow deposit on Venus. Geological Society, London, Special Publications, 401(1), 97–106. https://doi.org/10.1144/SP401.1

Ghent, R., & Hansen, V. (1999). Structural and kinematic analysis of eastern Ovda Regio, Venus: Implications for crustal plateau formation. Icarus, 139(1), 116–136. https://doi.org/10.1006/icar.1999.6085

Gilmore, M. S., Darby Dyar, M., Mueller, N., Brossier, J., Santos, A. R., Ivanov, M., et al. (2023). Mineralogy of the Venussurface. Space Science Reviews, 219(7), 52. https://doi.org/10.1007/s11214-023-00988-6

Grosfils, E. B., Aubele, J., Crumpler, L., Gregg, T. K., & Sakimoto, S. (2000). Volcanism on Earth's seafloor and Venus. In J. R. Zimbleman & T. K. Gregg (Eds.), Environmental effects on volcanic eruptions: From deep oceans to deep space (pp. 113–142). Springer US.

Grosfils, E. B., & Head, J. W., III. (1995). Radiating dike swarms on Venus: Evidence for emplacement at zones of neutral buoyancy. Planetary and Space Science, 43(12), 1555–1560. https://doi.org/10.1016/0032-0633(95)00084-4

Guest, J. E., Beratan, K., Head, J. W., Bulmer, M. H., Weitz, C., Greeley, R., et al. (1992). Small volcanic edifices and volcanism in the plains of Venus. Journal of Geophysical Research, 97(E10), 15949–15966. https://doi.org/10.1029/92JE01438

Guest, J. E., & Stofan, E. R. (1999). A new view of the stratigraphic history of Venus. Icarus, 139(1), 55–66. https://doi.org/10.1006/icar.1999.6091

Gülcher, A. J., Gerya, T. V., Montési, L. G., & Munch, J. (2020). Corona structures driven by plume–lithosphere interactions and evidence for ongoing plume activity on Venus. Nature Geoscience, 13(8), 547–554. https://doi.org/10.1038/s41561-020-0606-1

Hahn, R. M., & Byrne, P. K. (2023a). A global catalog of deformed volcanoes Venus. (Version 1) [Dataset]. Washington University in St. Louis. https://doi.org/10.7936/6rxs-103646

Hahn, R. M., & Byrne, P. K. (2023b). A morphological and spatial analysis of volcanoes on Venus. Journal of Geophysical Research: Planets, 128(4), e2023JE007753. https://doi.org/10.1029/2023JE007753

Head, J. W. (1996). Volcano instability development: A planetary perspective. Geological Society, London, Special Publications, 110(1), 25–43. https://doi.org/10.1144/gsl.sp.1996.110.01.02

Head, J. W., Crumpler, L. S., Aubele, J. C., Guest, J. E., & Saunders, R. S. (1992). Venus volcanism: Classification of volcanic features and structures, associations, and global distribution from Magellan data. Journal of Geophysical Research, 97(E8), 13153–13197. https://doi.org/10.1029/92JE01273

Head, J. W., & Wilson, L. (1986). Volcanic processes and landforms on Venus: Theory, predictions, and observations. Journal of Geophysical Research, 91(B9), 9407–9446. https://doi.org/10.1029/JB091iB09p09407

Head, J. W., & Wilson, L. (1992). Magma reservoirs and neutral buoyancy zones on Venus: Implications for the formation and evolution of volcanic landforms. Journal of Geophysical Research, 97(E3), 3877–3903. https://doi.org/10.1029/92JE00053

Holohan, E. P., Poppe, S., Delcamp, A., Byrne, P. K., Walter, T. R., de Vries, B. V. W., & Kervyn, M. (2023). Transition from volcano-sagging to volcano-spreading. Earth and Planetary Science Letters, 604, 118012. https://doi.org/10.1016/j.epsl.2023.118012

Ivanov, M. A., & Head, J. W. (2011). Global geological map of Venus. Planetary and Space Science, 59(13), 1559–1600. https://doi.org/10.1016/j.pss.2011.07.008

Ivanov, M. A., & Head, J. W. (2015). The history of tectonism on Venus: A stratigraphic analysis. Planetary and Space Science, 113, 10–32. https://doi.org/10.1016/j.pss.2015.03.016

Ivanov, M. A., & Head, J. W., III. (1999). Stratigraphic and geographic distribution of steep-sided domes on Venus: Preliminary results from regional geological mapping and implications for their origin. Journal of Geophysical Research, 104(E8), 18907–18924. https://doi.org/10.1029/1999JE001039

James, P. B., Zuber, M. T., & Phillips, R. J. (2013). Crustal thickness and support of topography on Venus. Journal of Geophysical Research: Planets, 118(4), 859–875. https://doi.org/10.1029/2012JE004237

Kear, D. (1964). Volcanic alignments north and west of New Zealand's central volcanic region. New Zealand Journal of Geology and Geophysics, 7(1), 24–44. https://doi.org/10.1080/00288306.1964.10420155

Keddie, S. T., & Head, J. W. (1995). Formation and evolution of volcanic edifices on the Dione Regio rise, Venus. Journal of Geophysical Research, 100(E6), 11729–11754. https://doi.org/10.1029/95JE00822

Kervyn, M., Boone, M. N., de Vries, B. V. W., Lebas, E., Cnudde, V., Fontijn, K., & Jacobs, P. (2010). 3D imaging of volcano gravitational deformation by computerized X-ray micro-tomography. Geosphere, 6(5), 482–498. https://doi.org/10.1130/GES00564.1

Kiefer, W. S., & Hager, B. H. (1989). The role of mantle convection in the origin of the Tharsis and Elysium provinces of Mars. In MEVTV workshop on early tectonic and volcanic evolution of Mars (pp. 48–50).

Konopliv, A. S., Banerdt, W. B., & Sjogren, W. L. (1999). Venus gravity: 180th degree and order model. Icarus, 139(1), 3–18. https://doi.org/10.1006/icar.1999.6086

Krassilnikov, A. S., & Head, J. W. (2003). Novae on Venus: Geology, classification, and evolution. Journal of Geophysical Research, 108(E9), 5108. https://doi.org/10.1029/2002JE001983

Le Corvec, N., Spörli, K. B., Rowland, J., & Lindsay, J. (2013). Spatial distribution and alignments of volcanic centers: Clues to the formation of monogenetic volcanic fields. Earth-Science Reviews, 124, 96–114. https://doi.org/10.1016/j.earscirev.2013.05.005

López, I. (2011). Embayed intermediate volcanoes on Venus: Implications for the evolution of the volcanic plains. Icarus, 213(1), 73–85. https://doi.org/10.1016/j.icarus.2011.02.022

López, I., Lillo, J., & Hansen, V. L. (2008). Regional fracture patterns around volcanoes: Possible evidence for volcanic spreading on Venus. Icarus, 195(2), 523–536. https://doi.org/10.1016/j.icarus.2007.12.026

Madonia, P., Cangemi, M., Olivares, L., Oliveri, Y., Speziale, S., & Tommasi, P. (2019). Shallow landslide generation at La Fossa cone, Vulcano Island (Italy): A multidisciplinary perspective. Landslides, 16(5), 921–935. https://doi.org/10.1007/s10346-019-01149-z

Márquez, A., López, I., Herrera, R., Martín-González, F., Izquierdo, T., & Carreno, F. (2008). Spreading and potential instability of Teide volcano, Tenerife, Canary Islands. Geophysical Research Letters, 35(5), 36. https://doi.org/10.1029/2007GL032625

Martínez-Moreno, F. J., Santos, F. M., Madeira, J., Pous, J., Bernardo, I., Soares, A., et al. (2018). Investigating collapse structures in oceanic islands using magnetotelluric surveys: The case of Fogo Island in Cape Verde. Journal of Volcanology and Geothermal Research, 357,152–162. https://doi.org/10.1016/j.jvolgeores.2018.04.028

McClain, C. R., & Lundsten, L. (2015). Assemblage structure is related to slope and depth on a deep offshore Pacific seamount chain. Marine Ecology, 36(2), 210–220. https://doi.org/10.1111/maec.12136

McGovern, P. J., Grosfils, E. B., Galgana, G. A., Morgan, J. K., Rumpf, M. E., Smith, J. R., & Zimbelman, J. R. (2015). Lithospheric flexure and volcano basal boundary conditions: Keys to the structural evolution of large volcanic edifices on the terrestrial planets.

Geological Society, London, Special Publications, 401(1), 219–237. https://doi.org/10.1144/SP401.7

McGovern, P. J., & Morgan, J. K. (2009). Volcanic spreading and lateral variations in the structure of Olympus Mons, Mars. Geology, 37(2), 139–142.1. https://doi.org/10.1130/G25180A.1

McGovern, P. J., & Solomon, S. C. (1993). Patterns of deformation and volcanic flows associated with lithospheric loading by large volcanoes on Venus. In Tectonic history of the terrestrial planets.

McGovern, P. J., & Solomon, S. C. (1997). Filling of flexural moats around large volcanoes on Venus: Implications for volcano structure and global magmatic flux. Journal of Geophysical Research, 102(E7), 16303–16318. https://doi.org/10.1029/97JE01318

McGovern, P. J., & Solomon, S. C. (1998). Growth of large volcanoes on Venus: Mechanical models and implications for structural evolution. Journal of Geophysical Research, 103(E5), 11071–11101. https://doi.org/10.1029/98JE01046

McGovern, P. J., Solomon, S. C., Head, J. W., III, Smith, D. E., Zuber, M. T., & Neumann, G. A. (2001). Extension and uplift at Alba Patera, Mars: Insights from MOLA observations and loading models. Journal of Geophysical Research, 106(E10), 23769–23809. https://doi.org/10.1029/2000JE001314

McGovern, P. J., Solomon, S. C., Smith, D. E., Zuber, M. T., Simons, M., Wieczorek, M. A., et al. (2004). Correction to "Localized gravity/ topography admittance and correlation spectra on Mars: Implications for regional and global evolution". Journal of Geophysical Research,109(E7), 19-1. https://doi.org/10.1029/2002JE001854

McGuire, W. J. (1996). Volcano instability: A review of contemporary themes. Geological Society, London, Special Publications, 110, 1–23. https://doi.org/10.1144/GSL.SP.1996.110.01.01

McGuire, W. J. (2003). Volcano instability and lateral collapse. Revista, 1, 33–45.

McKenzie, D., Barnett, D. N., & Yuan, D. N. (2002). The relationship between Martian gravity and topography. Earth and Planetary Science Letters, 195(1–2), 1–16. https://doi.org/10.1016/S0012-821X(01)00555-6

Mège, D., & Masson, P. (1996). A plume tectonics model for the Tharsis province, Mars. Planetary and Space Science, 44(12), 1499–1546. https://doi.org/10.1016/S0032-0633(96)00113-4

Mitchell, N. C. (2001). Transition from circular to stellate forms of submarine volcanoes. Journal of Geophysical Research, 106(B2), 1987–2003. https://doi.org/10.1029/2000JB900263

Morris, E. C. (1982). Aureole deposits of the Martian volcano Olympus Mons. Journal of Geophysical Research, 87(B2), 1164–1178. https://doi.org/10.1029/JB087iB02p01164

Murray, J., van Wyk de Vries, B., Marquez, A., Williams, D., Byrne, P., Muller, J.-P., & Kim, J.-R. (2010). Late-stage water eruptions from Ascraeus Mons volcano, Mars: Implications

for its structure and history. Earth and Planetary Science Letters, 294(3–4), 479–491. https://doi.org/10.1016/j.epsl.2009.06.020

Nakamura, K. (1977). Volcanoes as possible indicators of tectonic stress orientation—Principle and proposal. Journal of Volcanology and Geothermal Research, 2, 1–16. https://doi.org/10.1016/0377-0273(77)90012-9

Oakley, A. J., Taylor, B., Fryer, P., Moore, G. F., Goodliffe, A. M., & Morgan, J. K. (2007). Emplacement, growth, and gravitational deformation of serpentinite seamounts on the Mariana forearc. Geophysical Journal International, 170(2), 615–634. https://doi.org/10.1111/j.1365-246X.2007.03451.x

Parfitt, E. A., Wilson, L., & Head, J. W., III. (1993). Basaltic magma reservoirs: Factors controlling their rupture characteristics and evolution. Journal of Volcanology and Geothermal Research, 55(1–2), 1–14. https://doi.org/10.1016/0377-0273(93)90086-7

Pavri, B., Head, J. W., III, Klose, K. B., & Wilson, L. (1992). Steep-sided domes on Venus: Characteristics, geologic setting, and eruption conditions from Magellan data. Journal of Geophysical Research, 97(E8), 13445–13478. https://doi.org/10.1029/92JE01162

Pettengill, G. (1991). MGN V RDRS derived mosaic image data record full res V1.0. [Dataset]. NASA Planetary Data System. https://doi.org/10.17189/1522523

Platz, T., & Michael, G. (2011). Eruption history of the Elysium volcanic province, Mars. Earth and Planetary Science Letters, 312(1–2), 140–151. https://doi.org/10.1016/j.epsl.2011.10.001

Plesa, A. C., Padovan, S., Tosi, N., Breuer, D., Grott, M., Wieczorek, M. A., et al. (2018). The thermal state and interior structure of Mars. Geophysical Research Letters, 45(22), 12–198. https://doi.org/10.1029/2018GL080728

Plescia, J. B. (2003). Tharsis Tholus: An unusual Martian volcano. Icarus, 165(2), 223–241. https://doi.org/10.1016/S0019-1035(03)00199-4

Plescia, J. B. (2004). Morphometric properties of Martian volcanoes. Journal of Geophysical Research, 109(E3), E03003. https://doi.org/10.1029/2002JE002031

Quartau, R., Trenhaile, A. S., Mitchell, N. C., & Tempera, F. (2010). Development of volcanic insular shelves: Insights from observations and modelling of Faial Island in the Azores Archipelago. Marine Geology, 275(1–4), 66–83. https://doi.org/10.1016/j.margeo.2010.04.008

Quick, L. C., Glaze, L. S., Baloga, S. M., & Stofan, E. R. (2016). New approaches to inferences for steep-sided domes on Venus. Journal of Volcanology and Geothermal Research, 319, 93–105. https://doi.org/10.1016/j.jvolgeores.2016.02.028

Ramirez, C. F. (1988). The geology of Socompa volcano and its debris avalanche deposit, northern Chile (Doctoral dissertation). The Open University.

Richards, J. P., & Villeneuve, M. (2001). The Llullaillaco volcano, northwest Argentina: Construction by Pleistocene volcanism and destruction by sector collapse. Journal of

Volcanology and Geothermal Research, 105(1–2), 77–105. https://doi.org/10.1016/S0377-0273(00)00245-6

Roberts, J. H., & Zhong, S. (2004). Plume-induced topography and geoid anomalies and their implications for the Tharsis rise on Mars. Journal of Geophysical Research, 109(E3), E01009. https://doi.org/10.1029/2003JE002226

Roberts, J. H., & Zhong, S. (2006). Degree-1 convection in the Martian mantle and the origin of the hemispheric dichotomy. Journal of Geophysical Research, 111(E6), E06013. https://doi.org/10.1029/2005JE002668

Rogers, P. G., & Zuber, M. T. (1998). Tectonic evolution of Bell Regio, Venus: Regional stress, lithospheric flexure, and edifice stresses. Journal of Geophysical Research, 103(E7), 16841–16853. https://doi.org/10.1029/98JE00585

Romero, J. E., Polacci, M., Watt, S., Kitamura, S., Tormey, D., Sielfeld, G., et al. (2021). Volcanic lateral collapse processes in mafic arc edifices: A review of their driving processes, types and consequences. Frontiers in Earth Science, 9, 639825. https://doi.org/10.3389/feart.2021.639825

Ryan, M. P., Koyanagi, R. Y., & Fiske, R. S. (1981). Modeling the three-dimensional structure of macroscopic magma transport systems: Application to Kilauea Volcano, Hawaii. Journal of Geophysical Research, 86(B8), 7111–7129. https://doi.org/10.1029/JB086iB08p07111

Ryan, W. B., Carbotte, S. M., Coplan, J. O., O'Hara, S., Melkonian, A., Arko, R., et al. (2009). Global multi-resolution topography synthesis. Geochemistry, Geophysics, Geosystems, 10(3), Q03014. https://doi.org/10.1029/2008GC002332

Scheirer, D. S., & Macdonald, K. C. (1995). Near-axis seamounts on the flanks of the East Pacific rise, 8°N to 17°N. Journal of Geophysical Research, 100(B2), 2239–2259. https://doi.org/10.1029/94JB02769

Scheirer, D. S., Macdonald, K. C., Forsyth, D. W., & Shen, Y. (1996). Abundantseamounts of the Rano Rahiseamount field near the southern East Pacific rise, 15S to 19S. Marine Geophysical Researches, 18(1), 13–52. https://doi.org/10.1007/BF00286202

Schmidt, R., & Schmincke, H. U. (2002). From seamount to oceanic island, Porto Santo, central East-Atlantic. International Journal of Earth Sciences, 91(4), 594–614. https://doi.org/10.1007/s00531-001-0243-x

Siebert, L. (1984). Large volcanic debris avalanches: Characteristics of source areas, deposits, and associated eruptions. Journal of Volcanology and Geothermal Research, 22(3–4), 163–197. https://doi.org/10.1016/0377-0273(84)90002-7

Simkin, T. (1973). Origin of some flat-topped volcanoes and guyots. In R. Shagam, R. B. Hargraves, W. J. Morgan, F. B. Van Houton, C. A. Burk, H. D. Holland, et al. (Eds.), Studies in Earth and space sciences (pp. 193–194). Geological Society of America Memoir.

Smith, D. K. (1996). Comparison of the shapes and sizes of seafloor volcanoes on Earth and "pancake" domes on Venus. Journal of Volcanology and Geothermal Research, 73(1–2), 47–64. https://doi.org/10.1016/0377-0273(96)00007-8

Smrekar, S., Hensley, S., Nybakken, R., Wallace, M. S., Perkovic-Martin, D., You, T. H., et al. (2022). VERITAS (Venus emissivity, radio science, InSAR, topography, and spectroscopy): A discovery mission. In 2022 IEEE Aerospace Conference (AERO) (pp. 1–20). IEEE. https://doi.org/10.1109/AERO53065.2022.9843269

Smrekar, S. E. (1994). Evidence for active hotspots on Venus from analysis of Magellan gravity data. Icarus, 112(1), 2–26. https://doi.org/10.1006/icar.1994.1166

Solomon, S. C., & Head, J. W. (1990). Tepev Mons and the elastic lithosphere of Venus: An assessment of flexure models. In Abstracts of the lunar and planetary science conference (Vol. 21).

Solomon, S. C., Smrekar, S. E., Bindschadler, D. L., Grimm, R. E., Kaula, W. M., McGill, G. E., et al. (1992). Venus tectonics: An overview of Magellan observations. Journal of Geophysical Research, 97(E8), 13199–13255. https://doi.org/10.1029/92JE01418

Spohn, T., Acuña, M. H., Breuer, D., Golombek, M., Greeley, R., Halliday, A., & Sohl, F. (2001). Geophysical constraints on the evolution of Mars. In Chronology and evolution of Mars: Proceedings of an ISSI workshop, 10–14 April 2000, Bern, Switzerland (pp. 231–262). Springer Netherlands.

Staudigel, H., & Koppers, A. A. (2015). Seamounts and island building. In The encyclopedia of volcanoes (pp. 405–421). Academic Press.

Stofan, E. R., Anderson, S. W., Crown, D. A., & Plaut, J. J. (2000). Emplacement and composition of steep-sided domes on Venus. Journal of Geophysical Research, 105(E11), 26757–26771. https://doi.org/10.1029/1999JE001206

Stofan, E. R., & Head, J. W. (1990). Coronae of Mnemosyne Regio: Morphology and origin. Icarus, 83(1), 216–243. https://doi.org/10.1016/0019-1035(90)90016-3

Stofan, E. R., Sharpton, V. L., Schubert, G., Baer, G., Bindschadler, D. L., Janes, D. M., & Squyres, S. W. (1992). Global distribution and characteristics of coronae and related features on Venus: Implications for origin and relation to mantle processes. Journal of GeophysicalResearch, 97(E8), 13347–13378. https://doi.org/10.1029/92JE01314

Thomas, P. J., Squyres, S. W., & Carr, M. H. (1990). Flank tectonics of Martian volcanoes. Journal of Geophysical Research, 95(B9), 14345–14355. https://doi.org/10.1029/JB095iB09p14345

Tibaldi, A. (1995). Morphology of pyroclastic cones and tectonics. Journal of Geophysical Research, 100(B12), 24521–24535. https://doi.org/10.1029/95JB02250

Tibaldi, A. (2001). Multiple sector collapses at Stromboli volcano, Italy: How they work. Bulletin of Volcanology, 63(2–3), 112–125. https://doi.org/10.1007/s004450100129

Tibaldi, A., Bistacchi, A., Pasquare, F. A., & Vezzoli, L. (2006). Extensional tectonics and volcano lateral collapses: Insights from Ollagüe Volcano (Chile-Bolivia) and analogue modelling. Terra Nova, 18(4), 282–289. https://doi.org/10.1111/j.1365-3121.2006.00691.x

Tibaldi, A., Corazzato, C., Kozhurin, A., Lagmay, A. F., Pasquarè, F. A., Ponomareva, V. V., et al. (2008). Influence of substrate tectonic heritage on the evolution of composite volcanoes: Predicting sites of flank eruption, lateral collapse, and erosion. Global and Planetary Change, 61(3–4), 151–174. https://doi.org/10.1016/j.gloplacha.2007.08.014

Tibaldi, A., Corazzato, C., Marani, M., & Gamberi, F. (2009). Subaerial-submarine evidence of structures feeding magma to Stromboli Volcano, Italy, and relations with edifice flank failure and creep. Tectonophysics, 469(1–4), 112–136. https://doi.org/10.1016/j.tecto.2009.01.031

Treiman, A. H. (2007). Geochemistry of Venus' surface: Current limitations as future opportunities. In L. W. Esposito, E. R. Stofan, & T. E. Cravens (Eds.), Exploring Venus as a terrestrial planet. https://doi.org/10.1029/176GM03

van Wyk de Vries, B., & Borgia, A. (1996). The role of basement in volcano deformation. Geological Society, London, Special Publications,110(1), 95–110. https://doi.org/10.1144/GSL.SP.1996.110.01.07

van Wyk de Vries, B., & Davies, T. (2015). Landslides, debris avalanches, and volcanic gravitational deformation. In H. Sigurdsson (Ed.), The encyclopedia of volcanoes (pp. 665–685). Academic Press. https://doi.org/10.1016/C2015-0-00175-7

van Wyk de Vries, B., & Francis, P. W. (1997). Catastrophic collapse at stratovolcanoes induced by gradual volcano spreading. Nature, 6631,387–390. https://doi.org/10.1038/387387a0

van Wyk de Vries, B., Kerle, N., & Petley, D. (2000). Sector collapse forming at Casita volcano, Nicaragua. Geology, 28(2), 167–170. https://doi.org/10.1130/0091-7613(2000)28<167:SCFACV>2.0.CO;2

van Wyk de Vries, B., & Matela, R. (1998). Styles of volcano-induced deformation: Numerical models of substratum flexure, spreading and extrusion. Journal of Volcanology and Geothermal Research, 81(1–2), 1–18. https://doi.org/10.1016/S0377-0273(97)00076-0

van Wyk de Vries, B., Self, S., Francis, P. W., & Keszthelyi, L. (2001). A gravitationalspreading origin for the Socompa debris avalanche. Journal of Volcanology and Geothermal Research, 105(3), 225–247. https://doi.org/10.1016/S0377-0273(00)00252-3

Vogt, P. R., & Smoot, N. C. (1984). The Geisha Guyots: Multibeam bathymetry and morphometric interpretation. Journal of Geophysical Research, 89(B13), 11085–11107. https://doi.org/10.1029/JB089iB13p11085

Voight, B., & Elsworth, D. (1997). Failure of volcano slopes. Géotechnique, 47, 1–31. https://doi.org/10.1680/geot.1997.47.1.1

Wadge, G., Francis, P. W., & Ramirez, C. F. (1995). The Socompa collapse and avalanche event. Journal of Volcanology and Geothermal Research, 66(1–4), 309–336. https://doi.org/10.1016/0377-0273(94)00083-S

Walker, G. P. (1989). Gravitational (density) controls on volcanism, magma chambers and intrusions. Australian Journal of Earth Sciences, 36(2), 149–165. https://doi.org/10.1080/08120098908729479

Watanabe, K., Ono, K., Sakaguchi, K., Takada, A., & Hoshizumi, H. (1999). Co-ignimbrite ash-fall deposits of the 1991 eruptions of Fugen-dake, Unzen Volcano, Japan. Journal of Volcanology and Geothermal Research, 89(1–4), 95–112. https://doi.org/10.1016/S0377-0273(98)00126-7

Wessel, P. (2007). Seamount characteristics. In T. J. Pitcher, T. Morato, P. J. B. Hart, M. R. Clark, N. Haggan, & R. S. Santos (Eds.), Seamounts: Ecology, fisheries & conservation (pp. 1–25). Blackwell Publishing.

Wooller, L., de Vries, B. V. W., Murray, J. B., Rymer, H., & Meyer, S. (2004). Volcano spreading controlled by dipping substrata. Geology, 32(7), 573–576. https://doi.org/10.1130/G20472.1

Wright, I. C., Chadwick, W. W., Jr., de Ronde, C. E., Reymond, D., Hyvernaud, O., Gennerich, H. H., et al. (2008). Collapse and reconstruction of Monowai submarine volcano, Kermadec arc, 1998–2004. Journal of Geophysical Research, 113(B8), 63. https://doi.org/10.1029/2007JB005138

Wyrick, D., Ferrill, D. A., Morris, A. P., Colton, S. L., & Sims, D. W. (2004). Distribution, morphology, and origins of Martian pit crater chains. Journal of Geophysical Research, 109(E6), 195. https://doi.org/10.1029/2004JE002240

Zimbelman, J. R., & Edgett, K. S. (1992). The Tharsis Montes, Mars: Comparison of volcanic and modified landforms. In Proceedings of lunar and planetary science (Vol. 22). Lunar and Planetary Institute.

Chapter 4:
Kernel Density Analysis for Predicting the Locations of Future Volcano Formation on Venus

Abstract

The surface of Venus appears to be geologically young and until recently it was unknown whether or not the planet was geologically active. Following the recent discovery of ongoing volcanic activity on Venus, efforts have been made to locate other regions across the planet that might also be geologically active. In this study, we use kernel density analysis as a method for predicting the possible locations of future volcano formation across nine Venusian topographic rises, and nine volcanic fields based on the distribution of past volcanoes. Additionally, we enhance the resulting volcano-formation probability maps with geological information related to the locations of recent volcanism from thermal and radar emissivity studies, edifice alignments, and areas with high spatial density of volcanoes. We note that Atla, Imdr, Dione, and Themis Regiones have high emissivity values consistent with recent volcanism, and six of the nine topographic rises have high-volcano-spatial-density regions where there are approximately ten volcanoes per square kilometer. Furthermore, we note that all 18 study regions have at least one dominant orientation of volcanoes and 17 study regions have high-volcano-spatial-density regions co-located with dominant vent alignments. These regions may indicate areas of magma generation and/or preferred magma pathways to the surface. Volcano formation probability maps developed

in this study can be used to identify regions that are statistically likely to host new edifice formation across Venus, and can be verified by future missions.

4.1 Introduction

The recent discovery of active volcanism on Venus (Herrick and Hensley, 2023) has fueled the search for additional evidence for such activity, with a particular emphasis on regions predicted to correspond to mantle upwellings based on geological and geophysical data (Smrekar, 1994; Stofan et al., 1995). Kernel density estimation (KDE) is a non-parametric density estimation tool (Silverman 1986) that has been extensively used on Earth as a method for predicting the probable location of future volcanic events based on observations of past such events (Connor & Connor, 2009; Germa et al., 2013; Bevilacqua et al., 2015; Bartolini et al., 2015; Galindo et al., 2016; Mazzarini et al., 2016; Tadini et al., 2017). The output of KDE is an areal density map that highlights regions with an increased probability of future vent formation given the spatial distribution of existing volcanic constructs (Conner et al., 2018). Here, a "vent" may refer to a discrete edifice with positive topography, or a volcanic fissure from which magma erupts. These volcano spatial density maps, often called vent opening probability maps, volcano formation probability maps, or susceptibility maps, may also incorporate additional geophysical and structural information such as gravity anomalies, maps of eruptive fissures, dikes, and faults, etc. (Conner et al., 2000; Cappello et al., 2012; Bartolini et al., 2013; Galindo et al., 2016) to make more robust predictions.

On Earth, vent opening probability maps are typically developed to forecast and mitigate potential hazards such as effusive lava flows or pyroclastic density currents (Connor and Connor, 2009; Bartolini et al., 2013; Bertin et al., 2019). For example, Cappello et al. (2012) utilized KDE

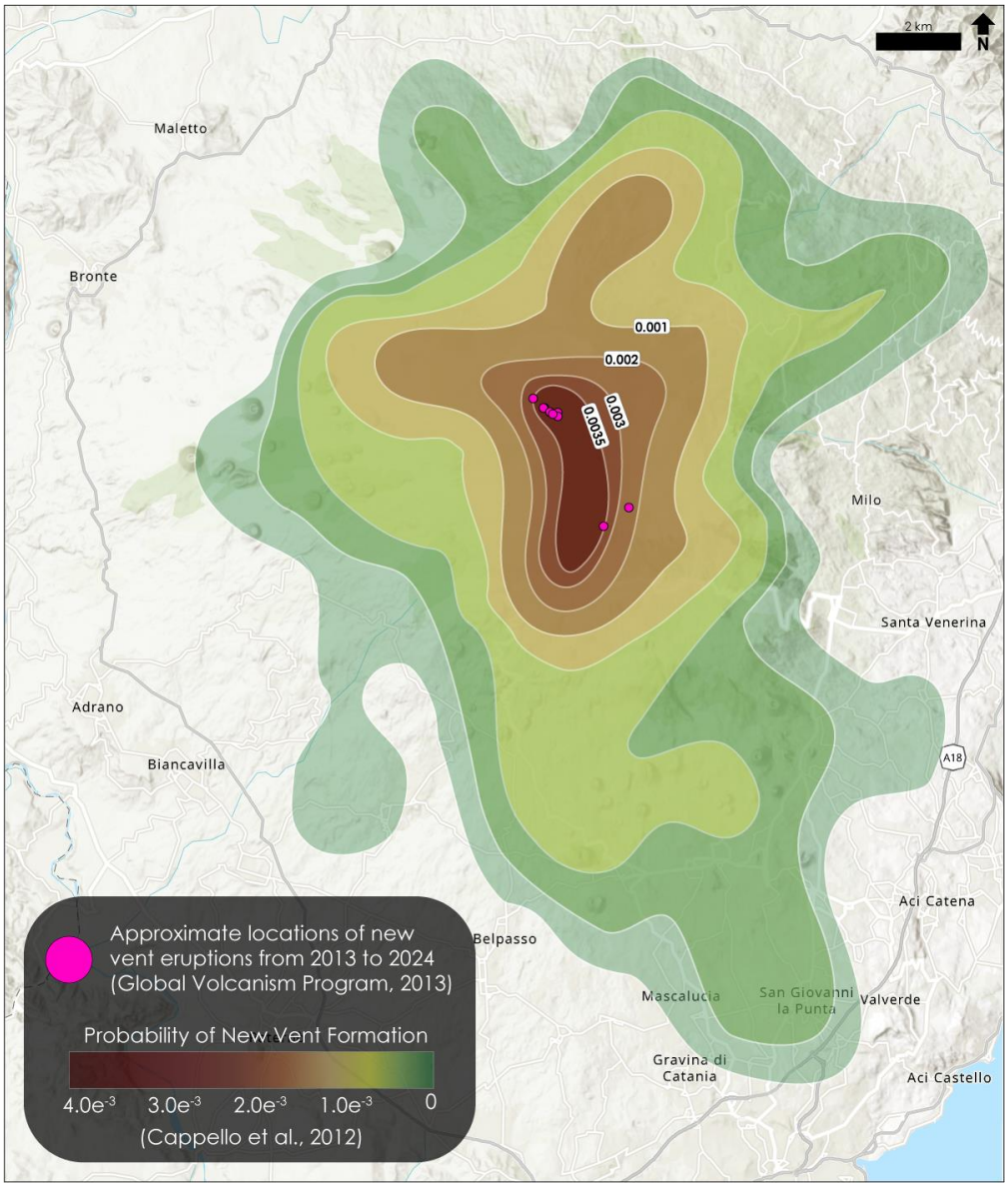

Figure 4.1: Vent opening probability map for Mount Etna, Italy. Approximate locations of new vent fissures that formed from 2013 to 2024 are shown as pink circles. Map is adapted from Cappello et al. (2012). Basemap is ESRI World Topographic Map and Hillshade.

paired with statistical analysis of structural features linked to flank eruptions, such as fissures, dikes, and faults, from the last 2,000 years to develop a vent opening probability map at Mount Etna, a basaltic volcano on the Ionian coast of Sicily, Italy. The resulting vent opening probability map identified a N–S aligned region that passes through the central summit craters of Etna as the highest likelihood area for future vent formation (Cappello et al., 2012) (**Figure 4.1**). Since 2013,

the Smithsonian Institution's Global Volcanism Program (GVP) database (Global Volcanism Program, 2013) has documented the formation of ten new vent fissures at Mount Etna. Of these newly formed vents, 80% (8/10) are within the highest probability regions for new vent formation developed for Mount Etna by Cappello et al. (2012), and the remaining 20% (2/10) of vents are just outside this region, but well within the bounds of prediction for a future event (**Figure 4.1**). Indeed, the kernel density and statistical analysis developed by Cappello et al. (2012) accurately forecasted the locations of new vent eruptions at Mount Etna over the last decade, validating this approach for delineating the most likely regions to search for future volcanic constructs.

In our study, we use KDE to identify regions on Venus that are most likely to host new eruptive, cone-building activity on the basis of the locations of existing constructs from our global catalog of volcanoes on Venus (Hahn and Byrne, 2023). Our database contains the locations of over 85,000 edifices across the planet, and includes detailed morphological data for volcanoes >5 km in diameter (Hahn and Byrne, 2023). Here, we exclusively consider volcanoes and not fissures because our global catalog only documents instances of discrete edifices with positive topography, and does not include the delineation of any possible fissures. Specifically, we focus on volcanoes ≤20 km in diameter that are associated with nine topographic rises, and nine volcanic fields from our global catalog (Hahn and Byrne, 2023).

The KDE technique is only suitable for developing vent opening probability maps associated with volcanoes that have a single eruptive episode (i.e., monogenetic) (e.g., Germa et al., 2013; Bartolini et al., 2015; Bebbington, 2015; Mazzarini et al., 2016; Schmidt et al., 2022), or with vents (e.g., parasitic cones or vent fissures) forming on the flanks of a larger volcano (e.g., Mount Fuji, Japan) (Cappello et al., 2012; Zuccarello et al., 2023). Importantly, the KDE method cannot be used to predict when a polygenetic volcano, typically a large edifice that has experienced

a history of several eruptive episodes from a single eruptive vent (e.g., Volcán de Colima, Mexico) (de Silva and Lindsay, 2015), will erupt again.

The application of KDE assumes that the past pattern of volcano formation is controlled by the same tectonic and/or magmatic mechanisms that govern future cone-building events (Connor et al., 2018). Here, we also search for preferred orientations of volcanoes at each study site by conducting volcano-alignment analyses. The spatial arrangement of volcanoes provides information on the local stress field at the time of eruption, and may even offer insight into the presence and scale of eruptive fissures and/or lithospheric-scale fracture systems, information that can in turn be incorporated into subsequent eruptive probability maps (Galindo et al., 2016).

The goal of this study is to develop a series of volcano formation probability maps at candidate hotspot regions (e.g., Alpha and Beta Regiones (Smrekar, 1994)) and volcanic fields across Venus to facilitate the identification of areas that are statistically likely to see new edifices form. These maps can be used to inform plans by future missions to Venus such as NASA's VERITAS (Smrekar et al., 2022) and ESA's EnVision (Ghail et al., 2018) to search for new volcanic eruptive events on Venus.

4.1.1 Study Sites

Two distinct styles of volcanic center may be present on Venus: those linked to a productive shallow magma reservoir fed from a deeper seated mantle source (e.g., large volcanoes and coronae at topographic rises), and those forming from melt sources with supply rates too low to support the formation of shallow magma reservoirs (e, g., volcanic fields) (Head et al., 1992; Crumpler et al., 1997). By analyzing edifices associated with both topographic rises and volcanic fields, we are including all end-member styles of volcanism within our predictive analysis.

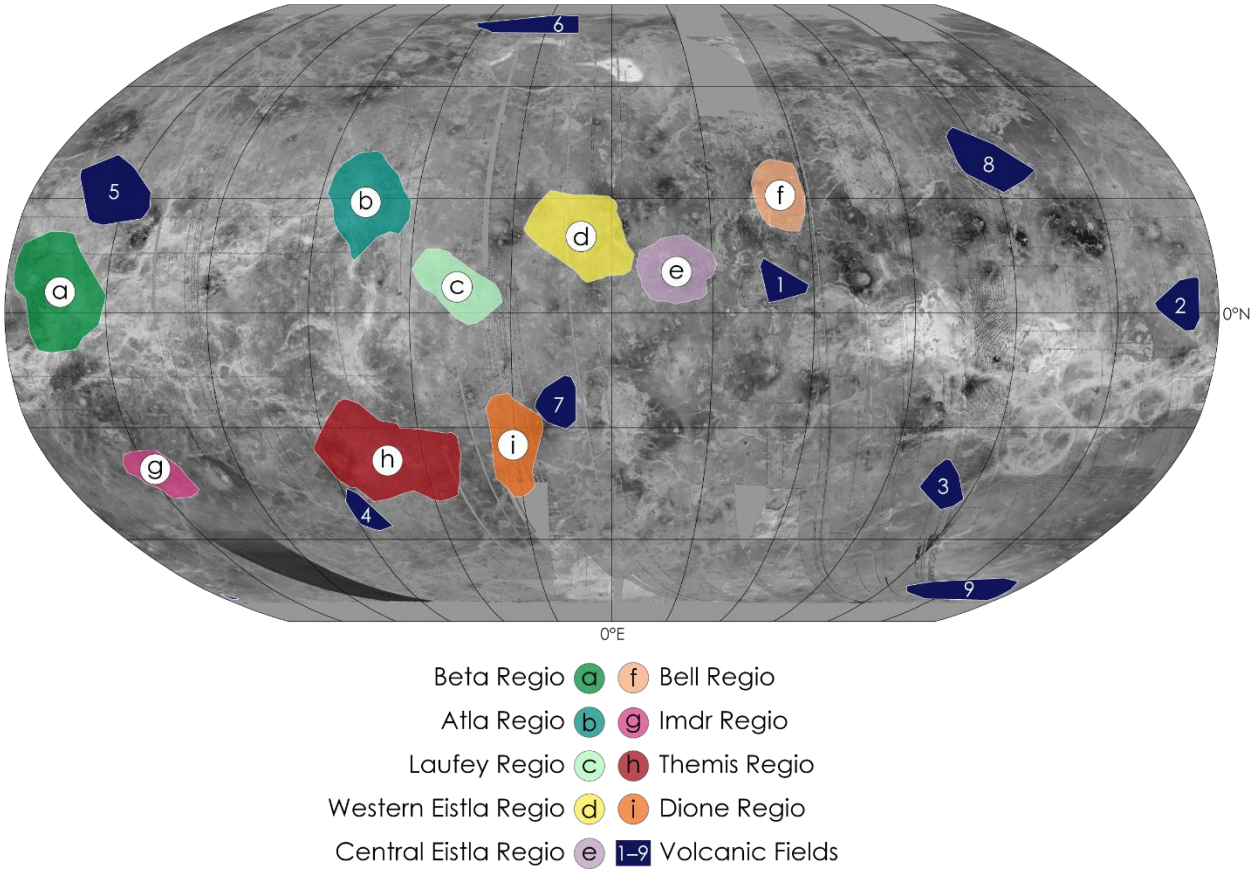

Figure 4.2: Global map detailing the polygon boundaries developed for each of the nine topographic rises and nine volcanic fields in this analysis. Basemap is Magellan FMAP left- and right-look global mosaics. The map is in Robinson projection, centered at 0°E.

Topographic Rises

Topographic rises on Venus are characterized by their broad domical shape, and have diameters on the order of 1,000–2,000 km, extensive volcanism, positive geoid anomalies, and widespread rifts, which suggest that these regions are underlain by mantle upwellings (Smrekar, 1994; Stofan et al., 1995; Smrekar and Sotin, 2012; Smrekar et al., 2018). For this study, we selected nine topographic rises linked to mantle upwellings: Atla, Bell, Beta, Dione, Eistla (central and western), Imdr, Laufey, and Themis Regiones (Basilevsky et al., 1986; Kiefer and Hager, 1991; Senske et al., 1992; Smrekar, 1994; Stofan et al., 1995; Smrekar et al., 1997; Brian et al., 2004) (**Figure 4.2**). We specifically focused on regions linked to mantle upwellings because

extensive volcanism in these areas is common and well documented (Stofan et al., 1995, 1997; Stofan and Smrekar, 2005; Ivanov and Head, 2013). Furthermore, large volcanoes and coronae at several of these rises (e.g., Imdr, and Themis Regiones) have been proposed to be active geologically recently based on anomalously high thermal emissivity values derived from the Visible and Infrared Thermal Imaging Spectrometer (VIRTIS) on ESA's Venus Express spacecraft (Smrekar et al., 2010; Stofan et al., 2016).

Table 4.1.
Study Site Properties: Topographic Rises

Topographic Rise	Length (km)	Width (km)	Area (km²)	Number of volcanoes (≤20 km in diameter)
Atla[a,b]	3000	2300	5,491,858	594
Bell[a,c]	1700	1400	1,843,009	109
Beta[d,e]	2500	1800	3,739,225	437
Central Eistla[a,f]	2000	1700	2,817,559	717
Dione[g]	2600	1100	2,540,578	909
Imdr[a]	1450	1200	1,172,791	381
Laufey[h]	2600	1200	2,678,242	495
Themis[i,j]	2700	2500	5,871,944	527
Western Eistla[a,e]	3000	2000	4,436,803	1399

[a]Stofan et al., (1995). [b]Philips, (1994). [c]Campbell and Rogers, (1994). [d]Basilevsky and Head, (2007). [e]Senske et al., (1992). [f]Smrekar and Stofan, (1999). [g]Keddie and Head, (1995). [h]Brian et al., (2004). [i]Stofan et al., (2016). [j]Kappel et al., 2016.

We delineated each topographic rise by generating 100 km-contour lines from the Magellan global altimetry dataset (Ford, 1992) and extracting that contour which fully encompassed the regional topographic high broadly corresponding to each study site. To ensure accuracy, we also consulted previous research that described the approximate dimensions of each of the nine regions (**Table 4.1**).

Atla Regio:

Atla Regio is located in the western hemisphere of Venus and is approximately centered on the equator, ranging in size from 1,200 × 1,600 km (Stofan et al, 1995) to 2,500 × 2,500 km

(Philips, 1994). A broad topographic rise that reaches an elevation of 3 km above the surrounding plains (Senske et al., 1992), Atla is part of the approximately triangular Beta–Atla–Themis (BAT) region, an area known for its relatively enhanced volcanism and extensive rifting (Airey et al., 2017; Crumpler et al., 1997). Numerous large volcanic centers such Maat Mons, where recent volcanic activity was discovered (Herrick and Hensely, 2023), Ozza Mons, and Ongwuti Mons (Basilevsky, 1993; Bilali et al., 2023), are found within Atla Regio, along with five major rift zones including Ganis, Dali, and Parga Chasmata (Senske et al., 1995; Bilali et al., 2023).

Bell Regio:

Bell Regio is an approximately 1,500 km-diameter topographic rise that spans Venus 18°–42° N to 32°–58° E (Campbell and Rogers, 1994). Unlike many of the other highland regions on Venus (e.g., Atla and Beta Regiones), Bell Regio is not dissected by large-scale rift zones (Rogers and Zuber, 1998). However, much like the other topographic rises discussed in this paper, Bell Regio boasts several large volcanoes such as Nyx and Tepev Montes, as well as the 370 km-diameter Nefertiti corona (Campbell and Rogers, 1994).

Beta Regio:

Located in the northern mid-latitudes, Beta Regio is a topographic rise that extends 2,000 km × 2,500 km in diameter, and rises >5 km above mean planetary radius (6,051 km) (Stofan et al., 1989; Basilevsky and Head, 2007). Like Atla, Beta Regio makes up one "vertex" of the BAT region and is dominated by volcanism and extensive rifting, too (Stofan et al., 1989). Two large shield volcanoes, Theia and Rhea Montes (Campbell et al., 1984), are situated in the approximate center of Beta Regio and are bisected by the N–S trending Devana Chasma, a deep, a ~160 km-wide tectonic rift that extends through the rise (Basilevsky and Head, 2007).

Dione Regio:

Dione Regio is an oval-shaped area located in the southern hemisphere of Venus and occupies a region 1,200 km × 2,700 km in extent (Keddie and Head, 1995). Three large edifices, Ushas, Innini, and Hathor Montes, are aligned N–S in the central portion of Dione, and a fourth, Nepthys Mons, is located in the western portion of the rise (Keddie and Head, 1995). Recent evaluation of radar-bright deposits at Hathor and Innini Montes (Campbell et al., 2017), as well as assessment of VIRTIS-derived emissivity anomalies (Smrekar et al., 2010), suggest that volcanism at these two volcanoes could be relatively recent.

Central Eistla Regio:

Situated to the southeast of Ishtar Terra, Eistla Regio is an extensive highland region over 8,000 km in diameter, and comprises three discrete topographic rises (Senske et al., 1992). We focus on the central and western highland regions within Eistla Regio. Central Eistla Regio measures ~1,200 km in diameter and was classified as a corona-dominated topographic rise by Stofan et al. (2005). Two volcanoes, Irnini and Anala Montes are located within Central Eistla, and were interpreted as shield volcanoes by some researchers (e.g., Solomon et al., 1992, McGill, 1994) but were also proposed to be more similar to coronae based on their corona-like summit features (Stofan et al., 2005).

Western Eistla Regio:

To the west of Central Eistla is Western Eistla Regio, a region measuring ~3,200 km × 2,000 km in area (Senske et al., 1992). Western Eistla is classified as a volcano-dominated topographic rise (Stofan et al., 1995), and contains two large edifices, Sif and Gula Montes, and Idem-Kuv, a 250 km diameter corona (Senske et al., 1992). Additionally, a rift system, Guor Linea,

extends ~850 km from the southeast flank of Gula Mons (Grimm and Philips, 1992; Solomon et al., 1992).

Imdr Regio:

Imdr Regio is situated in the southwest quadrant of the planet and has a diameter of ~ 1200 km ×1400 km and a height of 1.6 km above the surrounding plains (Stofan et al., 1995). Idunn Mons, Imdr Regio's only large edifice, measures 200 km in diameter and is thought to be geologically recently active based on high emissivity anomaly measurements from ESA's VIRTIS instrument (Smrekar et al., 2010; D'Innecco et al., 2017, 2021). Like many of the other topographic rises, Imdr Regio also hosts a rift zone, Olapa Chasma, a NW–SE-trending rift that extends from the NW edge of Imdr down to the SE portion, where it intersects with Idunn Mons (D'Incecco et al. 2020).

Laufey Regio:

Positioned within Navka Planitia, Laufey Regio is a 0.5 km-tall topographic rise that is ovular in shape and has an area of ~2,000 km by 1,000 km. (Brian et al., 2004). Three large volcanoes, Var, Atanua, and Tuli Montes, and two coronae, Hulda and Madderakka, are situated within Laufey. Several sets of small fracture belts are located near the summit of Var Mons, with a large-scale rift system, Nang-byon Chasma, extending ~400 km north from the center of Var (Brian et al., 2004).

Themis Regio:

Themis Regio is a broad rise standing 0.5 km tall and measuring approximately 2,300 km × 1,700 km in span (Stofan et al., 2016). Themis is located at the southern edge of Parga Chasma, a system of rifts that extends ~8,000 km towards Atla Regio (Senke et al., 1991; Stofan et al., 1992), and is occupied by thirteen coronae and six volcanoes with diameters >50 km, along with

numerous smaller shields (Stofan et al., 2016). As is the case at Dione and Imdr Regiones, anomalously high emissivity values associated with volcanoes such as Mielikki and Chloris Montes in Themis, as well as gravity data and geologic mapping, suggest that the region is a currently active mantle upwelling (Stofan et al., 2010, 2016).

Volcanic Fields

Table 4.2.
Study Site Properties: Volcanic Fields

Volcanic Fields[a]	Length (km)	Width (km)	Area (km²)	Number of volcanoes (≤20 km in diameter)
VF1	1500	1200	1,023,862	82
VF2	1500	1400	1,415,164	374
VF3	1500	900	957,975	233
VF4	1200	800	555,507	267
VF5	2500	1500	2,871,177	1162
VF6	700	500	347,641	116
VF7	1400	1300	1,278,144	1244
VF8	2000	13000	2,071,930	1807
VF9	1400	1000	760,702	513

[a]Hahn and Byrne (2023).

On Venus, localized concentrations of relatively small (≤20 km in diameter) volcanoes are referred to as "shield fields" (Aubele & Slyuta, 1990; Crumpler & Aubele, 2000; Ivanov & Head, 2004; Kreslavsky & Head, 1999). They are the equivalent to volcanic fields on Earth, and may contain tens to hundreds of small-volume (<1 km³), generally mafic volcanoes that are assumed to be the result of individual short-lived eruptive events lasting a month to several years (Connor and Conway, 2000). Examples of volcanic fields on Earth include the Abu monogenetic volcano group in Japan and the Snake River Plain in Idaho, USA (Kiyosugi et al., 2010; Morgan & McIntosh, 2005). For this study, we used a dataset volcanic fields from our global catalog (Hahn & Byrne, 2023), which contains the polygon boundary of 566 volcanic fields across Venus. Fields were filtered to remove any that intersected the nine topographic rises, and any smaller than 500 km in

diameter to ensure analysis was completed on volcanic fields comparable in size to the topographic rises (**Tables 4.1 & 4.2**). Of the remaining volcanic fields, nine were randomly selected for this analysis (**Figure 4.2**).

4.2 Methods

4.2.1 Kernel Density Estimation

In the ESRI ArcGIS Pro 3.0 environment, we used our global catalog of volcanoes on Venus (Hahn and Byrne, 2023) to extract all volcanoes ≤20 km in diameter contained by the boundary for each of the 18 study sites. In this analysis, we focus on relatively small volcanoes (i.e., those ≤20 km in diameter) that are likely monogenetic and erupt only a single time for kernel density analysis.

Two parts make up the kernel density function: the probability density function (PDF) and the bandwidth or smoothing parameter (Cañón-Tapia and Mendoza-Borunda, 2014). Based on the bandwidth and the shape of the kernel (Kiyosugi et al., 2010), the PDF spreads probability away from the event (i.e., the volcano). The bandwidth value directly impacts the smoothness of the resulting density plot. A small bandwidth value or smoothing parameter will focus the probability close to the locations of the mapped volcanoes, whereas a larger value will distribute the probability more broadly. For this analysis, we employed the "sum of the asymptotic mean square error" (SAMSE) (Duong and Hazelton, 2003) optimized bandwidth algorithm, which has been commonly used to develop vent opening probability maps on Earth (Germa et al., 2013; Connor et al., 2018; Schmidt et al., 2022). Optimized bandwidth algorithms reduce the subjectivity of the user arbitrarily selecting a bandwidth value, and instead give an unbiased estimate of bandwidth elements based on distances between neighboring events (again, in this case, volcanoes).

Furthermore, the SAMSE algorithm generates an elliptical kernel (described by the matrix parameter *H*) instead of the more common circular kernel (e.g., Weller et al., 2006; Canon-Tapia, 2013). Elliptical kernels are more sensitive to structural/tectonic controls on volcano distribution and alignment (Kiyosugi et al., 2010; Connor et al., 2018). We employed a two-dimensional, direction-varying elliptical kernel bandwidth to calculate the spatial variation in density, $\hat{\lambda}(s)$, at each grid point (s). which is given (Wand and Jones 1993, 1994) by:

$$\hat{\lambda}(s) = \frac{1}{2\pi\sqrt{|H|}} \sum_{i=1}^{N} exp\left[-\frac{1}{2} b^T b\right]$$

where,

$$b = H^{-\frac{1}{2}} d.$$

The elliptical kernel bandwidth, described here by the matrix parameter H, is a 2 × 2 element matrix, $|H|$ is the determinant of H, and $H^{-\frac{1}{2}}$ is the inverse of the square root of H. The total number of volcanoes is given by *N*. The variable d is a 1 × 2 distance matrix that describes the N–S and E–W distance from *s* to each vent location, b is the cross product of d and $H^{-\frac{1}{2}}$, and b^T is the transform of b. Therefore, the spatial intensity at a given point is calculated by applying the Gaussian kernel function using the distance to each volcano, smoothing the intensity as specified by the bandwidth (in this case, the SAMSE-derived bandwidth values), and then summing each volcano's contribution to the intensity estimation (Germa et al., 2013). The resulting maps of volcano spatial density reveal areas with both higher and lower concentrations of volcanoes, which can also be interpreted as regions of highest and lowest probability of new volcano formation. Regions with the highest concentrations of volcanoes, and also the highest probability for future cone-building events (i.e., high-volcano-spatial-density regions), can then be extracted as possible regions of interest.

Uncertainty in Kernel Density Analysis

Several assumptions underpin, and sources of uncertainty exist, in spatial density estimates. For this analysis, we must explicitly assume that the tectonic and/or magmatic factors controlling future volcano formation are the same processes that governed volcano formation in the past. Furthermore, these processes are operating in a steady-state, so the past pattern of volcanic activity is representative of future activity (c.f., Connor et al., 2015; 2018).

Uncertainties in KDE can stem from parameters such as the bandwidth estimate and the volcano locations (Connor and Connor, 2009; Connor et al., 2018). Here, we sought to minimize uncertainty arising from bandwidth selection by employing a bandwidth optimization algorithm that uses a data-driven approach to identifying the ideal bandwidth value. The SAMSE algorithm is particularly sensitive to individual volcano locations and as a result may obscure fine-scale structure by underfitting the data (Bebbington, 2015; Connor et al., 2018) and producing a smoother (less clustered) volcano spatial density map. For our purposes, a smoother map is acceptable, as our objective is to identify the *general* areas where we expect to see future volcanoes to form in a field, based on the locations of existing cones, which can then be tested by upcoming missions to Venus. Furthermore, our global catalog was developed using the Magellan SAR FMAP (full-resolution radar map) left- and right-look global mosaics, which has a resolution of 75 m-per-pixel (75 m/px) (Pettengill, 1991). Due to the relatively coarse nature of these datasets, it is difficult to identify small volcanoes (<1 km in diameter), and as such these smaller edifices are not included in our global catalog, and are therefore not incorporated into any KDEs. Future missions to Venus (e.g., VERITAS) will collect higher resolution SAR data, which may reveal volcanoes smaller than 1 km in diameter. These edifices may be newly formed volcanoes, or they may have formed

prior to the Magellan mission, but were too small to reliable resolve with the Magellan SAR datasets. Due to these resolution constraints, we propose that volcano formation maps developed in this study are only accurate for predicting the locations of future volcanoes >1 km in diameter.

4.2.2 Volcano Alignment Analysis

Volcano alignment analysis has been widely used to search for preferred orientations of clusters of shield volcanoes on Earth (Connor et al., 1992; Cebria et al., 2011; Roberts et al., 2011) and on other planets (Bleacher et al., 2009; Richardson et al., 2013, 2021; Thomson and Lang, 2016). Alignments of edifices can be attributed to the effects of magma source geometry, the regional tectonic stress field, pre-existing structures in the lithosphere (e.g., faults or fractures), or changes in the local stress field, and are a useful tool in understanding the relationships between the location of a given volcano and the geometry of the underlying magma plumbing system (Le Corvec et al., 2013; Tadini et al., 2014).

Here, we used the two-point azimuth approach (Lutz, 1986; Wadge and Cross, 1988, 1989; Cebria et al., 2011) to search for and identify any preferred orientations of volcanoes ≤20 km in diameter at each of the 18 study sites. This analysis was conducted with MATLAB R2022a. For each study site, the latitude and longitude of each volcano ≤20 km in diameter was imported and the geodesic distance (using the Venus reference ellipsoid) and azimuth from each volcano to every other volcano was calculated to measure the length and orientation of all lines connecting each edifice. Duplicate instances of distance and azimuth were removed.

Cebria et al. (2011) found that on Earth, eruptive centers are more closely related to nearby volcanoes rather than further edifices because lines that connect long distance volcanoes will be oriented along the major axis direction of the volcanic field itself, whereas proximal vents are more likely to have related crustal ascent pathways. Through Monte Carlo modeling and skewness

analysis of the Michoacán-Guanajuato volcanic field in Mexico and the Calatrava volcanic field in Spain, Cebria et al. (2011) noted that dominant orientations between volcanoes are more easily revealed when only considering edifices connected at shorter distances (i.e., along the same fracture). Therefore, to identify alignments between volcanoes proximal to one another, Cebria et al. (2011) chose to only include two-point azimuths that met a critical value of less than one-third the mean length of all inter-volcano line segments.

Here, we adopted the method of Cebria et al. (2011) and filtered out any azimuth values greater than the critical value calculated at each study site (see Appendix A.3 for critical values calculated for each study site). This part of our study resulted in 18 polar histograms (one for each site) detailing the orientations of volcanoes ≤20 km in diameter within each region.

4.3 Results

Table 4.3.
SAMSE Kernel Properties: Topographic Rises

Topographic Rise	Smoothing distance N–S (km)[a]	Smoothing distance E–W (km)[a]	Orientation[a]	Intensity in highest volcano density region (volcanoes/ km^2)[b]
Atla	2.55	2.36	NNW	2.97
Bell	1.79	1.15	NNE	6.87
Beta	2.51	2.08	NNW	3.50
Central Eistla	1.61	1.40	NNW	13.62
Dione	1.66	1.33	NNW	9.09
Imdr	0.90	1.52	NNW	11.24
Laufey	1.41	2.04	NNW	7.43
Themis	2.32	3.27	NNW	2.42
Western Eistla	1.51	1.89	NNW	11.19

[a]The smoothing distance refers to the length and width (km) of the elliptical kernel for each study site, and the orientation describes the strike of the major axis of each kernel ellipse.
[b]The intensity corresponds to the number of volcanoes per square kilometer in the highest volcano density region (e.g., the 25th percentile region) for each study site.

Table 4.4.
SAMSE Kernel Properties: Volcanic Fields

Volcanic Field	Smoothing distance N–S (km)[a]	Smoothing distance E–W (km)[a]	Orientation[a]	Intensity in highest volcano density region (volcanoes/ km^2)[b]
VF1	0.76	1.23	NNW	2.31
VF2	0.77	0.65	NNW	7.34
VF3	0.73	1.08	NNW	4.12
VF4	0.65	0.85	NNW	7.18
VF5	0.88	1.23	NNW	6.19
VF6	3.79	0.29	NNE	2.07
VF7	0.55	0.68	NNE	18.77
VF8	0.71	0.89	NNW	12.41
VF9	0.42	7.55	NNE	2.42

[a]The smoothing distance refers to the length and width (km) of the elliptical kernel for each study site, and the orientation describes the strike of the major axis of each kernel ellipse.
[b]The intensity corresponds to the number of volcanoes per square kilometer in the highest volcano density region (e.g., the 25th percentile region) for each study site.

4.3.1 Volcano Formation Probability Maps

Kernel density analysis was conducted in the *R* environment with functions from the freely available 'ks' package (Duong et al., 2007). The latitude and longitude of the centroid of each volcano ≤20 km in diameter from our global catalog (Hahn and Byrne, 2023) contained within the bounds of each of the nine hotspot regions, and each of the nine volcanic fields were used as the input points (**Tables 4.1 & 4.2**). For each of the 18 regions, the SAMSE bandwidth selector algorithms yields a 2 × 2 element matrix, which describes the size and orientation of the kernel (**Tables 4.3 & 4.4**), resulting in a total of 18 volcano spatial density maps—or, functionally, probability maps of future eruptive sites (**Figures 4.3** & **4.4**). Maps in **Figures 4.3** and **4.4** display the 25th, 50th, 75th, and 95th percentile of vent density as contours that correspond to the probability of future volcanoes forming in each quartile at each topographic rise, and volcanic field, respectively. For example, at Atla Regio (**Figure 4.3a**), locations with the 4.0e−03 contour

(i.e., the 50th quartile) will have spatial density >4.0 × 10^{-3} km^{-2}; given an eruption that leads to the construction of a volcano, there is a 50% chance it will occur within that contour boundary.

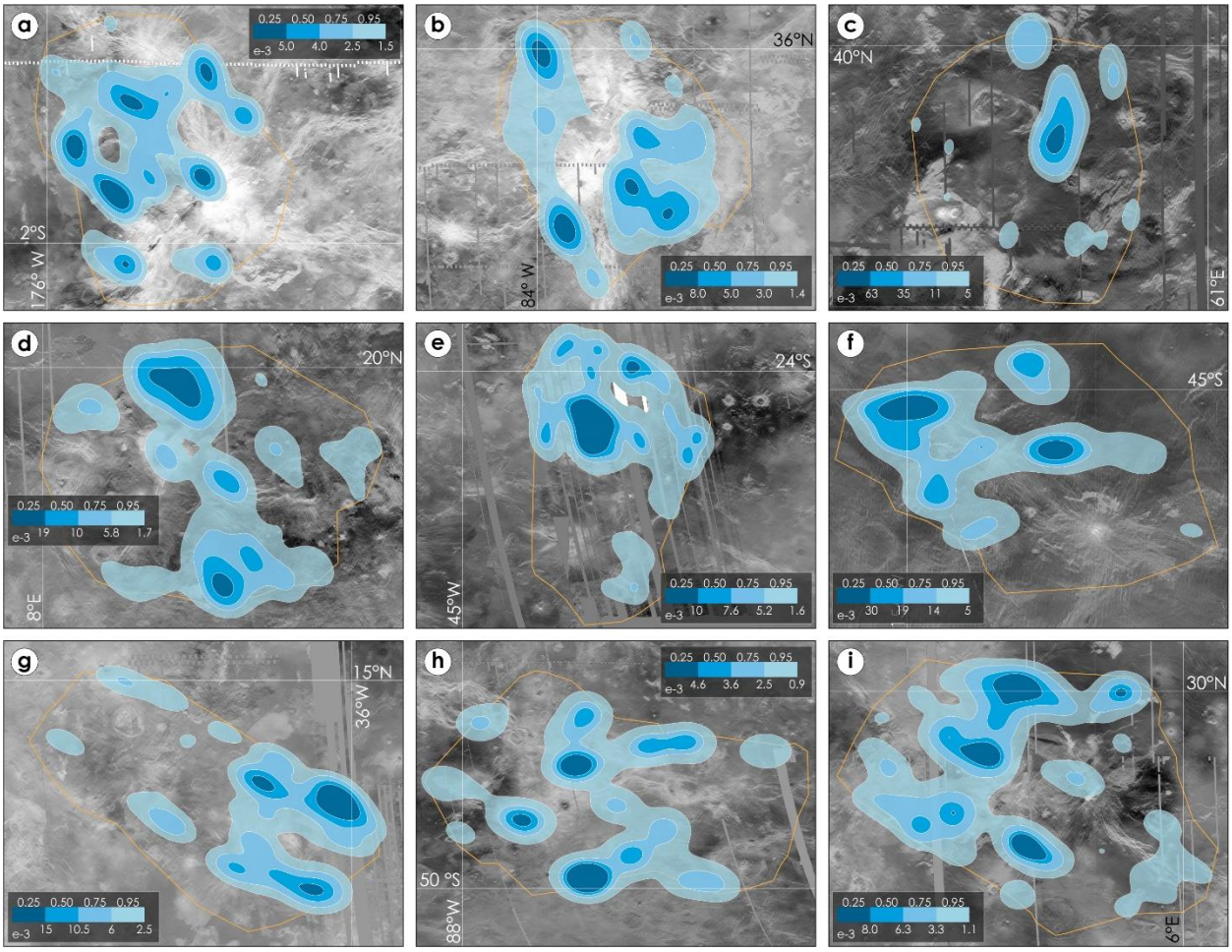

Figure 4.3: Volcano opening probability maps developed using the SAMSE bandwidth optimization algorithms for each of the nine topographic rises in this analysis, which includes (**a**) Atla, (**b**) Beta, (**c**) Bell, (**d**) Central Eistla, (**e**) Dione, (**f**) Imdr, (**g**) Laufey, (**h**) Themis, and (**i**) Western Eistla Regiones. Contours are shown at 25th, 50th, 75th, and 95th percentiles. Orange outlines in each map represent the contour boundary developed for each region. Basemaps are Magellan FMAP left- and right-look global mosaics, and all maps are shown in an Equirectangular projection.

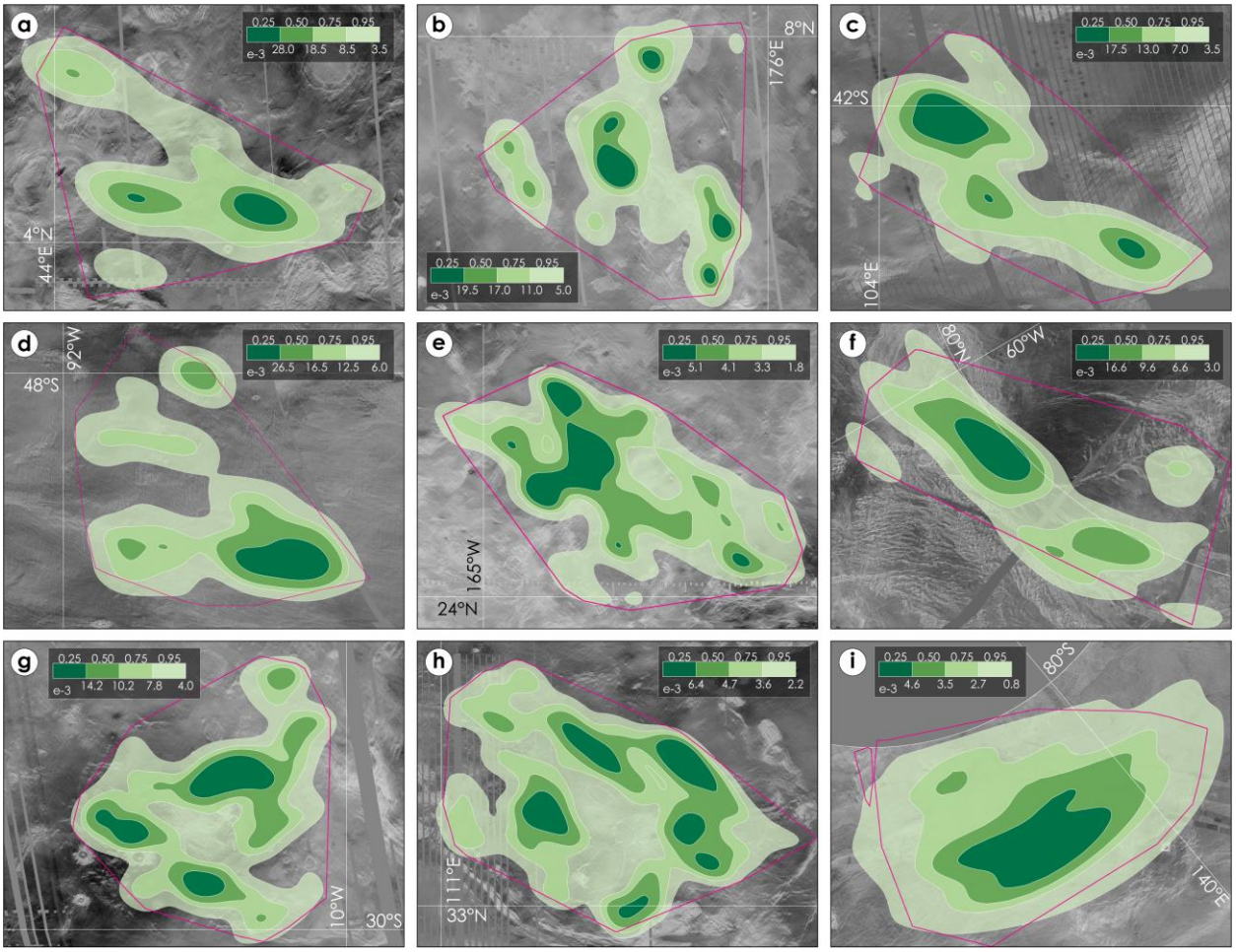

Figure 4.4: Volcano opening probability maps developed using the SAMSE bandwidth optimization algorithms for each of the nine volcanic fields in this analysis, which includes (**a**) VF1, (**b**) VF2 (**c**) VF3, (**d**) VF4, (**e**) VF5, (**f**) VF6, (**g**) VF7, (**h**) VF8, and (**i)** VF9. Contours are shown at 25th, 50th, 75th, and 95th percentiles. Pink outlines in each map represent the volcanic field boundary developed by Hahn and Byrne (2023). Basemaps are Magellan FMAP left- and right-look global mosaics, and all maps are shown in an Equirectangular projection, except for panels (**f**) and (**i**), which are in stereographic projection.

4.3.2 Volcano Alignments

The volcano alignment directions for each study site across Venus were plotted as polar histograms from 0 to 360 degrees. There is a wide range of alignment directions associated with topographic rises (**Figure 4.5**) and volcanic fields (**Figure 4.6**). To better discern if there is a dominant edifice orientation within each region, we employed the Omnibus test from CircStat, a MATLAB Toolbox for Circular Statistics developed by Berens (2009). The Omnibus test makes

no assumptions about the underlying distribution of each dataset, and simply tests for circular uniformity (Berens 2009). We employed the Omnibus test and calculated the test statistic, *P*, for the azimuths at each of the nine study sites:

$$P = \frac{1}{2^{N-1}}(N - 2m) \binom{N}{m},$$

where *N* is the total number of azimuths and *m* is the minimum number of samples falling in 180° of the circle (Berens, 2009). For all 18 study sites we calculated $P < 0$ at the 0.05 significance level, indicating that we can reject the null hypothesis that the dataset is uniformly distributed around the circle. This finding suggests that there *are* preferred orientations between volcanoes at each of the 18 study sites. To identify the dominant vent orientation at each study site, inter-vent azimuths were divided into 12 bins, and the average and standard deviation were calculated (**Figures 4.5 & 4.6**) (Cebria et al., 2011; Richardson et al., 2013). Bins that have a value greater than the mean bin value plus one standard deviation are considered anomalously high and may reflect the dominant orientation of volcanoes at each study site (shown as darker blue and darker green wedges in **Figures 4.5** and **4.6**, respectively.). Mean bin values and standard deviations for each study site can be found in Appendix A.3.

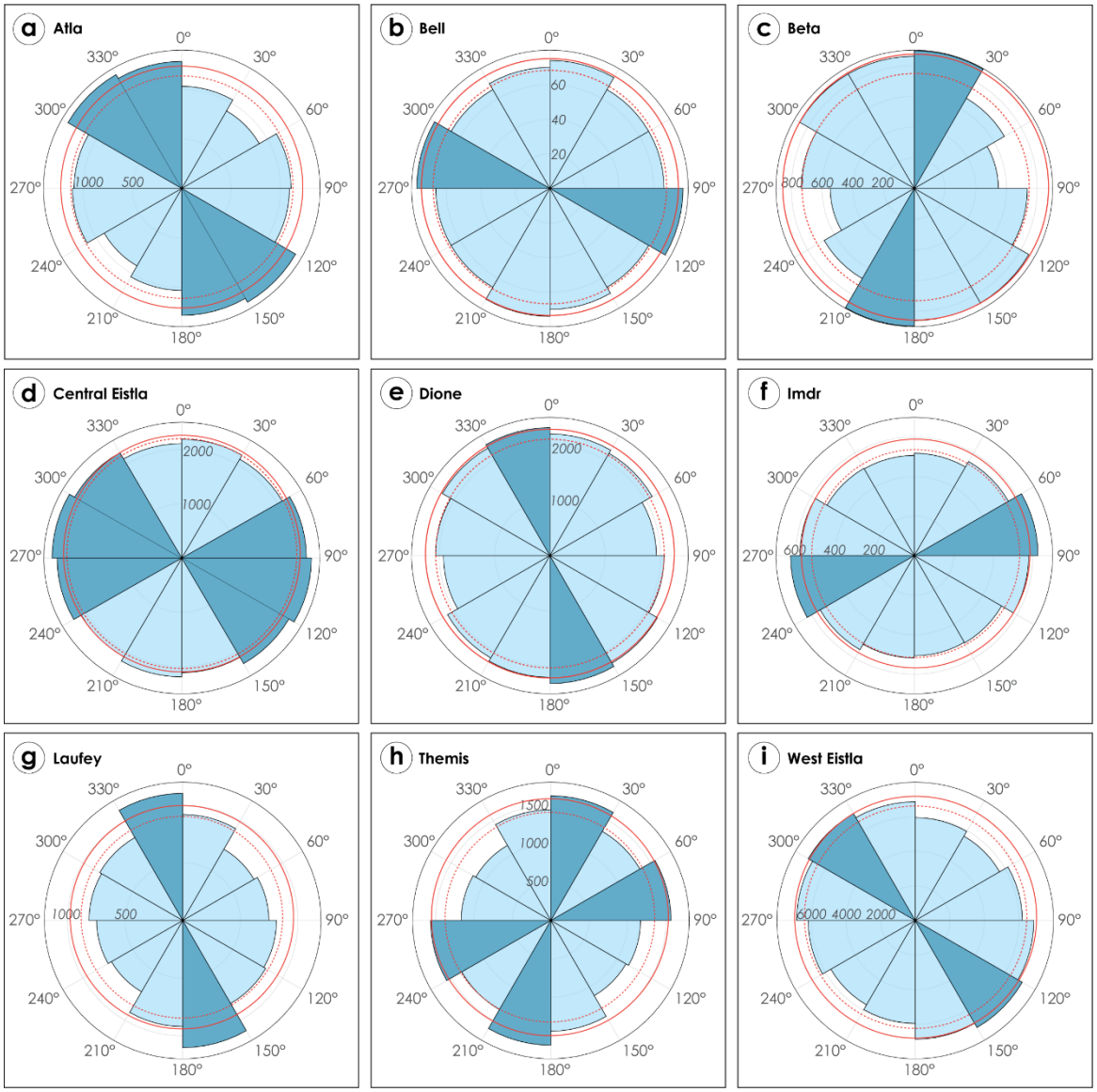

Figure 4.5: Polar histograms of intervent alignments for each topographic rise in this analysis. Alignments are only shown for azimuth values lower than the critical value calculated at each topographic rise (c.f. Cebria et al., 2011). The dotted orange line represents the mean quantity of inter-volcano relationships, and the dashed orange line indicates the mean quantity plus one standard deviation. Dark blue directional wedges have quantities of inter-volcano relationships greater than the mean value plus one standard deviation and thus represent a dominant orientation of volcanoes in each region. Critical values, mean values, and standard deviations for each region can be found in Appendix A.3.

Figure 4.6: Polar histograms of intervent alignments for each volcanic field in this analysis. Alignments are only shown for azimuth values lower than the critical value calculated at each field (c.f. Cebria et al., 2011). The dotted pink line represents the mean quantity of inter-volcano relationships, and the dashed pink line indicates the mean quantity plus one standard deviation. Dark green directional wedges have quantities of inter-volcano relationships greater than the mean value plus one standard deviation and thus reflect a dominant orientation of volcanoes in each field. Critical values, mean values, and standard deviations for each region can be found in Appendix A.3.

4.4 Discussion

Incorporating relevant information about the regional geology can produce more robust kernel density estimates and resulting volcano probability maps (Connor et al., 2018). Here, we further identify specific regions within the 18 study sites that are most likely to see future volcanic constructional activity based on evidence for active and/or recent volcanism, volcano alignments, high spatial concentrations of volcanoes, and proximal tectonic structures indicative of a stress state conducive to eruptions.

4.4.1 Regions with Recent Geologic Activity

Regions hosting putative, geologically recent volcanism have been identified across Venus using radar and thermal emissivity measurements and stratigraphic relations. Structures at several topographic rises have been linked with anomalously high thermal emissivity measurements at 1 μm (Smrekar et al., 2010; Stofan et al., 2016) from the Venus Express VIRTIS instrument (Helbert et al., 2008; Mueller et al., 200). Large volcanoes in Imdr (Idunn Mons), Dione (Hathor and Innini Montes), and Themis Regiones (Mielikki Mons), as well as large coronae in Themis Regio (Shulamite and Shiwanokia), all have lava flows associated with unusually high thermal emissivity values. These anomalously high values have been interpreted to indicate relatively fresh basalt with low degrees of weathering, suggesting geologically recent activity (Mueller et al., 2008; Smrekar et al., 2010; Stofan et al., 2016). Tectonic structures such as Olapa Chasma in Imdr Regio and Ganis Chasma in Atla Regio are also hypothesized to be relatively young based on stratigraphical analysis (Basilevsky, 1993; D'Incecco et al., 2020), thermal anomalies identified by the Venus Monitoring Camera (VMC), onboard Venus Express, (Shalygin et al., 2012, 2015), and Magellan radar emissivity anomalies (Brossier et al., 2022). Most compellingly, evidence for volcanotectonic collapse during the Magellan mission on the flank of Maat Mons in Atla Regio

strongly suggests that such activity volcanic activity on Venus continues to the present (Herrick and Hensely, 2023).

On the basis of these observations and interpretations, we propose that Atla, Dione, Imdr, Themis Regiones, and volcanic field 7, which is just 50 km NE of Dione Regio, should be prioritized by future missions in the search of ongoing or recent volcanism on Venus. VIRTIS data are only available for relatively high latitudes in the southern hemisphere (Smrekar et al., 2010), and it is possible that other areas across Venus also show high thermal emissivity consistent with an interpretation of contemporary volcanic activity. The Venus Emissivity Mapper (VEM) onboard VERITAS (Helbert et al., 2019) and the VenSpec instrument suite on EnVision (Helbert et al., 2019) will allow for the development of global emissivity maps for Venus. These global-scale emissivity maps alongside regions identified in this study as having a high probability of future volcanic construct formation, can directly inform the search for new or recent volcanism across the planet.

4.4.2 Regions with Volcano Alignments

Alignments of volcanoes within volcanic fields or on the flanks of polygenetic volcanoes suggests eruptions along fissures fed by dikes (MacDonald, 1972; Paulson and Wilson. 2010), and could inform the location of future edifices. In this study, based on results from the Omnibus Test, we find that volcanoes at each of the 18 sites have at least one statistically significant orientation of volcanoes (**Figures 4.5** & **4.6**).

Le Corvec et al. (2013) analyzed vent alignments at 37 volcanic fields in varying tectonic settings across Earth and found that fields in extensional environments generally show two or more preferred vent alignments. Extensive rift systems crosscut Atla, Beta, Themis, Imdr, and Laufey Regiones (e.g., Devana Chasma in Beta Regio), with smaller-scale extensional structures typically

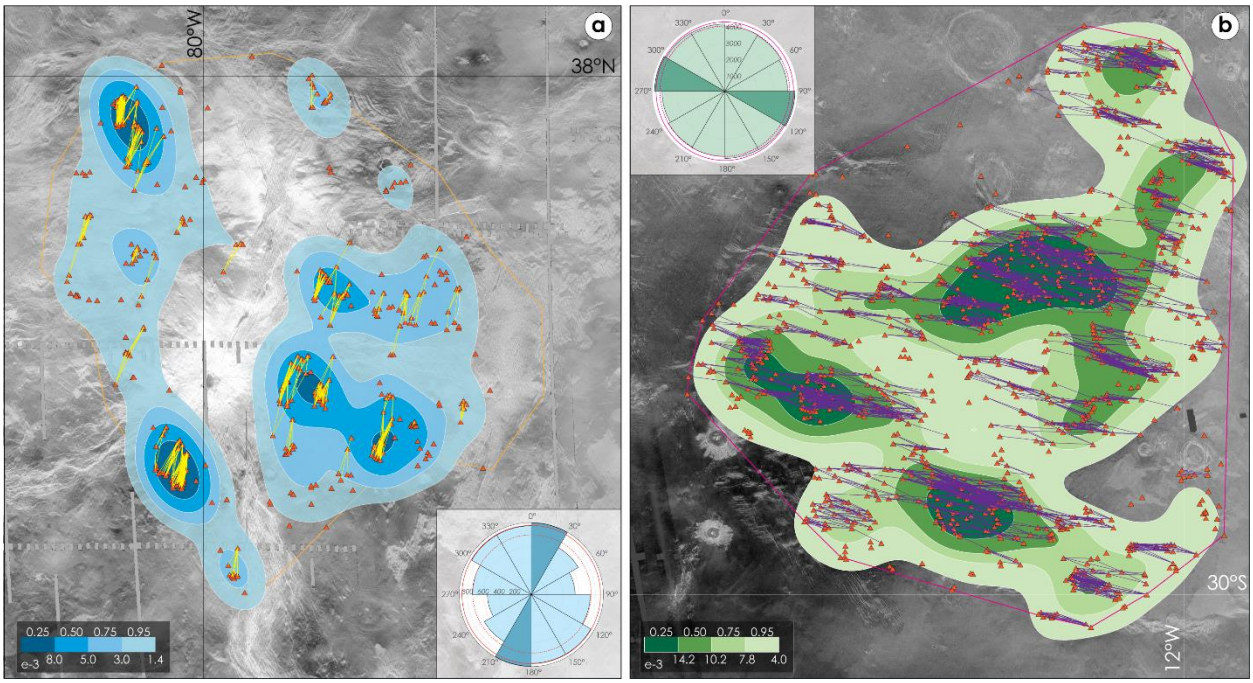

Figure 4.7: Maps detailing the dominant volcano alignments at a topographic rise (**a**) and a volcanic field (**b**). Map (**a**) shows the dominant orientation of volcanoes ≤20 km in diameter (orange triangles) at Beta Regio is ~NNE–SSW (yellow lines). Map (**b**) shows the dominant orientation of volcanoes ≤20 km in diameter (orange triangles) at VF7 is ~E–W (purple lines). Both maps include the volcano opening probability maps developed using the SAMSE bandwidth optimization algorithms (**Figures 4.3b** and **4.4g**), and insets of their respective polar histograms (**Figures 4.5b** and **4.6g)**. Basemaps are Magellan FMAP left- and right-look global mosaics, and all maps are shown in an Equirectangular projection

linked with coronae or large volcanoes (e.g., Irnini Mons in central Eistla Regio) present in central and western Eistla, Bell, and Dione Regiones. In an extensional environment, pre-existing fractures and mechanical segmentation along rifts can lead to dike propagation in numerous directions resulting in several volcano orientations (Le Corvec et al., 2013). This process could have occurred at Atla, Central Eistla, and Themis Regiones, which each have two or more dominant volcano alignments. Other topographic rises, such as Beta (**Figure 4.7a**) and Imdr Regions, exhibit a single dominant alignment of edifices, but still have numerous orientations of volcanoes throughout the region (**Figure 4.5**).

All nine volcanic fields analyzed in this are crosscut by small-scale extensional structures (e.g., groove belts (Ivanov and Head, 2011)), as well as compressional structures (e.g., wrinkle ridges) (Hahn and Byrne, 2023). We find that each field is associated with a single dominant alignment of volcanoes (**Figures 4.6** & **4.7b**). Le Corvec et al. (2013) found that volcanic fields associated with a single alignment of edifices are most commonly associated with a strike-slip tectonic setting. Although possible instances of strike-slip tectonism has been noted in other regions of Venus (e.g., Riedel fracture patterns on the southern border of Ovda Regio (Romeo et al., 2005)), there is no evidence of strike-slip style tectonics at any of the nine volcanic fields in this study. On Venus, volcanic fields are commonly associated with volcanic plains, extensive sheets of lava linked with flood volcanism (Head et al., 1991; Guest et al., 1992). It is possible that portions of volcanic fields were resurfaced, effectively erasing evidence of other volcano alignments, or tectonic structures, and resulting in a single dominant alignment of volcanoes.

More information on the age or timing of fault activity in each region could further narrow down possible sites where future activity might occur at each study site. For example, vent-opening probability maps developed for fissure vents on Mount Etna incorporated data from seismic, tomographic, and geodetic studies to identify faults that are actively and passively involved in the eruptive process based on their location and orientation within the volcano (Capello et al., 2012). The EnVision mission will carry a subsurface radar sounder to help establish the stratigraphic relationships between different geologic units on Venus (Bruzzone et al., 2020). Should these data resolve near-surface faults and fault geometries, it may be possible to correlate such structures with mapped volcanoes on the surface to further strengthen the predictive capabilities of the approach we use here.

4.4.3 High-volcano-spatial-density-regions

The SAMSE algorithm produced a kernel with an average smoothing distance of ~1.8 km in the E–W direction and ~1.9 in the N–S direction for the topographic rises (**Table 4.3**), and average smoothing distance of ~2.0 km in the E–W direction and ~0.6 in the N–S direction for the volcanic fields (**Table 4.4**). These smoothing bandwidths are comparable to SAMSE bandwidths calculated for the Auckland volcanic field, NZ (0.9 km in the E–W direction and 3.4 km in the N–S direction (Bebbington, 2015)), but are much smaller when compared with other volcanic fields on Earth such as the Yucca Mountain Region, USA (28.8 km in the E–W direction and 9.8 km in the N–S direction (Connor and Connor, 2009)). Variations in the orientation and size of the kernel bandwidth implies differences in the tectonic control on magma ascent and the productivity of the melt source (Cappello et al., 2012). A smaller bandwidth value will be derived for volcanic fields with volcanoes close one another (e.g., sites in this study), whereas a large bandwidth value is calculated when volcanoes are distributed farther from each other (e.g., the Yucca Mountain Region) (Germa et al., 2013).

The small kernel bandwidth values calculated for all 18 regions in this analysis suggests that volcanoes ≤20 km in diameter are close together or clustered at topographic rises and volcanic fields on Venus. These clusters of volcanoes are reflected in the resulting probability maps for each region, with the darkest blue regions in **Figure 4.3** and the darkest green regions in **Figure 4.4** indicating the highest spatial density region of volcanoes (e.g., the 25^{th} percentile contour). Clusters or regions of high-volcano-spatial density are common in volcanic fields on Earth, and may indicate areas of magma generation at depth and/or preferential pathways of magma ascent (Connor, 1990; Germa et al., 2013). Furthermore, new volcano construction has the highest probability of occurring in regions affected by the same type of eruption or volcanic activity in the

past (e.g., Jaquet et al., 2008; Capello et al., 2012), making these high-volcano-spatial-density regions ideal candidate locations to search for future edifice formation. Here, we isolate the high-volcano-spatial-density regions by extracting the polygons delineating the 25% kernel density contour boundary at each of the 18 study sites in ArcGIS Pro.

For the topographic rises, we find a total of 27 high-volcano-spatial-density regions, ranging in size from ~4,100 km^2 to ~122,000 km^2. Similarly, we extracted 23 high-volcano-spatial-density regions from the volcanic fields, which are ~4,500 km^2 to ~178,000 km^2 in area. Note that five regions were excluded from this analysis due to their anomalously small sizes. Although each of these 50 high-volcano-spatial-density regions represents a cluster of volcanoes ≤20 km in diameter, the number of volcanoes within these clusters is not uniform across all 18 study sites. The spatial intensity is calculated by multiplying the spatial density, $\hat{\lambda}(s)$, by the total number of volcanoes in each region, *N*, and describes the number of volcanos per km² (**Tables 4.3** & **4.4**). The high-volcano-spatial-density regions at the three topographic rises that comprise the BAT region have the lowest spatial intensity, with an average of three volcanoes/km², compared to the other six rises, which have an average of ten volcanoes/km² (**Table 4.3**). This finding suggests that the intensity of volcanism producing volcanoes ≤20 km in diameter in the BAT region is lower than at topographic rises across the rest of the planet. The BAT region contains ~49 large (>100 km in diameter) edifices (Hahn and Byrne, 2023), as well as numerous coronae, and volcanoes ≤20 km in diameter in the region could form as a result of late-stage waning of the magma supply feeding the larger volcanoes and coronae in the region, similar to process that forms small shields on the flanks of large volcanoes such as Mauna Kea and Mount Etna (Crumpler et al., 1997). Indeed, we note that two high-volcano-spatial-density regions in Atla Regio each overlap with a large edifice (Sapas and Ozza Montes), and two high-volcano-spatial-density regions, one in both

Beta and Regio, and one in Themis Regio, each overlap with coronae, suggesting a genetic link between these structures and small edifices. Alternatively, fewer small volcanoes in the BAT region compared with other topographic rises could be a result of volcanic resurfacing, where erupted materials from the numerous large volcanoes and coronae in the region buried those smaller edifices still large enough to be resolved with Magellan radar imagery. Likewise, we find that volcanic fields that are spatially proximal to large volcanoes and coronae, have a lower spatial intensity of volcanoes than fields that are not associated with any larger structures (**Table 4.4**). For example, volcanic field 8 has the highest spatial intensity at ~19 volcanoes/km². This volcanic field does not contain any large volcanoes or coronae, with the nearest structures ~1,500 km and 500 km away, respectively. Volcanic fields with lower spatial intensities (e.g., VF 4 and VF 5) each overlap with at least one corona and large edifice, again suggesting that these larger structures in the region are feeding the smaller edifices.

4.4.4 Regions Associated with Extensional Structures

Monogenetic vent emplacement is mechanically much easier in extensional systems, where a horizontally extensional stress regime offers intrusions multiple paths to the surface, in contrast to contractional systems where horizontally compressive stresses constrain magma ascent to already established conduits (Nakamura 1977), and even then only when critically stressed. Indeed, on Earth, volcanic field formation is most commonly related to extensional tectonic regimes (e.g., Snake River volcanic field, USA (Hughes et al., 2002); Jaraguay volcanic field, Mexico (Calmus et al., 2011); Kula volcanic field, Turkey (Tokcaer et al., 2005)).

We find that 46% (23/50) of the high-volcano-spatial-density regions are crosscut by an extensional structure (e.g., a rift zone), and an additional 14% (7/50) are within 50 km of such structures (pink ovals in **Figure 4.8**). By analogy with Earth, a similar process of volcanic fields

preferentially forming in extensional settings presumably occurs on Venus—such that high-volcano-spatial-density regions that coincide with or are proximal to extensional structures are good candidate locations to search for the formation of new volcanoes either during the VERITAS and EnVision missions or by comparison with data from those missions and Magellan observations.

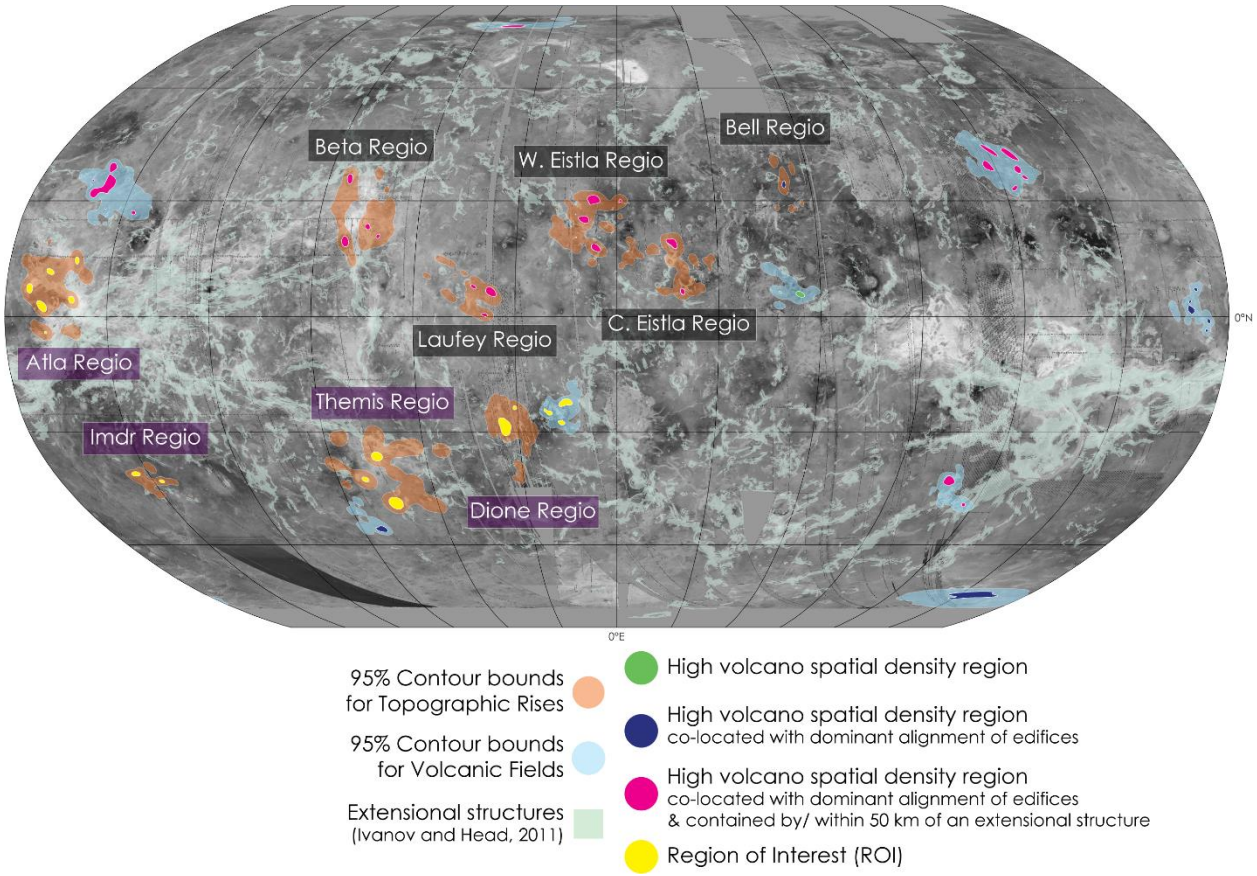

Figure 4.8: Global view of volcano opening probability maps showing the 95% contour boundary for topographic rises (orange polygons), volcanic fields (light blue), and the highest volcano spatial density regions for each study site (green, blue, pink, and yellow ovals). Blue ovals indicate high volcano density regions that are co-located with dominant orientations of volcanoes, pink ovals correspond to high volcano density regions that are co-located with dominant orientations of volcanoes and are also within/ 50 km within an extensional structure (light green polygons), and yellow ovals (ROIs) correspond to high volcano density regions that are co-located with dominant orientations of volcanoes, overlap with or are within 50 km of an extensional structure, and are also located in areas hypothesized to host recent geologic activity (purple text boxes). Basemap is Magellan FMAP left- and right-look global mosaics. The map is in Robinson projection, centered at 0°E.

4.5 Conclusions

Kernel density analysis of an existing volcanic edifice catalog (Hahn & Byrne, 2023) revealed that the most probable locations where future volcanoes will form on the basis of past events at nine, broad topographic rises, and nine volcanic fields on Venus. Kernel density analysis is a powerful forecasting tool, but is based on the assumption that future activity is controlled by the same magmatic and tectonic factors that governed past activity (Connor et al., 2018). Therefore, we bolstered our study by focusing on regions with the highest spatial density of existing edifices, as these regions likely represent preferential pathways of magma ascent (Connor, 1990; Germa et al., 2013).

We also conducted edifice alignment analysis to identify any preferred orientations of existing volcanoes that might indicate regional-scale control of eruptive locations by faults, from which future cones may form (Rooney et al., 2011; Le Corvec et al., 2013). Furthermore, we note that 60% (30/50) of the high-volcano-spatial-density regions overlap with or are encompassed by an extensional structure or system (e.g., a rift zone). Additionally, we documented regions that earlier studies have identified as recently volcanically active based on radar and thermal emissivity values or stratigraphic relationships (e.g., Smrekar et al., 2010; Stofan et al., 2016; Brossier et al., 2022). Our final global map shows the broadest 95% contour for kernel density maps developed for each study region, and also includes specific areas of interest based on vent alignments, volcano spatial density, proximal extensional structures, and possibility of active volcanism based on previous studies (e.g., Smrekar et al., 2010; Stofan et al., 2016) (**Figure 4.8**). We predict the most fruitful sites for future volcano formation are those within high-volcano-spatial-density regions, have a statistically significant orientation of volcanoes, are within 50 km of an extensional

structure, and are associated with geologically young topographic rises (yellow ovals in **Figure 4.8**).

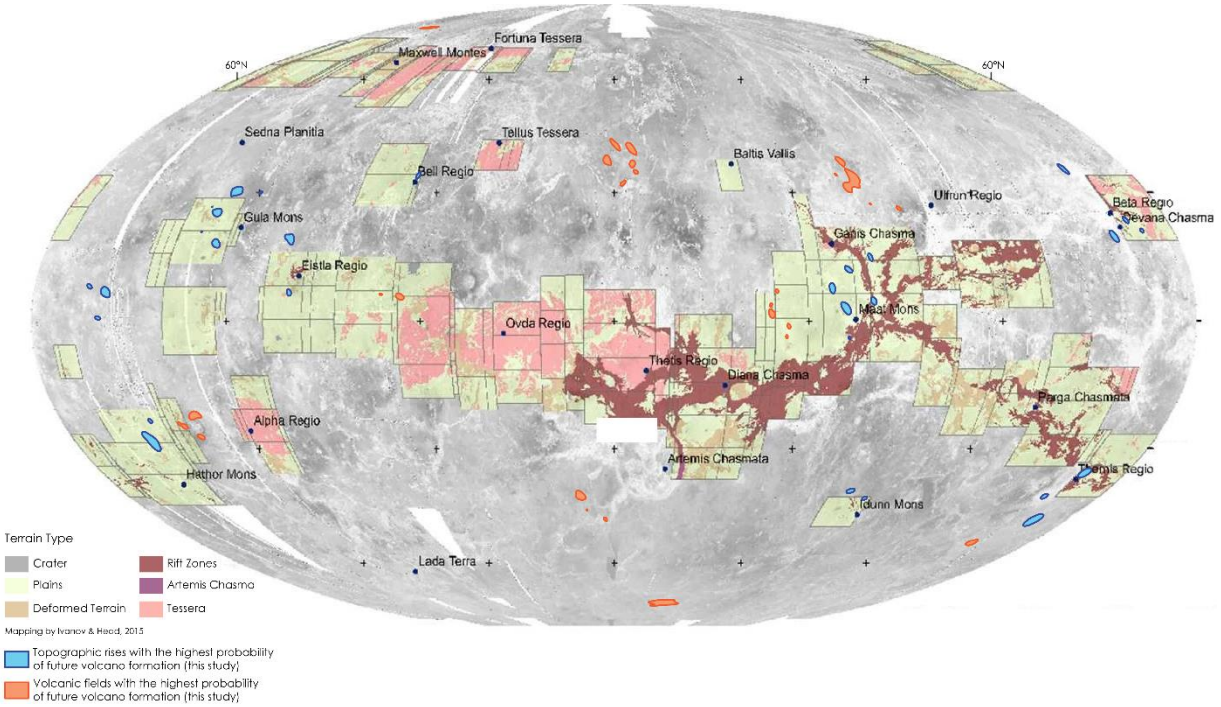

Figure 4.9: Global map of geologic terrains and landforms that are possible regions of interest defined in EnVision's Science Operations Reference Scenario (ESA, 2024), overlain by regions identified in this study as having the highest probability of new volcano formation at nine topographic rises (blue circles with darker blue outline), and nine volcanic fields (orange circles with darker orange outline) across Venus. The map is in Mollweid projection, centered at 120°E. Figure is adapted from the EnVision Assessment Study Report (ESA, 2024) and Ivanov and Head, (2015).

Our findings can inform future planned exploration of Venus, such as NASA's VERITAS (Smrekar et al., 2022) and ESA's EnVision (Ghail et al., 2018). Indeed, the EnVision Assessment Study Report (ESA, 2024) includes a regional/targeted surface map of possible regions of interest across Venus for which the mission's Venus Synthetic Aperture Radar (VenSAR) instrument will acquire data with a spatial resolution of both 30 and 10 meters per pixel. These regions of interest partially encompass six out of nine of the topographic rises in this study (Bell, Atla, Dione, Central, and Western Eistla, Themis Regiones), and three out of the nine volcanic fields (VF1, VF2, and VF7) (**Figure 4.9**). The results of this study can help inform the selection of the final regions of

interest to include higher resolution radar imagery of Venus where new volcanoes are statistically most likely to form. The identification and quantification of new sites of constructional volcanism across the planet will improve our understanding of the styles, and eruptive rates of volcanoes on Venus, in turn shedding light on the interior structure of the planet.

References

Airey, M. W., Mather, T. A., Pyle, D. M., & Ghail, R. C. (2017). The distribution of volcanism in the Beta-Atla-Themis region of Venus: Its relationship to rifting and implications for global tectonic regimes. *Journal of Geophysical Research: Planets*, *122*(8), 1626-1649.

Aubele, J. C., & Slyuta, E. N. (1990). Small domes on Venus: Characteristics and origin. *Earth, Moon, and Planets*, 50(1), 493–532. https://doi.org/10.1007/BF00142404

Bartolini, S., Bolós, X., Martí, J., Pedra, E. R., & Planagumà, L. (2015). Hazard assessment at the quaternary La Garrotxa volcanic field (NE Iberia). *Natural Hazards*, *78*, 1349-1367. https://doi.org/10.1007/s11069-015-1774-y

Bartolini, S., Cappello, A., Martí, J., & Del Negro, C. (2013). QVAST: a new Quantum GIS plugin for estimating volcanic susceptibility. *Natural Hazards and Earth System Sciences*, *13*(11), 3031-3042. https://doi.org/10.5194/nhess-13-3031-2013

Basilevsky, A. T. (1993). Age of rifting and associated volcanism in Atla Regio, Venus. *Geophysical research letters*, *20*(10), 883-886.

Basilevsky, A. T. (1993). Age of rifting and associated volcanism in Atla Regio, Venus. *Geophysical research letters*, *20*(10), 883-886. https://doi.org/10.1029/93GL00736

Basilevsky, A. T., & Head, J. W. (2007). Beta Regio, Venus: Evidence for uplift, rifting, and volcanism due to a mantle plume. Icarus, 192(1), 167-186. https://doi.org/10.1016/j.icarus.2007.07.007

Basilevsky, A. T., Pronin, A. A., Ronca, L. B., Kryuchkov, V. P., Sukhanov, A. L., & Markov, M. S. (1986). Styles of tectonic deformations on Venus: Analysis of Venera 15 and 16 data. *Journal of Geophysical Research: Solid Earth*, *91*(B4), 399-411. https://doi.org/10.1029/JB091iB04p0D399

Bebbington, M. S. (2015). Spatio-volumetric hazard estimation in the Auckland volcanic field. *Bulletin of Volcanology*, *77*(5), 39. https://doi.org/10.1007/s00445-015-0921-3

Berens, P. (2009). CircStat: a MATLAB toolbox for circular statistics. *Journal of statistical software*, *31*, 1-21. https://doi.org/10.18637/jss.v031.i10

Bertin, D., Lindsay, J. M., Becerril, L., Cronin, S. J., & Bertin, L. J. (2019). MatHaz: a Matlab code to assist with probabilistic spatio-temporal volcanic hazard assessment in distributed

volcanic fields. *Journal of Applied Volcanology*, *8*, 1-25. https://doi.org/10.1186/s13617-019-0084-6

Bevilacqua, A., Isaia, R., Neri, A., Vitale, S., Aspinall, W. P., Bisson, M., ... & Rosi, M. (2015). Quantifying volcanic hazard at Campi Flegrei caldera (Italy) with uncertainty assessment: 1. Vent opening maps. *Journal of Geophysical Research: Solid Earth*, 120(4), 2309-2329. https://doi.org/10.1002/2014JB011775

Bleacher, J. E., Glaze, L. S., Greeley, R., Hauber, E., Baloga, S. M., Sakimoto, S. E., & Glotch, T. D. (2009). Spatial and alignment analyses for a field of small volcanic vents south of Pavonis Mons and implications for the Tharsis province, Mars. *Journal of Volcanology and Geothermal Research*, 185(1–2), 96–102. https://doi.org/10.1016/j.jvolgeores.2009.04.008

Brian, A. W., Stofan, E. R., Guest, J. E., & Smrekar, S. E. (2004). Laufey Regio: A newly discovered topographic rise on Venus. *Journal of Geophysical Research: Planets*, *109*(E7). https://doi.org/10.1029/2002JE002010Citations

Brossier, J., Gilmore, M. S., & Head, J. W. (2022). Extended rift-associated volcanism in Ganis Chasma, Venus detected from Magellan radar emissivity. *Geophysical Research Letters*, *49*(15), e2022GL099765. https://doi.org/10.1029/2022GL099765

Bruzzone, L., Bovolo, F., Thakur, S., Carrer, L., Donini, E., Gerekos, C., ... & Sbalchiero, E. (2020, September). Envision mission to venus: Subsurface radar sounding. In *IGARSS 2020-2020 IEEE International Geoscience and Remote Sensing Symposium* (pp. 5960-5963). IEEE. https://doi.org/10.1109/IGARSS39084.2020.9324279.

Calmus, T., Pallares, C., Maury, R. C., Aguillón-Robles, A., Bellon, H., Benoit, M., & Michaud, F. (2011). Volcanic markers of the post-subduction evolution of Baja California and Sonora, Mexico: Slab tearing versus lithospheric rupture of the Gulf of California. *Pure and Applied Geophysics*, *168*, 1303-1330. https://doi.org/10.1007/s00024-010-0204-z

Campbell, B. A., & Rogers, P. G. (1994). Bell Regio, Venus: Integration of remote sensing data and terrestrial analogs for geologic analysis. *Journal of Geophysical Research: Planets*, *99*(E10), 21153-21171.

Campbell, B. A., Morgan, G. A., Whitten, J. L., Carter, L. M., Glaze, L. S., & Campbell, D. B. (2017). Pyroclastic flow deposits on Venus as indicators of renewed magmatic activity. *Journal of Geophysical Research: Planets*, 122(7), 1580-1596. https://doi.org/10.1002/2017JE005299

Campbell, D. B., Head, J. W., Harmon, J. K., & Hine, A. A. (1984). Venus: Volcanism and rift formation in Beta Regio. *Science*, 226(4671), 167-170. https://doi.org/10.1126/science.226.4671.167

Cañón-Tapia, E. (2013). Volcano clustering determination: Bivariate Gauss vs. Fisher kernels. *Journal of Volcanology and Geothermal Research*, 258, 203–214. https://doi.org/10.1016/j.jvolgeores.2013.04.015

Cañon-Tapia, E., & Mendoza-Borunda, R. (2014). Insights into the dynamics of planetary interiors obtained through the study of global distribution of volcanoes I: Empirical calibration on Earth. *Journal of Volcanology and Geothermal Research*, 281, 53–69. https://doi.org/10.1016/j.jvolgeores.2014.05.013

Cappello, A., Neri, M., Acocella, V., Gallo, G., Vicari, A., & Del Negro, C. (2012). Spatial vent opening probability map of Etna volcano (Sicily, Italy). *Bulletin of Volcanology*, *74*, 2083-2094. https://doi.org/10.1007/s00445-012-0647-4

Cebriá, J. M., Martín-Escorza, C., López-Ruiz, J., Morán-Zenteno, D. J., & Martiny, B. M. (2011). Numerical recognition of alignments in monogenetic volcanic areas: Examples from the Michoacán-Guanajuato Volcanic Field in Mexico and Calatrava in Spain. *Journal of Volcanology and Geothermal Research, 201*(1-4), 73-82. https://doi.org/10.1016/j.jvolgeores.2010.07.016

Cebriá, J. M., Martín-Escorza, C., López-Ruiz, J., Morán-Zenteno, D. J., & Martiny, B. M. (2011). Numerical recognition of alignments in monogenetic volcanic areas: Examples from the Michoacán-Guanajuato Volcanic field in Mexico and Calatrava in Spain. *Journal of Volcanology and Geothermal Research*, 201(1–4), 73–82. https://doi.org/10.1016/j.jvolgeores.2010.07.016

Connor, C. B., & Connor, L. J. (2009). Estimating spatial density with kernel methods. In C. B. Connor, N. A. Chapman, & L. J. Connor (Eds.), Volcanic and tectonic hazard assessment for nuclear facilities (pp. 346–368). Cambridge University Press.

Connor, C. B., & Conway, F. M. (2000). Basaltic volcanic fields. In H. Sigurdsson, B. Houghton, S. R. McNutt, H. Rymer, & J. Stix (Eds.), *Encyclopedia of volcanoes* (Vol. 1, pp. 331–343). Academic Press.

Connor, C. B., Connor, L. J., Germa, A., Richardson, J. A., Bebbington, M. S., Gallant, E., & Saballos, A. (2018). How to use kernel density estimation as a diagnostic and forecasting tool for distributed volcanic vents. *Statistics in Volcanology*, *4*(1), 3. https://doi.org/10.5038/2163-338X.4.3

Connor, C. B., Condit, C. D., Crumpler, L. S., & Aubele, J. C. (1992). Evidence of regional structural controls on vent distribution: Springerville Volcanic Field, Arizona. *Journal of Geophysical Research*, 97(B9), 12349–12359. https://doi.org/10.1029/92JB00929

Connor, C., Bebbington, M., & Marzocchi, W. (2015). Probabilistic volcanic hazard assessment. In *The Encyclopedia of Volcanoes* (pp. 897-910). Academic Press.

Crumpler, L. S., & Aubele, J. (2000). Volcanismon Venus. In H. Sigurdson, B. Houghton, H. Rymer, J. Stix, & S. McNutt (Eds.), *Encyclopedia of volcanoes* (pp. 727–770). Academic Press.

Crumpler, L. S., Aubele, J. C., Senske, D. A., Keddie, S. T., Magee, K. P., & Head, J. W. (1997). Volcanoes and centers of volcanism on Venus. In S. W. Bougher, D. M. Hunten, & R. J. Philips (Eds.), *Venus II: Geology, geophysics, atmosphere, and solar*

wind environment (pp. 697–756). The University of Arizona Press. https://doi.org/10.2307/j.ctv27tct5m.26

D'Incecco, P., Filiberto, J., López, I., Gorinov, D. A., Komatsu, G., Martynov, A., & Pisarenko, P. (2021). The young volcanic rises on Venus: A key scientific target for future orbital and in-situ measurements on Venus. *Solar System Research, 55*, 315-323. https://doi.org/10.1134/S0038094621040031

de Silva, S., & Lindsay, J. M. (2015). Primary volcanic landforms. In *The encyclopedia of volcanoes* (pp. 273-297). Academic Press.

D'Incecco, P., López, I., Komatsu, G., Ori, G. G., & Aittola, M. (2020). Local stratigraphic relations at Sandel crater, Venus: Possible evidence for recent volcano-tectonic activity in Imdr Regio. *Earth and Planetary Science Letters*, 546, 116410. https://doi.org/10.1016/j.epsl.2020.116410

D'Incecco, P., Müller, N., Helbert, J., & D'Amore, M. (2017). Idunn Mons on Venus: Location and extent of recently active lava flows. *Planetary and Space Science*, *136*, 25-33. https://doi.org/10.1016/j.pss.2016.12.002

Duong, T. (2007). ks: Kernel density estimation and kernel discriminant analysis for multivariate data in R. *Journal of Statistical Software*, 21(7), 1–16. https://doi.org/10.18637/jss.v021.i07

Duong, T., & Hazelton, M. (2003). Plug-in bandwidth matrices for bivariate kernel density estimation. *Journal of Nonparametric Statistics*, 15(1), 17–30. https://doi.org/10.1080/10485250306039

El Bilali, H., Ernst, R. E., Buchan, K. L., & Head, J. W. (2023). Dyke swarms record the plume stage evolution of the Atla Regio superplume on Venus. *Communications Earth & Environment*, *4*(1), 235.

El Bilali, H., Ernst, R. E., Buchan, K. L., & Head, J. W. (2023). Dyke swarms record the plume stage evolution of the Atla Regio superplume on Venus. *Communications Earth & Environment*, *4*(1), 235. https://doi.org/10.1038/s43247-023-00901-7

ESA (2024), "EnVision, Understanding why Earth's closest neighbour is so different", Definition Study Report (Red Book), ESA document reference ESA/SCI(2024), January, 2024, 11 pp.,https://sites.lesia.obspm.fr/envision/2024/03/01/envision-definition-study-report-redbook/

Ford, P. G. (1992). MGN V RDRS 5 global data record topographic V1.0 [Dataset]. NASA Planetary Data System. https://doi.org/10.17189/1522522

Galindo, I., Romero, M. C., Sánchez, N., & Morales, J. M. (2016). Quantitative volcanic susceptibility analysis of Lanzarote and Chinijo Islands based on kernel density estimation via a linear diffusion process. *Scientific reports*, *6*(1), 27381. https://doi.org/10.1038/srep27381

Germa, A., Connor, L. J., Cañon-Tapia, E., & Le Corvec, N. (2013). Tectonic and magmatic controls on the location of post-subduction monogenetic volcanoes in Baja California, Mexico, revealed through spatial analysis of eruptive vents. *Bulletin of Volcanology*, 75, 1-14. https://doi.org/10.1007/s00445-013-0782-6

Ghail, R. C., Hall, D., Mason, P. J., Herrick, R. R., Carter, L. M., & Williams, E. (2018). VenSAR on EnVision: Taking earth observation radar to Venus. *International journal of applied earth observation and geoinformation*, *64*, 365-376. https://doi.org/10.1016/j.jag.2017.02.008

Global Volcanism Program. (2013). In E. Venzke (Ed.), Volcanoes of the World, v. 4.9.0. Smithsonian Institution. https://doi.org/10.5479/si.GVP.VOTW4-2013

Guest, J. E., Beratan, K., Head, J. W., Bulmer, M. H., Weitz, C., Greeley, R., et al. (1992). Small volcanic edifices and volcanism in the plains of Venus. *Journal of Geophysical Research*, 97, 15949. https://doi.org/10.1029/92JE01438

Hahn, R. M., & Byrne, P. K. (2023). A Morphological and Spatial Analysis of Volcanoes on Venus. *Journal of Geophysical Research: Planets*, *128*(4), e2023JE007753. https://doi.org/10.1029/2023JE007753

Hahn, R.M. & Byrne, P. K. (2022). A global catalog of volcanoes and volcanic fields on Venus [V2] (version 2) [Dataset]. Washington University in St. Louis. https://doi.org/10.7936/8XY0-X885

Head, J. W., Crumpler, L. S., Aubele, J. C., Guest, J. E., & Saunders, R. S. (1992). Venus volcanism: Classification of volcanic features and structures, associations, and global distribution from Magellan data. *Journal of Geophysical Research: Planets*, 97, 13153–13197. https://doi.org/10.1029/92JE01273

Helbert, J., Müller, N., Kostama, P., Marinangeli, L., Piccioni, G., & Drossart, P. (2008). Surface brightness variations seen by VIRTIS on Venus Express and implications for the evolution of the Lada Terra region, Venus. *Geophysical Research Letters*, *35*(11). https://doi.org/10.1029/2008GL033609

Herrick, R. R., & Hensley, S. (2023). Surface changes observed on a Venusian volcano during the Magellan mission. *Science*, *379*(6638), 1205-1208.

Hughes, S. S., Wetmore, P. H., Casper, J. L., & Bonnichsen, B. (2002). Evolution of Quaternary tholeiitic basalt eruptive centers on the eastern Snake River Plain, Idaho. *Tectonic and Magmatic Evolution of the Snake River Plain Volcanic Province: Idaho Geological Survey Bulletin*, *30*, 363-385.

Ivanov, M. A., & Head, J. W. (2013). The history of volcanism on Venus. *Planetary and Space Science*, *84*, 66-92. https://doi.org/10.1016/j.pss.2013.04.018

Ivanov, M. A., & Head, J. W. (2004). Stratigraphy of small shield volcanoes on Venus: Criteria for determining stratigraphic relationships and assessment of relative are and temporal

abundance. *Journal of Geophysical Research*, 109(E10), E10001. https://doi.org/10.1029/2004JE002252

Jaquet, O., Connor, C., & Connor, L. (2008). Probabilistic methodology for long-term assessment of volcanic hazards. *Nuclear technology*, *163*(1), 180-189. https://doi.org/10.13182/NT08-A3980

Kappel, D., Arnold, G., & Haus, R. (2016). Multi-spectrum retrieval of Venus IR surface emissivity maps from VIRTIS/VEX nightside measurements at Themis Regio. *Icarus*, 265, 42-62. https://doi.org/10.1016/j.icarus.2015.10.014

Keddie, S. T., & Head, J. W. (1995). Formation and evolution of volcanic edifices on the Dione Regio rise, Venus. *Journal of Geophysical Research: Planets*, 100(E6), 11729-11754. https://doi.org/10.1029/95JE00822

Kiefer, W. S., & Hager, B. H. (1991). A mantle plume model for the equatorial highlands of Venus. *Journal of Geophysical Research: Planets*, *96*(E4), 20947-20966. https://doi.org/10.1029/91JE02221

Kiyosugi, K., Connor, C. B., Zhao, D., Connor, L. J., & Tanaka, K. (2010). Relationships between volcano distribution, crustal structure, and P-wave tomography: An example from the Abu monogenetic volcano group, SW Japan. *Bulletin of Volcanology*, 72(3), 331–340. https://doi.org/10.1007/s00445-009-0316-4

Kreslavsky, M. A., & Head III, J. W. (1999). Morphometry of small shield volcanoes on Venus: Implications for the thickness of regional plains. *Journal of Geophysical Research*, 104(E8), 18925–18932. https://doi.org/10.1029/1999JE001042

Le Corvec, N., Spörli, K. B., Rowland, J., & Lindsay, J. (2013). Spatial distribution and alignments of volcanic centers: Clues to the formation of monogenetic volcanic fields. *Earth-Science Reviews*, 124, 96–114. https://doi.org/10.1016/j.earscirev.2013.05.005

Lutz, T. M. (1986). An analysis of the orientations of large-scale crustal structures: A statistical approach based on areal distributions of pointlike features. *Journal of Geophysical Research: Solid Earth*, *91*(B1), 421-434. https://doi.org/10.1029/JB091iB01p00421

MacDonald, G. A. (1972). Composite lava flows on Haleakala Volcano, Hawaii. *Geological Society of America Bulletin*, *83*(10), 2971-2974. https://doi.org/10.1130/0016-7606(1972)83[2971:CLFOHV]2.0.CO;2

Mazzarini, F., Le Corvec, N., Isola, I., & Favalli, M. (2016). Volcanic field elongation, vent distribution, and tectonic evolution of a continental rift: The Main Ethiopian Rift example. *Geosphere*, *12*(3), 706-720. https://doi.org/10.1130/GES01193.1

McGill, G. E. (1994). Hotspot evolution and Venusian tectonic style. *Journal of Geophysical Research: Planets*, *99*(E11), 23149-23161. https://doi.org/10.1029/94JE02319

Morgan, L. A., & McIntosh, W. C. (2005). Timing and development of the Heise volcanic field, Snake River Plain, Idaho, western USA. *Geological Society of America Bulletin*, 117(3), 288–306. https://doi.org/10.1130/B25519.1

Mueller, N., Helbert, J., Hashimoto, G. L., Tsang, C. C., Erard, S., Piccioni, G., & Drossart, P. (2008). Venus surface thermal emission at 1 μm in VIRTIS imaging observations: Evidence for variation of crust and mantle differentiation conditions. *Journal of Geophysical Research: Planets*, *113*(E5). https://doi.org/10.1029/2008JE003118

Nakamura, K. (1977). Volcanoes as possible indicators of tectonic stress orientation—principle and proposal. *Journal of volcanology and Geothermal Research*, *2*(1), 1-16. https://doi.org/10.1016/0377-0273(77)90012-9

Phillips, R. J. (1994). Estimating lithospheric properties at atla regio, venus. *Icarus*, *112*(1), 147-170. https://doi.org/10.1006/icar.1994.1175

Richardson, J. A., Bleacher, J. E., & Glaze, L. S. (2013). The volcanic history of Syria Planum, Mars. *Journal of Volcanology and Geothermal Research*, 252, 1–13. https://doi.org/10.1016/j.jvolgeores.2012.11.007

Richardson, J. A., Bleacher, J. E., Connor, C. B., & Glaze, L. S. (2021). Small volcanic vents of the Tharsis volcanic province, Mars. *Journal of Geophysical Research: Planets*, 126(2), e2020JE006620. https://doi.org/10.1029/2020JE006620

Roberts, K. S., Stewart, S. A., Davies, R. J., & Evans, R. J. (2011). Sector collapse of mud volcanoes, Azerbaijan. *Journal of the Geological Society*, 168(1), 49–60. https://doi.org/10.1144/0016-76492010-115

Rogers, P. G., & Zuber, M. T. (1998). Tectonic evolution of Bell Regio, Venus: Regional stress, lithospheric flexure, and edifice stresses. *Journal of Geophysical Research: Planets*, *103*(E7), 16841-16853.

Romeo, I., Capote, R., & Anguita, F. (2005). Tectonic and kinematic study of a strike-slip zone along the southern margin of Central Ovda Regio, Venus: Geodynamical implications for crustal plateaux formation and evolution. Icarus, 175(2), 320-334. https://doi.org/10.1016/j.icarus.2004.11.007

Rooney, T. O., Bastow, I. D., & Keir, D. (2011). Insights into extensional processes during magma assisted rifting: Evidence from aligned scoria cones. *Journal of Volcanology and Geothermal Research*, *201*(1-4), 83-96. https://doi.org/10.1016/j.jvolgeores.2010.07.019

Schmidt, C., Laag, C., Whitehead, M., Profe, J., Aka, F. T., Hasegawa, T., & Kereszturi, G. (2022). The complexities of assessing volcanic hazards along the Cameroon Volcanic Line using spatial distribution of monogenetic volcanoes. *Journal of Volcanology and Geothermal Research*, *427*, 107558. https://doi.org/10.1016/j.jvolgeores.2022.107558

Senske, D. A., Head, J. W., Stofan, E. R., & Campbell, D. B. (1991). Geology and structure of Beta Regio, Venus: Results from Arecibo radar imaging. *Geophysical Research Letters*, *18*(6), 1159-1162.

Senske, D. A., Schaber, G. G., & Stofan, E. R. (1992). Regional topographic rises on Venus: Geology of western Eistla Regio and comparison to Beta Regio and Atla Regio. *Journal of Geophysical Research: Planets*, *97*(E8), 13395-13420. https://doi.org/10.1029/92JE01167

Shalygin, E. V., Basilevsky, A. T., Markiewicz, W. J., Titov, D. V., Kreslavsky, M. A., & Roatsch, T. (2012). Search for ongoing volcanic activity on Venus: Case study of Maat Mons, Sapas Mons and Ozza Mons volcanoes. *Planetary and Space Science*, *73*(1), 294-301. https://doi.org/10.1016/j.pss.2012.08.018

Shalygin, E. V., Markiewicz, W. J., Basilevsky, A. T., Titov, D. V., Ignatiev, N. I., & Head, J. W. (2015). Active volcanism on Venus in the Ganiki Chasma rift zone. *Geophysical Research Letters*, *42*(12), 4762-4769. https://doi.org/10.1002/2015GL064088

Silverman, B. W. (1998). Density estimation for statistics and data analysis. Routledge.

Smrekar, S. E. (1994). Evidence for active hotspots on Venus from analysis of Magellan gravity data. *Icarus*, *112*(1), 2-26. https://doi.org/10.1006/icar.1994.1166

Smrekar, S. E., & Sotin, C. (2012). Constraints on mantle plumes on Venus: Implications for volatile history. *Icarus*, *217*(2), 510-523. https://doi.org/10.1016/j.icarus.2011.09.011

Smrekar, S. E., Davaille, A., & Sotin, C. (2018). Venus interior structure and dynamics. *Space Science Reviews*, *214*, 1-34. https://doi.org/10.1007/s11214-018-0518-1

Smrekar, S. E., Stofan, E. R., Mueller, N., Treiman, A., Elkins-Tanton, L., Helbert, J., ... & Drossart, P. (2010). Recent hotspot volcanism on Venus from VIRTIS emissivity data. *Science*, *328*(5978), 605-608. https://doi.org/10.1126/science.1186785

Smrekar, S., Hensley, S., Nybakken, R., Wallace, M. S., Perkovic-Martin, D., You, T. H., ... & Mazarico, E. (2022, March). VERITAS (Venus emissivity, radio science, InSAR, topography, and spectroscopy): a discovery mission. In *2022 IEEE Aerospace Conference (AERO)* (pp. 1-20). IEEE. https://doi.org/10.1109/AERO53065.2022.9843269.

Solomon, S. C., Smrekar, S. E., Bindschadler, D. L., Grimm, R. E., Kaula, W. M., McGill, G. E., ... & Stofan, E. R. (1992). Venus tectonics: An overview of Magellan observations. *Journal of Geophysical Research: Planets*, *97*(E8), 13199-13255. https://doi.org/10.1029/92JE01418

Stofan, E. R., Brian, A. W., & Guest, J. E. (2005). Resurfacing styles and rates on Venus: Assessment of 18 Venusian quadrangles. *Icarus*, *173*(2), 312-321. https://doi.org/10.1016/j.icarus.2004.08.004

Stofan, E. R., Sharpton, V. L., Schubert, G., Baer, G., Bindschadler, D. L., Janes, D. M., & Squyres, S. W. (1992). Global distribution and characteristics of coronae and related features on Venus: Implications for origin and relation to mantle processes. *Journal of Geophysical Research: Planets*, 97(E8), 13347-13378. https://doi.org/10.1029/92JE01314

Stofan, E. R., Smrekar, S. E., Bindschadler, D. L., & Senske, D. A. (1995). Large topographic rises on Venus: Implications for mantle upwelling. *Journal of Geophysical Research: Planets*, *100*(E11), 23317-23327. https://doi.org/10.1029/95JE01834

Stofan, E. R., Smrekar, S. E., Mueller, N., & Helbert, J. (2016). Themis Regio, Venus: Evidence for recent (?) volcanism from VIRTIS data. *Icarus*, *271*, 375-386. https://doi.org/10.1016/j.icarus.2016.01.034

Stofan, E. R.J. W. HeadD. B. CampbellS. H. ZiskA. F. BogomolovO. N. RzhigaA. T. BasilevskyN. Armand, Geology of a rift zone on Venus: Beta Regio and Devana Chasma, *Geol. Soc. Am. Bull.*, 101, 143–156, 1989

Tadini, A., Bevilacqua, A., Neri, A., Cioni, R., Aspinall, W. P., Bisson, M., ... & Pistolesi, M. (2017). Assessing future vent opening locations at the Somma-Vesuvio volcanic complex: 2. Probability maps of the caldera for a future Plinian/sub-Plinian event with uncertainty quantification. *Journal of Geophysical Research: Solid Earth*, *122*(6), 4357-4376. https://doi.org/10.1002/2016JB013860

Tadini, A., Bonali, F. L., Corazzato, C., Cortes, J. A., Tibaldi, A., & Valentine, G. A. (2014). Spatial distribution and structural analysis of vents in the Lunar Crater Volcanic Field (Nevada, USA). *Bulletin of volcanology*, *76*, 1-15. https://doi.org/10.1007/s00445-014-0877-8

Thomson, B. J., & Lang, N. P. (2016). Volcanic edifice alignment detection software in MATLAB: Test data and preliminary results for shield fields on Venus. *Computers & Geosciences*, 93, 1–11. https://doi.org/10.1016/j.cageo.2016.04.012

Tokçaer, M., Agostini, S., & Savaşçin, M. Y. (2005). Geotectonic setting and origin of the youngest Kula volcanics (western Anatolia), with a new emplacement model. *Turkish Journal of Earth Sciences*, *14*(2), 143-166.

Valentine, G. A., & Connor, C. B. (2015). Basaltic volcanic fields. In *The encyclopedia of volcanoes* (pp. 423-439). Academic Press.

Wadge, G., & Cross, A. (1988). Quantitative methods for detecting aligned points: an application to the volcanic vents of the Michoacan-Guanajuato volcanic field, Mexico. *Geology*, *16*(9), 815-818. https://doi.org/10.1130/0091-7613(1988)016<0815:QMFDAP>2.3.CO;2

Wand, M. P., & Jones, M. C. (1993). Comparison of smoothing parameterizations in bivariate kernel density estimation. *Journal of the American Statistical Association*, 88(422), 520–528. https://doi.org/10.1080/01621459.1993.10476303

Wand, M. P., & Jones, M. C. (1994). Multivariate plug-in bandwidth selection. *Computational Statistics*, 9, 97–116.

Weller, J. N., Martin, A. J., Connor, C. B., Connor, L. J., & Karakhanian, A. (2006). Modelling the spatial distribution of volcanoes: An example from Armenia. In H. M. Mader, S. G.

Coles, C. B. Connor, & L. J. Connor (Eds.), Statistics in volcanology (pp. 77–88). Geological Society of London. https://doi.org/10.1144/IAVCEI001.7

Zuccarello, F., Bilotta, G., Ganci, G., Proietti, C., & Cappello, A. (2023). Assessing impending hazards from summit eruptions: the new probabilistic map for lava flow inundation at Mt. Etna. *Scientific Reports*, *13*(1), 19543. ; https://doi.org/10.3390/rs14061366

Appendix

A.1 Datasets used in Chapter 2

All datasets and associated ReadME files developed and used in chapter two are publicly available in two locations:

1. Supplementary data files published with the corresponding paper.

   Hahn, R. M., & Byrne, P. K. (2023). A Morphological and Spatial Analysis of Volcanoes on Venus. *Journal of Geophysical Research: Planets*, 128(4), e2023JE007753. https://doi.org/10.1029/2023JE007753
2. Washington University in St. Louis Research Data

   Hahn, Rebecca M. and Byrne, Paul K., "A Global Catalog of Volcanoes and Shield Fields on Venus." [Dataset Version 2]. Washington University in St. Louis (2023). https://doi.org/10.7936/8xy0-x885

A 1.1 Brief Description of Datasets used in Chapter 2:

Title of Dataset: A Global Catalog of Volcanoes and Volcanic Fields on Venus [Version 2]

General Description of Chapter 2 Datasets:

This database includes 8 shapefiles and 8 corresponding csv files. The shapefiles denote the spatial geometry (point or polygon) of volcanoes and volcanic fields on Venus, and corresponds to the tabular data in each accompanying csv file.

1. Filename: 01_small_lessthan5km.shp

   Short description: Shapefile containing point locations for volcanoes <5 km in diameter on Venus. Data is in Equirectangular Venus projection.

2. Filename: 01_small_lessthan5km.csv

   Short description: CSV table containing point locations for volcanoes <5 km in diameter on Venus.

3. Filename: 02_small_lessthan5km_lowres.shp

   Short description: Shapefile containing point locations for volcanoes <5 km in diameter on Venus that are considered "low resolution". Data is in Equirectangular Venus projection.

4. Filename: 02_small_lessthan5km_lowres.csv

   Short description: CSV table containing point locations for volcanoes <5 km in diameter on Venus that are considered "low resolution".

5. Filename: 03_intermediate_5to100km.shp

   Short description: Shapefile containing polygon geometry and associated morphological data for volcanoes 5–100 km in diameter on Venus. Data is in Equirectangular Venus projection.

6. Filename: 03_intermediate_5to100km.csv

   Short description: CSV table containing centroid coordinates and morphological data for volcanoes 5–100 km in diameter on Venus.

7. Filename: 04_intermediate_greaterthan50km.shp

   Short description: Shapefile containing polygon geometry and associated morphological data for a subset of volcanoes 50–100 km in diameter on Venus that were high enough resolution for height to be calculated using the Magellan altimetry. Data is in Equirectangular Venus projection.

8. Filename: 04_intermediate_greaterthan50km.csv

   Short description: Shapefile containing polygon geometry and associated morphological data for a subset of volcanoes 50–100 km in diameter on Venus that were high enough resolution for height to be calculated using the Magellan altimetry. Data is in Equirectangular Venus projection.

9. Filename: 05_large_greaterthan100km.shp

   Short description: Shapefile containing polygon geometry and associated morphological data for volcanoes >100 km in diameter on Venus. Data is in Equirectangular Venus projection.

10. Filename: 05_large_greaterthan100km.csv

    Short description: CSV table containing centroid coordinates and morphological data for volcanoes >100 km in diameter on Venus.

11. Filename: 06_greaterthan50km_Herrick.shp

    Short description: Shapefile containing polygon geometry and associated morphological data for a subset of volcanoes >50 km in diameter on Venus that fall within the Herrick et al. (2012) stereo-derived DEMs. Data is in Equirectangular Venus projection.

12. Filename: 06_greaterthan50km_Herrick.csv

    Short description: CSV table containing centroid coordinates and morphological data for volcanoes >50 km in diameter on Venus that fall within the Herrick et al. DEMs.

13. Filename: 07_deformed.shp

    Short description: Shapefile containing polygon geometry and associated morphological data for volcanoes that have undergone gravitational deformation on Venus. Data is in Equirectangular Venus projection.

14. Filename: 07_deformed.csv

    Short description: CSV table containing centroid coordinates and morphological data for volcanoes that have undergone gravitational deformation on Venus.

15. Filename: 08_volcanic_fields.shp

    Short description: Shapefile containing polygon geometry and associated morphological data for volcanic fields on Venus. Data is in Equirectangular Venus projection.

16. Filename: 08_volcanic_fields.csv

    Short description: CSV table containing centroid coordinates and morphological data for volcanic fields on Venus.

A.2 Datasets used in Chapter 3

All datasets and associated ReadME files developed and used in chapter three are publicly available in two locations:

1. Supplementary data files published with the corresponding paper.

   Hahn, R. M., & Byrne, P. K. (2024). A Global Survey of Gravitationally Deformed Volcanoes on Venus. *Journal of Geophysical Research: Planets*, 129(2), e2023JE008241. http://dx.doi.org/10.1029/2023JE008241

2. Washington University in St. Louis Research Data

   Hahn, Rebecca M. and Byrne, Paul K., "A Global Catalog of Deformed Volcanoes on Venus." [Dataset Version 1]. Washington University in St. Louis (2023). https://doi.org/10.7936/6rxs-103646

A 2.1 Brief Description of Datasets used in Chapter 3:

***Title of Dataset*:** A Gl2bal Catalog of Deformed Volcanoes on Venus

General Description of Chapter 3 Datasets:

This catalog includes one shapefile and one CSV file. The CSV file is tabular versions of the shapefile, and contains data on the morphology and spatial relationships between 162 deformed volcanoes on Venus.

Relationship with Chapter 2 Datasets*:*

In our Global Catalog of Volcanoes and Volcanic Fields on Venus (Hahn & Byrne, 2023), we document a unique subset of volcanoes that have undergone gravitational deformation (07_deformed.shp/07_deformed.csv). In this new dataset we have refined our selection of this subset of deformed volcanoes, and have expanded our morphological analysis. Our initial dataset

of deformed volcanoes (07_deformed.shp/07_deformed.csv) contained 182 deformed volcanoes and included the latitude and longitude at the center of each volcano, and the area of the deformed volcano (which may have included debris aprons or other deformational features that extend away from the base of the edifice). The updated and refined version of this dataset contains 162 deformed volcanoes, and includes an additional 11 data fields (e.g., average deformed volcano width, and length).

1. Filename: Deformed_volcanoes_Venus.shp

   Short description: Shapefile containing polygon locations, morphological data, and spatial relationships for deformed volcanoes on Venus. Data is in Equirectangular Venus projection.

2. Filename: Deformed_volcanoes_Venus.csv

   Short description: CSV table containing location data, morphological data, and spatial relationships for deformed volcanoes on Venus.

A.3 Datasets used in Chapter 4

Locations of volcanoes ≤20 km in diameter used in Chapter 4 are from our Global Catalog of Volcanoes and Volcanic Fields on Venus (See Appendix A.1 for a detailed description and repository information on this dataset)

Datasets from our Global Catalog of Volcanoes and Volcanic Fields on Venus used in Chapter 4:

1. 01_small_lessthan5km.shp/ 01_small_lessthan5km.csv
2. 02_small_lessthan5km_lowres.shp/ 02_small_lessthan5km_lowres.csv
3. 03_intermediate_5to100km.shp/ 03_intermediate_5to100km.csv (filtered to only include volcanoes 5–20 km in diameter)

A.3.1 Volcano Alignment Analysis Parameters

Volcano alignment analysis was performed following the methods established by Cebria et al. (2011), where distances and azimuths between volcanoes in a given volcanic field are filtered by a critical value, d_{crit}. Cebria et al. (2011) found that eruptive centers are more closely related to neighboring vents, than those far away, which instead record the overall orientation of the volcanic field. Therefore, the optimum cutoff length is given by the critical value, d_{crit} which is greater than or equal to one-third of the mean azimuth length, μ, minus the standard deviation, σ.

$$d_{crit} \leq \frac{\mu - \sigma}{3}$$

Table A.3.1
Values calculated for vent alignment analysis at topographic rises

Topographic Rise	Critical Value[a] (km)	Omnibus Test[b] P-value at 0.05 significance level	Mean[c] (μ)	Standard Deviation[d] (σ)	$\mu + 1\sigma$[e]	Dominant orientation[f] (°)
Atla	187.16	3.97×10^{-49}	1125.00	151.14	1276.10	120–180
Bell	57.34	2.82×10^{-10}	69.83	4.53	74.36	90–120
Beta	166.00	1.48×10^{-137}	762.67	128.83	891.50	0–30
Central Eistla	122.62	2.91×10^{-229}	2208.00	91.05	2299.10	60–150
Dione	100.62	2.02×10^{-301}	2147.00	131.93	2278.90	150–180
Imdr	70.10	6.76×10^{-24}	548.30	44.87	593.20	60–90
Laufey	101.20	2.34×10^{-36}	854.67	138.58	989.25	150–180
Themis	199.81	1.16×10^{-86}	1377.00	193.77	1570.80	0–30, 60–90
Western Eistla	152.18	0	6441.00	573.30	7014.10	120–150

[a]Critical value is calculated using the formula above, and filtering out all distances and azimuths greater than that value (Cebria et al., 2011).
[b]The Omnibus test for circular uniformity (Berens, 2009). The null hypothesis of this test is that the dataset is uniformly distributed around the unit circle. If $p < 0.05$, the null hypothesis is rejected.
[c]Mean azimuth value of inter-volcano relationships with data divided into 12 bins.
[d]Standard deviation of inter-volcano relationships with data divided into 12 bins.
[e]Mean azimuth plus one standard deviation of inter-volcano relationships.
[f]Bins that have values > $\mu + 1\sigma$ have anomalously high inter-volcano relationships and likely represent a dominant vent orientation.

Table A.3.2
Values calculated for vent alignment analysis at volcanic fields

Volcanic Field	Critical Value[a] (km)	Omnibus Test[b] P-value at 0.05 significance level	Mean[c] (μ)	Standard Deviation[d] (σ)	$\mu + 1\sigma$[e]	Dominant orientation[f] (°)
VF1	78.22	1.31×10^{-4}	41.67	7.05	48.72	90–120
VF2	97.07	3.73×10^{-76}	584.00	28.90	612.90	30–60
VF3	72.44	4.13×10^{-11}	164.33	27.54	191.87	150–180
VF4	55.89	3.91×10^{-13}	225.33	22.68	248.01	60–90
VF5	134.56	2.95×10^{-63}	3382.20	300.42	3682.60	150–180
VF6	42.21	3.69×10^{-6}	67.50	16.17	83.67	60–90
VF7	92.61	0	4130.20	153.56	4283.70	90–120
VF8	126.04	0	8845.30	265.16	9110.50	120–150
VF9	68.38	2.90×10^{-57}	766.67	24.98	791.65	30–60

[a]Critical value is calculated using the formula above, and filtering out all distances and azimuths greater than that value (Cebria et al., 2011).
[b]The Omnibus test for circular uniformity (Berens, 2009). The null hypothesis of this test is that the dataset is uniformly distributed around the unit circle. If $p < 0.05$, the null hypothesis is rejected.
[c]Mean azimuth value of inter-volcano relationships with data divided into 12 bins.
[d]Standard deviation of inter-volcano relationships with data divided into 12 bins.
[e]Mean azimuth plus one standard deviation of inter-volcano relationships.
[f]Bins that have values > $\mu + 1\sigma$ have anomalously high inter-volcano relationships and likely represent a dominant vent orientation.